A synthetic dendritic cell platform for immune activation

Loek Eggermont

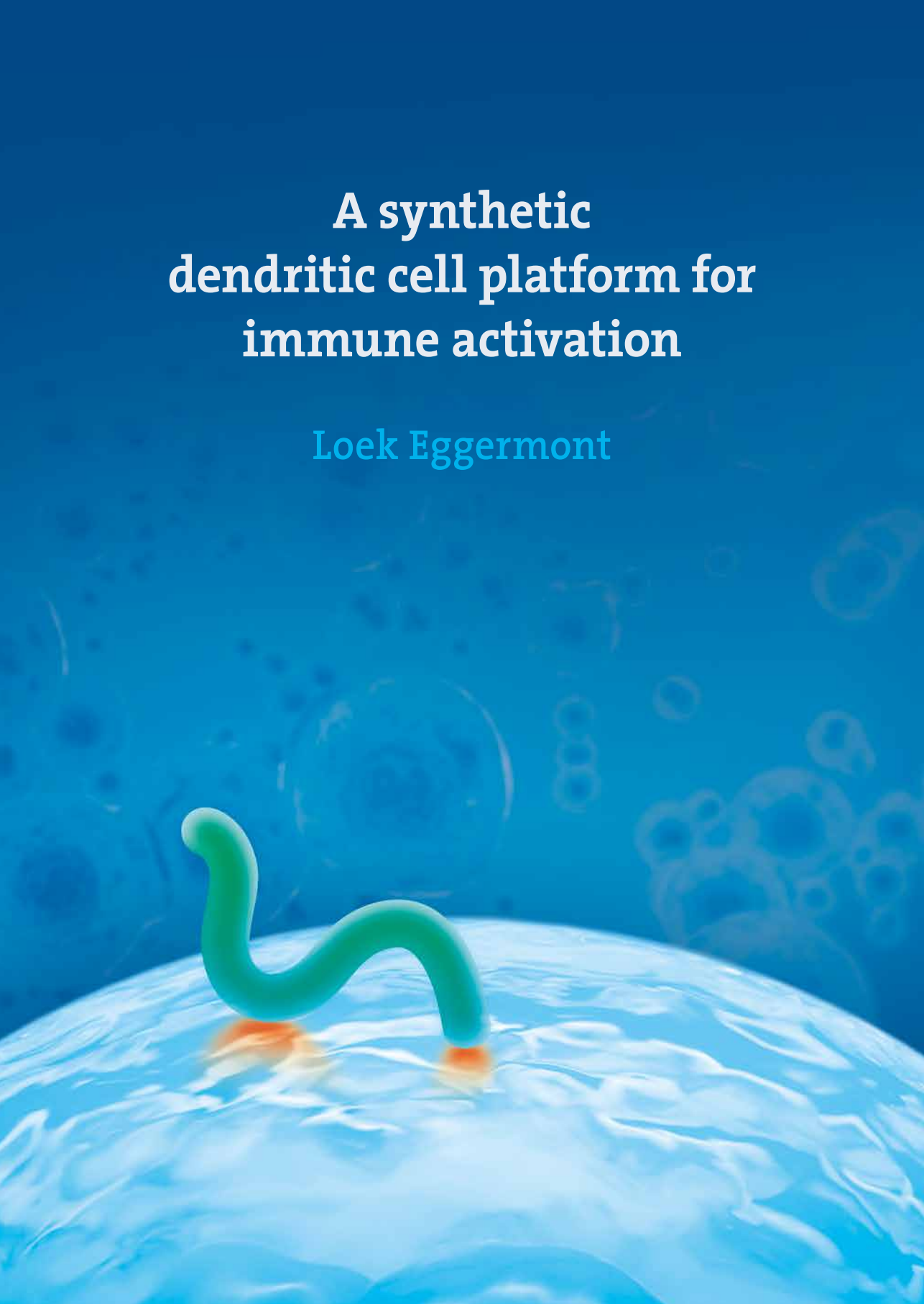

The research presented in this thesis was performed at the Department of Tumor Immunology, Radboud Institute for Molecular Life Sciences, Radboud University Medical Center, Nijmegen, the Netherlands. The research presented in this thesis was financially supported by the European Research Council (ERC).

ISBN
978-94-92896-55-1

Design/lay-out
Promotie In Zicht, Arnhem

Print
Ipskamp Printing, Enschede

A synthetic dendritic cell platform for immune activation

Proefschrift

ter verkrijging van de graad van doctor
aan de Radboud Universiteit Nijmegen
op gezag van de rector magnificus prof. dr. J.H.J.M. van Krieken,
volgens besluit van het college van decanen
in het openbaar te verdedigen op woensdag 19 september 2018
om 14.30 uur precies

door

Loek Josephus Eggermont
geboren op 3 augustus 1990
te Kekerdom

Promotor
Prof. dr. C.G. Figdor

Copromotoren
Dr. J. Tel (Technische Universiteit Eindhoven)
Dr. R. Hammink

Manuscriptcommissie
Prof. dr. I. Joosten (voorzitter)
Dr. P.H.J. Kouwer
Prof. dr. ir. J.C.M. van Hest (Technische Universiteit Eindhoven)

Contents

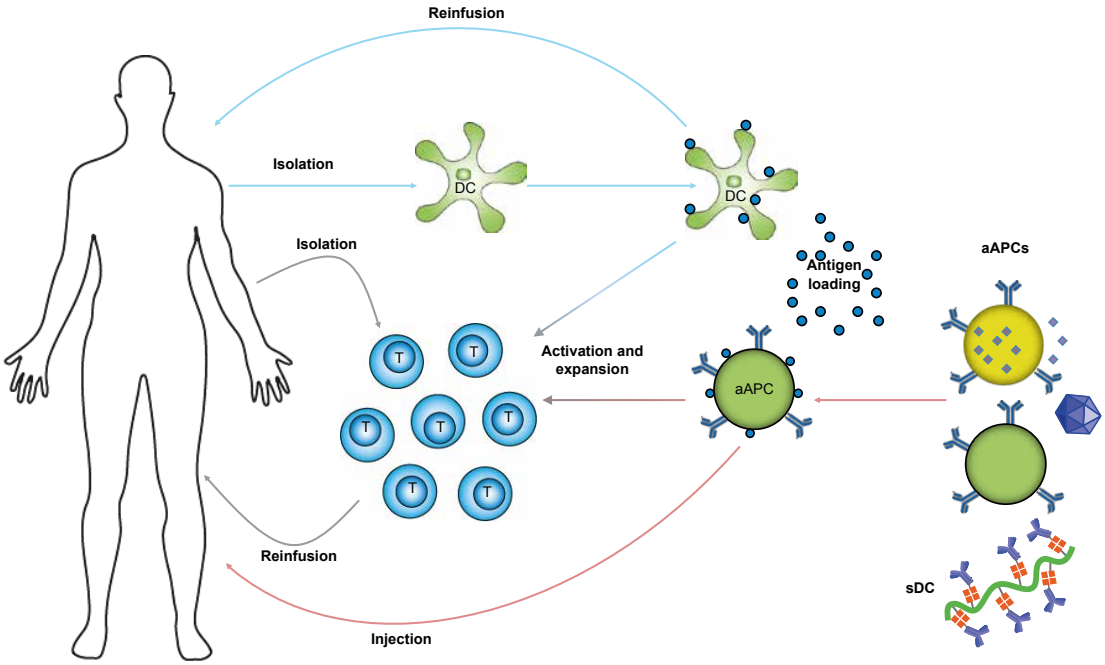
Reinfusion
Isolation
DC
DC
Isolation
Antigen
loading
aAPCs
Activation and
expansion
aAPC
T
T
T
T
T
T
T
Reinfusion
sDC
Injection

1

Introduction and scope of this thesis

Nanofilaments as novel artificial antigen-presenting cells:
A promising approach towards efficient cancer immunotherapy

Loek Eggermont, Leonie Paulis, Jurjen Tel, Carl G. Figdor

Adapted from: Trends in Biotechnology, 2014, 32(9), 456-465

Abstract

Active anti-cancer immune responses depend on efficient presentation of tumor antigens and co-stimulatory signals by antigen-presenting cells (APCs). Therapy with autologous natural APCs is costly and time-consuming, and results in variable outcomes in clinical trials. Therefore, development of artificial APCs (aAPCs) has attracted significant interest as an alternative. We discuss the characteristics of various types of acellular aAPCs, and their clinical potential in cancer immunotherapy. The size, shape, and ligand mobility of aAPCs, and their presentation of different immunological signals, can all have significant effects on cytotoxic T cell activation. Novel optimized aAPCs, combining carefully tuned properties, may lead to efficient immunomodulation and improved clinical responses in cancer immunotherapy. Semi-flexible nanofilaments based on polyisocyanopeptides may therefore be particularly promising scaffolds for development of aAPCs.

Keywords: artificial antigen-presenting cell, synthetic dendritic cell, immunotherapy, cancer

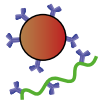

1.1 Towards efficient cancer immunotherapy: advances in developing artificial antigen-presenting cells

Advances in cancer immunotherapy

In cancer immunotherapy, the immune system is either passively or actively exploited to target and kill cancer cells. In this way, higher specificity for malignant cells may be achieved than with conventional cancer therapeutics. This approach thus avoids off-target toxicities while still inducing highly potent anti-cancer responses. By targeting tumor cells or their microenvironment, passive immunotherapy exploiting monoclonal antibodies has proven beneficial clinical effects in several malignancies [1,2]. In active immunotherapy, immune cells are stimulated and instructed to actively fight cancer and, although more challenging, this approach is extremely promising. Active immunotherapy is highly dependent on efficient stimulation of antigen-specific immune cells, such as killer T cells and antibody-producing B cells. In adoptive T cell transfer, isolated autologous tumor-specific T cells are expanded *ex vivo* and, after sufficient stimulation, are re-infused into the cancer patient, where these cells are expected to elicit potent anti-tumor responses (Figure 1, gray arrows) [3].

A more recent trend in adoptive T cell transfer exploits molecular biology approaches to create more active T cells with higher target affinities and prolonged lifetimes (Figure 1, green arrow). For this purpose, T cells have been constructed that express transgenic T cell receptors (TCRs) with increased affinity for their peptide-major histocompatibility complex (MHC) complexes, or chimeric antigen receptors that can target antigens independent of MHC through antibody-derived ligand binding domains. Engineered T cells have been clinically applied and show good results, but several issues need to be addressed, including on-target and off-target toxicities, undesirable immune responses to chimeric antigen receptors and engineered TCRs, and the possibility of transformation, either because of virus-related insertional mutagenesis or due to misguided T cell lifetime engineering. Furthermore, engineered T cells do not differentiate into memory cells, and therefore no immunological memory is created. These fundamental issues need to be resolved before engineered T cells can be broadly implemented as anti-cancer therapy [4,5].

In vivo, induction of T cell responses is highly dependent on interactions with professional antigen-presenting cells (APCs), in particular dendritic cells (DCs), which present tumor-specific antigens. Therefore, to induce *in vivo* T cell activation, cancer patients are vaccinated with APCs [6]. In contrast to engineered T cells, these approaches make use of physiological interactions, which minimizes the risk of serious adverse side effects. Natural APCs, in particular DCs, are well equipped to induce efficient activation and expansion of tumor antigen-specific naïve T cells, which can lead to induction of large populations of T cells, including $CD8^+$ cytotoxic T lymphocytes (CTLs) that can kill cancer cells (Figure 1, blue arrows). Several studies

now indicate that the use of natural APCs in cancer treatment is associated with a beneficial clinical outcome with minor adverse side effects, emphasizing the promise of active immunotherapy [3,6–8].

Unfortunately, the use of natural APCs such as DCs over the years has also highlighted several serious limitations. Lack of knowledge of the optimal antigen-loaded DC combined with deleterious effects of immunosuppressive factors in the tumor microenvironment may be responsible for the mixed results that observed in clinical trials [9–12]. In addition, isolation and *ex vivo* stimulation of autologous DCs proved time-consuming and expensive, and the quality of *ex vivo*-generated DCs can be variable [9,13,14]. The use of patient-derived, autologous DCs therefore limits standardization of DC-based treatment protocols [9,14].

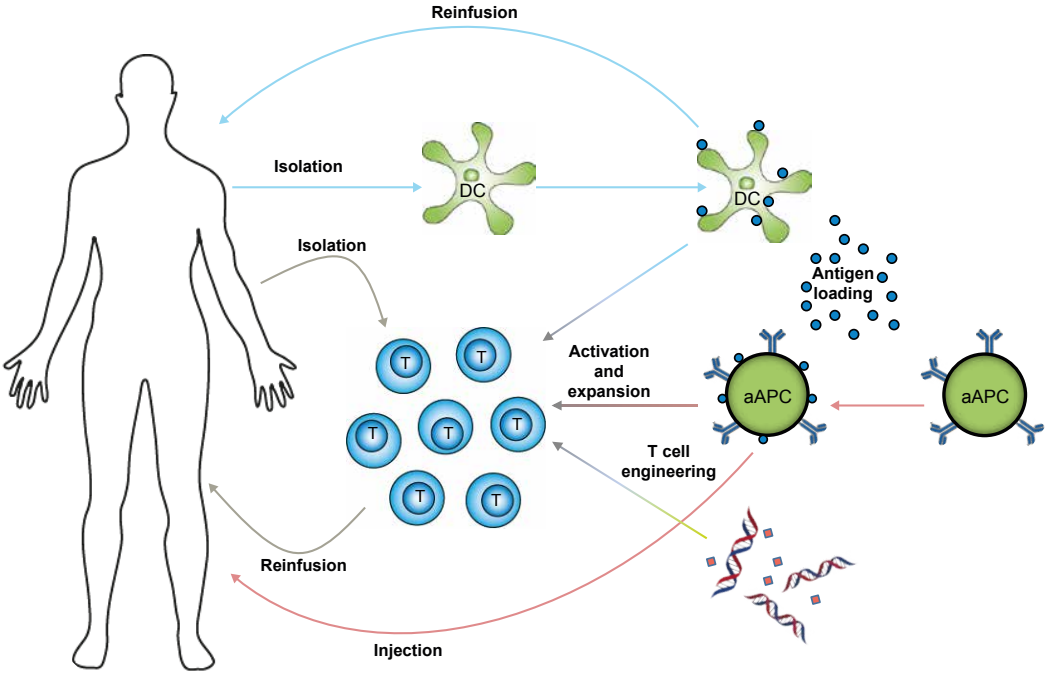

Figure 1 Different strategies for active cancer immunotherapy. T cell activation can be induced either *ex vivo* or *in vivo* by autologous DCs (blue arrows), aAPCs (red arrows), or by engineering of T cells through transgenic delivery of TCRs and life-time engineering, for example using small molecule inhibitors (green arrow). *Ex vivo*-activated autologous T cells can be adoptively transfered into patients (grey arrows), to specifically kill cancer cells. Alternatively, injection of APCs can lead to *in vivo* aAPC immunotherapy without the need for autologous cell cultures (red arrows).

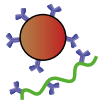

Artificial APCs for T cell activation

To overcome the disadvantages and difficulties in using autologous APCs, artificial APCs (aAPCs) have been developed as an alternative for both *ex vivo* and *in vivo* induction of tumor-specific CTLs (Figure 1, red arrows) [15,16]. Whereas natural APCs may be influenced by the tumor microenvironment and unknown signaling moieties may be present on their surface, artificial presentation of antigens allows for better defined systems with more control over the signals presented. Furthermore, the use of aAPCs does not require time-consuming and expensive cell-culture strategies and can be developed into an off-the-shelf technology [14,15]. However, aAPCs are not equipped with a machinery to actively migrate into tissues. In this review, advances in aAPC development are discussed for both *ex vivo* and *in vivo* application in cancer immunotherapy.

Cell-based aAPCs

Genetically modified xenogeneic or allogeneic cells, such as *Drosophila* cells, murine fibroblasts, and human erythroleukemia cells, have been used as aAPCs [17–19]. These cells are easier to handle and are better defined than DCs, allowing for more control over the delivered signals. In addition, cellular aAPCs are stable cell lines that can be stored for extended times and as such can thus be obtained from a readily accessible source [16]. However, a major disadvantage is their allogeneic nature. The use of human cell-based aAPCs has recently been extensively reviewed, so this review is restricted to the use of acellular aAPCs for active cancer immunotherapy [20].

Acellular synthetic aAPCs for efficient expansion of CTLs

Although cellular aAPCs can induce high expansion rates of $CD8^+$ T cells, they do not easily allow for specific control of expression levels of T cell-activating signals. In addition, non-tumor antigens and other stimulatory or inhibitory molecules may be present on cellular aAPCs [13,21]. To better define the delivery of distinct signals, red blood cells have been used as scaffolds to chemically introduce T cell stimulatory proteins [22]. To circumvent the use of allogeneic cells altogether, acellular aAPCs have been developed. Compared to cellular aAPCs, acellular aAPCs allow for a more stringent control over the signals delivered and are attractive tools because of their relatively easy preparation. These synthetic entities can be designed to be either non-specific or antigen-specific by presenting T cell-activating antibodies (such as anti-CD3) or peptide-MHC complexes, respectively. In general, aAPCs approaches have focused on induction of $CD8^+$ CTLs through MHC I stimulation, because these cells are capable of antigen-specific tumor cell lysis. Other immune cells, such as $CD4^+$ T helper cells, can assist in shaping the anti-cancer immune response by helping in the activation of CTLs. Therefore, efforts have also been made, albeit to a lesser extent, to activate these cells via MHC II. Artificial APCs comprising various sizes, surface ligand

distributions, ligand mobilities, and shapes have been developed, and these properties can all affect T cell activation. The wide variety of acellular aAPC structures (Figure 2, Table S1) reflects different attempts to mimic different aspects of natural DCs.

Rigid spherical microsized aAPCs

To mimic natural APCs, several cell-sized, rigid, bead-based aAPCs have been developed. Because of their homogenous size distribution and straightforward functionalization, these beads have been extremely useful in determining the various signals necessary for T cell activation. In addition, these more simplistic systems have been used to induce T cell activation for clinical purposes [16].

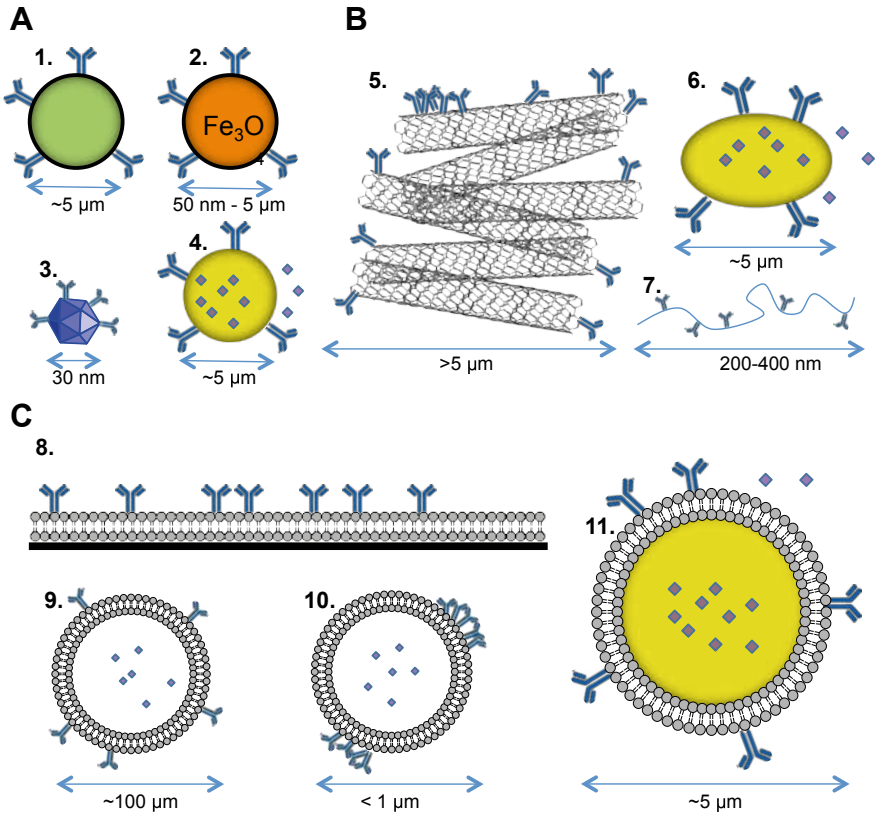

Figure 2 Different types of synthetic aAPCs. **(A)** rigid spherical particles (**1.** polystyrene latex microbeads, **2.** magnetic nano- and microparticles, **3.** nanosized quantum dots and **4.** PLGA microspheres) **(B)** Non-spherical particles (**5.** carbon nanotube bundles, **6.** ellipsoid PLGA microparticles and **7.** nanoworms) and **(C)** Fluidic lipid bilayer-containing systems (**8.** 2D-supported lipid bilayers (2D-SLBs), **9.** liposomes, **10.** RAFTsomes/microdomain-liposomes and **11.** SLB-particles).

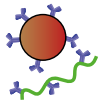

Latex microbeads

To induce T cell expansion, spherical polystyrene beads can be coated with antibodies against CD3 and CD28. It was shown that T cell activation was optimally induced by microbeads ranging in size between 4 and 5 μm [23]. Ligand density and bead size, rather than the amount of beads, were important parameters for T cell activation. However, these non-specific particles could only induce long-term proliferation of $CD4^+$ helper T cells, and did not support the growth of $CD8^+$ CTLs for extended culture periods, indicating that $CD8^+$ T cells require additional stimulation to maintain their effector functions [24]. Furthermore, anti-CD3 stimulation has been associated with a loss of antigen specificity when expanding enriched $CD8^+$ T cell populations [19]. These reported problems can be avoided by replacing anti-CD3 with specific peptide-MHC complexes in combination with co-stimulatory signals [25].

These beads were successfully used to produce large numbers of functional antigen-specific CTLs against different targets, including melanoma antigens TRP-2 and Mart-1 [16,26]. To induce long-term expansion of $CD8^+$ T cells using latex microbeads, cells require the presence of IL-2. It was recently demonstrated that IL-2 may also be replaced by IL-21 or a combination of IL-15 and IL-21, which leads to unique functional CTL phenotypes [27,28]. Improved stimulation of T cells can also be achieved by coating beads with anti-4-1BB or 4-1BBL, ICAM-1, and CD83 [26,29,30].

A single peptide-MHC complex has a low intrinsic affinity for its specific TCR [31]. To enhance this affinity, multimers of MHC complexes have been developed, such as human leukocyte antigen (HLA) tetramers [32–34]. In addition, IgG-HLA dimers, which consist of IgG molecules containing two MHC complexes that can be easily uploaded with any desired antigen, have been developed. In this way, aAPCs can be made antigen-specific by uploading IgG-HLA dimers with any desired epitope [35]. Dimers have also been applied to synthetic nanoparticles, including dextran-coated iron oxide magnetic particles (50-100 nm) and dextran-coated quantum dots (30 nm). Although previous research using bead-based systems indicated only very low T cell activation below 3 μm [23], these nano-aAPCs showed improved *in vivo* efficacy compared to microsized beads. Although first studies demonstrated that these particles exhibited similar or even improved *ex vivo* T cell activation, the same group later showed better activation for micro-aAPCs using this type of particle [36], which is in accordance with previous literature [23]. Their ability to stimulate T cells despite their small size may be attributed to the use of IgG-MHC, which contains a flexible hinge region [37]. In general, it is thought that microbeads are better suited to stimulate T cells because, owing to the lower curvature of their surface, a microbead can make more interactions with the cell than a nanosized spherical bead. Recently, this was demonstrated by directly comparing different nano-and microparticles as pMHC/anti-CD28-presenting aAPCs for CD8+ T cell activation. Cell-sized microbeads only require 3 pMHC per T-cell for efficient activation, whereas particles of 300 and

600 nms need about 200 pMHCs per T-cell, demonstrating that particle concentration and ligand density are important parameters for efficient activation. With sufficient ligand density, these nanoparticles can stimulate TCR signaling microclusters, whereas microbeads can probably trigger multiple clusters simultaneously. At the same time, 50 nm aAPCs require more than 10.000 pMHCs per T cell and can only efficiently stimulate T cells in saturating conditions, owing to the fact that only single TCRs are targeted by this type of particle. Thus, 300-nm nanoparticles can be developed into efficient nano-aAPCs, but are not as efficient as cell-sized microbeads [38].

Polystyrene-coated magnetic microbeads

Because polystyrene particles are not biodegradable and may be toxic or induce embolisms *in vivo,* they must be removed from the CTL population before *ex vivo*-expanded T cells are infused into patients [9]. For this purpose, microsized magnetic latex-coated beads have been developed by coating an iron oxide core with polystyrene, which allows for straightforward removal of aAPCs by magnetic depletion before reinfusion of CTLs. These beads were initially coated with anti-CD3 and anti-CD28 for nonspecific $CD4^+$ T cell amplification [39]. Again, replacement of anti-CD3 with peptide-MHC complexes results in antigen-specific T cell expansion [32]. Similar to the nonmagnetic latex beads, these particles can be easily prepared and are readily available [9].

Importantly, T cells expanded *ex vivo* using anti-CD3/anti-CD28–coated magnetic beads have been applied in Phase I clinical trials in patients with metastatic breast cancer, chronic myeloid leukemia and carcinomas. Although infusion of expanded CTLs resulted in mixed anti-tumor responses, in some cases bead-expanded cells induced tumor regression or even complete remission, indicating that adoptive T cell transfer using bead-based aAPC-expanded T cells could be an effective cancer treatment. However, these trials also showed a risk of developing non-tumor specific cytotoxicity or graft versus host disease [40–43].

Biodegradable poly(lactic-co-glycolic acid) microparticles

Bead-based aAPCs can provide strong proliferative signals to $CD8^+$ T cells. Natural APCs provide a third signal (Box 1, Box 2), besides MHC-mediated antigen presentation and membrane receptor-based co-stimulation, in the form of soluble secreted cytokines. $CD8^+$ T cells require continuous paracrine delivery of cytokines such as IL-2 during the first few hours for proper activation, and these are initially provided by APCs and later by $CD4^+$ helper cells. Besides paracrine delivery, trans-presentation of IL-2 on CD25 also plays an important role in initial activation of naïve T cells [44]. At later time points, CTLs also require cytokine stimulation to maintain proliferation, but high IL-2 concentrations and exposure for extended times may negatively impact T cells [45]. When using polystyrene beads, cytokines have to be added to the culture,

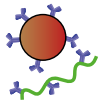

Box 1 Signals for T cell activation

Activation signal 1 – antigen recognition
T cell activation occurs after a T cell receptor (TCR) recognizes a specific peptide antigen presented on MHC complexes of an antigen-presenting cell. In general, extracellular peptides are presented on MHC class II, which is recognized by the TCR in conjunction with the CD4 T cell co-receptor, while MHC class I carries peptides derived from intracellular proteins and are recognized by the TCR in conjunction with a CD8 T cell co-receptor. Ligation of the TCR by a peptide-MHC complex or binding of agonistic antibodies directed towards CD3 leads to activation of the CD3 signal-transduction complex, which transduces essential signals necessary for activation of the T cell.

Activation signal 2 – Co-stimulation
In order to become fully activated, T cells require a second signal next to TCR-mediated antigen recognition. This antigen independent signal is provided in the form of co-stimulatory molecules that are upregulated on the antigen-presenting cells when they encounter stress, infection or cellular damage. These molecules can interact with receptors on the T cell, of which CD28 is the best studied. This receptor interacts with the co-stimulatory molecules B7-1 (CD80) or B7-2 (CD86) on the APC, which can also transduce inhibitory signals by ligation of CTLA4 on the T cell. Other co-stimulatory receptors on T cells include Inducible co-stimulator (ICOS), CD27 and 4-1BB (CD137), which bind to ICOS-L, CD70 and 4-1BBL, respectively.

Activation signal 3 - Cytokines
T cell activation and differentiation can be further directed through binding of cytokines to cytokine receptors. These cytokines can be produced by either the APC or $CD4^+$ T helper cells and, especially for $CD8^+$ T cells, are essential for cell survival and productive immune responses. IL-2, the most important cytokine for $CD8^+$ T cell survival, is secreted in low amounts by APCs during initial T cell encounter and is produced in larger amounts by activated $CD4^+$ T cells. Other cytokines that can assist in T cell activation include IL-12, IL-15, IL-21 and type I interferons (IFNα/β). Especially IL-12 and IFNα/β seem to be essential for effective T cell function. In addition to immunostimulatory cytokines, immunoinhibitory cytokines such as IL-4, IL-5, IL-10 are capable to dampen the immune response or can lead to tolerance. Therefore, signal 3 is regarded most important in shaping the immune response.

leading to high overall concentrations and possible side effects due to co-injection of IL-2 during reinfusion of T cells into patients [9]. Implementation of mechanisms that allow for paracrine cytokine release by aAPCs may therefore further improve their potential to activate and differentiate T cells. In particular, cytokine release may be essential for the development of functional $CD8^+$ T cells that can generate potent immune responses. This may be the one most important characteristic of an aAPC.

Box 2 Signal transmission by APCs

To efficiently induce tumor-specific CTLs, several signals need to be transferred from APCs to naïve T cells (Figure I). Antigen recognition represents the first signal, which occurs through the interaction of specific T cell receptors (TCRs) with peptide-major histocompatibility complexes (MHC) on APCs. APCs can contain two different types of MHC complexes. MHC class I molecules present antigens derived from intracellular proteins and bind to T cells expressing the CD8 co-receptor, while MHC class II molecules, which present extracellular peptides, can bind to $CD4^+$ T cells. Activated $CD8^+$ T cells, or CTLs, are capable of antigen-specific cell lysis, whereas $CD4^+$ T cells, known as T helper cells, release cytokines to stimulate CTL activation and antibody production by B cells. In artificial systems, peptide-MHC complexes can be replaced by antibodies binding the $CD3$ subunit of the MHC complex, which leads to non-antigen specific T cell activation. Besides signal 1, a second signal, co-stimulation by APC cell surface molecules, is passed on to the naïve T cells. This co-

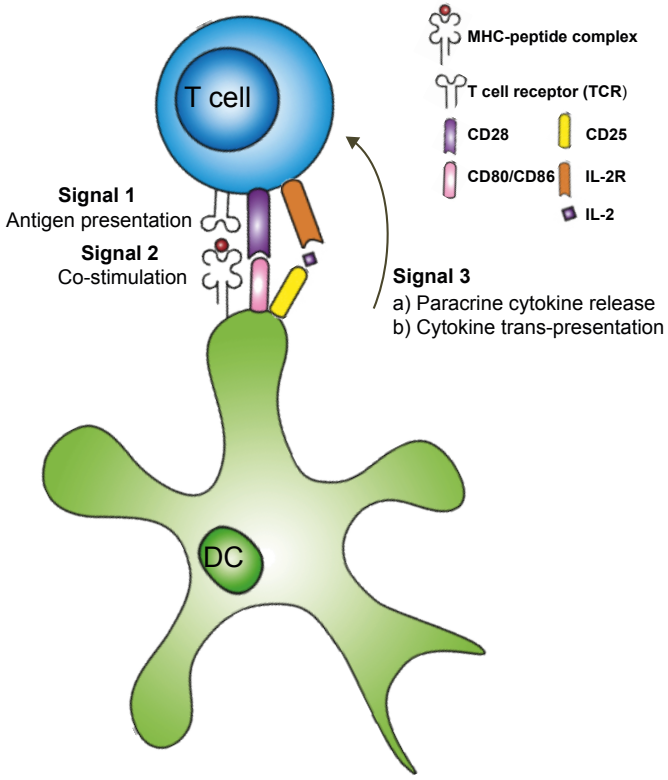

Figure I Different signals leading to induction of T cell activation and expansion.

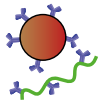

stimulation is necessary for proper T cell activation. CD80 and CD86, which bind to CD28 on T cells, are the most prominent co-stimulatory signals. Additional co-stimulatory molecules, such as 4-1BB and CD83, are also expressed on APCs. Finally, to induce more efficient expansion and specific differentiation of T cells, immune cells release cytokines, such as IL-2, IL-15 and IL-21, which can be seen as the third signal. Additionally, T-cell-APC interactions are guided by adhesion molecules. Important adhesion molecule interactions include those of ICAM-1 (CD54) and LFA-3 (CD58) on APCs binding to LFA-1 and LFA-2 on T cells, respectively. Similar to natural APCs, the success of aAPCs depends to a great extent on the efficient presentation of these different signals to naïve T cells [6,9,15].

To facilitate release of cytokines or other soluble factors from aAPCs, biodegradable systems have been developed. These biodegradable aAPCs present signals on their surface, similar to polystyrene particles, but now this is combined with a slow release of IL-2 or other soluble molecules of interest. Particles composed of the biodegradable co-polymer PLGA have been extensively applied in slow release systems. Although it can be challenging to stably present molecules on the surface of biodegradable PLGA particles owing to loss of surface-bound molecules as the particle degrades [15], incorporation of avidin-palmitate conjugates facilitated incorporation of all three signals in one aAPC [46,47]. Surface ligand presentation of these IL-2 releasing particles was stable for 20 days, and they led to significantly higher induction of IFNγ secretion by murine and human T cells compared to magnetic beads in the presence of soluble IL-2 and reached peak activation profiles at lower aAPC concentrations [47]. Furthermore, it was shown that this paracrine release by aAPCs, in contrast to exogenous addition, can induce local accumulation of IL-2 near the contact area with the T cell, thereby significantly altering the activation and proliferation of $CD4^+$ and $CD8^+$ T cells, leading to apoptosis of $CD4^+$ T cells and enhanced proliferation of $CD8^+$ killer T cells [45,48]. It is likely that the high synaptic concentration that results from paracrine IL-2 delivery can be detected by the low-affinity IL-2 receptor, which is constitutively expressed by T cells. After 24 hours of antigen stimulation, T cells can also express the high-affinity IL-2 receptor, and lower amounts of IL-2 may be needed [45]. Similar to latex beads, PLGA particles of 6-10 μm in size were most effective inducers of T cell activation and expansion *ex vivo* [47]. Slow release of anti-CTLA4-antibodies together with IL-2 further boosts activation of T cells by biodegradable microparticles [49].

Cytokines are essential for induction of potent $CD8^+$ T cells (Box 3), but it is difficult to design non-biodegradable aAPCs, such as latex microbeads, capable of releasing cytokines for extended periods of time. To circumvent this problem, cytokines may be presented by surface receptors similar to CD25, as also occurs on DCs [44]. However, It is questionable whether sufficiently high concentrations of cytokines will be available. Alternatively, agonistic antibodies may be used, which could also be bound

to non-biodegradable aAPC structures. So far, only biodegradable aAPCs have been used for cytokine delivery, which may induce a more natural response via paracrine delivery. However, it should be noted that because of their biodegradable nature, these aAPCs might release their stimulatory surface molecules, which may influence their efficacy for T cell activation.

Box 3 Cytokine delivery for T cell activation

Inflammatory cytokines are essential for the survival (in particular IL-2), proliferation and functional differentiation of $CD8^+$ T cells. However, most aAPCs are not capable of releasing sufficient cytokine levels and require the addition of additional cytokines in cell cultures, which may not be as effective as either paracrine delivery or trans-presentation (by CD25) by antigen-presenting cells [44]. This underscores the importance in incorporating cytokine release systems in aAPC designs. Since IL-2 may also induce regulatory T cells that inhibit immune responses, additional cytokines are required to further induce effective T cell responses and avoid tolerance (non-responsive T cells). Therefore, development of aAPCs that deliver other soluble factors, or can trigger cytokine receptors in different ways (for example by using antibodies), could lead to major improvements in T cell survival and function. Interesting candidates include IL-12 and type I IFN, usually produced by DCs, which are responsible for prolonged T cell survival. These cytokines are necessary for memory T cell development and strong effector function of $CD8^+$ T cells. Another interesting combination of cytokines is the combination of IL-15 and IL-21. IL-15, which are similar to IL-2, but do not lead to $CD8^+$ T cell apoptosis. These cytokines have been used to rescue tumor-reactive $CD8^+$ T cells *in vivo* [120]. In addition, IL-21 was demonstrated to act in synergy with IL-15 [28]. Additional cytokines, such as IFNγ and IL-7, can be secreted by the T cell itself or by stromal cells in the lymph node and may therefore not be essential for aAPC mediated delivery.

Importance of ligand mobility and pre-clustering for T cell activation

Although rigid spherical beads can be efficiently used for T cell stimulation, the membrane of natural APCs is much more dynamic than the outer surface of latex-coated and PLGA particles. To more closely mimic natural systems, lipid bilayer surfaces and liposomes have been used as aAPC, thereby demonstrating a significant effect of membrane fluidity and receptor pre-clustering on T cell activation.

2D surface membrane mimics

The immunological synapse (IS) was originally identified as a membrane structure of approximately 70 μm^2 that forms upon APC-T cell contact and consists of peptide-MHC complexes interacting with TCRs, surrounded by a ring of interacting adhesion molecules. More recent research indicates that this is a dynamic structure, which is

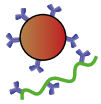

formed after TCRs cluster together in microclusters that eventually move towards the IS centre. It was recently shown that TCR-containing vesicles excreted within the IS are also important for signal transmission [50]. In general, efficient $CD4^+$ and $CD8^+$ T cell activation is associated with the formation of a functional IS [51]. Synthetic 2D cell-surface mimics have played an important role in the elucidation of the structure, function, and mechanisms of IS formation [51]. Planar membrane surfaces can easily be functionalized with various ligand compositions and allow for the use of high-resolution microscopy techniques, making it an attractive tool to study cell membrane interactions [52].

To examine the effect of membrane fluidity on synapse formation and T cell activation, lipid bilayers can be deposited on glass surfaces to form supported lipid bilayers (SLBs). Variation of the membrane fluidity of these lipid bilayers revealed that more fluid membranes are better capable of forming ISs, leading to improved $CD4^+$ T cell activation compared to more rigid membranes [53]. In addition, 2D surface patterning has been used to study the effect of spatial organization of anti-CD3 and anti-CD28 on $CD4^+$ T cell activation. Lithographic definition of the positions of proteins on a surface revealed that spatial organization is important for efficient IS formation and thus for T cell activation [54]. T cell responses were most efficient when co-stimulating molecules (anti-CD28) surrounded anti-CD3 compared to other organizations [54,55]. Incorporation of protein patterns onto aAPCs may therefore provide a new level of control over T cell proliferation [56]. Although there may be small differences between ISs of $CD4^+$ and $CD8^+$ T cells, the general organization and dynamics are similar between the various T cell subsets [57]. Rigid nanopatterned surfaces have also been useful in determining optimal ligand densities needed for optimal stimulation of T cells. In this way, it was established that distances between anti-CD3 or peptide-MHC ligands need to in the range of 30-100 nm to induce T-cell stimulation, with higher densities showing more potent responses [58–60].

Although synthetic 2D cell surfaces, and in particular the 2D-supported lipid bilayers (2D-SLBs), were useful in clarifying the mechanisms of T cell activation, at present they are less suitable as 'off-the-shelf' aAPCs owing to their fragility and limited lifetime [56]. Furthermore, it should be noted that most cell-surface membrane mimics used to date lack organizers, such as a cytoskeleton, which play an important role in the distribution of transmembrane molecules, usually resulting in a non-random distribution but rather organization into microdomains, whereby groups of surface receptors are clustered together.

Liposomes, RAFTsomes and microdomain-liposomes

To facilitate T cell activation in a more natural context similar to the fluid membrane interactions of natural APCs and T cells, MHC-containing liposomes have been generated. Phospholipid bilayer vesicles with randomly distributed peptide-MHC

complexes have been used mainly to study the physiological mechanisms of $CD4^+$ T cell activation [61,62], but have not extensively been used as aAPCs [16,61].

It has been shown that pre-clustering of peptide-MHC complexes in lipid raft microdomains on APCs dramatically increases their antigen presentation efficacy [63]. It is likely that this allows for better docking to their counterpart TCRs on T cells, which are initially also distributed as microdomains. Therefore, liposomes have been designed containing lipid raft microdomains with pre-clustered MHC complexes, which aids in IS formation. These liposomes, also known as RAFTsomes, can be made by incorporating DC-derived lipid rafts in liposomal phospholipid bilayers [64]. However, at present these RAFTsomes are not as efficient as natural DCs or other aAPCs in stimulating $CD4^+$ T cell proliferation [64], probably because they lack a cytoskeleton-mediated surface organization. Another method of pre-clustering molecules on liposomes makes use of ganglioside GM1-containing liposomes. A high density of ligands can be created by taking advantage of the high affinity of the cholera toxin B subunit for GM1, which is a component of lipid rafts. These microdomain aAPCs have been used for *ex vivo* T cell activation studies, and showed improved antigen-specific $CD4^+$ T cell stimulation compared to liposomes with randomly distributed MHC molecules [65]. Importantly, it has been shown that these aAPCs are better equipped to stimulate $CD8^+$ T cells compared to magnetic beads, leading to higher numbers and more efficient CTLs specific for MART-1 in melanoma skin cancer [66].

3D-supported lipid bilayers (3D-SLB)

Although the fluidity of liposomes is a great advantage for T cell stimulation, they are substantially less stable than solid particles. This problem may be solved by using solid particles as a scaffold for a lipid bilayer. These SLB-particles combine the fluidity of liposomal bilayers with advantageous properties of solid particles, such as their high stability [15]. Several 3D-SLBs have been constructed, including lipid bilayers on a core of hydrogel, PLGA, or silica [67–69]. Using cell-sized silica beads coated with a lipid bilayer, it was shown that 3D-SLBs can boost CTL responses in antigen-primed T cells more efficiently than liposomes. By contrast, 3D-SLBs were not able to initiate primary T cell expansion, probably due to lack of soluble factors such as IL-2 [70]. In another approach, lipid bilayers were isolated from Ag-bearing cells and adsorbed onto latex microspheres. Perhaps cytoskeleton-organized microdomains might be grafted onto these latex spheres, but no significant change in T cell activation was observed when compared to rigid latex beads [23]. Alternatively, tumor-cell derived plasma membrane vesicles have been deposited on both silica and latex microbeads, leading to large multivalent immunogens, which have an increased immunostimulating activity compared to the nanosized tumor-derived vesicles [71]. Although the use of 3D-SLBs is a promising approach, most recent reports have been made on SLBs that need membranes extracted from tumor cells for T cell activation. Recently,

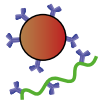

magnetic nanoparticles coated with fragments from leukocyte membranes and chemically modified with stimulatory ligands were established as efficient aAPCs. These magnetosomes can efficiently activate T cells, and also for these particles, membrane fluidity played an important role, since pre-crosslinking the membrane significantly decreases their stimulatory capacity [72].

Solid microbeads

Instead of using complex 3D-SLBs, making aAPCs out of softer materials can be an effective alternative to the classic rigid microbeads. T-cell stimulation with anti-CD3- and anti-CD28-coated PDMS surfaces or beads can provide an extended proliferative phase, especially for scaffolds with lower stiffness [73,74]. In contrast to results obtained with PDMS, experiments on polyacrylamide gels show that higher rigidity is beneficial for efficient T-cell activation. On these gels it was also demonstrated that TCR signalling is mechanoresponsive and that cytoskeletal contractility plays an important role in this process [75], Possibly, local surface shape and nanoscale rigidity of PDMS surfaces could account for the different responses observed for these different materials [74].

As was described above for 2D surfaces, stimulating T cells using surfaces with defined ligand orientations can also improve responses. To implement this knowledge in an aAPC design, a variety of Janus particles, particles that have two or more surface areas with distinct functionalities, have been developed. In this way, the bull's eye pattern of the immune synapse can be mimicked. Interestingly, improved T cell responses were observed after stimulation with 'reversed IS' patterned beads that contain a patch of integrin ligands surrounded by stimulatory anti-CD3 antibodies [76]. Furthermore, two-faced magnetic Janus microparticles have also been used to remotely control the onset of T-cell stimulation by rotating these particles in a magnetic field [77]. In addition, nano-Janus particles have further highlighted the importance of high local ligand densities on nanosized aAPCs [78].

Importance of aAPC shape

Most aAPC systems use spherical particles to stimulate T cells. However, natural APCs, especially DCs, are not spherical, and therefore the aAPC shape may be modified to increase the contact area with T cells. It will be interesting to design and test differently shaped particles and examine nanoclustering of ligands. This may assist in more efficient TCR nanoclusters on the T cell surface. As described below, shape appears to be an important parameter for T cell activation that should be taken into account when designing aAPCs.

Ellipsoid PLGA microparticles

Besides spherical forms, PLGA-based microparticles have also been used as non-spherical particles [47]. To closely mimic the natural situation and increase the particle contact area,

ellipsoid PLGA-based aAPCs were prepared using film-stretching methods [79,80]. Interestingly, particle shape had significant effect on the stimulation of T cells by aAPCs. Elongated particles with a more ellipsoid shape were more efficient as aAPCs than spherical particles and can induce stronger $CD8^+$ T cell proliferation. These findings may be explained by the fact that T cells have more and larger biomimetic interactions with these aAPCs, thereby favoring the flatter, longer side of the ellipse, which may provide a larger IS-like contact area [80]. Similarly, ellipsoid nano-particles induce stronger antigen-specific T cell activation compared to their spherical counterparts. In addition, stretched particles exhibit reduced non-specific uptake by macrophages [81].

Carbon nanotube bundles

To both increase the surface area of particles and facilitate more options for surface modifications, single-walled carbon nanotubes have been used for efficient T cell stimulation [82]. Using anti-CD3-coated tubes, large surface particles evoked higher aspecific T cell activation and IL-2 production than polystyrene beads. These functionalized nanotubes appear to cluster into large microsized aggregates with a high surface area, perhaps mimicking cell-surface microdomains [82]. As already demonstrated for fluid membranes and microdomain liposomes, nanopatterning is an extremely important issue that deserves further study to improve aAPC-mediated T cell activation. Chemical modification of nanotubes might also lead to a local clustering of antibodies on their surfaces, with a positive effect on T cell activation. Furthermore, this modification causes the nanotubes to have a negative surface charge, resembling that of natural APCs, which might also help in interactions with T cells [83]. It was recently demonstrated that peptide-MHC complexes can also be stably linked to nanotubes, which makes it possible to use these aAPCs for antigen-specific T cell stimulation [84]. By combining a large surface area for interaction, pre-clustered antibodies and a negative surface charge, these carbon nanotube bundles seem extremely potent for *ex vivo* T cell activation [82].

Nanofilaments

Lipid bilayer aAPCs have shown that membrane fluidity, which allows ligand motility, positively affects T cell activation. In addition, the shape of particles appears to have a great influence on this process, resulting in enhanced responses when T cells have a larger contact area and can thus better fit onto the aAPCs. A novel promising approach incorporates both of these features into an aAPC system exploiting so-called nanoworms, composed of semi-flexible filamentous polymers comprising poly(isocyano dipeptides) (PICs) with oligoethylene oxide side chains, which can be decorated with molecules for antigen presentation and co-stimulation in a highly controlled fashion [85]. In this thesis, PIC-protein conjugates are developed to form a potent new class of aAPCs, called synthetic Dendritic Cells.

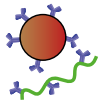

aAPC development for active *in vivo* immunotherapy

Ex vivo expansion and subsequent injection of autologous CTLs is one approach for induction of anti-tumor immune responses. However, the survival and function of these cells can be highly variable after reinfusion into patients [34,86,87]. In addition, the culturing of autologous T cells is a time-consuming, labor-intensive and costly procedure [88]. Alternatively, to avoid the use of autologous cells, aAPCs can be administered directly into patients to stimulate $CD8^+$ T cell responses *in situ,* allowing for true 'off-the shelf' cancer immunotherapy.

When considering *in vivo* T cell targeting through injection of aAPCs, several additional properties, besides high T cell stimulation, should be taken into account, including the pharmacokinetics and biocompatibiliy of these systems. Therefore, optimal size, surface modifications, shape and targeting moieties have been extensively investigated for biomaterials used in drug delivery [80,89–92].

Several aAPCs have been tested for *in vivo* induction of tumor cell killing through $CD8^+$ T cell expansion. To the best of our knowledge, one of the first *in vivo* aAPC immunotherapies was performed in mice using silica microspheres bearing either peptide-MHC class I complexes or covered with tumor cell membranes [70]. In mice, these aAPCs could not induce immune responses on their own, but were able to augment responses in the presence of antigen-bearing stimulator tumor cells, which could not be achieved by using liposomes as aAPCs [93]. In combination with the chemotherapeutic agent cyclophosphamide, these particles induced regression of established progressing tumors in mice [94]. Variable success was observed for these large multivalent immunogens in Phase I and II clinical trials for the treatment of melanoma and renal cell carcinoma; in some cases, partial responses were induced [95,96]. However, the limited availability of autologous tumor-cell membranes to cover the silica beads restricts the wide applicability of this approach.

In another strategy, microsized polystyrene beads coated with tumor antigen-specific peptide-MHC complexes, anti-CD28 and anti-4-1BB, were injected into tumor-bearing mice. These beads efficiently decreased tumor sizes and delayed tumor progression [34,97]. Similar results were obtained for magnetic polystyrene microbeads in a mouse tumor model [98]. Interestingly, when compared to spherical PLGA microparticles, ellipsoid particles were most efficient in reducing tumor sizes and extending survival times in melanoma-bearing mice, again emphasizing the importance of size and shape [80]. Incorporation of IL-2 into biodegradable particles also improved their efficacy reduced tumor growth kinetics in mice engrafted with B16 tumors [9]. IL-2 encapsulation can also be combined in SLB particles with small-molecule inhibitors, such as TGF-β inhibitors, which increased activity of intratumoral T cells *in vivo* [99].

Although no *in vivo* toxicities were observed, several of the aAPCs used so far are non-deformable, large, and in some cases non-biodegradable, which may lead to embolisms, making clinical approval for *in vivo* use difficult [9,16].

Thus, in contrast to microbeads, nanosized particles might be safer and have a better chance of obtaining clinical approval. Particle sizes below 100 nm enable easy entry into the lymphatic system and allow for transportation to the lymph nodes, where particles can gain access to larger numbers of T cells [100]. For example, MHC class II-containing RAFTsomes, which are flexible nanoparticles, were able to induce $CD4^+$ T cell responses that prevented EG.7 tumor inoculation and reduced tumor sizes in mice [64]. Unfortunately, generation of these nanoparticles requires DC-derived lipid rafts, and therefore does not completely eliminate the need for isolation and culture of autologous APCs. Also leukocyte-membrane coated magnetosomes can efficiently activate T cells *in vivo*. To further improve anti-tumor responses, their magnetic properties can be used to guide these particles to tumors [72].Alternatively, completely synthetic nanosized aAPCs have also been tested for their *in vivo* potential in cancer immunotherapy. Both dextran-coated iron oxide magnetic particles (50-100 nm) and dextran-coated quantum dots (30 nm) can effectively stimulate tumor antigen-specific T cells and inhibit tumor growth *in vivo*. They are also more efficiently distributed and better capable of reaching T cell pools in mice than micro-aAPCs [37]. In addition, active clustering of magnetic nanoparticle-labelled TCRs by applying a magnetic field can further improve T-cell responses and *in vivo* anti-tumor responses [38,101]. Pharmacokinetics and *in vivo* T cell responses can be further boosted by making use of non-spherical ellipsoid nanoparticles [81].

Future aAPC development for more potent immunotherapy

The efficacy of signal presentation by aAPCs and the resulting T cell activation are highly dependent on the properties of the materials used. For future aAPC development, the previously discussed properties should be optimally tuned to induce higher clinical responses. *Ex vivo* activation of T cells for subsequent reinfusion into patients has proven most effective with large microsized particles. To further improve aAPCs for *ex vivo* T cell activation, current knowledge about the optimal choice of surface molecules, cytokine release, particle shape, ligand mobility, and ligand orientation should be applied in a microsized system, preferably one that can be quickly separated from the T cell population before reinfusion into a patient. The use of 3D-SLB particles constitutes a promising, yet rarely applied system that would allow for incorporation of these features. For example, future acellular 'off-the-shelf' aAPCs could be made by coating ellipsoid PLGA microparticles with GM1-microdomain-containing lipid bilayers, allowing for more optimally shaped and stable particles with ligands pre-clustered in microdomains, high membrane fluidity, and an ability to release paracrine cytokines and small-molecule drugs [15,99]. Furthermore, incorporation of magnetic nanoparticles may be possible for straightforward separation of particles and cells after incubation and expansion. aAPCs that closely mimic features of natural DCs should in this way improve the clinical efficiency of *ex vivo*-generated T cells.

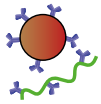

In vivo, active aAPC immunotherapy, although more challenging, is also particularly promising. This approach does not depend on autologous T cells, significantly lowering labor and costs. However, injection of microsized aAPCs may be unsafe, and therefore biocompatible nanoparticulate constructs are preferred. Nanoparticles in the size range of 10-100 nm and with stretched shapes have favorable biodistributions [37,81,100]. Therefore, the use of semi-flexible nanofilaments is a promising approach for *in vivo* application. These polymers are small in size and have a high degree of flexibility, allowing extensive contacts with the T cell membrane and the dynamic interactions that are necessary for potent signal transduction [85]. For *in vivo* application of aAPCs, development of nanosized particles combining these properties may be important to boost clinical responses in cancer immunotherapy [15].

Concluding remarks and future perspectives

The development of aAPCs for cancer immunotherapy is a highly promising approach. The *ex vivo* use of these systems for T cell expansion has significant advantages over the use of autologous APCs, and initial results from clinical studies are encouraging. Therefore, further development of microparticles for this purpose should exploit the effects of size, shape, ligand mobility, and ligand distribution. The development of nanosized aAPCs with improved flexibility, optimal shape, and efficient signal presentation for direct *in vivo* aAPC immunotherapy is desirable and holds marked promise. This approach could eliminate the need for costly and laborious cell culture and lead to broadly accessible 'off-the-shelf' cancer immunotherapeutics. This highlights the need for research into nano-aAPCs that exhibit more potent *in vivo* CTL responses.

1.2 Water-soluble polyisocyanopeptides for biological applications

To induce efficient T cell activation *in vivo*, aAPCs are preferably small, have a stretched shape and should be flexible, at least to a certain degree. Water-soluble polyisocyanopeptides (PICs), a class of polymers that was mentioned previously, can provide scaffolds that combine these properties to form a promising class of aAPCs, called 'nanoworms' or 'synthetic Dendritic Cells' (sDCs). Before their application as aAPCs, these PICs were studied extensively in the search for new materials with structural and mechanical properties resembling natural polymers. Their unique characteristics have great potential for application of PICs in catalysis and biomedical applications.

PICs were developed as derivatives of helical polyisocyanide polymers, which form their helical backbone. Helical polyisocyanides can be synthesized from isocyanides using a nickel(II)-catalyzed polymerization reaction [102,103]. During polymerization,

a helical conformation containing four repeats per turn is formed. This conformation can be stabilized when bulky groups are present in the isocyanide side chains. By making use of chiral catalysts or monomers, right- and left-handed helices can be synthesized in a highly controlled fashion [104]. These helices can also be stabilized further through hydrogen bonding by using dipeptide or tripeptide chains in the isocyanide side chains [105,106]. Due to this hydrogen bonding, highly stable and relatively stiff helices are formed that can only be unfolded by strong acids [107]. Isocyanopeptide polymers synthesized from dialanines or trialanines (polyisocyanopeptides or PICs), contain peptide side chains that display β-sheet-like packing along the isocyanide backbone [108]. This well-defined structure, which has resulted in the synthesis of markedly long (100 nm - μm-scale) and rigid polymers, are particularly interesting for ordering of electronically or optically active molecules, such as was done with chromophores for electronic applications [109,110].

To make these polymers water-soluble and use them in biological applications, oligo(ethylene glycol) tails can be added to the peptide side chains. Incorporation of oligo ethylene glycols results in non-ionic water-soluble polymers (Figure 3). By co-polymerization of azide-functionalized monomers, azide-PICs are formed that can be post modified with biological functionalities through bio-orthogonal strain-promoted alkyne-azide cycloaddition (click) reactions When tri- and tetra ethylene glycol-containing PICs are used, remarkable thermoresponsive properties are observed [112]. For tri-ethylene glycol-modified PICs, short polymers precipitate at temperatures above 18 °C, whereas longer polymers do not precipitate, but instead form a hydrogel at this temperature. For tetra ethylene glycol-PICs, this transition was seen at 42 °C. This thermoresponsive gelation is a result of polymer chain bundling and is completely

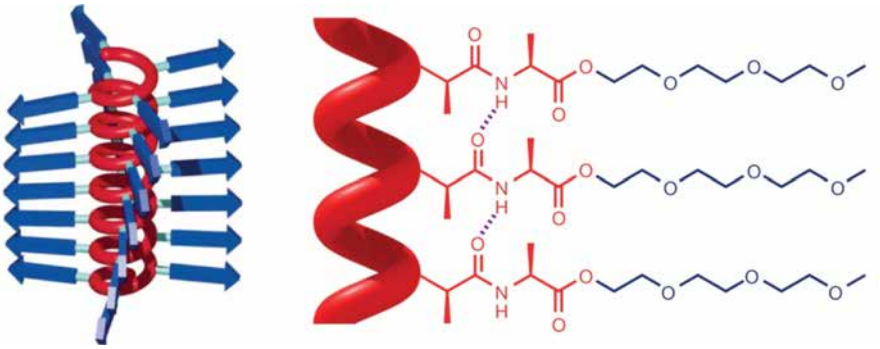

Figure 3 Side chains of PICs important for semi-flexibility and water-solubility. **(A)** Side chains of PICs show a β-sheet-like packing along the polyisocyanide helix **(B)** Peptides in the side chains (red) can form hydrogen bonds to stabilize helix formation of the red polyisocyanide backbone, leading to (semi)-rigidity in these polymers. Addition of oligo ethylene glycols (blue) makes these polymers water-soluble and thermoresponsive. Adapted with permission from [111].

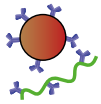

reversible when temperatures are lowered again. Interestingly, these hydrogels exhibit mechanical properties, in particular nonlinear stress responses, closely resembling those of biopolymer networks [111]. Because of this, and because these polymers are in gel-form at 37 °C, several possible biological applications have been reported using tri-ethyleneglycol-PIC hydrogels as 3D scaffolds [111,113–115].

These PIC hydrogels have possible applications in wound healing, as (immune) cell depots and as 3D cell culture scaffolds. For the latter purpose, PICs were recently introduced as a novel 3D matrix for culture of stem cells [115]. Because the non-linear stress response, or strain-stiffening, is similar to that of biopolymer hydrogels and can be easily manipulated, PIC hydrogels were used to assess the effects of strain-stiffening on stem cell differentiation. These experiments identified strain-stiffening as a key regulator in this process [115]. Instead of physically crosslinking polymers to form hydrogels when temperatures are increased, hybridizing strands of DNA can also be applied as stimuli-responsive cross-linkers [114]. Also when cross-linked through DNA interactions, these hydrogels exhibit mechanical properties similar to biological filaments [113]. In chapter 5, we demonstrate that DNA linkers can also be used as responsive elements in water-soluble filamentous PICs. Importantly, the various applications of PIC hydrogels have led to strategies to functionalize water-soluble PICs. Furthermore, the hydrogel-based experiments have demonstrated that these polymers are non-toxic and suitable for biological applications. Both the functionalization methods and biocompatibility were essential for the development of filamentous water-soluble PICs for biological applications.

PICs as synthetic Dendritic Cells – In contrast to tri-ethylene glycol-PICs, tetra-ethylene glycol-polymers do not form hydrogels at 37 °C, but instead exist as single filamentous semi-flexible nanoworms [111]. Because of their relatively high rigidity (for synthetic polymers) and high length, PICs coated with biomolecules, can efficiently mediate multivalent interactions with cell surfaces, which can play a role in many biological applications [116]. Making use of this multivalency, synthetic Dendritic Cells (sDCs) have been developed by conjugating stimulatory anti-CD3 antibodies to PICs. Compared to both unbound anti-CD3 or anti-CD3-coated PLGA microparticles, sDCs increased IFNy secretion and proliferation of stimulated T cells. In addition, it was demonstrated that these ~200 nm long structures were biocompatible and non-toxic [117]. To further boost T-cell activation, stimulatory anti-CD28 antibodies were also conjugated to PICs (Figure 4).

Stimulation of T cells with these anti-CD3/CD28-PICs further increased IFNy release and induced robust proliferation of T-cells. In addition, it was established that conjugating both these antibodies to a single scaffold is essential for their high stimulatory capacity, since stimulation of T-cells with a mixture of anti-CD3-PIC and anti-CD28-PIC was not as effective (Figure 5). Stimulation with CD3/CD28-PLGA

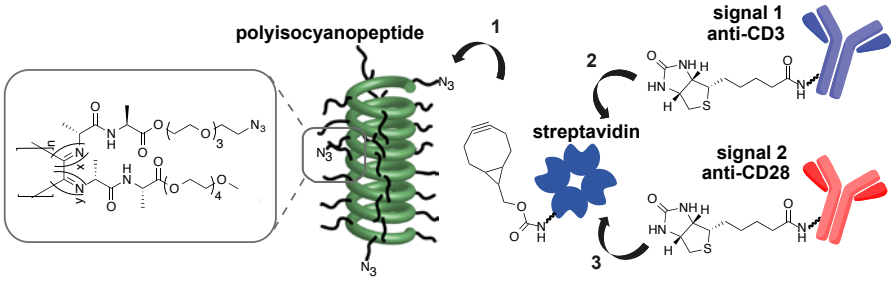

Figure 4 Synthesis of PIC-based synthetic DCs. Filamentous azide-PICs were synthesized by co-polymerization of tetra-ethylene glycol containing isocyanopeptides together with azide-functionalized monomers. BCN-functionalized streptavidin was reacted to the azide-PICs through strain-promoted alkyne azide cycloaddition (SPAAC). Next, biotinylated anti-CD3 and anti-CD28 stimulatory antibodies were conjugated to PIC-streptavidin to form the two-signal synthetic DCs. Adapted with permission from [118].

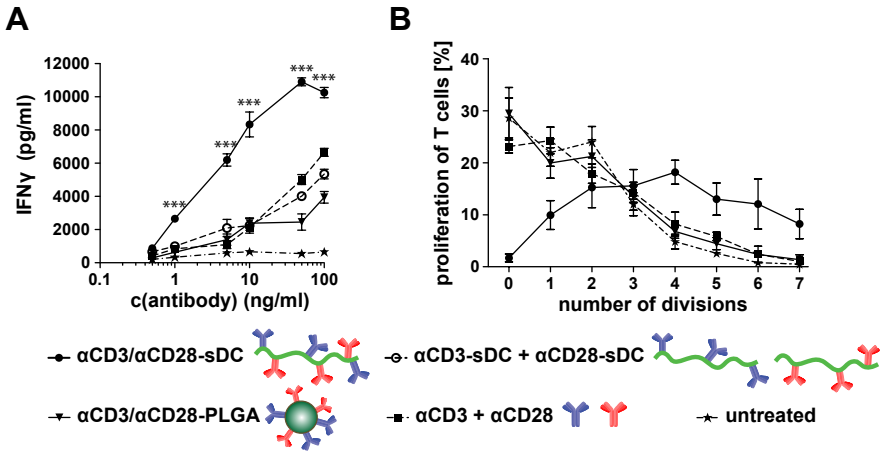

Figure 5 Antibody-functionalized PICs are efficient synthetic DCs. Peripheral blood lymphocytes were stimulated with different concentrations of stimulatory antibodies against CD3 and CD28. Antibodies were either given mixed in unbound form, mixed conjugated on separate PIC scaffolds, co-conjugated onto PLGA microparticles or co-conjugated on a single PIC polymer. **(A)** IFNγ concentrations in the supernatant after 16 h of stimulation. **(B)** Proliferation of T cells measured by CFSE dilution, depicted as number of divisions, after 4 days of stimulation using 5 ng/ml of antibodies. Adapted with permission from [118].

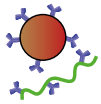

particles with similar antibody densities could not induce the same level of T cell activation. [118]. With this work, tetra-ethylene glycol-PIC-protein conjugates were established as promising novel aAPCs. These aAPCs have the potential to become highly efficient, off-the-shelf nanovaccines for cancer therapy. Their semi-flexibility, high aspect ratio and multivalent binding capacity make them excellent candidates for future aAPC-based therapies that can overcome drawbacks of the traditional aAPC scaffolds described in the first part of this introduction [117–119].

1.3 Aim and scope of this thesis

The initial papers by our group established proof-of-principle for PIC-antibody conjugates as efficient sDCs. To further develop these polymers for immune therapies, the mechanisms that govern their effects on T-cells needs to be further investigated. In addition, to optimize our sDC designs the impact of different co-stimuli and cytokines on T-cell responses needs to be further established. To be able to apply these aAPCs for direct *in vivo* immune therapy, instead of *ex vivo* activation of T cells, polyclonal stimulation of TCRs with anti-CD3 antibodies need to be replaced with an antigen-specific approach. The work described in this thesis aims to further understand and optimize PIC-based sDCs and their interactions with T-cells. Designs used for these PICs are summarized in Figure 6.

After the introduction, this thesis continues to further explore how multivalent anti-CD3-PICs control the activation of T-cells (chapter 2). Here, the effect of anti-CD3 antibody density and the role of the length of the scaffold on T-cell signaling and activation are described.

Up to this point, the use of streptavidin as a linker molecule was sufficient for proof-of-principle experiments. However, to increase complexity of linkers and for *in vivo* applicability of the sDC system, in chapter 3 this streptavidin linkage is replaced by a more direct approach, making use of only a short PEG spacer. In addition, a novel method for PIC-protein conjugate purification is introduced to increase both yield and purity of synthetic DCs. It is demonstrated in chapter 4 that this novel design can be used to generate potent sDCs. Through incorporation of a wide variety of antibodies, the effect of distinct types of co-stimulation could be tested. In addition, the introduction of this simple PEG linker was a first step towards introduction of more complex linkers, such as the force-responsive DNA linkers described in chapter 5. These linkers were used to further study interactions of PIC-antibody conjugates with T cells.

Increased yields and purity of the affinity-based purification allows for the use of PIC-based sDCs to target molecules with widespread biological activity, such as cytokines, to T cells. In chapter 6, the stimulatory capacity of purified PICs linked to anti-CD3 and cytokines IL-2 and IFNα is explored.

To translate this knowledge into an antigen-specific PIC-based sDC, chapter 7 describes the synthesis of peptide-MHC-presenting PICs. In addition, preliminary data on both *in vitro* and *in vivo* T-cell stimulation with these novel antigen-specific sDCs is discussed. This thesis finishes with a discussion of possible applications of these novel sDCs and possible future directions for application of PIC-conjugates in immunotherapy will be considered (Chapter 8).

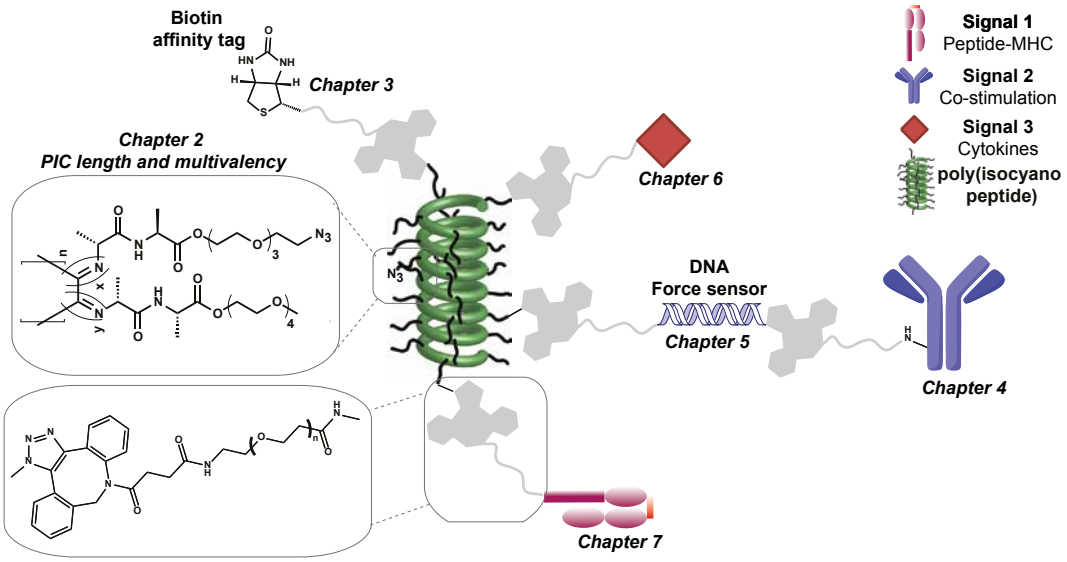

Figure 6 Molecular structure, linkers and biomolecules used in PIC-bioconjugates in the work presented in this thesis.

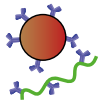

References

1 Weiner, L.M. *et al.* (2010) Monoclonal antibodies: versatile platforms for cancer immunotherapy. *Nat. Rev. Immunol.* 10, 317–27

2 Nelson, A.L. *et al.* (2010) Development trends for human monoclonal antibody therapeutics. *Nat. Rev. Drug Discov.* 9, 767–74

3 Rosenberg, S.A. and Dudley, M.E. (2009) Adoptive cell therapy for the treatment of patients with metastatic melanoma. *Curr. Opin. Immunol.* 21, 233–240

4 Kalos, M. and June, C.H. (2013) Adoptive T cell transfer for cancer immunotherapy in the era of synthetic biology. *Immunity* 39, 49–60

5 Vonderheide, R.H. and June, C.H. (2014) Engineering T cells for cancer: our synthetic future. *Immunol. Rev.* 257, 7–13

6 Palucka, K. and Banchereau, J. (2012) Cancer immunotherapy via dendritic cells. *Nat. Rev. Cancer* 12, 265–77

7 Cheever, M.A. and Higano, C.S. (2011) PROVENGE (Sipuleucel-T) in prostate cancer: the first FDA-approved therapeutic cancer vaccine. *Clin. Cancer Res.* 17, 3520–6

8 Yee, C. *et al.* (2002) Adoptive T cell therapy using antigen-specific CD8+ T cell clones for the treatment of patients with metastatic melanoma: in vivo persistence, migration, and antitumor effect of transferred T cells. *Proc. Natl. Acad. Sci. U. S. A.* 99, 16168–16173

9 Steenblock, E.R. *et al.* (2009) Antigen presentation on artificial acellular substrates: modular systems for flexible, adaptable immunotherapy. *Expert Opin. Biol. Ther.* 9, 451–464

10 Melief, C.J.M. (2008) Cancer Immunotherapy by Dendritic Cells. *Immunity* 29, 372–383

11 Steinman, R.M. and Banchereau, J. (2007) Taking dendritic cells into medicine. *Nature* 449, 419–26

12 Palucka, K. and Banchereau, J. (2013) Dendritic-Cell-Based Therapeutic Cancer Vaccines. *Immunity* 39, 38–48

13 Butler, M.O. *et al.* (2007) Long-lived antitumor CD8+ lymphocytes for adoptive therapy generated using an artificial antigen-presenting cell. *Clin. Cancer Res.* 13, 1857–1867

14 Kim, J. V *et al.* (2004) The ABCs of artificial antigen presentation. *Nat. Biotechnol.* 22, 403–410

15 Sunshine, J.C. and Green, J.J. (2013) Nanoengineering Approaches to the Design of Artificial Antigen-Presenting Cells. *Nanomedicine* 8, 1173–1189

16 Turtle, C.J. and Riddell, S.R. (2010) Artificial antigen-presenting cells for use in adoptive immunotherapy. *Cancer J.* 16, 374–381

17 Sun, S. *et al.* (1996) Dual Function of Drosophila Cells as APCs for Naive CD8+ T Cells: Implications for Tumor Immunotherapy. *Immunity* 4, 555–564

18 Papanicolaou, G.A. *et al.* (2003) Rapid expansion of cytomegalovirus-specific cytotoxic T lymphocytes by artificial antigen-presenting cells expressing a single HLA allele. *Blood* 102, 2498–505

19 Maus, M. V *et al.* (2002) Ex vivo expansion of polyclonal and antigen-specific cytotoxic T lymphocytes by artificial APCs expressing ligands for the T-cell receptor, CD28 and 4-1BB. *Nat. Biotechnol.* 20, 143–8

20 Butler, M.O. and Hirano, N. (2014) Human cell-based artificial antigen-presenting cells for cancer immunotherapy. *Immunol. Rev.* 257, 191–209

21 Dupont, J. *et al.* (2005) Artificial antigen-presenting cells transduced with telomerase efficiently expand epitope-specific, human leukocyte antigen-restricted cytotoxic T cells. *Cancer Res.* 65, 5417–27

22 Sun, X. *et al.* (2017) Surface-Engineering of Red Blood Cells as Artificial Antigen Presenting Cells Promising for Cancer Immunotherapy. *Small* DOI: 10.1002/smll.201701864

23 Mescher, M.F. (1992) Surface contact requirements for activation of cytotoxic T lymphocytes. *J. Immunol.* 149, 2402–2405

24 Deeths, M.J. and Mescher, M.F. (1997) B7-1-dependent co-stimulation results in qualitatively and quantitatively different responses by CD4+ and CD8+ T cells. *Eur. J. Immunol.* 27, 598–608

25 Oelke, M. *et al.* (2003) Ex vivo induction and expansion of antigen-specific cytotoxic T cells by HLA-Ig-coated artificial antigen-presenting cells. *Nat. Med.* 9, 619–24

26 Lu, X. *et al.* (2008) Adoptive transfer of pTRP2-specific CTLs expanding by bead-based artificial antigen-presenting cells mediates anti-melanoma response. *Cancer Lett.* 271, 129–139

27 Casey, K.A. and Mescher, M.F. (2007) IL-21 promotes differentiation of naive CD8 T cells to a unique effector phenotype. *J. Immunol.* 178, 7640–8

28 Yu, X. *et al.* (2013) Artificial antigen-presenting cells plus IL-15 and IL-21 efficiently induce melanoma-specific cytotoxic CD8+ CD28+ T lymphocyte responses. *Asian Pac. J. Trop. Med.* 6, 467–472

29 Rudolf, D. *et al.* (2008) Potent costimulation of human CD8 T cells by anti-4-1BB and anti-CD28 on synthetic artificial antigen presenting cells. *Cancer Immunol. Immunother.* 57, 175–83

30 Deeths, M.J. and Mescher, M.F. (1999) ICAM-1 and B7-1 provide similar but distinct costimulation for CD8 + T cells , while CD4 + T cells are poorly costimulated by ICAM-1. *Eur. J. Immunol.* 29, 45–53

31 Corr, M. *et al.* (1994) T cell receptor-MHC class I peptide interactions: affinity, kinetics, and specificity. *Science* 265, 946–9

32 Maus, M. V *et al.* (2003) HLA tetramer-based artificial antigen-presenting cells for stimulation of CD4+ T cells. *Clin. Immunol.* 106, 16–22

33 Jiang, X. *et al.* (2007) HLA Tetramer Based Artificial Antigen-Presenting Cells Efficiently Stimulate CTLs Specific for Malignant Glioma. *Clin. Cancer Res.* 13, 7329–34

34 Shen, C. *et al.* (2013) Latex bead-based artificial antigen-presenting cells induce tumor-specific CTL responses in the native T-cell repertoires and inhibit tumor growth. *Immunol. Lett.* 150, 1–11

35 Oelke, M. and Schneck, J.P. (2010) Overview of a HLA-Ig based "' Lego-like system '" for T cell monitoring , modulation and expansion. *Immunol. Res.* 47, 248–256

36 Perica, K. *et al.* (2014) Magnetic field-induced T cell receptor clustering by nanoparticles enhances T cell activation and stimulates antitumor activity. *ACS Nano* 8, 2252–60

37 Perica, K. *et al.* (2014) Nanoscale Artificial Antigen Presenting Cells for T Cell Immunotherapy. *Nanomedicine* 10, 119–129

38 Hickey, J.W. *et al.* (2017) Biologically Inspired Design of Nanoparticle Artificial Antigen-Presenting Cells for Immunomodulation. *Nano Lett.* DOI: 10.1021/acs.nanolett.7b03734

39 Levine, B.L. *et al.* (1997) Effects of CD28 costimulation on long-term proliferation of CD4+ T cells in the absence of exogenous feeder cells. *J. Immunol.* 159, 5921–30

40 Rapoport, A.P. *et al.* (2009) Rapid immune recovery and graft-versus-host disease-like engraftment syndrome following adoptive transfer of Costimulated autologous T cells. *Clin. Cancer Res.* 15, 4499–507

41 Hardy, N.M. *et al.* (2011) Phase I trial of adoptive cell transfer with mixed-profile type-I/type-II allogeneic T cells for metastatic breast cancer. *Clin. Cancer Res.* 17, 6878–87

42 Porter, D.L. *et al.* (2006) A phase 1 trial of donor lymphocyte infusions expanded and activated ex vivo via CD3/CD28 costimulation. *Blood* 107, 1325–31

43 Lum LG, LeFever AV, Treisman JS, Garlie NK, H.J.J. (2001) Immune Modulation in Cancer Patients After Adoptive Transfer of Anti-CD3/Anti-CD28-Costimulated T Cells-Phase I Clinical Trial. *J. Immunother.* 24, 408–419

44 Wuest, S.C. *et al.* (2011) A role for interleukin-2 trans-presentation in dendritic cell-mediated T cell activation in humans, as revealed by daclizumab therapy. *Nat. Med.* 17, 604–9

45 Steenblock, E.R. *et al.* (2011) An artificial antigen-presenting cell with paracrine delivery of IL-2 impacts the magnitude and direction of the T cell response. *J. Biol. Chem.* 286, 34883–34892

46 Fahmy, T.M. *et al.* (2005) Surface modification of biodegradable polyesters with fatty acid conjugates for improved drug targeting. *Biomaterials* 26, 5727–5736

47 Steenblock, E.R. and Fahmy, T.M. (2008) A comprehensive platform for ex vivo T-cell expansion based on biodegradable polymeric artificial antigen-presenting cells. *Mol. Ther.* 16, 765–772

48 Han, H. *et al.* (2011) A novel system of artificial antigen-presenting cells efficiently stimulates Flu peptide-specific cytotoxic T cells in vitro. *Biochem. Biophys. Res. Commun.* 411, 530–5

49 Zhang, L. *et al.* (2017) Paracrine release of IL-2 and anti-CTLA-4 enhances the ability of artificial polymer antigen-presenting cells to expand antigen-specific T cells and inhibit tumor growth in a mouse model. *Cancer Immunol. Immunother.* 66, 1229–1241

50 Choudhuri, K. *et al.* (2014) Polarized release of T-cell-receptor-enriched microvesicles at the immunological synapse. *Nature* advance on,

51 Kaizuka, Y. *et al.* (2007) Mechanisms for segregating T cell receptor and adhesion molecules during immunological synapse formation in Jurkat T cells. *Proc. Natl. Acad. Sci. U. S. A.* 104, 20296–20301

52 Irvine, D.J. and Doh, J. (2007) Synthetic surfaces as artificial antigen presenting cells in the study of T cell receptor triggering and immunological synapse formation. *Semin. Immunol.* 19, 245–254

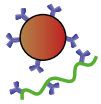

53 Hsu, C.-J. *et al.* (2012) Ligand mobility modulates immunological synapse formation and T cell activation. *PLoS One* 7, e32398

54 Doh, J. and Irvine, D.J. (2006) Immunological synapse arrays: patterned protein surfaces that modulate immunological synapse structure formation in T cells. *Proc. Natl. Acad. Sci. U. S. A.* 103, 5700–5

55 Shen, K. *et al.* (2008) Micropatterning of costimulatory ligands enhances CD4+ T cell function. *Proc. Natl. Acad. Sci. U. S. A.* 105, 7791–6

56 Shen, K. and Milone, M. (2009) Nanoengineering of Immune Cell Function. *Mater. Res. ...* DOI: 10.1557/PROC-1209-YY03-01.Nanoengineering

57 Dustin, M.L. *et al.* (2010) Understanding the structure and function of the immunological synapse. *Cold Spring Harb. Perspect. Biol.* 2, a002311

58 Deeg, J. *et al.* (2013) T cell activation is determined by the number of presented antigens. *Nano Lett.* 13, 5619–5626

59 Delcassian, D. *et al.* (2013) Ligand nanoarrays control immunoreceptor signaling in T cells and NK cells. *Nano Lett.* 13, 1–9

60 Matic, J. *et al.* (2013) Fine tuning and efficient T cell activation with stimulatory αCD3 nanoarrays. *Nano Lett.* 13, 5090–5097

61 Prakken, B. *et al.* (2000) Artificial antigen-presenting cells as a tool to exploit the immune "synapse". *Nat. Med.* 6, 1406–10

62 Mallet-Designe, V.I. *et al.* (2003) Detection of low-avidity CD4+ T cells using recombinant artificial APC: following the antiovalbumin immune response. *J. Immunol.* 170, 123–31

63 Anderson, H.A. *et al.* (2000) Concentration of MHC class II molecules in lipid rafts facilitates antigen presentation. *Nat. Immunol.* 1, 156–62

64 Ding, Q. *et al.* (2013) RAFTsomes containing epitope-MHC-II complexes mediated CD4+ T cell activation and antigen-specific immune responses. *Pharm. Res.* 30, 60–69

65 Giannoni, F. *et al.* (2005) Clustering of T Cell Ligands on Artificial APC Membranes Translocation to the T Cell Plasma Membrane. *J. Immunol.* 174, 3204–3211

66 Zappasodi, R. *et al.* (2008) The effect of artificial antigen-presenting cells with preclustered anti-CD28/-CD3/-LFA-1 monoclonal antibodies on the induction of ex vivo expansion of functional human antitumor T cells. *Haematologica* 93, 1523–1534

67 Jin, T. *et al.* (1996) Lipobeads: a hydrogel anchored lipid vesicle system. *FEBS Lett.* 397, 70–74

68 Hu, C.-M.J. *et al.* (2011) Erythrocyte membrane-camouflaged polymeric nanoparticles as a biomimetic delivery platform. *Proc. Natl. Acad. Sci. U. S. A.* 108, 10980–5

69 Ashley, C.E. *et al.* (2011) The targeted delivery of multicomponent cargos to cancer cells by nanoporous particle-supported lipid bilayers. *Nat. Mater.* 10, 389–397

70 Goldstein, S. a and Mescher, M.F. (1986) Cell-sized, supported artificial membranes (pseudocytes): response of precursor cytotoxic T lymphocytes to class I MHC proteins. *J. Immunol.* 137, 3383–3392

71 Mescher, M.F. and Savelieva, E. (1997) Stimulation of Tumor-Specific Immunity Using Tumor Cell Plasma Membrane Antigen. *Methods* 12, 155–164

72 Zhang, Q. *et al.* (2017) Biomimetic Magnetosomes as Versatile Artificial Antigen-Presenting Cells to Potentiate T-Cell-Based Anticancer Therapy. *ACS Nano* DOI: 10.1021/acsnano.7b04955

73 O'Connor, R.S. *et al.* (2012) Substrate Rigidity Regulates Human T Cell Activation and Proliferation. *J. Immunol.* 189, 1330–1339

74 Lambert, L.H. *et al.* (2017) Improving T Cell Expansion with a Soft Touch. *Nano Lett.* 17, 821–826

75 Judokusumo, E. *et al.* (2012) Mechanosensing in T lymphocyte activation. *Biophys. J.* 102, L5–L7

76 Chen, B. *et al.* (2014) Janus Particles as Artificial Antigen-Presenting Cells for T Cell Activation. *ACS Appl. Mater. Interfaces* 6, 18435–18439

77 Lee, K. *et al.* (2016) Janus Particles Remote Control of T Cell Activation Using Magnetic Janus Particles Angewandte. *Angew. Chemie* 47405, 7384–7387

78 Lee, K. *et al.* (2017) Janus nanoparticles for T cell activation: clustering ligands to enhance stimulation. *J. Mater. Chem. B* 5, 4410–4415

79 Yoo, J.J.-W. and Mitragotri, S. (2010) Polymer particles that switch shape in response to a stimulus. *Proc. Natl. Acad. Sci.* 107, 11205–11210

80 Sunshine, J.C. *et al.* (2014) Particle shape dependence of CD8+ T cell activation by artificial antigen presenting cells. *Biomaterials* 35, 269–277
81 Meyer, R.A. *et al.* (2015) Biodegradable Nanoellipsoidal Artificial Antigen Presenting Cells for Antigen Specific T-Cell Activation. *Small* 11, 1519–1525
82 Fadel, T.R. *et al.* (2008) Enhanced cellular activation with single walled carbon nanotube bundles presenting antibody stimuli. *Nano Lett.* 8, 2070–6
83 Fadel, T.R. *et al.* (2010) Clustering of stimuli on single-walled carbon nanotube bundles enhances cellular activation. *Langmuir* 26, 5645–54
84 Fadel, T.R. *et al.* (2013) Adsorption of multimeric T cell antigens on carbon nanotubes: effect on protein structure and antigen-specific T cell stimulation. *Small* 9, 666–72
85 Mandal, S. *et al.* (2013) Therapeutic nanoworms: towards novel synthetic dendritic cells for immunotherapy. *Chem. Sci.* 4, 4168
86 Durai, M. *et al.* (2009) In vivo functional efficacy of tumor-specific T cells expanded using HLA-Ig based artificial antigen presenting cells (aAPC). *Cancer Immunol. Immunother.* 58, 209–20
87 Mitchell, M.S. (2002) Phase I Trial of Adoptive Immunotherapy With Cytolytic T Lymphocytes Immunized Against a Tyrosinase Epitope. *J. Clin. Oncol.* 20, 1075–1086
88 Paulis, L.E. *et al.* (2013) Dendritic cell-based nanovaccines for cancer immunotherapy. *Curr. Opin. Immunol.* 25, 389–395
89 Doshi, N. *et al.* (2009) Red blood cell-mimicking synthetic biomaterial particles. *Proc. Natl. Acad. Sci. U. S. A.* 106, 21495–21499
90 Merkel, T.J. *et al.* (2011) Using mechanobiological mimicry of red blood cells to extend circulation times of hydrogel microparticles. *Proc. Natl. Acad. Sci. U. S. A.* 108, 586–591
91 Champion, J.A. *et al.* (2007) Particle shape : A new design parameter for micro- and nanoscale drug delivery carriers. *J. Control. release* 121, 3–9
92 Han, H. *et al.* (2013) Spatial charge configuration regulates nanoparticle transport and binding behavior in vivo. *Angew. Chem. Int. Ed. Engl.* 52, 1414–9
93 Rogers, J. and Mescher, M.F. (1992) Augmentation of in vivo cytotoxic T lymphocyte activity and reduction of tumor growth by large multivalent immunogen. *J. Immunol.* 149, 269–76
94 Mescher, M.F. and Rogers, J.D. (1996) Immunotherapy of established murine tumors with large multivalent immunogen and cyclophosphamide. *J. Immunother. Emphasis Tumor Immunol.* 19, 102–12
95 Mitchell, M.S. (2004) Phase I Trial of Large Multivalent Immunogen Derived from Melanoma Lysates in Patients with Disseminated Melanoma. *Clin. Cancer Res.* 10, 76–83
96 Dudek, A.Z. *et al.* (2008) Autologous large multivalent immunogen vaccine in patients with metastatic melanoma and renal cell carcinoma. *Am. J. Clin. Oncol.* 31, 173–81
97 Shen, C. *et al.* (2007) Induction of tumor antigen-specific cytotoxic T cell responses in naïve mice by latex microspheres-based artificial antigen-presenting cell constructs. *Cell. Immunol.* 247, 28–35
98 Ugel, S. *et al.* (2009) In vivo administration of artificial antigen-presenting cells activates low-avidity T cells for treatment of cancer. *Cancer Res.* 69, 9376–84
99 Park, J. *et al.* (2012) Combination delivery of TGF- inhibitor and IL-2 by nanoscale liposomal polymeric gels enhances tumour immunotherapy. *Nat. Mater.* 11, 895–905
100 Cai, S. *et al.* (2011) Lymphatic drug delivery using engineered liposomes and solid lipid nanoparticles. *Adv. Drug Deliv. Rev.* 63, 901–908
101 Perica, K. *et al.* (2015) Enrichment and Expansion with Nanoscale Artificial Antigen Presenting Cells for Adoptive Immunotherapy. *ACS Nano* 9, 6861–6871
102 van Beijnen, A.J.M. *et al.* (1983) Helical Configuration of Poly(iminomethylenes). Synthesis and CD Spectra of Polymers Derived from Optically Active Isocyanides. *Macromolecules* 16, 1679–1689
103 Deming, T.J. and Novak, B.M. Organometallic Catalysis in Air and Water: Oxygen-Enhanced, Nickel-Catalyzed Polymerizations of Isocyanides. , *Macromolecules*, 24. Jan-(1991) , American Chemical Society, 326–328
104 Nolte, R.J.M. (1994) Helical poly(isocyanides). *Chem. Soc. Rev.* 23, 11
105 Metselaar, G.A. *et al.* (2007) Polyisocyanides derived from tripeptides of alanine. *Chem. - A Eur. J.* 13, 950–960

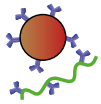

106 Cornelissen, J.J.L.M. *et al.* (2001) Synthesis and characterization of polyisocyanides derived from alanine and glycine dipeptides. *J. Polym. Sci. Part A Polym. Chem.* 39, 4255–4264

107 Cornelissen, J.J.L.M. *et al.* (2003) Conformational analysis of dipeptide-derived polyisocyanides. *J. Polym. Sci. Part A Polym. Chem.* 41, 1725–1736

108 Metselaar, G.A. *et al.* (2001) -Helical Polymers from Isocyanopeptides. *Science (80-.).* 293, 676–680

109 Palermo, V. *et al.* (2010) Macromolecular scaffolding: The relationship between nanoscale architecture and function in multichromophoric arrays for organic electronics. *Adv. Mater.* 22, E81–E88

110 Rowan, A.E. *et al.* (2010) Macromolecular multi-chromophoric scaffolding. *Chem. Soc. Rev.* 39, 1576–1599

111 Kouwer, P.H.J. *et al.* (2013) Responsive biomimetic networks from polyisocyanopeptide hydrogels. *Nature* 493, 651–655

112 Koepf, M. *et al.* (2013) Preparation and characterization of non-linear poly(ethylene glycol) analogs from oligo(ethylene glycol) functionalized polyisocyanopeptides. *Eur. Polym. J.* 49, 1510–1522

113 Deshpande, S.R. *et al.* (2016) DNA-Responsive Polyisocyanopeptide Hydrogels with Stress-Stiffening Capacity. *Adv. Funct. Mater.* 26, 9075–9082

114 Deshpande, S.R. *et al.* (2017) A biomimetic stress sensitive hydrogel controlled by DNA nanoswitches. *Biomacromolecules* 18, 3310–3317

115 Das, R.K. *et al.* (2015) Stress-stiffening-mediated stem-cell commitment switch in soft responsive hydrogels. *Nat. Mater.* 15, 318–325

116 Mahon, E. and Barboiu, M. (2015) Synthetic multivalency for biological applications. *Org. Biomol. Chem.* 13, 10590–10599

117 Mandal, S. *et al.* (2013) Therapeutic nanoworms: towards novel synthetic dendritic cells for immunotherapy. *Chem. Sci.* 4, 4168

118 Mandal, S. *et al.* (2015) Polymer-based synthetic dendritic cells for tailoring robust and multifunctional T cell responses. *ACS Chem. Biol.* 10, 485–492

119 Eggermont, L.J. *et al.* Towards efficient cancer immunotherapy: Advances in developing artificial antigen-presenting cells. , *Trends in Biotechnology*, 32. Sep-(2014) , Elsevier, 456–465

120 Klebanoff, C.A. *et al.* (2004) IL-15 enhances the in vivo antitumor activity of tumor-reactive CD8+ T cells. *Proc. Natl. Acad. Sci. U. S. A.* 101, 1969–74

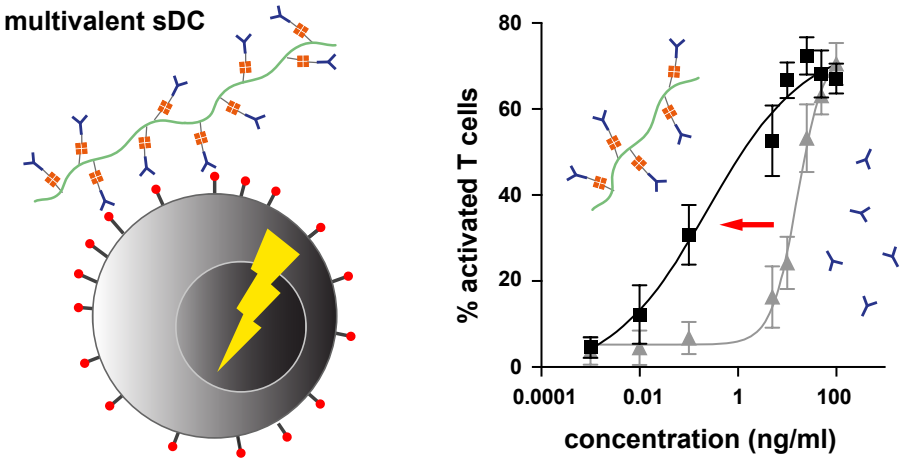
multivalent sDC
% activated T cells
80
60
40
20
0
0.0001
0.01
1
100
concentration (ng/ml)

2

Controlling T-Cell Activation with Synthetic Dendritic Cells Using the Multivalency Effect

Roel Hammink*, Subhra Mandal*, Loek Eggermont, Marco Nooteboom, Peter Willems, Jurjen Tel, Alan Rowan, Carl Figdor, and Kerstin Blank

ACS Omega, 2017, 2(3), 937-945

*contributed equally

Abstract

Artificial antigen-presenting cells (aAPCs) have recently gained a lot of attention. They efficiently activate T cells and serve as powerful replacements for dendritic cells in cancer immunotherapy. Focusing on a specific class of polymer-based aAPCs, so-called synthetic Dendritic Cells (sDCs), we have investigated the importance of multivalent binding on T cell activation. Using antibody-functionalized sDCs, we have tested the influence of polymer length and antibody density. Increasing the multivalent character of the antibody-functionalized polymer lowered the effective concentration required for T cell activation. This was evidenced for both early and late stages of activation. The most important effect observed was the significantly prolonged activation of the stimulated T cells, indicating that multivalent sDCs sustain T cell signaling. Our results highlight the importance of multivalency for the design of aAPCs and will ultimately allow for better mimics of natural dendritic cells that can be used as vaccines in cancer treatment.

Introduction

One important goal of cancer immunotherapy is the replacement of costly dendritic cell (DC) vaccines with synthetic variants, thereby overcoming the need of generating a customized vaccine for every individual patient.[1] These synthetic variants, called artificial antigen presenting cells (aAPCs), are designed to prime T cells against cancer specific antigens. These aAPCs can be produced in a straightforward manner from synthetic building blocks, opening up the possibility for standardized "off-the-shelf" protocols[2] and circumventing elaborate and expensive personalized medicine. Different aAPC designs have been synthesized over the last years with scaffolds varying from polymer beads,[3-4] carbon nanotubes,[5] liposomes[6] and many others.[7] In general, the design of aAPCs is inspired by the natural DC and its interaction with the T cell. DC binding to T cells involves three main signals that are all required to fully activate the T cell: antigen-loaded major histocompatibility complexes (pMHC) of the DC bind to specific T cell receptors (TCR; signal 1). At the same time, co-stimulatory molecules on the DC surface interact with their T cell binding partners (signal 2). In addition to these receptor interactions, also soluble factors (cytokines) are involved in T cell activation (signal 3). In the first stage of activation, signal 1 interactions trigger the TCR, which is pre-arranged in nanoclusters in the T cell membrane (up to 20 TCRs per cluster).[8-12] In the next step, triggered TCR molecules re-arrange together with signal 2 interactions, to form larger signaling microclusters containing around 20-300 TCRs.[9,11,13-16] These contact areas between both cells are stabilized by a number of different adhesion molecules. After the initial stimulation, triggered microclusters move towards the so-called supramolecular adhesion complex (SMAC) where receptors and adhesion molecules are rearranged to form a 'bulls eye' pattern of micrometer size.[17] This process clearly involves the dynamic multivalent binding of many (different) binding partners.

Multivalent interactions generally form at the interface between two objects that carry multiple, complementary functionalities.[18-19] The simultaneous interaction between these functionalities enhances the binding strength (avidity), sometimes by several orders of magnitude compared to the affinity of the monovalent interaction.[20] This enhancement mainly originates from an increase in the effective concentration of identical binding partners. Once the first ligand is bound, the 'search volume' is reduced and the following binding events occur with a higher probability.[21] We have recently introduced a new multivalent aAPC design for activating T cells: synthetic Dendritic Cells (sDCs).[22-23] In this design, anti-CD3 antibodies (αCD3), which are known to trigger the TCR (signal 1), were bound to a semi-flexible and linear polyisocyanopeptide scaffold with a length of ~200 nm. Using these novel sDCs, T cell activation occurred at much lower doses of antibody compared to freely soluble αCD3. This is a direct consequence of the unique physical properties of the polymer scaffold.

Its high aspect ratio allows the efficient simultaneous binding of all αCD3 effector molecules to the T cell. At the same time, its nanometer size combined with its semi-flexibility promote the dynamic spatial rearrangement of polymer-bound effector molecules, mimicking the fluidity of the natural cell membrane and supporting receptor mobility. Coupling of additional anti-CD28 antibodies (αCD28; signal 2) to the sDC shaped the immunoresponse towards the induction of helper and killer T cells, without activating the regulatory T cell population.[23] Remarkably, this effect was only seen when both signals were bound to one and the same polyisocyanopeptide backbone, indicating that activation requires both signals to bind in close spatial proximity. These results already provided a first indication that multivalent binding of these sDCs does not only increase the binding strength of the interaction. The polymer concentrates the effector molecules in a locally confined area. It may therefore affect T cell signaling pathways and directly influence the strength and specificity of the T cell response.

Focusing on sDCs functionalized with only anti-CD3 antibodies (αCD3-sDC), we have now designed a series of experiments to investigate the effect and importance of multivalent binding of our sDCs. We have synthesized a library of αCD3-sDCs with different polymer lengths and αCD3 densities and investigated the influence of these parameters on T cell activation. Incubating T cells with the αCD3-sDCs, we show that an increase in polymer length and/or effector molecule density boosts both early (Ca^{2+}-signaling) and late (interferon γ release) stages of T cell activation and provide evidence that this effect goes beyond a simple avidity increase. A positive effect on T cell signaling is further demonstrated after removal of the αCD3-sDCs. T cell activation is sustained for extended periods of time (days), as confirmed by prolonged Ca^{2+}-signaling, expression of the early activation marker CD69 and the release of interferon γ (IFNγ).

Results and discussion

Synthesis of αCD3-sDCs. All polymer-αCD3 conjugates (i.e. the αCD3-sDCs) were synthesized according to previously published methods[22-23] (Fig. 1). The sDC scaffold is based on a water-soluble polyisocyanopeptide co-polymer bearing non-functional methoxy and functional azide groups. The corresponding methoxy and azide isocyanide monomers were polymerized using a nickel catalyst to obtain azide-functionalized polyisocyanopeptide polymers. The azide groups were subsequently utilized in a strain-promoted azide-alkyne cycloaddition (SPAAC) reaction with bicyclononyne-functionalized streptavidin (BCN-SAv).[24] The SAv molecules allow for the binding of biotinylated αCD3 antibodies to yield the αCD3-sDCs (Fig. 1a). In all experiments, the ratio between SAv and αCD3 was tuned to be 1:1.

Influence of αCD3-sDC length on T cell activation. Polyisocyanopeptides of different length were synthesized using different catalyst-to-monomer ratios during the polymerization reaction. Two polymers of different average lengths (**P1'** = 175 nm and **P2'** = 350 nm; azide:methoxy = 1:100) were synthesized using this strategy (Table S1; Figs. S1-S2). The density of SAv per polymer chain was determined using atomic force microscopy (AFM imaging; Table S2; Figs. S1 and S3). The **P1-SAv** and **P2-SAv** conjugates possess an average density of 1 SAv molecule per 110 nm and 120 nm, respectively. For the synthetic protocol used, we have shown earlier that one αCD3 antibody is bound per SAv molecule.[22-23] It can therefore be assumed that these values also represent the densities of αCD3 molecules on the αCD3-sDC conjugates **P1** and **P2** (Fig. 1b). This means that **P1** carries 1-2 αCD3 molecules per polymer, whereas the total number of αCD3 molecules on **P2** is ~3.

P1 and **P2** were compared to free αCD3 in a single-cell Ca^{2+}-signaling experiment (Fig. 2a). Ca^{2+}-release from the endoplasmic reticulum is one of the earliest activation events when triggering T cells at the TCR level. The subsequent complex interplay between Ca^{2+}-release from the endoplasmic reticulum and calcium influx across the plasma membrane via Ca^{2+}-release activated Ca^{2+} (CRAC) channels leads to oscillations of cytoplasmic calcium.[25] These calcium oscillations, which have a direct influence on T cell gene expression, were monitored using peripheral blood lymphocytes (PBLs) loaded with the Ca^{2+}-sensitive fluorescent dye Fura-2 (Table S3; Fig. S4 and movies

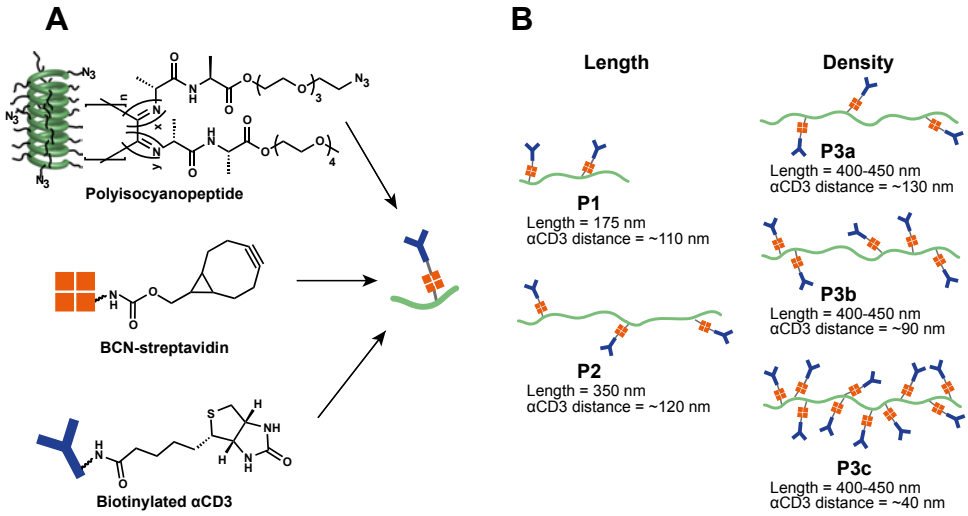

Figure 1 Schematic overview of the sDC library. **(A)** Experimental design for sDC synthesis. **(B)** Schematic overview of the sDCs used in this study (**P1-P3**) showing the corresponding polymer lengths and αCD3 densities.

M1-M2).[26] Determination of the number of Ca^{2+}-signaling cells during the first hour of treatment with **P1**, **P2** or free αCD3 (5 ng/ml and 25 ng/ml) revealed that the two αCD3-sDCs as well as free αCD3 caused a marked increase in the number of Ca^{2+}-signaling cells (above the 30 % background level of Ca^{2+}-signaling cells observed in the absence of any stimulant[27]). At 0.5 ng/ml this effect was only seen for **P2** and not for **P1** or free αCD3.

To probe the effect of the two αCD3-sDCs on a late and more robust event in T cell activation, we stimulated PBLs for 16 hours with **P1, P2** and αCD3 and measured the release of IFNγ. Both αCD3-sDCs stimulated the production of IFNγ over a range of concentrations from 0.05 to 100 ng/ml (Fig. 2b). At all concentrations tested, the effect of **P2** was most pronounced. Considering that **P1** and **P2** possess approximately the same αCD3 density, these results suggest that polymer length is a crucial design parameter. It increases the total number of αCD3 molecules per αCD3-sDC, thereby causing a stronger T cell stimulating effect.

Influence of αCD3 density on T cell activation. The previous experiment has shown that a density of one αCD3 antibody in 110-120 nm combined with a polymer length of maximally 350 nm (**P2**) leads to a small but clearly detectable increase in T cell activation. We therefore decided to increase both the polymer length and the αCD3 density to investigate the multivalency effect over a larger dynamic range. Increasing the number of azide functional groups (azide:methoxy = 1:70), polymer **P3'** with an average length of 400-450 nm was synthesized (Table S1; Figs. S1-S2). This polymer was then functionalized with a different number of SAv molecules per polymer, using different ratios of BCN-SAv:azide in the coupling reaction (0.5, 1 and 5 equivalents of BCN-SAv). Using AFM imaging, the average SAv density on these polymer conjugates was determined to be 1 SAv molecule in every ~130 nm (**P3a-SAv**, 0.5 eq.), ~90 nm (**P3b-SAv**, 1 eq.) and ~40 nm (**P3c-SAv**, 5 eq.) (Fig. 1b, Table S2; Fig. S1 and Fig. S3). Again, it was assumed that these values correspond to the density of αCD3 antibodies so that the αCD3-sDCs carry an average of 3-4 (**P3a-SAv**), 5 (**P3b-SAv**) or 10-11 (**P3c-SAv**) antibodies per polymer.

The single-cell Ca^{2+}-signaling assay shows a marked increase already at the lowest tested concentration of **P3c** (0.005 ng/ml; Fig. 2c). In sharp contrast, **P3a** and **P3b** displayed the same dose-dependency as free αCD3. Also for these αCD3-sDCs a more clear difference was observed in the IFNγ release assay. All three αCD3-sDCs were shown to be more effective than free αCD3 (Fig. 2d). Most importantly, a positive correlation was observed between αCD3 density and IFNγ release over the full range of tested concentrations (0.05-50 ng/ml). At the highest αCD3 concentration of 50 ng/ml, **P3a**, **P3b** and **P3c** induced a 2.4-, 3.5- and 6.1-fold increase of secreted IFNγ compared to free αCD3, respectively. Clearly, in addition to polymer length, αCD3 density is an important determinant for T cell activation by αCD3-sDCs.

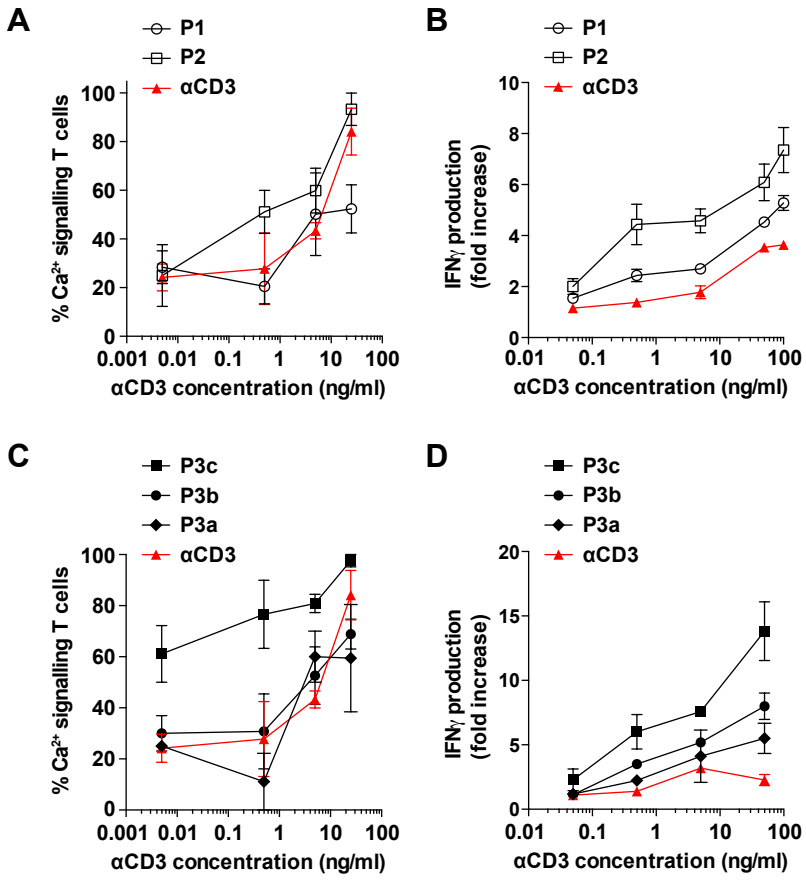

Figure 2 T cell activation using sDCs of different length and αCD3 density. **(A)** Fraction of activated PBLs as determined from single-cell Ca^{2+}-signaling measurements performed during the first hour of stimulation with **P1**, **P2** and free αCD3. **(B)** Relative increase in the concentration of IFNγ secreted by PBLs treated with **P1**, **P2** and free αCD3 for 16 hours. Untreated PBLs were used as a reference. **(C)** Fraction of activated PBLs as determined from single-cell Ca^{2+}-signaling measurements performed during the first hour of stimulation with **P3a**, **P3b**, **P3c** and free αCD3. **(D)** Relative increase in the concentration of IFNγ secreted by PBLs treated with **P3a**, **P3b**, **P3c** and free αCD3 for 16 hours. Untreated PBLs were used as a reference. For (a)-(c) the data represents the mean ± SEM of 3 independent experiments performed with T cells from different donors. For (d) the data represents the mean ± SEM of 2 independent experiments performed with T cells from different donors. The number of cells analyzed in the single-cell Ca^{2+}-signaling experiments (a, c) is summarized in Table S4.

Quantification of the multivalent enhancement factor. The above results show that both polymer length and αCD3 density are crucial design parameters for our sDC design. Together, these parameters determine the number of interactions that can form between the polymer and the T cell. To quantify the enhancement of the multivalent binding strength, dose-response curves were established for both free αCD3 and the best performing αCD3-sDC (**P3c**). The dose-response curves provide the basis for determining the EC_{50} values and allow for calculating an enhancement factor for the multivalent interaction. To construct these dose- response curves, single-cell Ca^{2+}-signaling experiments were performed over an extended range of αCD3 concentrations (0.001-100 ng/ml). Even though T cell activation was more difficult to quantify in the Ca^{2+}-signaling experiment, we have chosen this readout parameter as it corresponds to a very early activation event. We believe that an early readout parameter is more relevant for quantifying the multivalent binding strength than downstream parameters when signal amplification may have taken place.

When PBLs were treated with **P3c**, the smallest concentration that caused a detectable effect on the number of Ca^{2+}-signaling cells was a factor ~200-300 fold lower than for free αCD3 (Fig. 3), which is in line with previously reported results.[22] For free αCD3 an EC_{50} value of 16 ng/ml was found, whereas an EC_{50} value of 0.24 ng/ml was obtained for the multivalent **P3c**. This yields an enhancement factor of ~67 for the multivalent system (Fig. 3).[28] This remarkable enhancement clearly indicates that multivalency is one of the key parameters responsible for the increased potency of αCD3-sDCs. It is worth mentioning that the slope of the dose-response curve does usually contain additional information, e.g. about positive or negative cooperativity. The sDC polymers are heterogeneous, however, when considering both their length and the αCD3 density. It is therefore highly likely that the more gradual response to increasing the concentration of **P3c** is a direct result of this heterogeneity. We further note that it would be interesting to increase the αCD3 density on the polymer to determine if this multivalent system is characterized by an optimum loading. Despite several attempts, we have not been able to attach more αCD3 antibodies to the polymer, possibly due to steric hindrance.

Assuming that the enhancement factor purely characterizes the avidity increase of the multivalent interaction, the question remains if enhanced binding of the αCD3-sDC is the only parameter that determines T cell activation or if T cell signaling is also affected. The polymer linkage between several αCD3 antibodies efficiently directs these polymer-attached αCD3 antibodies to the same spatially confined area even if the overall αCD3 concentration is very low. It further enhances the probability of rebinding after dissociation (k_{off} = 0.39 s^{-1})[29] for individual polymer-attached αCD3 antibodies, thereby triggering a higher number of TCRs in close proximity. Considering the sequence of events occurring during T cell activation, this may directly lower the

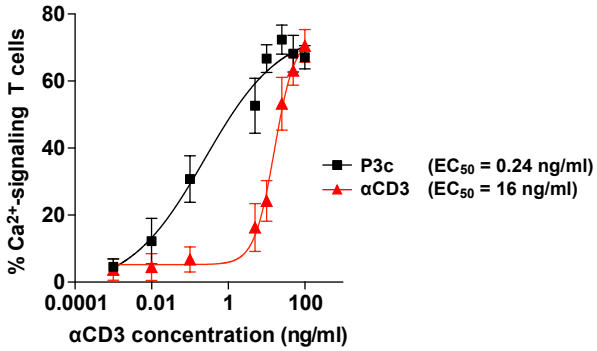

Figure 3 Dose-response curves for PBLs treated with P3c and free αCD3 as determined from single-cell Ca^{2+}-signaling experiments. EC_{50} values were determined using a four-parameter fit. The multivalent enhancement factor is calculated by dividing the EC_{50} of free αCD3 by the EC_{50} of **P3c**. The data represents the mean ± SEM of 3 independent experiments performed with PBLs from different donors. The number of cells analyzed is summarized in Table S4.

threshold concentration for T cell activation. A first indication for this can be obtained when re-considering the potency of the αCD3-sDCs **P3a**, **P3b** and **P3c** (Fig. 2c,d) that all bind in a multivalent fashion. During all experiments, the data was normalized to the αCD3 concentration so that the polymer concentration (i.e. the concentration of T cell stimulating entities; αCD3-sDCs) varies between the different samples. When normalizing the data with respect to the αCD3-sDC concentration, it becomes evident that a 1000-fold lower concentration of **P3c** is sufficient to obtain the same effect as with **P3a** (Fig. S5). This value is considerably larger than the multivalent enhancement factor determined above and may suggest that the co-localization of a certain number of αCD3 antibodies in a small area on the cell surface is a key factor for T cell activation. Interestingly, a total number of ~10 αCD3 antibodies (**P3c** carries ~10 antibodies) distributed over an area of several tens of nanometers matches with the predicted size of TCR nanoclusters that are pre-formed on the T cell surface.[8-10] It may therefore be speculated that αCD3-sDCs form a highly specific and dynamic multivalent interaction with these nanoclusters and that T cell fate is already determined at this very early stage of forming the initial contact with the T cell.[11]

Long-term effect of αCD3-sDC binding on T cell signaling. To investigate the effect of the αCD3-sDCs on T cell signaling in more detail, we designed a new series of experiments to obtain information about sustained T cell activation. Instead of measuring T cell activation in the continuous presence of the αCD3-sDCs or free antibodies, excess stimulant was washed off after 1 hour of treatment and T cell

activation was analyzed at several time points after removal of the stimulant. This allowed for determining the long-term effect of the initial stimulation, as no free stimulant was available for binding to the T cells after the medium was replaced. To quantify the effect, we have again performed single-cell Ca^{2+}-signaling experiments and determined the secretion of IFNγ. In addition, the expression of the surface activation marker CD69 was measured, which is another indicator of early T cell activation.

For the single-cell Ca^{2+}-signaling measurements, PBLs were treated with free αCD3 or **P3c** (12.5 ng/ml) for 1 hour. The stimulant was then removed, fresh medium was added and the cells were incubated without stimulant for another 15 or 23 hours. Fura-2 was added in the last 20 min of this extended incubation period and the fraction of Ca^{2+}-signaling cells was determined during the following hour (starting at 15 or 23 h after the initial addition of the stimulant; see Fig. S6 for a detailed timeline). A reference sample was imaged for 1 hour in the presence stimulant (0 h; Fig. S6). In agreement with the results presented above (Figs. 2c and 3) both free αCD3 and **P3c** (12.5 ng/ml) readily increased the number of Ca^{2+}-signaling T cells during the first hour of stimulation (Fig. 4a). In samples treated with free αCD3 the fraction of Ca^{2+}-signaling PBLs was significantly reduced at both post-stimulation time points (Fig. S7). In sharp contrast, the vast majority of **P3c**-treated PBLs remained active after removal of the stimulant. Even at 24 h hours after the initial stimulation with **P3c**, the fraction of Ca^{2+}-signaling T cells was still ~75%, indicating that the multivalent sDC causes a sustained stimulation of the intracellular pathways involved in Ca^{2+}-responses. Negative controls involving an isotope control ($mIgG_{2a}$ antibody), polymers with SAv but no αCD3 and non-treated cells did not show high amounts of activated T cells before and after removal of the stimulant (Fig. S7).

To support the results from the single-cell Ca^{2+}-signaling experiments, FACS analysis was performed to determine the expression of the surface marker CD69. T cells were treated with **P3c** or free αCD3 (1, 5 and 50 ng/ml) for 8 hours before placing the PBLs into fresh medium. At the time of removal of the stimulant higher numbers of CD69 expressing T cells were observed when the PBLs were treated with 50 ng/ml **P3c** than when they were treated with the same concentration of free αCD3 (Fig. 4b, Fig. S8). Based on the multivalent enhancement factor of 67 (Fig. 3) one would expect a similar level of activation for PBLs treated with 1 ng/ml of **P3c** or with 50 ng/ml of free αCD3. When comparing the initial time point at 8 hours, the **P3c** treated sample indeed contains approximately the same number of CD69 expressing cells. This amount increases during the next 40 h for the **P3c** treated sample, whereas it decreases for the sample treated with free αCD3.

To further confirm that T cells were showing sustained and robust activation for an extended period of time, IFNγ release assays were performed. PBLs were treated with 5 ng/ml **P3c** or free αCD3 for 16 hours, after which the cells where washed and

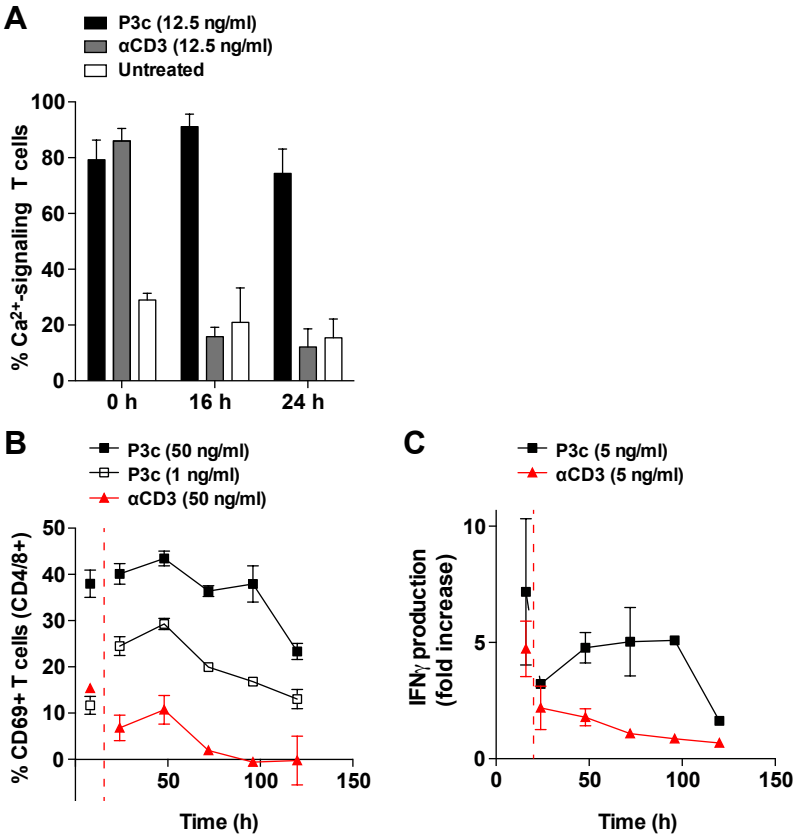

Figure 4 Analysis of sustained T cell activation. **(A)** Long-term Ca^{2+}-signaling after treating PBLs with 12.5 ng/ml **P3c** or free αCD3 for 1 hour. The first measurement (0 h) was performed directly on the microscope during 1 hour of incubation with the stimulant. The other time points represent the total time of the experiment (i.e. 1 hour incubation with the stimulant + incubation time after removal of the stimulant). For all experiments the data represents the mean ± SEM of 3 independent experiments performed with PBLs from different donors. The number of cells analyzed is summarized in Table S5. **(B)** Fraction of T cells expressing CD69 after treatment with **P3c** or free αCD3 for 8 hours. For **P3c** concentrations of 1 ng/ml and 50 ng/ml are shown. For αCD3 a concentration of 50 ng/ml is shown. The first measurement was performed directly before the stimulant was removed (8 hours). The following time points represent the total time of the experiment. For all experiments the data represents the mean ± SEM of 3 independent experiments performed with PBLs from different donors. **(C)** Concentration of secreted IFNγ after treating PBLs with 5 ng/ml **P3c** or αCD3 for 16 hours. The first measurement was performed directly before the stimulant was removed (16 hours). The following time points represent the total time of the experiment. Untreated PBLs were used as a reference. For all experiments, the data represents the mean ± SEM of 3 independent experiments performed with PBLs from different donors.

new medium was added. The supernatant was tested for IFNγ directly before the removal of the stimulant (16 hours) and a high concentration of IFNγ was determined for both treatment conditions as expected. At all subsequent time points (24, 48, 72, 96 and 120 hours after the initial stimulation), a clear difference was seen between T cells treated with **P3c** or free αCD3 (Fig. 4c). PBLs treated with free αCD3 do not seem to produce new IFNγ and a decrease in the IFNγ level is seen over time. In contrast, PBLs stimulated with **P3c** produced new IFNγ. Until the 96 hour time point an approximately constant level of IFNγ was maintained before a decrease of the IFNγ concentration was observed. Taken together, these results show that sDCs stimulate T cells over much longer periods of time compared to free αCD3 and this effect is observed for both early and late T cell activation markers.

Overall, these results show that αCD3-sDCs efficiently activate T cells, combining the benefits of multivalent binding with a spatially confined interaction with several TCRs. The equilibrium binding constant of the αCD3 antibody used is K_D = 680 μM[29] so that an overall increase in the multivalent binding strength is seen (enhancement factor of 67). At the same time, the antibody possesses a relatively fast kinetic off-rate k_{off} = 0.39 s^{-1} so that dissociation and immediate re-binding of individual polymer-attached αCD3 molecules is highly likely to occur while the sDC is bound to the cell surface. It has been proposed that such dynamic interactions are important factors contributing to T cell activation.[30] In addition to these thermodynamic and kinetic effects, the sDC polymers keep up to 10 individual effector molecule in close spatial proximity. It appears likely that one sDC binds within one nanocluster, where this proximity effect may have direct consequences for its signaling activity.[12] All together, these factors ensure efficient and long-lasting T cell activation. Even though this appears to be the most likely mechanism, other factors such as altered TCR endocytosis and exocytosis[16,31-32] or changes in membrane properties may contribute to the observed activation. Investigating these additional factors will be the subject of further study. Clearly, our sDC design is a powerful new tool that allows for studying the initial steps of T cell activation in more detail, incl. the role of TCR nanoclusters. As another important next step, the αCD3 antibody will be replaced with pMHC complexes. Natural pMHC complexes bind to the TCR with a slightly higher K_D, but similar off-rates when compared to the αCD3 antibody used.[33] The established sDC design principles can therefore be applied directly for the development of clinically relevant sDCs.

Conclusion

In summary, we have shown that polymer length and effector molecule density are key design parameters for the development of sDCs. These parameters have a direct effect on the valency of the sDC and, consequently, on the effective concentration required for T cell activation. In addition to this enhancement of the binding strength, robust and sustained T cell activation was observed that goes beyond a pure avidity effect. Our results show that the multivalent scaffold also affects T cell signaling pathways. Co-localization of several effector molecules in the same nano- or microcluster leads to a long lasting activation that cannot be achieved with non-polymer-bound antibodies. Future studies, using natural pMHCs as effector molecules, will be directed at elucidating the mechanistic origin of this sustained T cell response.

Experimental section

Polymer synthesis (P1'-P3'). Water-soluble polyisocyanopeptides were synthesized as described using our previously published method.[22] For the synthesis of **P1'** and **P2',** the functional azide monomer (N_3) and the non-functional methoxy monomer (OMe) were polymerized in a 1:100 ratio. For **P3',** a 1:70 N_3:OMe ratio was used to increase the number of possible coupling sites. The polymer length was controlled by the amount of nickel catalyst added in the polymerization reaction. A 1:200 ratio of catalyst: monomer was used for the synthesis of **P1'**. For **P2'** and **P3'** the catalyst:monomer ratio was 1:10000. The molecular weight of the polymers was determined from viscosity measurements (Table S1) as described previously.[22]

Synthesis of polymer-streptavidin conjugates. Streptavidin (SAv, Thermo Fisher Scientific) was functionalized with BCN-POE_3-NH-C(O)$CH_2CH_2CH_2$C(O)OSu (BCN-NHS; Synaffix) to couple it to the azide-groups on the polymer in a strain-promoted azide-alkyne cycloaddition (SPAAC) reaction.[24] The reaction was performed in borate buffer (10 mM, pH 8.5) using a 5 to 6-fold excess of BCN-NHS. Following incubation for 1.5 hours at room temperature, the mixture was purified by ultrafiltration (10 kDa cut-off) and gel filtration (PD-10 desalting column; GE Healthcare) to remove non-reacted BCN-NHS. During purification, the buffer was exchanged to phosphate buffered saline (PBS, pH 7.4). Mass spectrometry analysis (ESI-TOF) revealed that 1-4 BCN moieties were coupled per streptavidin molecule (BCN-SAv).

BCN-SAv was subsequently reacted with azide-bearing polyisocyanopeptide polymers. A 1:1 molar ratio of N_3:BCN-SAv was used for the synthesis of **P1-SAv** and **P2-SAv**. N_3:BCN-SAv ratios of 1:0.5, 1:1 and 1:5 were used for the synthesis of **P3a-SAv**, **P3b-SAv** and **P3c-SAv**, respectively. All reactions were performed in PBS. The reaction

mixtures were first incubated at room temperature for 1 hour and subsequently stirred at 4° C for 2.5 days. The resulting polymer-SAv conjugates were purified by ultrafiltration (100 kDa cut-off).

Characterization of polymer-streptavidin conjugates. The average polymer length and SAv density were determined with atomic force microscopy (AFM) using the method described earlier[22] (Fig. S1). The resulting histograms, displaying the distribution of polymer length and SAv distance of at least 41 individual polymers, are shown in Fig. S2 and Fig. S3. The results are summarized in Table S2.

Synthesis of sDCs (P1, P2, P3a-c). The polymer-SAv conjugates were incubated with biotinylated, monoclonal mouse anti-human CD3 antibodies (αCD3; clone OKT3; purified in house from the hybridoma cell line) to obtain the αCD3-functionalized polymers **P1**, **P2**, **P3a**, **P3b** and **P3c.** The polymer-SAv conjugates were incubated with the biotinylated antibodies in a 4:1 αCD3/SAv molar ratio. As previously described,[22] this 4:1 αCD3/SAv molar loading ratio yields a 1:1 binding ratio of αCD3 and SAv on the polymer backbone (αCD3-sDC).

Cell preparation and cell culture. Peripheral blood lymphocytes (PBLs) were obtained from buffy-coats of healthy individuals in accordance with institutional guidelines.[22] Briefly, peripheral blood mononuclear cells were obtained from Ficoll density centrifugation. Monocytes were removed using the plastic flask adherence method. The non-adherent PBLs were then maintained at 37 °C and 5 % CO_2 in complete medium: RPMI-1640 (Lonza), containing 10 % (v/v) fetal bovine serum (FBS, Gibco), 1 % (w/v) glutamine (Lonza), and 1x Antibiotic-Antimycotic (Gibco).

Single-cell Ca^{2+}-signaling. The fraction of PBLs responding to the αCD3-sDC treatment was determined in a single-cell Ca^{2+}-signaling assay using the ratiometric Ca^{2+}-indicator Fura-2. PBLs (10^5 cells) were loaded with 3 μM Fura-2 AM (Thermo Fisher) in complete medium for 1 hour at 37 °C and 5 % CO_2. Fura-2 loaded PBLs were washed twice with HEPES buffered saline (20 mM HEPES pH 7.4, 115 mM NaCl, 5.4 mM KCl, 1 mM $CaCl_2$, 0.8 mM $MgCl_2$, 13.8 mM glucose) and allowed to adhere to poly-D-L-lysine-coated (0.05 mg/ml; Sigma-Aldrich) glass bottom dishes (Nunc) at room temperature. Single-cell Ca^{2+}-measurements were performed as described before.[34] Dishes were placed on the stage of an inverted microscope (Axiovert 200M; Zeiss) equipped with a temperature-controlled CO_2 stage incubator (37 °C and 5 % CO_2) and a 63x, 1.25 NA objective (Plan NeoFluar). Fura-2 was excited at 340 nm and 380 nm alternatingly, using a monochromator (Polychrome IV; TILL Photonics). The emitted light was directed through a 415 DCLP dichroic mirror (Omega Optical) and a 510WB40 emission filter (Omega) onto a CoolSNAP HQ monochrome CCD camera (Roper Scientific).

The camera exposure time was 30 ms and the time between two ratio images was 2-4 s. All hardware was controlled with Metafluor 6.0 software (Universal Imaging). The images obtained were analyzed using Image-Pro Plus software (Media Cybernetics). Regions of interest (ROIs), corresponding to individual PBLs, were selected together with a cell-free ROI for background correction. For each ROI, the average pixel intensity was calculated for each excitation wavelength. After subtraction of the corresponding background value, the 340 nm/380 nm fluorescence emission ratio was calculated as a measure of the cytosolic Ca^{2+}-concentration. Increases in cytosolic Ca^{2+}-concentration were identified with GraphPad Prism 5 (GraphPad Software), using as criterion that the increase in the 340 nm signal is mirrored by a decrease in the 380 nm signal.

To investigate the early effects of different αCD3-sDCs on Ca^{2+}-signaling, a series of experiments was performed. These experiments include measurements to compare the effect of different αCD3-sDCs (experiments 1 and 2 in Table S3) and the dose dependences of **P3c** and freely soluble αCD3 (experiment 3 in Table S3). For these experiments, the dishes with the Fura-2 loaded T cells were placed onto the microscope and imaging was started. The different stimulants were added 5 min after the onset of imaging. After 1 h of imaging, 1 μg/ml of ionomycin was added to test for cell viability. The number of cells analyzed for every experimental condition tested is summarized in Table S4. Typical raw data of PBLs stimulated with αCD3-sDC or free αCD3 are shown in Fig. S4 and movies M1 and M2. The movies (60x speed) show Fura-2 loaded PBLs treated with free αCD3 (M1) or with the sDC-αCD3 **P3c** (M2). Each movie shows 5 min of baseline imaging and 1 h of imaging in the presence of stimulant. The last 5 min of each movie show the cells in the presence of ionomycin. The movies were captured with a frame rate of 0.25 s^{-1}. The data shows that PBLs display different patterns of Ca^{2+} signaling. In this study, we restricted ourselves to determining the fraction of Ca^{2+} signaling cells.

To establish the long-term effect of **P3c** on single-cell Ca^{2+}-signaling, PBLs were treated with the respective stimulant for 1 h, followed by incubation without stimulant for an extended period of time. The following conditions were tested: untreated, **P3c**, free αCD3, **P3-mIgG$_{2a}$** (isotype control; 40 nm mIgG$_{2a}$ spacing) and **P3c-SAv** (lacking αCD3). In more detail, PBLs (10^5 cells) were incubated with the respective stimulant (12.5 ng/ml) for 1 hour at 37 °C and 5 % CO_2. At the end of this stimulation period, the cells were washed with RPMI-1640 medium without serum and antibiotics to remove the stimulant. The cells were resuspended in fresh complete medium and maintained at 37 °C and 5 % CO_2 for another 15 h or 23 h (Fig. S6). During the last 20 min of this post-stimulation period, the cells were loaded with Fura-2. The Fura-2-loaded cells were washed twice with PBS + 1 % BSA (PBA) and imaged under the microscope for 1 h. Cell viability was assessed at the end of the measurement as described above (treatment with ionomycin for 5 min). To be able to compare these post-stimulation results with the previously obtained data, a '0 h' time point was taken where the PBLs

(10^5 cells) were first loaded with Fura-2 for 20 min and imaged exactly as described above.

Enzyme-linked immunosorbent assay (ELISA; IFNγ secretion). To investigate the effect of the different αCD3-sDCs on IFNγ secretion, PBLs (10^5 cells/well) were seeded in 96 well plates and treated with **P1**, **P2**, **P3a**, **P3b** and **P3c** or free antibodies (αCD3) at different concentrations (0.05, 0.5, 5, 50 and 100 ng/ml) for 16 h at 37 °C and 5 % CO_2. To determine the effect of polymer length, the treatment variables were **P1**, **P2** and free αCD3 along with an untreated control. The experiment was performed with PBLs from 3 different donors, each measured in duplicate. **P3a**, **P3b**, **P3c** were used to investigate the effect of αCD3 density (again using free αCD3 and untreated cells as a control). This experiment was performed with PBLs from 2 different donors (measured in duplicate). The concentration of secreted IFNγ was determined using a sandwich ELISA as described in our earlier publications.[22-23] Briefly, 96 well plates (Nunc Immunomodules) were coated with mouse anti- human IFNγ antibody (Thermo Fisher). After incubation at 4 °C overnight, the plates were washed and blocked with PBS/Tween (0.05 %) and PBS + 1 % BSA (PBA), respectively. IFNγ standards (Thermo Fisher) and supernatants (from treated and untreated cells) were added into the respective wells and incubated for 1 h at room temperature. After washing 3x with PBA, the concentration of IFNγ was detected using a biotinylated mouse anti-human IFNγ antibody (Thermo Fisher) and a streptavidin-horseradish peroxidase (HRP) conjugate (Life Technologies). HRP activity was detected using tetramethyl benzidine (TMB; Sigma Aldrich). Absorption at 450 nm was measured using an iMark Microplate Reader (Bio-Rad).

To measure the long-term effect of the αCD3-sDC treatment, PBLs (10^5 cells/well) were seeded in 96 well plates and treated with the respective stimulant at 5 ng/ml. The cells were incubated with the stimulant for 16 h at 37 °C and 5 % CO_2. After this incubation time, the cells were washed with RPMI-1640 medium without serum and antibiotics. They were then resuspended in fresh complete medium with serum to observe the activation state of the cells after the treatment was removed. The IFNγ concentration was determined directly before the medium was removed (16 hours) and at the following time points after the initial stimulation: 24, 48, 72, 96 and 120 h.

Flow cytometry (CD69 expression). To measure the long-term effect of the αCD3-sDC treatment on CD69 expression, PBLs (10^5 cells/well) were seeded in 96 well plates and treated with the respective stimulant (1, 5 and 50 ng/ml). The cells were incubated with the stimulant for 8 h at 37 °C and 5 % CO_2. After this incubation time, a sample was taken for analysis. The remaining cells were washed with RPMI-1640 medium without serum and antibiotics. They were then resuspended with fresh complete medium with serum to observe the activation state of the cells after the treatment

was removed. The cell suspensions were collected at the respective time points (24, 48, 72, 96 and 120 h after the initial stimulation) and used for flow cytometric analysis (CyAn ADP; Beckman Coulter) following the same methodology as described in our previous publications.[22-23]

Briefly, PBLs (treated or untreated) were washed twice with PBA to remove unbound sDCs or antibodies. PBLs were stained with antibodies specific for the CD4/8+ T cell subpopulations (APC-labeled mouse anti-human CD4/8 mAb; T cell marker; BD Pharmingen) and with PE-labeled mouse anti-human CD69 (eBioSciences). After 1 hour of incubation, the cells were again washed twice with PBA before performing flow cytometric analysis. The data obtained were analyzed using FlowJo ver. 9.2 Software (TreeStar Inc.). The gating strategy is shown in Fig. S9.

Associated content

Supporting Information. Characterization data for the polymer conjugates, experimental details of the single-cell Ca^{2+}-signaling experiments as well as additional control experiments are described in the supporting information. Movies M1 and M2 show representative data of the single-cell Ca^{2+}-signaling experiments. This material is available free of charge via the Internet at http://pubs.acs.org

Acknowledgment

This work was supported by grants from the Dutch Cancer Society (grants KUN2006-3699 and KUN2009-4402), the Dutch government to the Netherlands Institute for Regenerative Medicine (NIRM, grant FES0908), the European Research Council (ERC; grant ERC-2010-AdG269019, C.G.F.), the Netherlands Organization for Scientific Research (NWO; Spinoza award 2006, C.G.F; VICI grant 700.56.444, A.E.R.; VIDI grant 700.58.430, K.G.B.) as well as NanoNext (grants 7A.06 and 3D.12).

References

1. Banchereau, J.; Steinman, R. M. Dendritic cells and the control of immunity. *Nature* **1998,** *392*, 245-252.
2. Eggermont, L. J.; Paulis, L. E.; Tel, J.; Figdor, C. G. Towards efficient cancer immunotherapy: advances in developing artificial antigen-presenting cells. *Trends Biotechnol.* **2014,** *32*, 456-465.
3. Hardy, N. M.; Mossoba, M. E.; Steinberg, S. M.; Fellowes, V.; Yan, X. Y.; Hakim, F. T.; Babb, R. R.; Avila, D.; Gea-Banacloche, J.; Sportes, C.; Levine, B. L.; June, C. H.; Khuu, H. M.; Carpenter, A. E.; Krumlauf, M. C.; Dwyer, A. J.; Gress, R. E.; Fowler, D. H.; Bishop, M. R. Phase I trial of adoptive cell transfer with mixed-profile type-I/type-II allogeneic T cells for metastatic breast cancer. *Clin. Cancer Res.* **2011,** *17*, 6878-6887.
4. Garlie, N. K.; LeFever, A. V.; Siebenlist, R. E.; Levine, B. L.; June, C. H.; Lum, L. G. T cells coactivated with immobilized anti-CD3 and anti-CD28 as potential immunotherapy for cancer. *J. Immunother.* **1999,** *22*, 336-345.
5. Fadel, T. R.; Sharp, F. A.; Vudattu, N.; Ragheb, R.; Garyu, J.; Kim, D.; Hong, E.; Li, N.; Haller, G. L.; Pfefferle, L. D.; Justesen, S.; Herold, K. C.; Fahmy, T. M. A carbon nanotube-polymer composite for T-cell therapy. *Nat. Nanotechnol.* **2014,** *9*, 639-647.
6. Prakken, B.; Wauben, M.; Genini, D.; Samodal, R.; Barnett, J.; Mendivil, A.; Leoni, L.; Albani, S. Artificial antigen-presenting cells as a tool to exploit the immune 'synapse'. *Nat. Med.* **2000,** *6*, 1406-1410.
7. van der Weijden, J.; Paulis, L. E.; Verdoes, M.; van Hest, J. C. M.; Figdor, C. G. The right touch: design of artificial antigen-presenting cells to stimulate the immune system. *Chem. Sci.* **2014,** *5*, 3355-3367.
8. Lillemeier, B. F.; Mortelmaier, M. A.; Forstner, M. B.; Huppa, J. B.; Groves, J. T.; Davis, M. M. TCR and Lat are expressed on separate protein islands on T cell membranes and concatenate during activation. *Nat. Immunol.* **2010,** *11*, 90-96.
9. Schamel, W. W. A.; Alarcón, B. Organization of the resting TCR in nanoscale oligomers. *Immunol. Rev.* **2013,** *251*, 13-20.
10. Dinic, J.; Riehl, A.; Adler, J.; Parmryd, I. The T cell receptor resides in ordered plasma membrane nanodomains that aggregate upon patching of the receptor. *Sci. Rep.* **2015,** *5*, 10082.
11. Nika, K.; Acuto, O. Membrane nanodomains in T-cell antigen receptor signalling. *Essays Biochem.* **2015,** *57*, 165-175.
12. Pageon, S. V.; Tabarin, T.; Yamamoto, Y.; Ma, Y.; Nicovich, P. R.; Bridgeman, J. S.; Cohnen, A.; Benzing, C.; Gao, Y.; Crowther, M. D.; Tungatt, K.; Dolton, G.; Sewell, A. K.; Price, D. A.; Acuto, O.; Parton, R. G.; Gooding, J. J.; Rossy, J.; Rossjohn, J.; Gaus, K. Functional role of T-cell receptor nanoclusters in signal initiation and antigen discrimination. *Proc. Natl. Acad. Sci. U. S. A.* **2016,** *113*, E5454-E5463.
13. Varma, R.; Campi, G.; Yokosuka, T.; Saito, T.; Dustin, M. L. T cell receptor-proximal signals are sustained in peripheral microclusters and terminated in the central supramolecular activation cluster. *Immunity* **2006,** *25*, 117-127.
14. Yokosuka, T.; Saito, T. Dynamic regulation of T-cell costimulation through TCR–CD28 microclusters. *Immunol. Rev.* **2009,** *229*, 27-40.
15. Choudhuri, K.; Dustin, M. L. Signaling microdomains in T cells. *FEBS Lett.* **2010,** *584*, 4823-4831.
16. Hashimoto-Tane, A.; Saito, T. Dynamic Regulation of TCR–Microclusters and the Microsynapse for T Cell Activation. *Front. Immunol.* **2016,** *7*.
17. Fooksman, D. R.; Vardhana, S.; Vasiliver-Shamis, G.; Liese, J.; Blair, D. A.; Waite, J.; Sacristán, C.; Victora, G. D.; Zanin-Zhorov, A.; Dustin, M. L. Functional Anatomy of T Cell Activation and Synapse Formation. *Annu. Rev. Immunol.* **2010,** *28*, 79-105.
18. Mulder, A.; Huskens, J.; Reinhoudt, D. N. Multivalency in supramolecular chemistry and nanofabrication. *Org. Biomol. Chem.* **2004,** *2*, 3409-3424.
19. Krishnamurthy, V. M.; Estroff, L. A.; Whitesides, G. M. Multivalency in Ligand Design. In *Fragment-based Approaches in Drug Discovery*, Jahnke, W.; Erlanson, D. A., Eds. Wiley-VCH Verlag GmbH & Co. KGaA: Weinheim, 2006; Vol. 34, pp 11-53.
20. Kitov, P. I.; Bundle, D. R. On the Nature of the Multivalency Effect: A Thermodynamic Model. *J. Am. Chem. Soc.* **2003,** *125*, 16271-16284.

21. Huskens, J. Multivalent interactions at interfaces. *Curr. Opin. Chem. Biol.* **2006,** *10*, 537-543.
22. Mandal, S.; Eksteen-Akeroyd, Z. H.; Jacobs, M. J.; Hammink, R.; Koepf, M.; Lambeck, A. J. a.; van Hest, J. C. M.; Wilson, C. J.; Blank, K.; Figdor, C. G.; Rowan, A. E. Therapeutic nanoworms: towards novel synthetic dendritic cells for immunotherapy. *Chem. Sci.* **2013,** *4*, 4168-4174.
23. Mandal, S.; Hammink, R.; Tel, J.; Eksteen-Akeroyd, Z. H.; Rowan, A. E.; Blank, K.; Figdor, C. G. Polymer-Based Synthetic Dendritic Cells for Tailoring Robust and Multifunctional T Cell Responses. *ACS Chem. Biol.* **2015,** *10*, 485-492.
24. Dommerholt, J.; Schmidt, S.; Temming, R.; Hendriks, L. J. A.; Rutjes, F. P. J. T.; van Hest, J. C. M.; Lefeber, D. J.; Friedl, P.; van Delft, F. L. Readily Accessible Bicyclononynes for Bioorthogonal Labeling and Three-Dimensional Imaging of Living Cells. *Angew. Chem., Int. Ed. Engl.* **2010,** *49*, 9422-9425.
25. Joseph, N.; Reicher, B.; Barda-Saad, M. The calcium feedback loop and T cell activation: How cytoskeleton networks control intracellular calcium flux. *Biochim. Biophys. Acta, Biomembr.* **2014,** *1838*, 557-568.
26. Williams, D. A.; Fogarty, K. E.; Tsien, R. Y.; Fay, F. S. Calcium gradients in single smooth muscle cells revealed by the digital imaging microscope using Fura-2. *Nature* **1985,** *318*, 558-561.
27. Donnadieu, E.; Bismuth, G.; Trautmann, A. The intracellular Ca^{2+} concentration optimal for T cell activation is quite different after ionomycin or CD3 stimulation. *Pfluegers Arch.* **1995,** *429*, 546-554.
28. Montet, X.; Funovics, M.; Montet-Abou, K.; Weissleder, R.; Josephson, L. Multivalent Effects of RGD Peptides Obtained by Nanoparticle Display. *J. Med. Chem.* **2006,** *49*, 6087-6093.
29. Kjer-Nielsen, L.; Dunstone, M. A.; Kostenko, L.; Ely, L. K.; Beddoe, T.; Mifsud, N. A.; Purcell, A. W.; Brooks, A. G.; McCluskey, J.; Rossjohn, J. Crystal structure of the human T cell receptor CD3εγ heterodimer complexed to the therapeutic mAb OKT3. *Proc. Natl. Acad. Sci. U. S. A.* **2004,** *101*, 7675-7680.
30. Dushek, O.; van der Merwe, P. A. An induced rebinding model of antigen discrimination. *Trends Immunol.* **2014,** *35*, 153-158.
31. Griffiths, G. M.; Tsun, A.; Stinchcombe, J. C. The immunological synapse: a focal point for endocytosis and exocytosis. *J. Cell Biol.* **2010,** *189*, 399-406.
32. Choudhuri, K.; Llodra, J.; Roth, E. W.; Tsai, J.; Gordo, S.; Wucherpfennig, K. W.; Kam, L. C.; Stokes, D. L.; Dustin, M. L. Polarized release of T-cell-receptor-enriched microvesicles at the immunological synapse. *Nature* **2014,** *507*, 118-123.
33. Stone, J. D.; Chervin, A. S.; Kranz, D. M. T-cell receptor binding affinities and kinetics: impact on T-cell activity and specificity. *Immunology* **2009,** *126*, 165-176.
34. Visch, H.-J.; Koopman, W. J. H.; Zeegers, D.; van Emst-de Vries, S. E.; van Kuppeveld, F. J. M.; van den Heuvel, L. W. P. J.; Smeitink, J. A. M.; Willems, P. H. G. M. Ca^{2+}-mobilizing agonists increase mitochondrial ATP production to accelerate cytosolic Ca^{2+} removal: aberrations in human complex I deficiency. *Am. J. Physiol.* **2006,** *291*, C308-16.

Supplementary tables and figures

Table S1 Characteristics of the polymers.

Polymer	Catalyst ratio	N_3 ratio	M_v (kg/mol)[a]
P1'	1:200	1:100	200
P2'	1:10,000	1:100	628
P3'	1:10,000	1:70	577

[a] Determined from viscosity measurements.

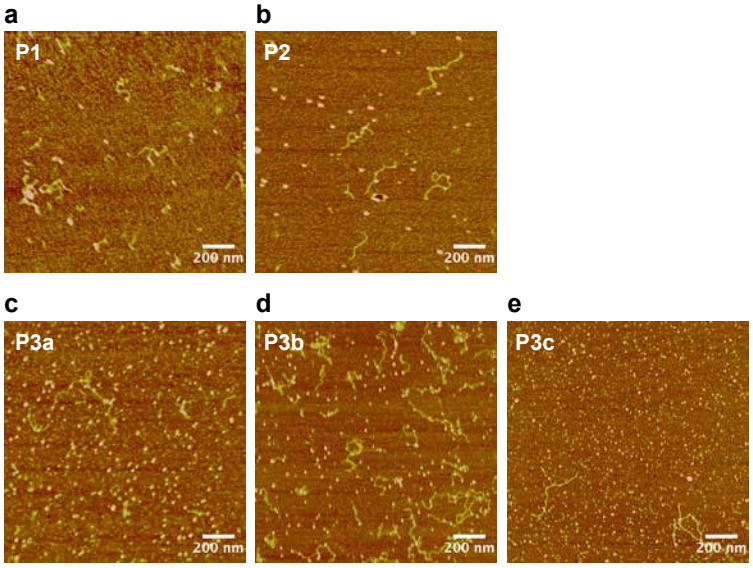

Figure S1 Representative AFM images of the polymer-SAv conjugates (**P1-P3c**) drop-casted on polylysine treated mica. Scale bar: 200 nm for **(a)**-**(e)**.

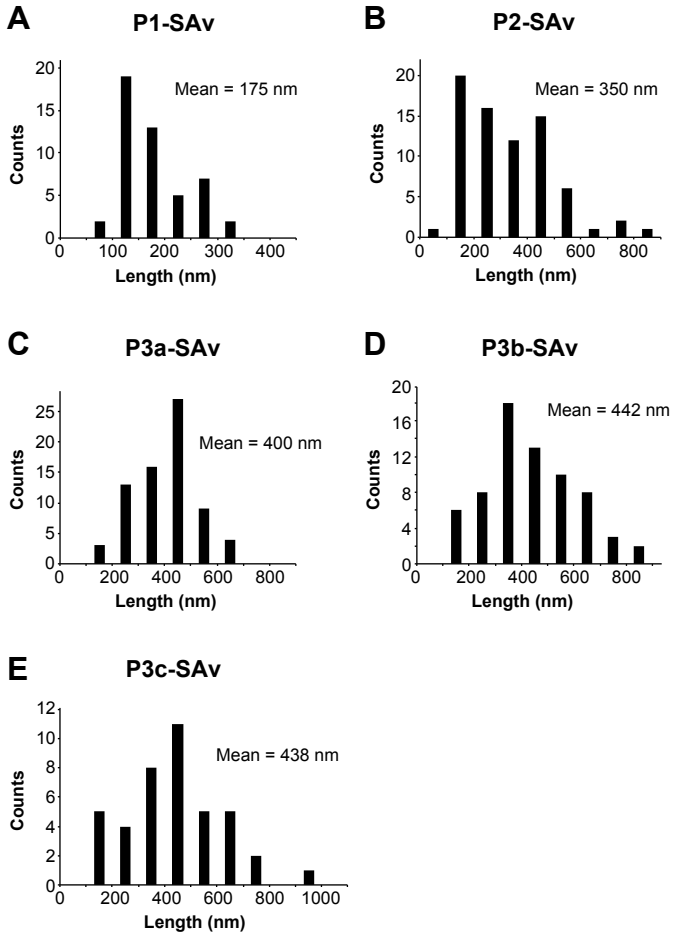

Figure S2 Length distribution of the different polymer-SAv conjugates as determined from AFM images. Each histogram contains at least 41 polymers: **(A) P1-SAv**, n = 48; **(B) P2-SAv**, n = 74; **(C) P3a-SAv**, n = 72; **(D) P3b-SAv**, n = 68; **(E) P3c-SAv**, n = 41.

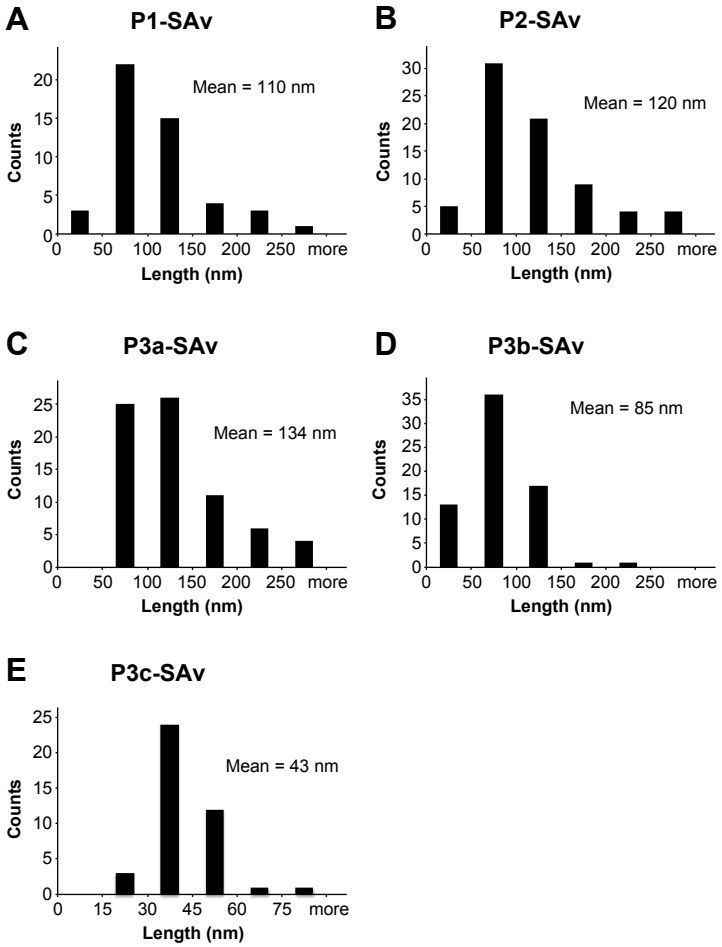

Figure S3 Average distance between SAv molecules determined from the AFM images. Each histogram contains at least 41 polymers: **(A) P1-SAv**, n = 48; **(B) P2-SAv**, n = 74; **(C) P3a-SAv**, n = 72; **(D) P3b-SAv**, n = 68; **(E) P3c-SAv**, n = 41.

Table S2 Characteristics of the polymer-SAv conjugates.

Polymer	SAv equivalents	Mean length (nm)[a]	Mean SAv distance (nm)[a]
P1	1	175	110
P2	1	350	120
P3a	0.5	400	134
P3b	1	442	85
P3c	5	438	43

[a] Determined with AFM imaging.

Table S3 Treatment conditions for the single-cell Ca^{2+}-signaling experiments.

Experiment	Stimulant	Imaging time	αCD3 concentration[a]
1. sDC length	i. **P1** ii. **P2** iii. free αCD3 iv. untreated	5 min baseline Ca^{2+} 1 h treatment 5 min ionomycin	0.005, 0.5, 5, 25 ng/ml
2. αCD3 density	i. **P3a** ii. **P3b** iii. **P3c** iv. free αCD3 v. untreated	5 min baseline Ca^{2+} 1 h treatment 5 min ionomycin	0.005, 0.5, 5, 25 ng/ml
3. dose-response curves	i. **P3c** ii. free αCD3 iii. untreated	5 min baseline Ca^{2+} 1 h treatment 5 min ionomycin	0.001, 0.01, 0.1, 5, 10, 25, 50, 100 ng/ml

[a] The concentration always refers to the amount of αCD3 bound to the αCD3-sDCs or present in freely soluble form (free αCD3).

Table S4 Number of cells analyzed for the single-cell Ca^{2+}-signaling experiments.

Experiment	Stimulant		c(αCD3)	Number of cells analyzed		
				Donor 1	Donor 2	Donor 3
1. sDC length	i.	**P1**	0.005 ng/ml	12	7	5
			0.5 ng/ml	12	5	6
			5 ng/ml	11	5	6
			25 ng/ml	6	7	6
	ii.	**P2**	0.005 ng/ml	12	6	6
			0.5 ng/ml	12	5	6
			5 ng/ml	12	7	6
			25 ng/ml	7	8	5
	iii.	αCD3	0.005 ng/ml	7	5	4
			0.5 ng/ml	6	3	6
			5 ng/ml	5	8	5
			25 ng/ml	7	7	6
2. αCD3 density	i.	**P3a**	0.005 ng/ml	4	4	4
			0.5 ng/ml	2	4	6
			5 ng/ml	4	4	4
			25 ng/ml	12	6	5
	ii.	**P3b**	0.005 ng/ml	6	6	5
			0.5 ng/ml	5	5	8
			5 ng/ml	8	5	7
			25 ng/ml	6	5	6
	iii.	**P3c**	0.005 ng/ml	6	6	6
			0.5 ng/ml	10	10	6
			5 ng/ml	8	8	5
			25 ng/ml	14	10	5
	iv.	αCD3	0.005 ng/ml	6	5	4
			0.5 ng/ml	7	4	6
			5 ng/ml	5	8	5
			25 ng/ml	7	7	6
3. dose-response curves	i.	**P3c**	0.001 ng/ml	44	31	33
			0.01 ng/ml	17	39	19
			0.1 ng/ml	22	21	22
			5 ng/ml	22	17	18
			10 ng/ml	23	14	22
			25 ng/ml	13	12	25
			50 ng/ml	14	24	24
			100 ng/ml	21	26	31
	ii.	αCD3	0.001 ng/ml	10	30	23
			0.01 ng/ml	24	26	26
			0.1 ng/ml	14	33	33
			5 ng/ml	17	16	15
			10 ng/ml	13	42	26
			25 ng/ml	8	21	15
			50 ng/ml	12	20	31
			100 ng/ml	11	25	21

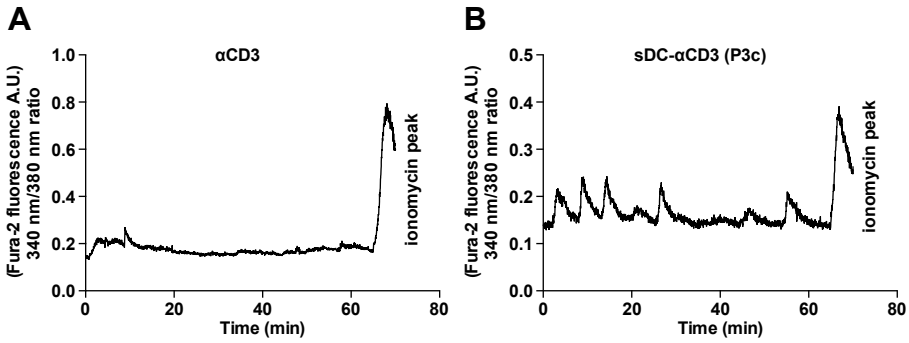

Figure S4 Single-cell Ca^{2+}-signaling experiments. Representative time traces (340 nm/380 nm ratio) for PBLs treated with free αCD3 **(A)** or **P3c (B)**.

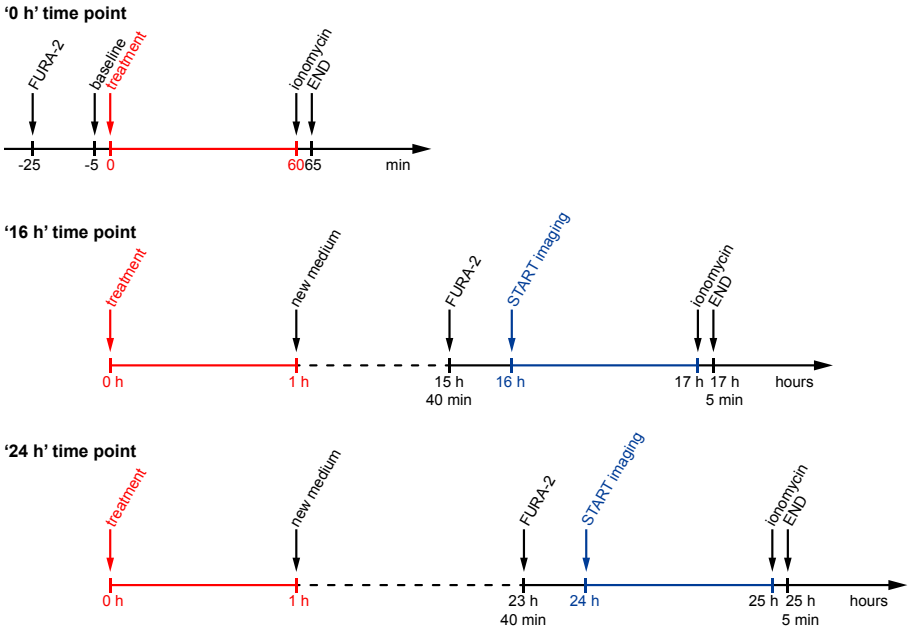

Figure S5 IFNγ secretion of PBLs treated with **P3a**, **P3b** or **P3c** normalized to polymer concentration.

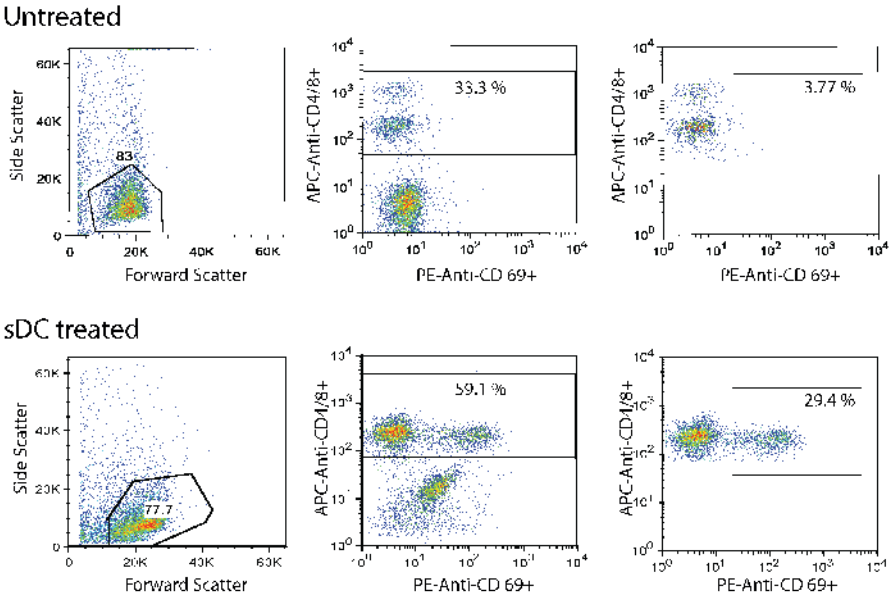

Figure S6 Timeline of the post-stimulation single-cell Ca^{2+}-signaling experiments. To obtain the 'o h' time point, the Fura-2 loaded cells were treated with the stimulant directly under the microscope and imaged for 1 h. For the '16 h' and '24 h' time points the cells were first treated with the respective stimulant for 1 h, washed to remove the stimulant and then incubated without stimulant for 15 h or 23 h, respectively. During the last 20 min of this incubation period, the cells were loaded with Fura-2. Imaging was started at the indicated time point. At the end of the 1 h imaging period, the cells were treated with ionomycin to determine cell viability. In this post-stimulation experiment, the '5 min' baseline was only determined for the 'o h' time point.

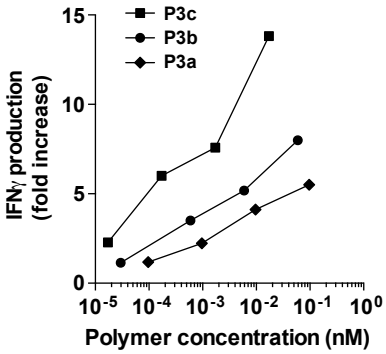

Figure S7 Results of the post-stimulation single-cell Ca^{2+}-signaling experiments. PBLs were treated with 12.5 ng/ml **P3c** or free αCD3 for 1 h. The stimulant was removed and the cells were incubated in fresh medium. Ca^{2+}-imaging was performed 16 h or 24 h after starting the treatment (15 h or 23 h after removal of the stimulant). As a reference, PBLs were also imaged under the microscope while the stimulant was added (0 h). The graph further shows data obtained for PBLs treated with the following controls: **P3**-SAv, **P3**-mIgG_{2a} (isotype control) or medium (untreated). For all experiments the data represents the mean ± SEM of 3 independent experiments performed with PBLs from different donors. The number of cells analyzed is summarized in Table S5. The asterisks represent the statistical significance at 'p' values of 0.001 (***). A clear difference is observed between the post-stimulation signaling of αCD3-sDC treated cells and the cells treated with the free αCD3 antibody or any of the controls. Of note, the untreated control shows a small fraction of PBLs (~30 %) that display spontaneous increases in the cytosolic Ca^{2+}-concentration (white bars). A similar percentage of PBLs (~26%) showing spontaneous Ca^{2+} oscillations (Ca^{2+} oscillations that occur in the absence of added stimulant) has been reported before (Donnadieu, E; Bismuth, G; Trautmann, A. The intracellular Ca^{2+} concentration optimal for T cell activation is quite different after ionomycin or CD3 stimulation. *Pfluegers Arch. – Eur. J. Physiol.* **1995**, 429 (4), 546-554).

Table S5 Number of cells analyzed for the post-stimulation Ca^{2+}-signaling experiments.

Stimulant		Incubation time	Number of cells analyzed		
			Donor 1	Donor 2	Donor 3
i.	**P3c**	0 h	15	14	11
		16 h	7	8	6
		24 h	10	7	7
ii.	αCD3	0 h	14	9	8
		16 h	9	9	7
		24 h	10	9	7
iii.	**P3**-mIgG$_{2a}$	0 h	10	9	6
		16 h	10	8	6
		24 h	10	9	5
iv.	**P3**-SAv	0 h	10	14	7
		16 h	11	11	5
		24 h	9	9	6
v.	untreated	0 h	9	7	8
		16 h	9	7	5
		24 h	9	9	7

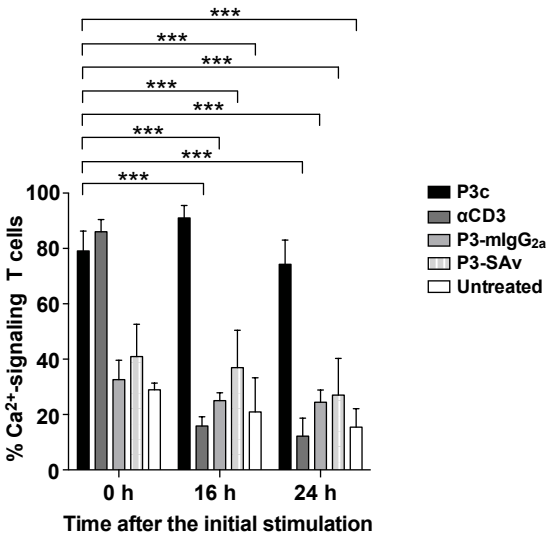

Figure S8 Post-stimulation analysis of CD69 expression. Percentage of CD69 expressing T cells after treatment with different concentrations of **P3c** or αCD3.

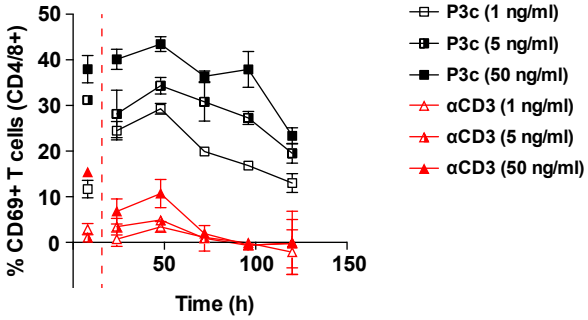

Figure S9 Post-stimulation analysis of CD69 expression. Percentage of CD69 expressing T cells after treatment with different concentrations of **P3c** or αCD3.

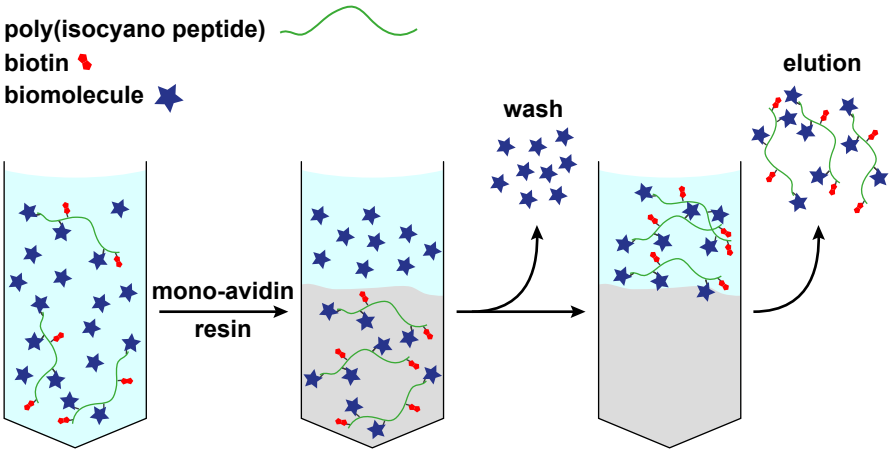
poly(isocyano peptide)
biotin
biomolecule
mono-avidin
resin
wash
elution

3

Affinity-Based Purification of Polyisocyanopeptide Bioconjugates

Loek Eggermont*, Roel Hammink*, Zisis Themistoklis, Jurjen Tel, Carl Figdor, Alan Rowan, Kerstin Blank

ACS Bioconjugate Chemistry, 2017, 28(10), 2560-2568

*contributed equally

Abstract

Water-soluble poly(isocyanopeptides) (PICs) are a new class of synthetic polymers that mimic natural protein-based filaments. Their unique semi-flexible properties combined with a length of several hundred nanometers have recently enabled a number of biomedical applications, ranging from tissue engineering to cancer immunotherapy. One crucial step toward the further development of PICs for these applications is the efficient and controlled synthesis and purification of PIC-biomolecule conjugates. Considering the large size of PICs and the biomolecules to be conjugated, conjugations reactions do usually not proceed to completion due to steric effects. As a consequence, purification of the reaction mixture is necessary to separate the obtained bioconjugates from unreacted biomolecules. As a direct result of the semi-flexible nature of PICs, standard polymer and/or protein purification methods based on molecular weight have not been successful. Here, we introduce a new affinity-based purification method utilizing biotin as an affinity tag. PICs decorated with a controlled and tunable density of biotin molecules (biotinPICs) were efficiently bound to and eluted from a mono-avidin resin in buffered aqueous solution. Using these biotinPICs, two different protein conjugates were synthesized, one carrying the enzyme alkaline phosphatase (PhoA) and the other T-cell activating anti-CD3 antibodies. The resulting biotinPIC-protein conjugates were successfully obtained in high purity (>90 %) and without any loss of protein activity. The high purity greatly simplifies the analysis of biotinPIC-bioconjugates, such as the determination of the average number of biomolecules conjugated per biotinPIC chain. Most importantly, it allows for the direct and straightforward application of the obtained bioconjugates in the desired applications. The new method developed may further be adapted for the purification of other advanced bioconjugates that are difficult to obtain in high purity with available standard methods.

Keywords

polymer bioconjugate, polyisocyanopeptide, streptavidin, avidin, biotin, affinity chromatography

Introduction

Following the synthesis of the first polymer-protein conjugate approximately 40 years ago,[1] the range of applications of these functional bioconjugates has grown enormously. The first and still most common motivation for the synthesis of polymer-protein conjugates is to improve the properties of therapeutic proteins. Nowadays, the conjugation of poly(ethylene glycol) (PEG) is a frequently employed strategy to increase protein solubility and stability, to reduce immunogenicity and to alter circulation half-life.[2-4] With continuous improvements in polymer synthesis and bioconjugation methods,[5-8] the range of applications has expanded and new classes of polymers have been utilized. For example, conjugation with stimuli-responsive polymers such as poly(N-isopropylacrylamide) (PNIPAAm) introduces additional functionality into the protein.[5,8,9] Making use of the temperature-sensitive behavior of PNIPAAm, the protein-polymer conjugate reversibly precipitates when increasing the temperature above the lower critical solution temperature (LCST) of PNIPAAm,[5] allowing for the development of advanced purification methods and diagnostic assays.[8,9] Linear or branched polymers with multiple reactive groups have been used as scaffolds for the synthesis of multivalent bioconjugates with increased binding strength[10-14] or of multifunctional entities that combine different activities.[12,13,15] The latter is of particular interest for engineering enzyme cascades where reaction intermediates need to be efficiently transferred between enzyme active sites.[15-17] Polymer-bioconjugates further find application for the synthesis of biocompatible hydrogels for tissue engineering applications[18-21] as well as for the synthesis of self-assembled nanostructures, where the biomolecules are used as functional material building blocks.[22,23]

Over the last years we have introduced water-soluble poly(isocyanopeptides) (PICs) as novel and versatile polymer scaffolds for biological applications.[24-26] PICs are long (100-1000 nm) and semi-flexible polymers that mimic the properties of many protein-based filaments found in nature, e.g. in the cytoskeleton and the extracellular matrix. Their semi-flexibility is a direct result of their helical secondary structure and represents a unique feature for synthetic polymers.[27,28] PICs are polymerized from isocyanide monomers that carry a short di-alanine peptide in every monomer. Upon folding into a helix, hydrogen bonds between the peptide amides stabilize the helical structure. PIC monomers are further functionalized with oligoethylene glycol chains to provide water solubility. When carrying a tri-ethylene glycol chain (EG_3), the corresponding PIC undergoes a sol-to-gel transition at a temperature of ~19 °C.[27,29] Consequently, EG_3-functionalized PICs form a hydrogel at room temperature. This hydrogel has been used in cell culture[21] and for sensing the binding of short oligonucleotides to their complementary sequence.[30]. In contrast, tetra-ethylene glycol (EG_4) functionalized polymers undergo a sol-to-gel transition at

40-45 °C.[27] These PICs are therefore fully dissolved at physiologically relevant temperatures, making them excellent scaffolds for the synthesis of polymer conjugates. As a first application, we have attached T cell stimulating antibodies to EG_4-functionalized PICs and used these PIC-antibody conjugates as novel artificial antigen presenting cells in immunotherapeutic applications.[11,12,14]

All these applications have in common that the PICs have to be functionalized with biomolecules. For the cell culture application, a short integrin-binding GRGDS peptide was grafted onto PICs to provide cell adhesion sites in the hydrogel.[21] In the sensing application, short DNA oligonucleotides were coupled to the PICs. These DNA sequences were subsequently cross-linked upon binding of an analyte.[30] For the immunotherapeutic application, the PICs were functionalized with streptavidin to allow for the subsequent binding of biotinylated antibodies.[11,12,14]

As a direct result of their unique physical properties, these semi-flexible PICs do not form a typical random coil structure in solution. This complicates the separation of polymer-biomolecule conjugates from non-reacted biomolecules, following a conjugation reaction. Despite careful optimization, neither dialysis nor size exclusion chromatography nor field flow fractionation methods were found to be successful. Ultrafiltration was identified as the only possible method for the purification of freshly synthesized PIC-bioconjugates, but more than 99% of the material was lost during the process.[11,12,14] As an alternative, the reaction between PICs and biomolecules was carefully optimized so that an almost quantitative coupling of biomolecules was achieved and no purification was needed. For small molecules, such as short peptides[21] and DNA oligonucleotides,[30] this method was successful. For large proteins, e.g. antibodies, the reaction with the PIC is not quantitative,[11,12,14] however, as steric effects limit the kinetics and the yield of the reaction. Clearly, an alternative and efficient purification method is needed to obtain pure PIC-bioconjugates in good yield.

Affinity tags such as the hexahistidine tag,[31] the strep-tag[32] or biotin[33] are frequently used for the purification of recombinantly expressed proteins from crude cell extracts. To the best of our knowledge, such a purification strategy has never been used for the purification of bioconjugates that contain a synthetic polymer. Inspired by the affinity tag method, a PIC polymer carrying biotin as an affinity tag was designed. Using this biotin-functionalized PIC (biotinPIC), affinity purification on a mono-avidin resin can potentially be used to remove unreacted biomolecules. Mono-avidin is a monomeric derivative of avidin that possesses a highly reduced affinity for biotin.[34] It has been shown that biotinylated molecules bind to mono-avidin agarose in a reversible manner and can be eluted competitively when adding high concentrations of free biotin.[35] Here, we describe the synthesis and characterization of biotinPIC polymers. We show that these biotinPICs reversibly bind to a mono-avidin resin and that this affinity purification method can be used for the purification of biotinPIC-bioconjugates. The versatility of this new purification method

is demonstrated using two different model proteins, an antibody and an enzyme. The enzyme (alkaline phosphatase from *E. coli*; PhoA) was chosen as it allows for the straightforward determination of the activity of the conjugated biomolecule. The antibody of choice is the same anti-CD3 antibody (αCD3) that has been used earlier for the synthesis of PIC-antibody conjugates for stimulating T cells.[11,12,14]

Results and discussion

Synthesis and characterization of biotin-functionalized polyisocyanopeptides. To investigate if the biotin affinity tag can be used for the purification of PIC-bioconjugates, biotin-functionalized polymers were synthesized (Figure 1) and used in a series of purification experiments. For this purpose, PICs containing azide-functionalized side chains in a pre-defined density were synthesized using the same method as described in our previous publications.[11,12,14,21,30] In short, functional azide monomers were copolymerized with monomers containing non-functional methoxy groups, using a nickel catalyst. The ratio of azide:methoxy monomers was chosen to be 1:30, yielding a statistical average distance between azides of 3 nm. Subsequently, the azide-functionalized PIC was reacted with different relative amounts of biotin-azadibenzo-

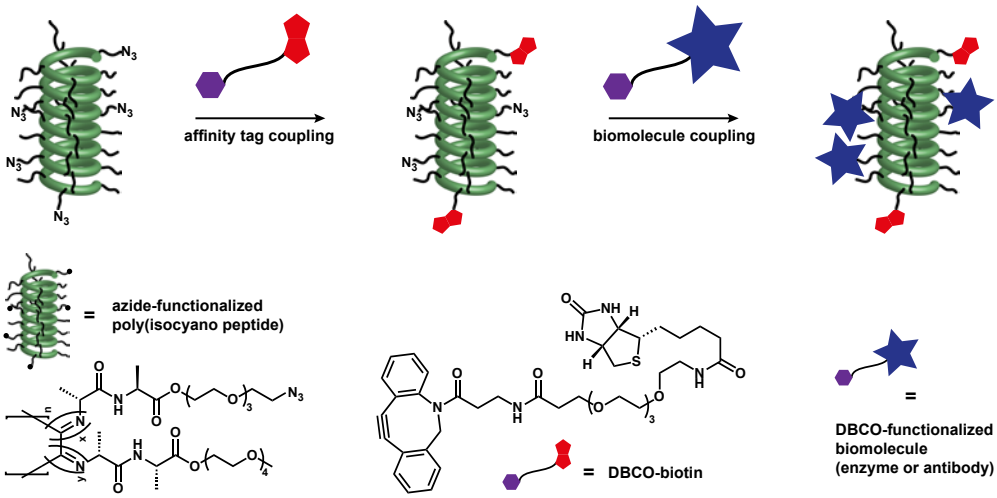

Figure 1 Conjugation strategy for the synthesis of biotin-functionalized polyisocyano-peptides that can be used for the subsequent coupling of DBCO-containing biomolecules. In this work, the biomolecule is either an antibody (αCD3) or an enzyme (PhoA).

cyclooctyne (biotin-EG_4-DBCO) in a strain-promoted azide-alkyne cycloaddition (SPAAC) reaction.[36] Assuming a quantitative yield of the reaction, biotinPICs with an average biotin spacing of 5, 7.5, 10 and 40 nm were prepared. Using this strategy, the remaining azide groups are available for a second SPAAC reaction that allows for the coupling of DBCO-functionalized biomolecules.

To optimize the biotin density necessary to bind and elute the biotinPICs from mono-avidin containing beads in a batch purification process, an incubation and elution protocol was developed. The polymers were diluted to 0.1-0.2 mg ml^{-1} in phosphate buffered saline (PBS) and mixed with a 50 % slurry of mono-avidin beads in a 1:1 (v/v) ratio. The binding of the biotinPICs to the beads was determined by measuring the concentration of unbound biotinPIC in the supernatant using circular dichroism (CD) spectroscopy. Due to the helical conformation of the PICs, this technique provides an indication of the polymer concentration, assuming that the polymer conformation is not altered during the experiment.[25,26,37] The CD spectrum of the PIC is characterized by a negative peak at λ = 360 nm and a larger positive peak with a maximum at λ = 272 nm (Figure S1). Calibration curves of the azide-functionalized PIC were determined at both wavelengths, showing that the corresponding peak heights scale linearly with polymer concentration (Figure S1). The analysis of the supernatants after 4 hours of incubation shows that the biotinPICs are able to bind to the mono-avidin beads. When comparing the samples with different biotin densities, clear differences are seen in the fraction of bound biotinPICs (Figure 2a). Polymers with the lowest biotin density (spacing of 1 biotin per 40 nm) showed little binding (~12%) and the majority of biotinPICs remained in the supernatant. Decreasing the biotin spacing to 10 nm already increased the fraction of bound biotinPICs to ~30%. A further decrease in the biotin spacing to 7.5 nm and 5 nm allowed for binding ~65-70% of the biotinPICsto the mono-avidin beads. The biotin spacing was not decreased further as a sufficient amount of free azides is required for further bioconjugation.

After having confirmed binding of the biotinPICs to mono-avidin beads, the elution protocol was optimized. The beads were first washed with PBS containing 0.1% Tween 20 (PBS-T, 2x) and PBS (4x) to remove any non-specifically bound polymers. During this extensive washing protocol, ~30% of the beads were lost, which reduces the total yield of eluted polymers. Following washing, PBS containing 2 mM biotin was added to the beads to elute the bound biotinPICs competitively. In the last step, the eluate was filtered over a frit with 20 µm pore size to remove residual mono-avidin beads. The CD spectrum of the eluted fractions was not altered when compared to the original polymer samples before purification, which indicates that the helical structure is not affected during the binding and elution process (Figure 2b). The fraction of eluted biotinPICs clearly correlates with the relative amount of biotinPIC initially bound to the beads and, consequently, also with the density of biotin coupled to the polymer. Only a small fraction (4 % of the original amount) was obtained for the

polymer with a biotin spacing of 40 nm. Higher fractions of 17, 34 and 35 % were obtained for the other polymers with a biotin spacing of 10, 7.5 and 5 nm, respectively (Figure 2a). Considering the loss of beads during the washing steps and the fraction of polymer that did not bind to the beads, elution with 2 mM biotin is sufficient to elute more than 50 % of the bound biotinPIC polymers.

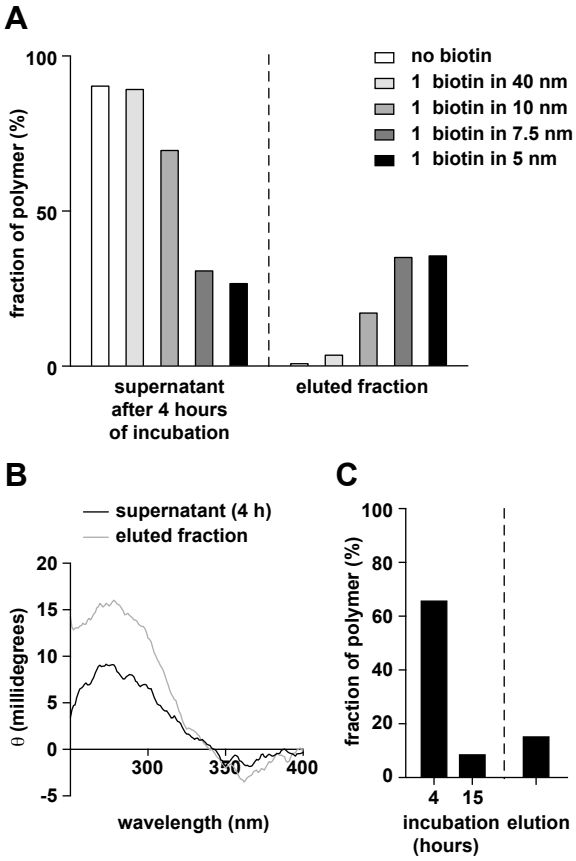

Figure 2 Binding and elution of biotinPICs to and from mono-avidin beads. **(A)** Binding and elution profiles for biotinPICs containing a different biotin density (EG_4 linker). Shown is the relative amount of biotinPIC in the supernatant after binding or elution. **(B)** CD spectrum of the supernatant after 4 hours of incubation. In addition, the eluted fraction is shown (data shown for 1 biotin in 7.5 nm. **(C)** Binding and elution profile of biotinPICs prepared with the long (3000 Da) PEG linker and a biotin spacing of 7.5 nm. Shown is again the relative amount of biotinPIC in the supernatant after binding and elution.

In addition to the biotin density, also the linker length between biotin and the PIC polymer backbone was investigated. To test for possible steric hindrance, the length of the PEG spacer between the biotin moiety and the DBCO functional group was increased. Using a PEG linker with a molecular weight of 3000 Da, biotinPIC polymers were prepared with an average biotin spacing of 7.5 nm. Binding of this polymer to the beads was considerably slower when compared to the previously used biotinPICs containing only the EG_4 linker. Only after 15 hours of incubation more than 90% of the polymer was bound. Unfortunately, elution of this polymer recovered only 15 % of the original amount (Figure 2c). Overall, it appears that the longer linker does not reduce, but instead increases steric hindrance thereby affecting both the kinetics of the interaction as well as the yield of the purification protocol.

Taken together, these results show that the biotinPIC with a biotin spacing of 7.5 nm coupled via the short linker performs best when considering both the requirements for an efficient purification as well as its future application. It shows good binding and a reasonable amount is eluted from the mono-avidin beads. At the same time, a sufficient number of azides is left for further conjugation. This biotinPIC was therefore selected as a model system to test whether this purification method can be used for the purification of biotinPIC-bioconjugates.

Synthesis and purification of alkaline phosphatase (PhoA) biotinPIC-bioconjugates. To investigate if biotinPIC-bioconjugates can be purified with the newly developed affinity-based method, biotinPICs were first functionalized with the enzyme PhoA. This was motivated by the availability of a large number of chromogenic and fluorogenic phosphoester substrates, which facilitate a straightforward comparison of enzyme activity before and after conjugation. To complement this sensitive activity readout, the enzyme was labeled with a fluorophore so that also the enzyme concentration can be determined easily during all steps of the experiment. PhoA was therefore reacted with the *N*-Hydroxysuccinimide (NHS) esters of DBCO- and AlexaFluor647 in a one-pot reaction. To determine the degree of labeling, the PhoA concentration was estimated with a BCA assay and the DBCO and AlexaFluor647 concentrations were determined with UV/VIS spectro-scopy. On average, 1.1 fluorophore molecules and 2.4 DBCO functional groups were coupled to the PhoA dimer. DBCO- and AlexaFluor647-labeled PhoA was then reacted with the biotinPIC polymer possessing a biotin spacing of 7.5 nm. Three different ratios of PhoA:azide were used for coupling the enzyme to the polymer (0.1, 0.2 and 0.5 eq. of PhoA with respect to azide groups). Assuming a quantitative reaction, this would result in an average PhoA spacing of 50, 25 and 10 nm.

The PIC-PhoA bioconjugates were then purified over mono-avidin beads, using the optimized method described earlier for biotinPICs. The purified PIC-PhoA conjugates were analyzed with atomic force microscopy (AFM). The AFM images were used to

count the number of enzymes attached to every individual polymer chain (Figure 3a and b, Figure S2) and the average spacing between PhoA molecules was determined to be 55 nm (PIC 0.2 eq PhoA) and 100 nm (PIC 0.1 eq PhoA). In parallel, the polymer concentration was determined in a CD measurement at a wavelength of 360 nm and the PhoA concentration was determined with a BCA assay. This measurement yielded a spacing of 70 nm for the biotinPIC functionalized with 0.2 eq. PhoA and of 155 nm for the biotinPIC functionalized with 0.1 eq PhoA (Figure 3c). Considering the error in the AFM-based estimation, these values agree very well. This proves that unreacted enzymes have been efficiently separated from the bioconjugates during the

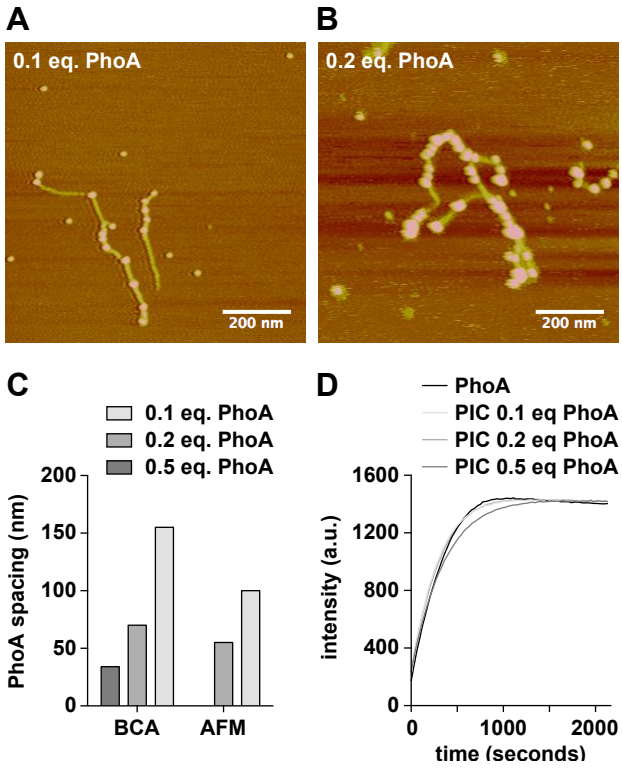

Figure 3 Synthesis and purification of biotinPIC-PhoA bioconjugates. **(A-B)** AFM images of biotinPICs reacted with 0.1 eq. PhoA or 0.2 eq. PhoA drop-casted on mica. The bright 'dots' correspond to the enzyme while the 'connecting line' represents the polymer. **(C)** Calculated PhoA distances on the biotinPIC backbone, determined either from the measured bulk concentrations (BCA) or the AFM measurement. **(D)** Enzyme activity measurements of the PIC-PhoA conjugates in comparison to non-conjugated PhoA. The curves display the mean of three independent measurements.

purification process. Unfortunately, no polymer bioconjugates were found on the mica surface for the biotinPIC functionalized with 0.5 eq PhoA, but the spacing determined from the bulk concentration assay was 34 nm. On average, the determined PhoA spacing is a factor 3 larger than the distances expected for a quantitative reaction, indicating a coupling efficiency of 30 %. This low coupling efficiency is expected for a reaction between two macro- molecules and again highlights the importance of a good purification method.

In the next step, it was examined if the biotinPIC-conjugated PhoA was still catalytically active (Figure 3d). The activity of the enzyme was tested using the fluorogenic substrate 9H-(1,3-dichloro-9,9-dimethylacridin-2-one-7-yl) phosphate (DDAO-phosphate).[38] PhoA dephosphorylates the DDAO fluorophore, thereby altering its photophysical properties (Figure S3). Enzymatic activity results in an increase in product fluorescence allowing for a straightforward kinetic measurement. The increase in product fluorescence was determined for the three PIC-PhoA conjugates and for a control sample containing non-conjugated enzyme of the same concentration (determined via the fluorescence intensity of the AlexaFluor647 label before the kinetic measurement was started). All samples show very similar enzyme activities (Figure 3d), indicating that the coupling and purification process does not inactivate the enzyme. Taken together, these results show that the new purification protocol is a highly powerful method for the purification of PIC-enzyme conjugates. In the next step, these conjugates could be used for forming enzyme-functionalized hydrogels for a number of different applications. Such nature-like hydrogels represent an interesting new method for enzyme immobilization, as their large pore size[27] allows for free substrate and product diffusion. PIC polymers are further highly versatile scaffolds for the co-conjugation of different functional entities[12] so that they represent an interesting new platform for the assembly of cascade reactions.

Synthesis and purification of anti-CD3 biotinPIC-bioconjugates. Having established that the new purification protocol can be used to purify PIC-bioconjugates, an antibody was conjugated to the biotinPIC in the next step to investigate the general applicability of the method. This was further motivated by our earlier experiments with anti-CD3 (αCD3) functionalized PICs that were shown to be highly effective as synthetic dendritic cells.[11,12,14] To obtain PIC-αCD3 of sufficient purity, the polymer conjugates had to be purified extensively using ultrafiltration, which resulted in a huge loss of both polymer and antibody (<1 % yield). Therefore, using the previously utilized αCD3 antibody, it was tested if the new affinity-based purification method can overcome these problems and yield PIC-αCD3 bioconjugates with increased yield and purity. In the earlier experiments, αCD3 was biotinylated and bound to a streptavidin-functionalized PIC polymer. As biotin is now used as the affinity tag for purification, the original design had to be adjusted to allow for a direct conjugation of αCD3 to the

azide-functionalized biotinPIC. To achieve this, αCD3 was functionalized with the DBCO-NHS ester, allowing for a direct conjugation to the biotinPIC. The degree of labeling, as determined by UV/VIS spectroscopy,[39] was between 2 and 2.5 DBCO molecules per antibody.

To investigate the influence of the antibody density on the performance of the biotin-tag based purification method, 4 different PIC-αCD3 bioconjugates were synthesized. DBCO-αCD3 was reacted with biotinPIC in PBS using 0.1, 0.3, 0.5 and 1 equivalents of antibody relative to azide groups. The resulting reaction mixtures were then incubated with mono-avidin beads. The ability of the PIC-αCD3 bioconjugates to bind to the resin was estimated by analyzing the supernatant with CD (Figure 4a, Figure S1). The binding efficiency of the PIC-αCD3 to the mono-avidin beads was typically in the range of 35-55 %, which was lower than for the biotinPIC without αCD3

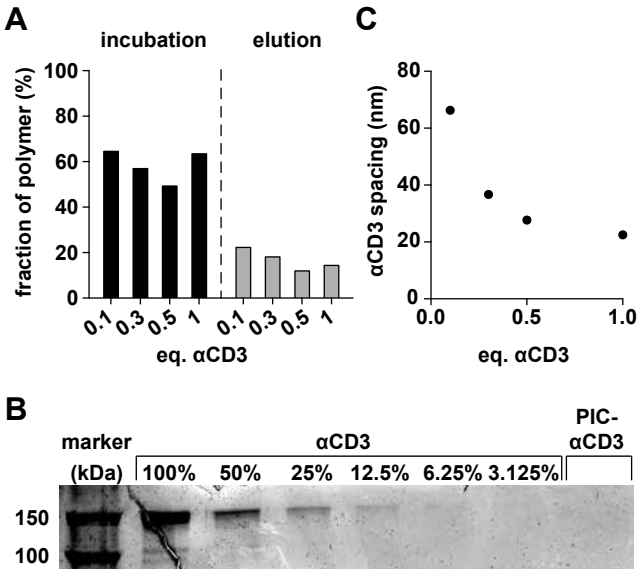

Figure 4 Purification of PIC-αCD3 bioconjugates using a biotin affinity tag. **(A)** Binding and elution profile of PIC-αCD3 to and from mono-avidin agarose beads. Shown is the relative amount of PIC-αCD3 in the supernatant, determined using CD measurements. **(B)** Non-reducing SDS-PAGE of the PIC-αCD3 sample (1 eq. of antibody with respect to azide groups) in comparison to different concentrations of αCD3. Shown are relative concentrations with respect to the amount of αCD3 used in the reaction mixture. **(C)**Calculated average distances between αCD3 on the biotinPIC backbone obtained for different equivalents of DBCO-αCD3 during the reaction.

(65-70 %). After extensive washing (2x PBS-T, 4x PBS), typically 10-25 % of the original amount of PIC-αCD3 could be eluted (Figure 4a). Compared to biotinPIC without αCD3 these yields are slightly lower, which is a direct result of a less efficient capture of the bioconjugate. This may originate from steric effects resulting from the large antibody or less favorable charge interactions between the antibody and mono-avidin.[40] In the case of unfavorable charge interactions, optimizing the buffer conditions in the capture and/or release step may lead to increased yields in future experiments. Still, the yields are significantly better than the yields obtained with the ultrafiltration protocol used before (<1 % yield).

In addition to the yield, also the purity of the PIC-αCD3 is a crucial aspect for the further optimization and applicability of these bioconjugates. A combination of methods was used to determine the remaining amount of non-conjugated αCD3 in the samples after affinity purification. Gel electrophoresis (SDS-PAGE) was performed under non-reducing conditions to keep the disulfide bonds of the antibody intact (Figure 4c). As the polymer bioconjugate is too large to enter the SDS-PAGE gel (Figure S4), it can be directly concluded that any protein of the size of ~150 kDa represents non-conjugated antibody. A comparison of the PIC-αCD3 sample (1 eq. of antibody with respect to azide groups) with different concentrations of free αCD3 shows that more than 92 % of the antibody in the affinity purified sample was conjugated to the polymer. This result is in line with the results obtained for the PIC-PhoA conjugates, where only a very small amount of non-conjugated PhoA was observed in the AFM images (Figure 3). This high purity of the PIC-αCD3 conjugates allows for a simple determination of the number and the statistical spacing of αCD3 on the polymer backbone. Knowing the molar concentrations of both the antibody and the biotinPIC, the number of αCD3 per polymer can simply be determined by dividing the two values (Figure 4c). The biotinPIC concentration was again determined by CD measurements and the αCD3 concentration was obtained from a BCA assay. For 0.1, 0.3, 0.5 and 1 equivalents of αCD3, an average antibody spacing of approximately 70, 40, 30 and 20 nm was found, respectively. When compared to the average antibody spacing calculated for a coupling efficiency of 100 % (50 nm, 17 nm, 10 nm and 5 nm), it can be concluded that between 25-70 % of αCD3 antibodies have coupled to the polymer, with a lower coupling efficiency being observed for larger equivalents of αCD3. This may directly result from the altered DBCO-αCD3:azide ratio or originate from steric hindrance, which prohibits access of αCD3 molecules to remaining coupling sites (Figure 4c).

Overall, our results clearly show that the purification of PIC-bioconjugates with an affinity tag is a powerful method for obtaining pure bioconjugates in high yield, which can be easily analyzed with standard spectroscopic methods. The affinity-based purification method developed now opens the way toward the synthesis of multi-functional conjugates. The greatly increased yield and purity allow for a step-wise

functionalization with different molecules, providing unprecedented control over the number and stoichiometry of functional entities. This method, therefore, represents a highly promising starting point for the further development of PIC-bioconjugates for immunotherapeutic applications as well as for designing enzyme cascade reactions, which both require the conjugation of multiple different biomolecules to a polymer scaffold.

Conclusion

In this study, an affinity-based purification method was developed that increases both the total yield as well as the purity of PIC-bioconjugates. PIC polymers were equipped with biotin tags that allow for the reversible binding of the resulting biotinPIC polymers to mono-avidin beads. For optimal binding, a minimum statistical spacing between individual biotin moieties of at least 7.5 nm was required. To demonstrate the application potential of this new purification method, two different biotinPIC-bioconjugates were successfully synthesized and purified. Although the final yield of the purification was only 10-25 %, it was significantly better than the previously used ultrafiltration method where the yield was below 1 %. The yields of the binding and elution steps may be further optimized when re-applying the supernatant to the mono-avidin beads or when using (strept)avidin mutants[41,42] or biotin derivatives[43,44] with different affinity. Alternatively, the strong biotin-streptavidin interaction may be utilized when integrating a cleavable linker[45] between the PIC and the biotin moiety. More importantly, the new method allowed for removing non-reacted biomolecules nearly quantitatively (>90 %), leading to highly pure biotinPIC-bioconjugates. As a consequence of this high purity, the analysis of these constructs was straightforward and the spacing of the conjugated biomolecules could be calculated from simply dividing the concentration of polymer by the concentration of the respective biomolecule. The densities calculated from bulk concentrations were in good agreement with the results from AFM imaging, where every individual biomolecule coupled to the polymer was visualized and counted. Furthermore, the developed purification method preserved the activity of the coupled biomolecule as was demonstrated with activity measurements for alkaline phosphatase. Altogether, a new versatile protocol was developed for the synthesis and purification of biotin-PIC-bioconjugates. This protocol will not only be highly useful for further developing these molecules toward applications, but also for the preparation of other complex and multifunctional bioconjugates.

Experimental procedures

Polymer synthesis. The PIC polymer used in this study was synthesized according to the procedure described in the literature.[11,12,14,21,30] In short, a 30:1 ratio of methoxy-terminated (1.124 g, 3.12 mmol) and azide-terminated (0.0038 g, 0.104 mmol) isocyano-peptide monomers were mixed in toluene (50 mg ml^{-1}) in a round bottom flask and stirred for 2 days until IR measurements showed the complete disappearance of the isocyanide peak. The solution was diluted with dichloromethane and precipitated in diisopropyl ether three times, resulting in an off-white solid (0.937 g, 82%). The resulting polymer contains a statistical density of 1 azide per 3 nm. The polymer was analyzed using viscometry as described previously (M_v= 490 kg mol^{-1}).[11]

Biotin-functionalization of PICs. The PIC polymer was dissolved in PBS (10 mM Na_2HPO_4, 2 mM KH_2PO_4, 137 mM NaCl, 2.7 mM KCl, pH 7.4) in a concentration of 1 mg ml^{-1}. Biotin-EG_4-DBCO (Click Chemistry Tools) dissolved in DMSO or DBCO-PEG_{3000Da}-biotin (Nanocs) dissolved in DMSO was added to this solution in the required amount (less than 5% of the total volume, see below). The mixture was stirred overnight and subsequently used for testing the mono-avidin purification protocol or for the conjugation of biomolecules. Four different biotinPIC polymers were prepared with a different density of biotin. To achieve this, the molar ratio of biotin-EG_4-DBCO:monomer was varied from 1:75, 1:100 and 1:400. Assuming a quantitative reaction, this yields an average biotin distance of 7.5, 10 and 40 nm, respectively. During the synthesis of the fourth polymer with a 1:50 molar ratio (5 nm biotin spacing) DIBO-AlexaFluor647 (Thermo Fisher Scientific) was added in a 1:500 ratio of dye:monomer to obtain a fluorescently labeled biotinPIC polymer for testing the migration of biotinPEG in SDS-PAGE (Figure S4). After stirring overnight, the mixture was precipitated in diisopropyl ether and dried in air. The dried material was dissolved in a concentration of 1 mg ml^{-1} in PBS.

Expression and purification of PhoA. The phoA gene was cloned from the plasmid pET-22b-phoA[46] into a vector of the pAK[47]/pKB[48] series, where the original lac promotor was replaced by the arabinose inducible P_{BAD} promotor. The sequence of the pelB signal peptide was replaced with the signal peptide of PhoA. The resulting plasmid pKB5-PhoA-His allows for the periplasmic expression of PhoA with a C-terminal His-tag. For protein expression, the plasmid was transformed into the *E. coli* K12 strain TB1 (New England Biolabs). The cultures were grown in SB medium (20 g l^{-1} tryptone, 10 g l^{-1} yeast extract, 5 g l^{-1} Nacl, 50 mM K_2HPO_4) at 25 °C and induced with 0.02 % (w/v) arabinose at an OD_{600} between 0.5-1. After 3 hours, the cells were harvested by centrifugation at 5000 rpm and 4 °C for 15 min. The cells were resuspended in 50 mM tricine pH 8.0, 300 mM NaCl (loading buffer) and lysed using sonication.

The lysate was cleared by centrifugation and the resulting supernatant was incubated at 80 °C for 10 min to denature proteins other than the heat stable PhoA-His. Denatured proteins were removed by centrifugation (2x 30 min, 20000 g) at 4°C and filtration through a 0.22 µm syringe filter. The resulting supernatant was loaded onto a Zn^{2+}-NTA column (His Gravi Trap equilibrated with $ZnCl_2$ instead of $NiCl_2$; GE Healthcare Life Sciences). Following a washing step with loading buffer (30 column volumes), the column was washed with 5 column volumes of loading buffer supplemented with 10 mM imidazole. The protein was eluted from the column with 50 mM tricine pH 8.0, 300 mM NaCl, 200 mM imidazole. The eluted protein was concentrated using ultrafiltration (10 kDa cut-off; Amicon Ultra-15 Centrifugal Filter Units; Merck Millipore). Lastly, the buffer was exchanged to 50 mM sodium borate pH 8.5 using a PD-10 desalting column (GE Healthcare Life Sciences). The purity was verified using SDS-PAGE and the correct molecular weight was confirmed with mass spectrometry (ESI-TOF). The protein concentration was determined from its absorbance at 280 nm (ε = 63260 M^{-1} cm^{-1} for the PhoA dimer) and confirmed using a BCA assay. The purified protein was stored in aliquots at -80 °C.

BCA assay. To determine the protein concentration, a micro BCA Protein Assay Kit (Thermo Fisher Scientific) was used. The assay was performed using the protocol supplied by the manufacturer. When determining the αCD3 or PhoA-His concentration, non-reacted αCD3 was used as the standard, spanning a concentration range from 7.8 µg ml^{-1} to 1 mg ml^{-1}. PIC-αCD3 samples were freeze-dried before the BCA assay and re-dissolved in PBS, to increase the sample concentration by a factor of 5-6.

Synthesis of AlexaFluor647-DBCO-PhoA. PhoA-His (~15 µM) was labeled with AlexaFluor647-NHS (Thermo Fisher Scientific) and DBCO-EG_4-NHS simultaneously (Click Chemistry Tools). Using DMSO stock solutions, 4 equivalents of AlexaFluor647-NHS and 4 equivalents of DBCO-EG_4-NHS were added, yielding a final concentration of 60 µM for both reagents. The DMSO content was ~10 % of the total volume. The reaction was incubated for 3-4 hours at 4 °C, followed by ultrafiltration with a 10 kDa cut-off. During ultrafiltration, the buffer was exchanged to 50 mM HEPES, pH 8.0. To determine the degree of labeling of the resulting AlexaFluor647-DBCO-PhoA-His, the protein concentration was first determined with a BCA assay. The DBCO and AlexaFluor647 concentrations were determined from UV/VIS measurements using an extinction coefficient of 12,000 M^{-1} cm^{-1} for DBCO (309 nm) and of 270,000 M^{-1} cm^{-1} for AlexaFluor647 (650 nm). This analysis yielded a degree of labeling of 2.5 DBCO and 1.1 AlexaFluor647 molecules per PhoA-His dimer.

Synthesis of αCD3-DBCO. The αCD3 antibodies (monoclonal mouse anti-human αCD3 clone OKT3; bioXcell) were dissolved in PBS. DBCO-EG_4-NHS (3.5 equivalents in DMSO)

was added to the antibody solution. The final concentration of αCD3 in the reaction mixture was 4 mg ml^{-1}. The mixture was stirred for 2 hours at 4 °C and subsequently purified using ultrafiltration (30 kDa cut-off; Amicon Ultra-15 Centrifugal Filter Units) to remove non-reacted DBCO-EG_4-NHS. The degree of labeling was determined from absorption measurements at 309 nm (DBCO) and 280 nm (αCD3). The signal at 280 nm was corrected for the absorption of DBCO using the following equation: Corrected absorption (280 nm) = absorption at 280 nm – (1.089 * absorption at 309 nm).[39] The DBCO concentration was calculated from the absorption at 309 nm (ε = 12,000 M^{-1} cm^{-1}). To obtain the αCD3 concentration, the corrected absorption at 280 nm (ε = 210,000 M^{-1} cm^{-1}) was used. Typically, this reaction yields a degree of labeling of 2-2.5 DBCO molecules per antibody.

Synthesis of biotinPIC-bioconjugates. All biotinPIC-bioconjugates were prepared using a similar protocol. A solution of biotinPIC (1 mg ml^{-1} stock solution in PBS) was added to the DBCO-functionalized biomolecules to obtain the desired ratios. The reaction mixture was stirred overnight at 4 °C and directly used for purification over mono-avidin beads (agarose-based; Thermo Fisher Scientific). PBS was used for the coupling and purification of αCD3-DBCO. HEPES was used for AlexaFluor647-DBCO-PhoA-His.

Circular Dichroism (CD) measurements. To prepare the CD standard curves, the azide-functionalized PIC was dissolved in a concentration of 1 mg ml^{-1} in PBS (Figure S1). This stock solution was used to prepare the following concentrations of the polymer: 0.025, 0.05, 0.1, 0.2 and 0.3 mg ml^{-1}. The CD spectrum of these samples was measured and corrected using a PBS blank. Standard curves were constructed for the CD signals measured at 272 nm or 360 nm, yielding calibration factors of ε_{272nm}= 525.6 mdeg mg^{-1} ml^{-1} and ε_{360nm}= -121.1 mdeg mg^{-1} ml^{-1}.

Purification using mono-avidin agarose. All buffers were freshly prepared and filtered before use. In general, 500-800 µl of a 50 % slurry containing regenerated and blocked mono-avidin beads was spun down in a Eppendorf tube and the supernatant was removed. The PIC-biomolecule mixture was added (250-400 µl) and the beads were incubated for 4 hours. Following incubation, the beads were spun down, the supernatant was removed and the remaining beads were washed with PBS containing 0.1% (v/v) Tween 20 (PBS-T, 2x) and with PBS (4x). The beads were then incubated with PBS containing 2 mM biotin for 1-2 hours to release the purified biotinPIC-bioconjugate. After completing affinity purification, the eluted samples were filtered to remove a small portion of remaining beads in the elution fraction. Filtering the samples with standard filters of 0.2-0.45 µm pore size did result in a huge loss of polymer so that a 1 ml column with a frit of 20 µm pore size (Screening Devices) was used instead. Using

this larger pore size, the loss of polymer during filtration was reduced to 10 %. During all steps of the purification, PBS was used for the PIC-αCD3 bioconjugate, while HEPES was used for the PIC-PhoA samples.

AFM measurements. The mono-avidin purified and filtered PIC-PhoA samples were drop casted (20 µl) onto freshly cleaved mica. After incubation on the surface for 20 seconds, the samples were removed and the surface was dried in a nitrogen stream. The samples were imaged with tapping mode in air, using a Nanoscope IV instrument (Bruker) and NSG-10 tapping mode tips (NT-MDT). The images were analyzed with ImageJ software.[49] The average spacing of PhoA molecules was calculated from the number of enzymes counted on a polymer of given length (Figure S2).

PhoA activity measurements. The fluorogenic substrate DDAO-phosphate (9H- (1,3-Dichloro-9,9-Dimethylacridin-2-One-7-yl) phosphate, diammonium salt; Thermo Fisher Scientific) was used for measuring the activity of the biotinPIC-PhoA bioconjugates. The substrate was dissolved in dry DMSO at a concentration of 40 µM. The biotinPIC-PhoA conjugates were diluted in activity buffer (50 mM HEPES pH 8.0, 100 mM KCl, 20 mM $MgCl_2$, 100 µM $ZnCl_2$) to obtain a PhoA concentration of 500 pM. DDAO-phosphate was added to a final concentration of 2 µM to start the measurement. The release of the fluorophore DDAO was followed in a micro- plate reader (λ_{ex} = 620 nm; λ_{em} = 660 nm; Tecan Infinite M200 PRO). The measurement was performed at 37 °C for 40 min (30 s intervals). All measurements were performed in triplicate. The data was corrected for auto-hydrolysis of the substrate.

Acknowledgment

The authors thank Florian Hollfelder for providing the plasmid pET-22b-PhoA, Kalyanasundaram Subramanian for cloning the PhoA expression plasmid as well as Reinhild Dünnebacke for PhoA expression and purification. This work was supported by grants from the Dutch Cancer Society (grants KUN2006-3699 and KUN2009-4402), the Dutch government to the Netherlands Institute for Regenerative Medicine (NIRM, grant FES0908), the Netherlands Organization for Scientific Research (NWO; Spinoza award 2006, C.G.F; VICI grant 700.56.444, A.E.R.; VIDI grant 700.58.430, K.G.B.) as well as NanoNext (grants 7A.06 and 3D.12), the European Research Council (ERC; grant ERC-2010-AdG269019, C.G.F.) and the Max Planck Society.

References

(1) Abuchowski, A., van Es, T., Palczuk, N. C., and Davis, F. F. (1977) Alteration of immunological properties of bovine serum albumin by covalent attachment of polyethylene glycol. *J. Biol. Chem. 252*, 3578.

(2) Harris, J. M., and Chess, R. B. (2003) Effect of pegylation on pharmaceuticals. *Nat. Rev. Drug Discovery 2*, 214.

(3) Pasut, G., Guiotto, A., and Veronese, F. M. (2004) Protein, peptide and non-peptide drug PEGylation for therapeutic application. *Expert Opin. Ther. Pat. 14*, 859.

(4) Veronese, F. M., and Pasut, G. (2005) PEGylation, successful approach to drug delivery. *Drug Discovery Today 10*, 1451.

(5) Boyer, C., Bulmus, V., Liu, J., Davis, T. P., Stenzel, M. H., and Barner-Kowollik, C. (2007) Well-Defined Protein–Polymer Conjugates via in Situ RAFT Polymerization. *J. Am. Chem. Soc. 129*, 7145.

(6) Gauthier, M. A., and Klok, H.-A. (2008) Peptide/protein-polymer conjugates: synthetic strategies and design concepts. *Chem. Commun.*, 2591.

(7) Klok, H.-A. (2009) Peptide/Protein–Synthetic Polymer Conjugates: Quo Vadis. *Macromolecules 42*, 7990.

(8) Cobo, I., Li, M., Sumerlin, B. S., and Perrier, S. (2015) Smart hybrid materials by conjugation of responsive polymers to biomacromolecules. *Nat. Mater. 14*, 143.

(9) Hoffman, A. S., and Stayton, P. S. (2007) Conjugates of stimuli-responsive polymers and proteins. *Prog. Polym. Sci. 32*, 922.

(10) Liu, S., Maheshwari, R., and Kiick, K. L. (2009) Polymer-Based Therapeutics. *Macromolecules 42*, 3.

(11) Mandal, S., Eksteen-Akeroyd, Z. H., Jacobs, M. J., Hammink, R., Koepf, M., Lambeck, A. J. A., van Hest, J. C. M., Wilson, C. J., Blank, K., Figdor, C. G., et al. (2013) Therapeutic nanoworms: towards novel synthetic dendritic cells for immunotherapy. *Chem. Sci. 4*, 4168.

(12) Mandal, S., Hammink, R., Tel, J., Eksteen-Akeroyd, Z. H., Rowan, A. E., Blank, K., and Figdor, C. G. (2015) Polymer-Based Synthetic Dendritic Cells for Tailoring Robust and Multifunctional T Cell Responses. *ACS Chem. Biol. 10*, 485.

(13) Bennett, N. R., Zwick, D. B., Courtney, A. H., and Kiessling, L. L. (2015) Multivalent Antigens for Promoting B and T Cell Activation. *ACS Chem. Biol. 10*, 1817.

(14) Hammink, R., Mandal, S., Eggermont, L. J., Nooteboom, M., Willems, P. H. G. M., Tel, J., Rowan, A. E., Figdor, C. G., and Blank, K. G. (2017) Controlling T-Cell Activation with Synthetic Dendritic Cells Using the Multivalency Effect. *ACS Omega 2*, 937.

(15) Grotzky, A., Nauser, T., Erdogan, H., Schlüter, A. D., and Walde, P. (2012) A Fluorescently Labeled Dendronized Polymer–Enzyme Conjugate Carrying Multiple Copies of Two Different Types of Active Enzymes. *J. Am. Chem. Soc. 134*, 11392.

(16) Schoffelen, S., and van Hest, J. C. M. (2012) Multi-enzyme systems: bringing enzymes together in vitro. *Soft Matter 8*, 1736.

(17) Wheeldon, I., Minteer, S. D., Banta, S., Barton, S. C., Atanassov, P., and Sigman, M. (2016) Substrate channelling as an approach to cascade reactions. *Nat. Chem. 8*, 299.

(18) Zhu, J. (2010) Bioactive modification of poly(ethylene glycol) hydrogels for tissue engineering. *Biomaterials 31*, 4639.

(19) Zhu, J., and Marchant, R. E. (2011) Design properties of hydrogel tissue-engineering scaffolds. *Expert Rev. Med. Devices 8*, 607.

(20) Kopecek, J., and Yang, J. (2012) Smart Self-Assembled Hybrid Hydrogel Biomaterials. *Angew. Chem., Int. Ed. 51*, 7396.

(21) Das, R. K., Gocheva, V., Hammink, R., Zouani, O. F., and Rowan, A. E. (2016) Stress-stiffening-mediated stem-cell commitment switch in soft responsive hydrogels. *Nat. Mater. 15*, 318.

(22) Velonia, K., Rowan, A. E., and Nolte, R. J. M. (2002) Lipase Polystyrene Giant Amphiphiles. *J. Am. Chem. Soc. 124*, 4224.

(23) Huang, X., Li, M., Green, D. C., Williams, D. S., Patil, A. J., and Mann, S. (2013) Interfacial assembly of protein–polymer nano-conjugates into stimulus-responsive biomimetic protocells. *Nat. Commun. 4*, 2239.

(24) Cornelissen, J. J. L. M., Donners, J. J. J. M., de Gelder, R., Graswinckel, W. S., Metselaar, G. A., Rowan, A. E., Sommerdijk, N. A. J. M., and Nolte, R. J. M. (2001) β-Helical Polymers from Isocyanopeptides. *Science 293*, 676.
(25) Schwartz, E., Koepf, M., Kitto, H. J., Nolte, R. J. M., and Rowan, A. E. (2011) Helical poly(isocyanides): past, present and future. *Polym. Chem. 2*, 33.
(26) Koepf, M., Kitto, H. J., Schwartz, E., Kouwer, P. H. J., Nolte, R. J. M., and Rowan, A. E. (2013) Preparation and characterization of non-linear poly(ethylene glycol) analogs from oligo(ethylene glycol) functionalized polyisocyanopeptides. *Eur. Polym. J. 49*, 1510.
(27) Kouwer, P. H. J., Koepf, M., Le Sage, V. A. A., Jaspers, M., van Buul, A. M., Eksteen-Akeroyd, Z. H., Woltinge, T., Schwartz, E., Kitto, H. J., Hoogenboom, R., et al. (2013) Responsive biomimetic networks from polyisocyanopeptide hydrogels. *Nature 493*, 651.
(28) van Buul, A. M., Schwartz, E., Brocorens, P., Koepf, M., Beljonne, D., Maan, J. C., Christianen, P. C. M., Kouwer, P. H. J., Nolte, R. J. M., Engelkamp, H., et al. (2013) Stiffness versus architecture of single helical polyisocyanopeptides. *Chem. Sci. 4*, 2357.
(29) Jaspers, M., Rowan, A. E., and Kouwer, P. H. J. (2015) Tuning Hydrogel Mechanics Using the Hofmeister Effect. *Adv. Funct. Mater. 25*, 6503.
(30) Deshpande, S. R., Hammink, R., Das, R. K., Nelissen, F. H. T., Blank, K. G., Rowan, A. E., and Heus, H. A. (2016) DNA-Responsive Polyisocyanopeptide Hydrogels with Stress-Stiffening Capacity. *Adv. Funct. Mater. 26*, 9075.
(31) Hochuli, E., Bannwarth, W., Dobeli, H., Gentz, R., and Stuber, D. (1988) Genetic Approach to Facilitate Purification of Recombinant Proteins with a Novel Metal Chelate Adsorbent. *Nat. Biotechnol. 6*, 1321.
(32) Schmidt, T. G. M., and Skerra, A. (2007) The Strep-tag system for one-step purification and high-affinity detection or capturing of proteins. *Nat. Protocols 2*, 1528.
(33) Wu, S.-C., and Wong, S.-L. (2006) Intracellular production of a soluble and functional monomeric streptavidin in Escherichia coli and its application for affinity purification of biotinylated proteins. *Protein Expression and Purif. 46*, 268.
(34) Green, N. M., and Toms, E. J. (1973) The properties of subunits of avidin coupled to Sepharose. *Biochem. J. 133*, 687.
(35) Henrikson, K. P., Allen, S. H. G., and Maloy, W. L. (1979) An avidin monomer affinity column for the purification of biotin-containing enzymes. *Anal. Biochem. 94*, 366.
(36) Debets, M. F., van Berkel, S. S., Schoffelen, S., Rutjes, F. P. J. T., van Hest, J. C. M., and van Delft, F. L. (2010) Aza-dibenzocyclooctynes for fast and efficient enzyme PEGylation via copper-free (3+2) cycloaddition. *Chem. Commun. 46*, 97.
(37) Kitto, H. J., Schwartz, E., Nijemeisland, M., Koepf, M., Cornelissen, J. J. L. M., Rowan, A. E., and Nolte, R. J. M. (2008) Post-modification of helical dipeptido polyisocyanides using the 'click' reaction. *J. Mater. Chem. 18*, 5615.
(38) Leira, F., Vieites, J. M., Vieytes, M. R., and Botana, L. M. (2000) Characterization of 9H-(1,3-dichlor-9,9-dimethylacridin-2-ona-7-yl)-phosphate (DDAO) as substrate of PP-2A in a fluorimetric microplate assay for diarrhetic shellfish toxins (DSP). *Toxicon 38*, 1833.
(39) Kotagiri, N., Li, Z., Xu, X., Mondal, S., Nehorai, A., and Achilefu, S. (2014) Antibody Quantum Dot Conjugates Developed via Copper-Free Click Chemistry for Rapid Analysis of Biological Samples Using a Microfluidic Microsphere Array System. *Bioconjugate Chem. 25*, 1272.
(40) Hvasanov, D., Nam, E. V., Peterson, J. R., Pornsaksit, D., Wiedenmann, J., Marquis, C. P., and Thordarson, P. (2014) One-Pot Synthesis of High Molecular Weight Synthetic Heteroprotein Dimers Driven by Charge Complementarity Electrostatic Interactions. *J. Org. Chem. 79*, 9594.
(41) Malmstadt, N., Hyre, D. E., Ding, Z., Hoffman, A. S., and Stayton, P. S. (2003) Affinity Thermoprecipitation and Recovery of Biotinylated Biomolecules via a Mutant Streptavidin–Smart Polymer Conjugate. *Bioconjugate Chem. 14*, 575.
(42) Laitinen, O. H., Hytönen, V. P., Nordlund, H. R., and Kulomaa, M. S. (2006) Genetically engineered avidins and streptavidins. *Cell. Mol. Life Sci. 63*, 2992.
(43) Hofmann, K., Wood, S. W., Brinton, C. C., Montibeller, J. A., and Finn, F. M. (1980) Iminobiotin affinity columns and their application to retrieval of streptavidin. *Proc. Natl. Acad. Sci. U. S. A. 77*, 4666.

(44) Hirsch, J. D., Eslamizar, L., Filanoski, B. J., Malekzadeh, N., Haugland, R. P., Beechem, J. M., and Haugland, R. P. (2002) Easily reversible desthiobiotin binding to streptavidin, avidin, and other biotin-binding proteins: uses for protein labeling, detection, and isolation. *Anal. Biochem. 308*, 343.
(45) Leriche, G., Chisholm, L., and Wagner, A. (2012) Cleavable linkers in chemical biology. *Bioorg. Med. Chem. 20*, 571.
(46) Huebner, A., Olguin, L. F., Bratton, D., Whyte, G., Huck, W. T. S., de Mello, A. J., Edel, J. B., Abell, C., and Hollfelder, F. (2008) Development of Quantitative Cell-Based Enzyme Assays in Microdroplets. *Anal. Chem. 80*, 3890.
(47) Krebber, A., Bornhauser, S., Burmester, J., Honegger, A., Willuda, J., Bosshard, H. R., and Plückthun, A. (1997) Reliable cloning of functional antibody variable domains from hybridomas and spleen cell repertoires employing a reengineered phage display system. *J. Immunol. Methods 201*, 35.
(48) Blank, K., Morfill, J., Gumpp, H., and Gaub, H. E. (2006) Functional expression of Candida antarctica lipase B in Escherichia coli. *J. Biotechnol. 125*, 474.
(49) Schneider, C. A., Rasband, W. S., and Eliceiri, K. W. (2012) NIH Image to ImageJ: 25 years of image analysis. *Nat. Methods 9*, 671.

Supplementary figures

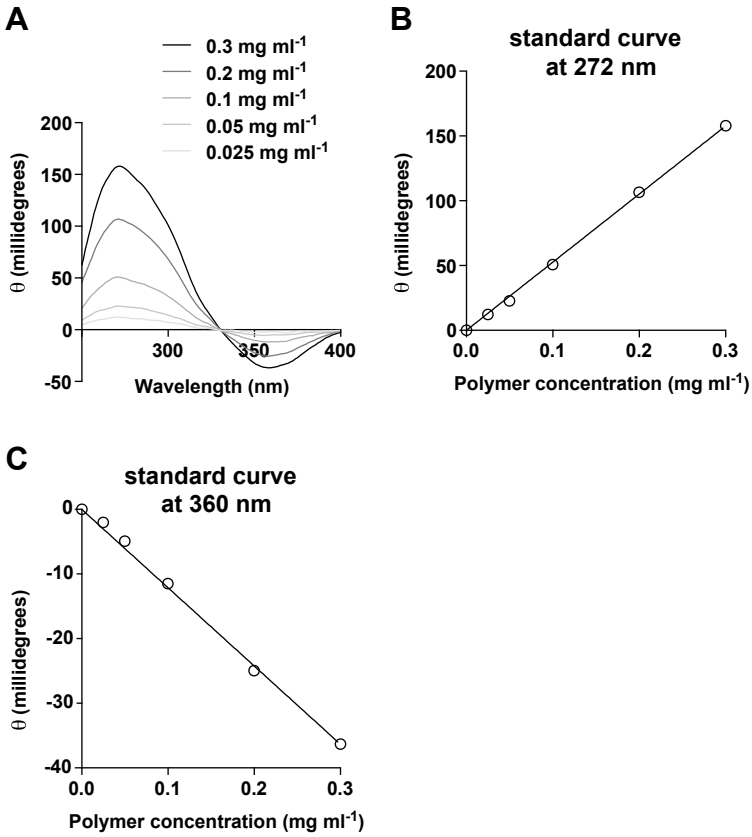

Figure S1 Calibration curves for determining the PIC polymer concentration from CD spectroscopy. **(A)** CD spectra of the PIC polymer measured at different concentrations. **(B)** Standard curve determined at 272 nm using a path length of 1 cm (slope: 525.6 mdeg ml mg^{-1}). **(C)** Standard curve determined at 360 nm using a path length of 1 cm (slope: -121.1 mdeg ml mg^{-1}).

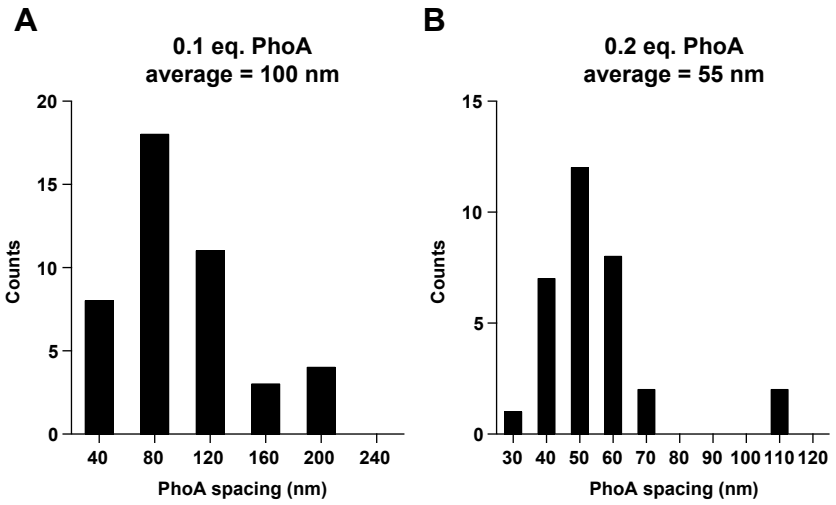

Figure S2 Average distance between PhoA molecules as determined from AFM imaging. **(A)** PIC-PhoA conjugate prepared with 0.1 eq. PhoA. **(B)** PIC-PhoA conjugate prepared with 0.2 eq. PhoA.

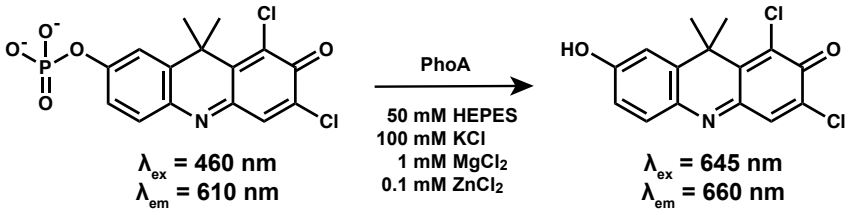

Figure S3 Enzymatic reaction converting DDAO-phosphate into DDAO.

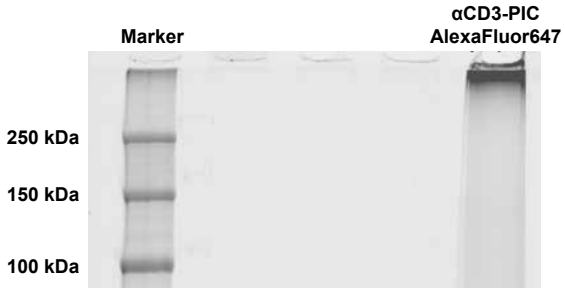

Figure S4 SDS-PAGE (non-reducing conditions) of a mono-avidin purified PIC-αCD3 bioconjugate (biotinPIC, 1 biotin in 50 nm). The αCD3 antibody was fluorescently labelled with AlexaFluor647. The fluorescence in the gel was scanned at an excitation wavelength of 633 nm. This result clearly shows that the PIC-αCD3 bioconjugate does not enter the gel.

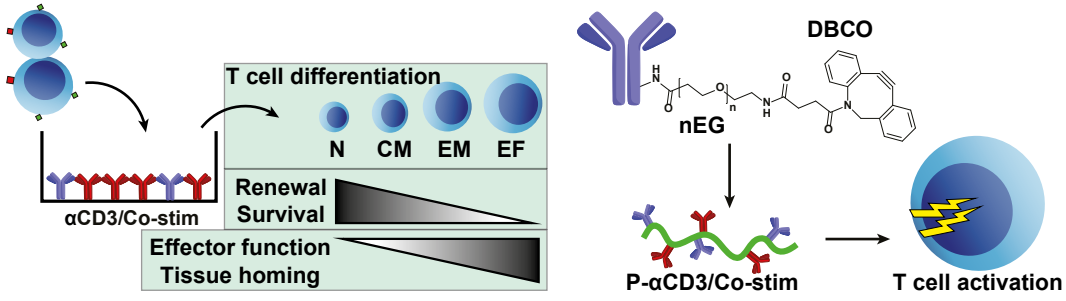
T cell differentiation
N
CM
EM
EF
Renewal
Survival
Effector function
Tissue homing
αCD3/Co-stim
DBCO
nEG
P-αCD3/Co-stim
T cell activation

4

Modular synthetic Dendritic Cells for co-stimulatory control over T cell differentiation

Loek Eggermont, Roel Hammink, Sigrid Kolders, Anne Heinemans,
Carla Rodriquez Mogeda, Florian Wimmers, Dion Voerman, Jurjen Tel, Carl Figdor

Abstract

Immunotherapies are highly dependent on T cell function, which may be controlled by distinct co-stimulatory signaling pathways. Therefore, triggering of co-stimulatory signaling in T cells is an attractive approach to induce anti-cancer responses. Antibodies that stimulate co-stimulatory molecules have induced potent immune responses, but can also lead to serious side effects due to off-target immune responses. Combined stimulation of specific T cell receptors (TCRs) and co-stimulatory molecules is an attractive approach to avoid these side effects. This can be achieved using synthetic mimics of immune cells, called synthetic Dendritic Cells (sDCs). These sDCs can provide efficient TCR signaling, using antibodies against CD3, and CD28 co-stimulation in close proximity on a filamentous nanosized scaffold. Stimulation of other co-stimulatory molecules with sDCs may lead to more control over T cell differentiation and functionality. Here, set out to develop a wide variety of co-stim-sDCs to obtain control over T cell function. For this, the co-stimulatory capacity of several antibodies was first tested when bound to a plate, which demonstrated that distinct co-stimulatory pathways can control the speed of T cell differentiation. To incorporate a wide variety of co-stimulatory molecules onto sDCs, a highly modular strategy is developed for their synthesis in which antibodies are conjugated to polyiscyanopeptides (PICs) through short PEG linkers. We demonstrate that the pH of antibody functionalization greatly affects the capacity of the synthesized αCD3-sDCs to stimulate T cells. Furthermore, providing αCD3 and co-stimulatory antibodies on one and the same scaffold results in highly enhanced activation of T cells. In the future, optimized co-stim-sDCs can be used to study co-stimulatory mechanisms and may be applied to induce distinct T cell functions.

Introduction

Over the last decade, immunotherapy has revolutionized cancer treatments for several malignancies. In particular, immune checkpoint blockade antibodies targeting co-inhibitory receptors CTLA-4 and PD-1 have shown impressive clinical responses, leading to marked increases in survival rates for advanced cancers [1,2]. Stimulation of CTLA-4 and PD-1 leads to inhibition of T cell activation. Blockade of these receptors releases this inhibition and can therefore boost anti-tumor immune responses [3]. Alternatively, instead of blocking co-inhibitory pathways, anti-tumor immunity can be evoked through stimulation of co-stimulatory pathways. Therefore, there is increasing attention for agonist antibodies against co-stimulatory receptors that can trigger these pathways [4]. These antibodies have induced potent anti-cancer responses in pre-clinical models and clinical trials, but have also led to toxic side effects in several cases [5]. In addition, development and application of agonist co-stimulatory antibodies has contributed to our understanding of the role of co-stimulation in the induction of T cell responses [6].

These clinical observations highlight the essential role that co-stimulation and co-inhibition play in T cell biology. TCR triggering (signal 1) in absence of co-stimulation (signal 2) leads to T cell anergy, which causes unresponsiveness towards the recognized antigens [7,8]. During T-cell activation, co-stimulatory molecules provide a second signal that determines the functional outcome of TCR signaling. Classically, CD28 was postulated as the co-stimulatory receptor in this two-signal model [6,9]. Indeed, CD28 is required in most antigen-dependent T cell responses, and is especially important for priming of naïve T cells [10,11]. Triggering of CD28 by B7 ligands expressed on dendritic cells (DCs) leads to enhanced and prolonged T-cell responses, characterized in particular by increased IL-2 secretion, cell survival and proliferation [9,12]. CD28 signaling is counteracted by upregulation of CTLA-4, which binds B7 ligands with high affinity and blocks TCR signaling [13].

Besides CD28, co-stimulation can also be provided through alternative pathways. For priming of naïve T cells, CD27 supports CD28 signals or prime T cells when the CD28 pathways is blocked [14,15]. Triggering of CD27 by CD70 or agonist antibodies promotes T cell proliferation, mainly by promoting survival of proliferating T cells [16]. Other co-stimulatory molecules are not expressed on naïve T cells, but upregulated after activation. These receptors include TNFR superfamily members 4-1BB, OX40, CD30 and GITR [17], SLAM-receptor CD150 [18], and Notch family member Notch2 [19]. The different signaling pathways of these groups of receptors can all synergize with TCR signaling to promote cytokine release and proliferation of T cells. For example, TNFR family proteins do this through binding of different TNF receptor-associated factor (TRAF) adaptors, that interact with downstream signaling molecules [6]. Conversely, CD28 does not bind to TRAFs, although signaling between CD28 and

TNFRs can overlap downstream [6]. For many co-stimulatory receptors it is not completely understood how distal signaling leads to downstream functions in T cells [17].

Nonetheless, it is becoming increasingly clear that the different co-stimulatory receptors each have distinct roles in regulating effector function in T cells [6,17]. In addition, it has been suggested that different co-stimulatory molecules may affect memory formation and effector differentiation of CD8+ T cells [6,20]. For clinical translation, this is especially important in application of adoptively transferred T cells [21]. Traditionally, T cells isolated from cancer patients are cultured *ex vivo* with anti-CD3 and anti-CD28 antibodies. However, making use of cytokines or alternative co-stimulatory molecules could have great impact on the clinical efficacy of these T cells [22,23]. In particular, the differentiation status of these cells seems to correlate with clinical responses [24,25]. Furthermore, in chimeric antigen receptor (CAR) T cells 4-1BB and OX40 signaling seem to counteract T cell exhaustion and induce increased T cell persistence compared to CD28 co-stimulation [26–28], which further highlights the distinct functions of co-stimulatory signaling. It is important to note that functional outcomes of co-stimulation are generally context-dependent. Because costimulatory receptors provide signaling together with TCR signaling, it remains a difficult task to dissect intracellular pathways and isolate their functional outcomes [17].

Synthetic mimics of immune cells, called artificial antigen-presenting cells (aAPCs), allow for a high level of control of the exact signals that are given to T cells. In this way, aAPCs provide a method to study signaling and functions for co-stimulatory molecule in the context of TCR signaling [29]. In addition, development of aAPCs that trigger various co-stimulatory molecules may lead to T cells with a variety of functions, which is interesting from a clinical point of view. Clinical application of agonist antibodies against co-stimulatory molecules in the context of TCR signaling, which could limit autoimmunity and toxic side effects of these antibodies, can be done using aAPCs. At this point, a variety of aAPCs have been developed that can induce co-stimulation through CD28. In addition, microbead-based aAPCs that incorporate 4-1BB have been developed [30,31], but other co-stimulatory molecules have not yet been applied in cell-free aAPC designs. Thus, there is a need for the development of highly modular aAPCs capable of ligating a variety of co-stimulatory molecules, which can provide a way to distinguish the distinct effects of each receptor on T cell function.

Previously, we developed filamentous PICs as a cell-free aAPC scaffolds, called synthetic Dendritic Cells (sDCs) [32–34]. These sDCs were synthesized by binding biotinylated antibodies to conjugates of polyisocyanopeptides (PICs) and streptavidin. Due to their semi-flexibility and high aspect ratio, PIC-antibody scaffolds were established as highly efficient sDCs capable of inducing robust T cell activation. It was

demonstrated that combining signal 1 and 2 on one and the same polymer leads to highly synergistic T cell responses [33]. This synergy of semi-flexible PICs can be used to study the effect of various co-stimulatory molecules in the context of TCR signaling. To test the wide variety of co-stimulatory molecules requires synthesis of a high number of different sDCs. This number increases even further when considering the large number of possible combinations of different co-stimulatory molecules, PIC-bound antibody densities or possible combinations with cytokines. Therefore, a highly modular synthetic strategy is essential to efficiently study co-stim-sDCs. This strategy requires a straightforward method to produce sDCs in a high yield and a straightforward method to adequately characterize the produced PIC-protein conjugates.

Although the previously used streptavidin-linked αCD3/CD28-PICs could efficiently stimulate T cells, their synthesis, purification and characterization is inefficient. Because of this, it is difficult to make a large variety of co-stimulatory sDCs using the previously described method. In chapter 3, the synthetic design of sDCs was optimized by replacing streptavidin with a short PEG linker, which allows for more straightforward analysis of PIC-protein conjugates. In addition, an affinity-based purification method was developed to obtain purified PIC-protein conjugates in higher yields [35]. This novel synthetic strategy was used to produce purified αCD3-PIC conjugates, but to this point these sDCs have not been applied to stimulate T cells.

Here, the concept of purified PIC-antibody conjugates, linked through PEG instead of streptavidin, is further optimized to obtain highly modular sDCs that can be efficiently synthesized and provide strong stimulatory signals. This modular strategy is used to synthesize sDCs containing agonistic antibodies against a variety of co-stimulatory molecules.

Results and discussion

Co-stimulation with plate-bound anti-CD27 accelerates T cell differentiation. CD28 has been widely studied as co-stimulatory molecule, which demonstrated that a second signal is essential for full-blown T cell activation. However, apart from CD28, T cells can express a variety of additional co-stimulatory molecules. Some of these receptors, CD28 and CD27 being the best known examples, are already expressed on naïve T cells, while others are upregulated after T cell activation [6]. The different co-stimulatory molecules may each have varying roles in T cell activation and stimulation of these receptors may each play a role in inducing unique phenotypes and functionalities of T cells [12,17]. Incorporation of additional co-stimulatory antibodies onto sDCs allows us to study the exact role of these molecules and could give rise to distinct subsets of T cells with interesting properties for clinical application. The small size of sDCs may allow control over T cell differentiation *in vivo*. Therefore,

we selected a variety of co-stimulatory antibodies and tested their (co-)stimulatory potential. For this, agonist antibodies were obtained that trigger CD27, 4-1BB, OX40, CD150, CD30, Notch2 and GITR. These co-stimulatory molecules were selected because they have been reported to influence memory or effector responses in CD8+ T cells, and because of the availability of agonistic antibodies that can trigger signaling when bound to these co-stimuli.

Synthesis of PIC-protein conjugates requires relatively high amounts of protein. However, most of the co-stimulatory antibodies are available in low quantities and production of large amounts of antibody is costly. Therefore, the stimulatory capacity of these antibodies was first screened when bound onto ELISA plates together with αCD3. In this way antibodies could be selected for co-stim-sDC synthesis. To establish the effect of αCD27 stimulation, naïve CD8 T cells were added to ELISA plates coated with αCD3, αCD3 and αCD28 or αCD3 and αCD27 (Figure 1a). After 6 days, T cell proliferation and survival was assessed by CFSE dilution (Figure 1b). Limited numbers of naïve CD8 T cells stimulated with only αCD3 survived up to this time point, and no proliferation of T cells was observed. In contrast, when also CD28 or CD27 was stimulated, high levels of proliferation were induced, demonstrating the high co-stimulatory capacity of the CD27 antibody. CD3/CD28-stimulated cells showed a further increased proliferation compared to CD3/CD27-coated plates. However, it should be noted that these experiments were performed at optimized CD3:CD28 ratios, whereas the CD3:CD27 ratio was not optimized.

To elucidate whether CD27 co-stimulation can induce distinct phenotypes from naïve CD8 T cells, cells were stained for CCR7 and CD45RA after 0, 6 and 13 days of plate-bound stimulation (Figure 1c). Before stimulation, cells mostly showed the CCR7+CD45RA+ naïve T cell phenotype. After 6 days of CD3/CD28 stimulation, a large population of T cells were CCR7+CD45RA-, which is consistent with a central memory phenotype. After 13 days, T cells were differentiated further into a CCR7-CD45RA- effector memory phenotype. Interestingly, CD3/CD27 stimulation leads to a decreased expression of CCR7 after 6 days compared to CD3/CD28 stimulation, indicating that they are already moving towards an effector memory phenotype. In addition, some of the CD3/CD27-stimulated cells have gained CD45RA expression after 13 days, which points towards development of an effector T cell phenotype. CD127 expression is also lost faster after CD3/CD27 stimulation, which is also consistent with effector memory formation (Figure S1a) [41]. Furthermore, loss of co-stimulatory molecule (CD28 or CD27) expression, which is indicative of differentiation towards a terminal effector phenotype, is increased after CD3/CD27 stimulation. These results demonstrate that CD27-induced co-stimulation leads to an increased speed of differentiation compared to CD28 co-stimulation. With regard to CD27-induced terminal differentiation, *in vivo* studies have shown conflicting results, suggesting that the outcome of co-stimulation-induced differentiation is highly context-

dependent [42–45]. Possibly, CD27 can only induce memory formation when high levels of IL-12 are present [44], or effector differentiation is a result of constitutive CD27 co-stimulation [43]. In addition, signal strength appears to be highly correlated to CD8 T cell differentiation and the progressive effector differentiation observed for both CD3/CD28 and CD3/CD27 stimulation is therefore likely to be a result of the strong and continued high-affinity signals given to the T cells [46].

T cell activation also leads to expression of additional co-stimulatory molecules, including 4-1BB, OX40 and CD150. To establish whether cell surface expression of these molecules is increased by our plate-bound stimulations, naïve CD8 T cells were again incubated on CD3/CD28 and CD3/CD27-coated ELISA plates and stained for inducible co-stimulatory molecules at different time points (Figure 1d). For both stimulations, expression of 4-1BB, OX40 and CD150 peaked after 3 days of stimulation, which is consistent with previous reports that report peaks of co-stimulatory molecules between 3-6 days [47,48]. CD3/CD27-stimulation led to increased upregulation of co-stimulatory molecules compared to CD3/CD28. In each case, 4-1BB was first expressed, followed by OX40 and finally CD150. Additionally, 4-1BB expression was higher compared to the other co-stimuli. Stimulation of naïve CD8 T cells using only αCD3 did not result in high expression of most inducible co-stimulatory molecules (Figure S1b). In fact, when only signal 1 was used, only a high Notch2 expression was induced after 3 days. After stimulation with CD3/CD28 and CD3/CD27, also Notch2, CD30 and GITR were induced after 3 days (Figure S1c). Similar to the other inducible costimulatory molecules, CD30 and GITR expression was reduced at later time points. However, Notch2 expression was retained at similar levels. Taken together, these experiments demonstrate that co-stimulation with both αCD28 and αCD27 lead to strong T cell activation, expression of additional co-stimuli and differentiation towards an effector phenotype, which is especially accelerated by stimulation of CD27.

Plate-bound anti-4-1BB accelerates differentiation of pre-activated T cells. After having established that the αCD27 antibody can provide strong co-stimulatory signals, the effect of inducible receptor stimulation was determined. CD3/CD28 and CD3/CD27 stimulation leads to high expression of a variety of additional co-stimulatory receptors after 3 days that are absent before stimulation. Therefore, naïve CD8 T cells were stimulated with plate-bound antibodies for 3 days, after which they were removed from these plates and added to a plate coated with αCD3 and antibodies against co-stimulatory molecules (Figure 2a). After 3 subsequent days of stimulation with these antibodies, cells were counted to assess the strength of stimulation of each condition. Re-stimulation of both CD3/CD28- or CD3/CD27-primed T cells with antibodies against CD28, CD27, 4-1BB, OX40 and CD150 increased cell numbers compared to αCD3 stimulation (Figure 2b). These results indicate a strong co-stimulatory capacity of these antibodies, making them interesting candidates for incorporation into sDCs.

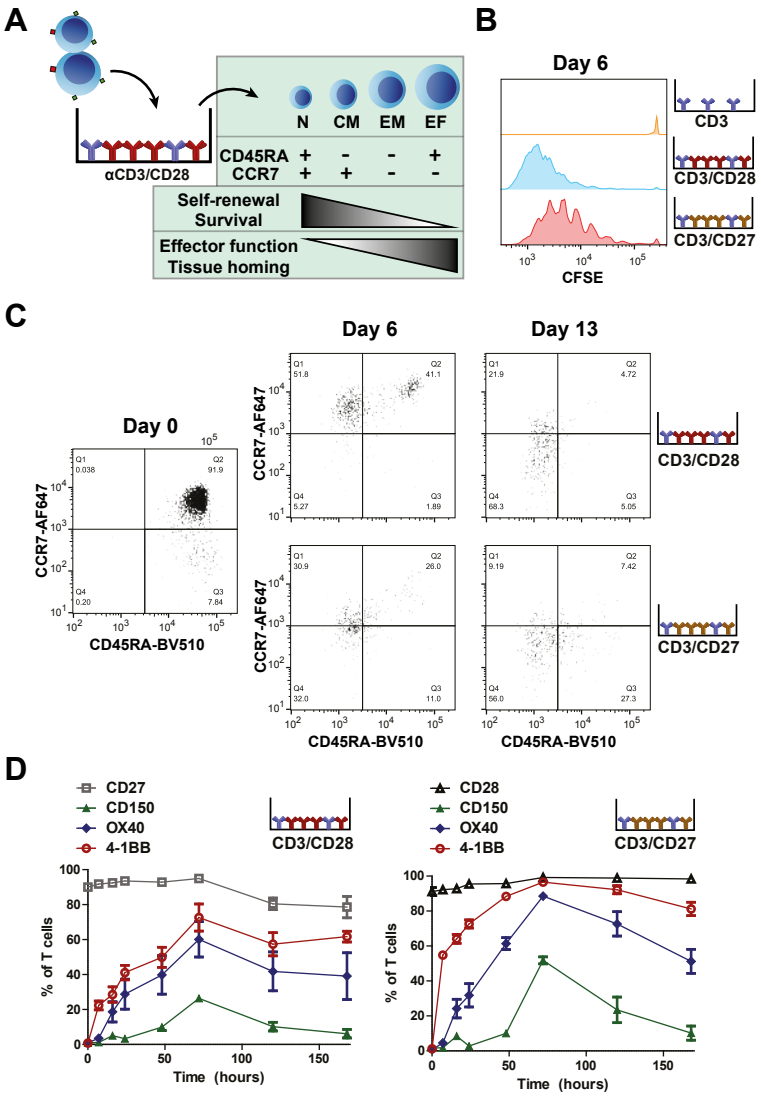

Figure 1 Screening of antibodies for CD28 and CD27 stimulation by plate-bound antibody stimulations of naïve CD8+ T cells. **(A)** Experimental strategy for screening of stimulatory capacity of co-stimulatory antibodies. Naïve CD8+ T cells were incubated on CD3/Co-stimulatory antibody-coated ELISA plates. At various time points, cells were removed from the wells and analyzed. **(B)** Proliferation of naïve CD8+ T cells as determined by CFSE dilution after 3 days of stimulation. Representative histogram of stimulations of two donors is depicted. **(C)** Expression of CCR7 and CD45RA as determined by flow cytometry after 6 days and 13 days of stimulation with plate-bound antibodies. Dot plots show representative example

of three independent observations. **(D)** Expression of co-stimulatory molecules CD27, CD28, 4-1BB, OX40 and CD150 after stimulation with plate-bound CD3/CD28 (left) or CD3/CD28 (right) antibodies. Average percentage of co-stimulus-expressing T cells after duplicate stimulations of two donors is depicted.

In contrast to these co-stimuli, stimulation of GITR, Notch2 or CD30 induced modest levels of proliferation or gave variable results (Figure S2a).

Next, the effect of triggering inducible co-stimulators on T cell differentiation was established. For this, T cells were first stimulated with plate-bound CD3/CD28 for 3 days, then stimulated with plate-bound CD3/CD27, CD3/4-1BB, CD3/OX40 or CD3/CD150. 6 days and 13 days after initial stimulation (or at day 3 and 10 of secondary stimulation), cells were stained for CCR7, CD45RA, CD27 and CD127. At day 6, T cells were generally CD45RA+CCR7+, indicating that the transfer step slightly slowed down differentiation. Interestingly, T cells stimulated with 4-1BB showed lower expression of both CD45RA and CCR7, which corresponds to a more differentiated memory phenotype. After 13 days, T cells had lost CD45RA expression and partially lost CCR7, pointing towards a late central memory phenotype (in transition to effector memory). For 4-1BB-stimulated T cells, CCR7 expression was again decreased compared to the other co-stimuli. In addition, 4-1BB-stimulated T cells showed a lower expression of CD127 and CD27 (Figure S2b), which is also associated with a more differentiated effector memory phenotype. Possibly, the accelerated and enhanced upregulation of 4-1BB compared to the other co-stimulators could account for the faster differentiation of 4-1BB-stimulated T cells [49]. Contrastingly, some *in vivo* experiments and CAR T cells with 4-1BB signaling domains have associated 4-1BB with memory formation, although 4-1BB signaling may also enhance survival of effector cells [42,50,51]. This enhanced survival, combined with the high signal strength of the plate-bound antibodies, may explain the observed high number of more differentiated cells.

Taken together, plate-bound antibody stimulations with CD3 combined with CD28, CD27, 4-1BB, OX40 or CD150 results in strong stimulation of T cells. Under continued stimulation, these cells progressively differentiate towards effector memory/effector T cells. Probably, this is a result of the strong CD3 signaling induced in this plate-bound system [46]. Priming with CD27 or re-stimulation after 3 days with 4-1BB appears to accelerate this differentiation process. Because T cell differentiation is highly context-dependent, these observations do not exclude a role of CD27 and 4-1BB in memory formation, which has been demonstrated by various research groups [42,43,45]. Because of the strong signals given to T cells in this system, mostly small differences in differentiation were observed. In addition, these co-stimulatory molecules could also have distinct roles in inducing other functionalities in T cells, including cytotoxicity or production of inflammatory cytokines. This still needs to be addressed in future experiments.

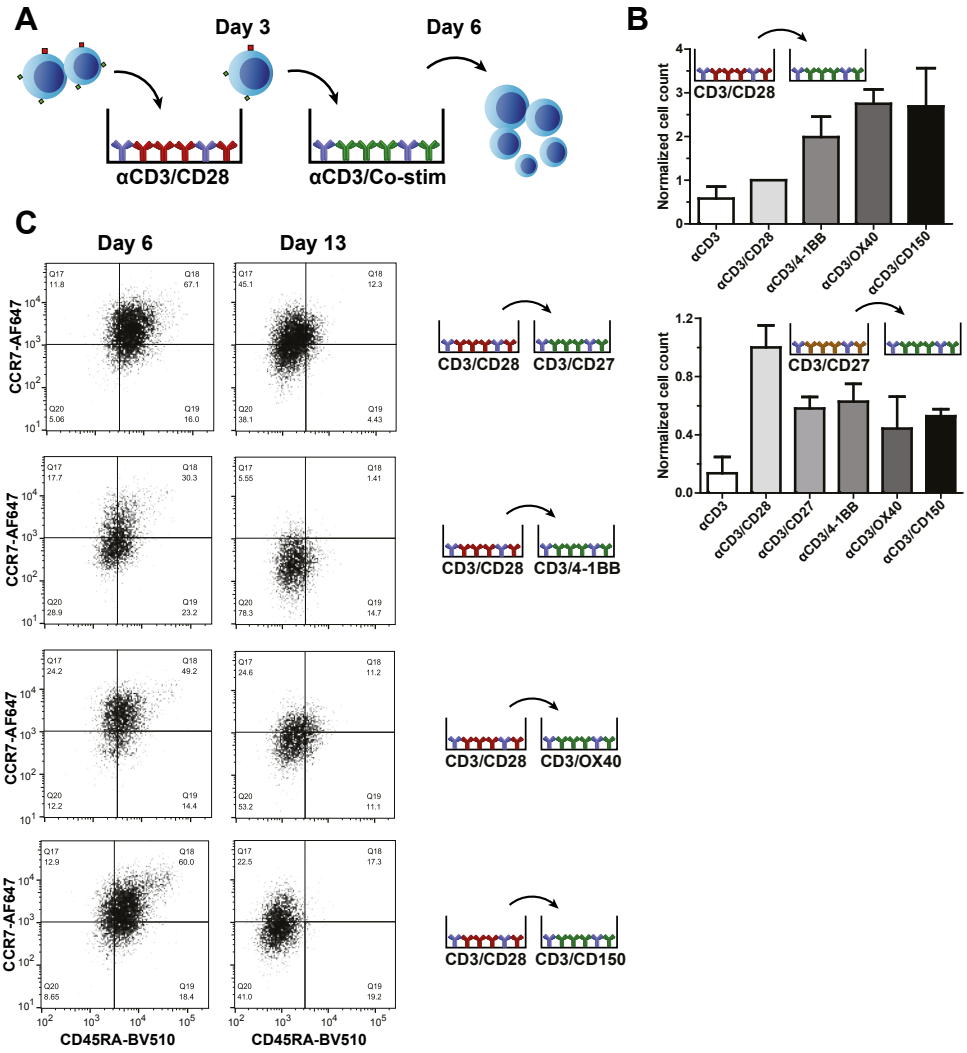

Figure 2 Stimulation of inducible co-stimulatory molecules on pre-activated CD8 T cells by plate-bound antibodies. **(A)** Experimental strategy for screening of stimulatory capacity of co-stimulatory antibodies. Naïve CD8+ T cells were incubated on αCD3/CD28 or αCD3/CD27-coated ELISA plates to induce expression of inducible co-stimulatory molecules. After 3 days, cells were transferred to plates coated with antibodies against inducible CD3 and co-stimulatory molecules. **(B)** Normalized cell counts at day 6 (or 3 days after second stimulation). Naïve CD8+ T cells were pre-stimulated with αCD3/CD28 (top) or αCD3/CD27 (bottom). After 3 days, cells were stimulated with antibodies depicted on x-axis. Values

were normalized to CD3/CD28-stimulated cell count and the average values + SEM from stimulation of two donors were plotted. **(C)** Expression of CCR7 and CD45RA as determined by flow cytometry after 6 days and 13 days of stimulation with plate-bound antibodies. Dot plots show representative example of three independent observations.

Modular synthesis of PEG-linked PIC-antibody conjugates. Experiments using plate-bound antibodies revealed a selection of antibodies that can provide strong co-stimulatory signaling. Next, we aimed to incorporate these antibodies into a nanosized sDC system. These sDCs need to be highly modular in order to study a wide variety of antibodies and combinations thereof. To achieve this, straightforward characterization and high yields are essential during sDC synthesis.

In chapter 2, multivalent streptavidin-linked PIC-antibody conjugates were established as potent sDCs [33]. However, the use of streptavidin as a linker complicates characterization of these conjugates and using this method to produce streptavidin-linked PIC-protein conjugates with both high purity and decent yield is challenging. Therefore, in chapter 3 a method for affinity-based purification of PIC-protein conjugates was developed [35]. Using this method purified PIC-αCD3 conjugates were developed with covalently bound antibodies linked through only a short polyethylene glycol (PEG) linker. Although characterization and purity of PIC-αCD3 conjugates were optimized, they were not applied as sDCs. Here, the modular method developed in chapter 3 was applied to synthesize a variety of PIC-antibody conjugates to optimize their activity in T cell activation assays and elucidate essential design parameters in PIC-based sDC synthesis.

PIC-antibody conjugates were synthesized as depicted in Figure 3a. First, antibodies were functionalized using DBCO-PEG-NHS esters. To determine the effect of linker length on sDC synthesis and activity, PEG linkers were used containing 4, 16 and 68 ethylene glycol (EG) units. Reactions were performed at pH 7.4, 8.3 and 9. At higher pH, amines on antibodies are increasingly deprotonated, which is necessary for efficient reactions with NHS esters. Functionalized antibodies were purified using spin filtration after which DBCO content could be characterized using UV-Vis spectrophotometry (Figure 3b). DBCO functionalization reactions were optimized to obtain an average degree of labeling (DOL) of 2-3 DBCO per antibody. While reactions with the short 4EG-linker where relatively efficient, reactions with the longer linkers required high amounts of DBCO-NHS esters in the reaction mixture to obtain the preferred DOL.

Functionalized antibodies were conjugated to biotin-containing azide-functionalized PICs. The resulting PIC-protein conjugates were purified over monoavidin beads as described in chapter 3. After this, antibody and PIC concentrations were measured using a BCA protein assay and circular dichroism (CD), respectively.

These concentrations were used to calculate the antibody density, or relative antibody spacing, conjugated to the PICs (Figure 3c). Relative ligand distance is essential for proper T cell activation, as has been demonstrated for protein-coated surfaces. In chapter 2 it was established that also for PIC-based sDCs antibody density is essential to induce potent T cell responses. Therefore, to study additional design parameters of sDCs, PIC-protein conjugates with similar antibody densities (or amounts of antibody per polymer chain) were selected. This allows for a fair comparison of the effect of pH and linker length. PIC-αCD3 (P-αCD3) conjugates where DBCO-functionalization was performed at different pH contained one antibody every 75-95 nm. Since the average PIC length was ~400 nm, these polymers contained ~4-6 antibodies per chain. For PIC-protein conjugates with different PEG linker lengths antibodies were spaced at 70-80 nm (~5-6 antibodies per polymer). To obtain PIC-antibody conjugates with similar densities, for DBCO-αCD3 with long PEG linkers approximately twice as much functionalized antibody had to be added to the reaction mixture, probably due to steric effects of the long PEG chains. αCD28-containing polymers were synthesized

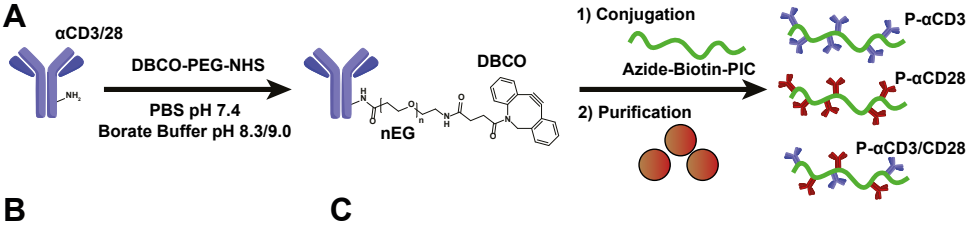

B

#	Ab	pH	EG	eq.	DOL
A1	αCD3	7.4	4	3.5	2.5
A2	αCD3	8.3	4	3.5	2.3
A3	αCD3	9.0	4	3.5	2.1
A4	αCD3	8.3	16	75	2.1
A5	αCD3	8.3	68	20	2.1
A6	αCD28	8.3	4	14	2.2
A7	αCD28	8.3	68	25	1.9

C

Sample name	Ab #	Spacing Ab (nm)	Mean Ab/PIC
P-4EG-αCD3 (7.4)	A1	74	5-6
P-4EG-αCD3 (8.3)	A2	68	5-6
P-4EG-αCD3 (9.0)	A3	97	4-5
P-16EG-αCD3 (8.3)	A4	71	5-6
P-68EG-αCD3 (8.3)	A5	77	5-6
P-68EG-αCD3 (8.3)	A5	54	7-8
P-4EG-αCD28	A6	122	3-4
P-68EG-αCD28	A7	102	3-4
P-4EG-αCD3/68EG-CD28	A2/A7	89	4-5
P-68EG-αCD3/68EG-CD28	A5/A7	93	4-5

Figure 3 Synthesis and characterization of PEG-linked PIC-antibody conjugates. **(A)** Synthetic strategy for the development of PEG-linked PIC-antibody conjugates. Antibodies against CD3 or CD28 were functionalized with DBCO-PEG-NHS esters with different PEG linker lengths (#EG) and at different pH. The resulting DBCO-functionalized antibodies were purified using spin filtration and reacted to azide- and biotin-containing PICs. The resulting PIC-antibody conjugates were purified over monovalent avidin beads. **(B)** Degree of DBCO labelling (DOL) for the different functionalized antibodies used for synthesis of PIC-antibody conjugates. **(C)** Analysis of antibody densities conjugated onto sDCs.

with antibodies spaced at ~90-120 nm (~3-5 antibodies per polymer). αCD3 density of polymers used in this experiment was slightly higher (spacing of ~55 nm, 7-8 antibodies per polymer).

T cell stimulation with PIC-αCD3 conjugates. To test the effect of pH during antibody DBCO functionalization, peripheral blood lymphocytes (PBLs) were incubated with different concentrations of unbound αCD3 and 4EG-linked polymers P-αCD3(pH7.4), P-αCD3(pH8.3) or P-αCD3(pH9) for 18 h (Figure 4a). After this, IFNγ concentrations in the supernatant were measured using ELISA. DBCO functionalization at pH 7.4 and subsequent PIC conjugation resulted in a reduction of the stimulatory capacity of αCD3. The activity of DBCO-PEG-NHS-functionalized antibodies that were not bound to PICs was comparable to non-functionalized αCD3 (Figure S3), indicating that PICs hamper antibody activity. However, at higher pH of functionalization, P-αCD3 stimulation induces a markedly increased IFNγ production compared to stimulation with unbound antibodies (Figure 4a). Probably, the increased pH leads to availability of additional amines on antibodies (by deprotonation) that can participate in reactions with NHS esters. In particular, the low pKa (8.9) of N-terminal amines are likely to allow functionalization at lower pH, while amines in lysine side chains with a pKa of 10.5 need a higher pH to be functionalized [36]. Functionalization of alternative amines may lead to DBCO conjugation at a different site on the antibody, which could cause a different orientation of antibodies when conjugated to PICs. Thus, this different orientation might liberate the antibodies from the steric effects that blocks the activity of P-αCD3(pH7.4).

Furthermore, the role of PEG linker length was established in similar experiments. PBLs were stimulated with different concentrations of unbound αCD3, P-4EG-αCD3, P-16EG-αCD3 and P-68EG-αCD3, and IFNγ secretion was measured (Figure 4b). Again, P-4EG-αCD3 induced significantly increased IFNγ secretion compared to unbound anti-CD3. P-αCD3 conjugates with longer PEG linkers induced slightly higher IFNγ production compared to P-4EG-αCD3. Possibly, the linkers generate a sDC scaffold with higher flexibility, which is an important parameter for aAPC development [37,38]. Alternatively, the longer linkers could allow for a further reduced obstruction of αCD3 activity by the PIC. However, these linkers do not give rise to functional sDCs when conjugated to αCD3 at pH 7.4 (Figure S3b), indicating that these linkers do not greatly affect the blocking effect of PICs. In the next chapter it is demonstrated that a more rigid double-stranded DNA-linker can be included in PIC-αCD3 conjugates using pH 7.4 functionalization without affecting αCD3 activity. Possibly, random coil formation due to the flexibility of PEG linkers only provide minimal spacing between antibodies and PICs and are therefore not able to relieve the blocking effect [39].

T cell stimulation with αCD28-containing PIC-protein conjugates. After having established the effect of antibody functionalization pH and PEG linker length for conjugation of signal 1 onto our sDCs, we tested the stimulatory capacity of sDCs containing both signal-1 and signal-2. Therefore, PBLs were labeled with CFSE, incubated with unbound αCD3 and αCD28, P-68EG-αCD3 and P-4/68EG-αCD28, or P-4/68EG-αCD3/68EG-CD28. After 18 hours, IFNγ concentrations in the supernatant were determined (Figure 5a) and after 3 days, proliferation was assessed through CFSE dilution (Figure 5b). Combined stimulation with P-αCD3 and P-αCD28 induced a marked increase in IFNγ secretion compared to unbound antibody stimulation. IFNγ levels were further increased by combining αCD3 and αCD28 on one and the same polymer chain. These co-conjugated αCD3/αCD28-sDCs also induced strong proliferation of T cells, which was also increased compared to stimulation with the mixture of P-αCD3 and P-αCD28. PEG linker length for P-αCD28 does not affect its stimulatory capacity. In addition, there is no difference in stimulation when linker length of αCD3 in P-αCD3/CD28 is changed. Thus, similar to the streptavidin-linked

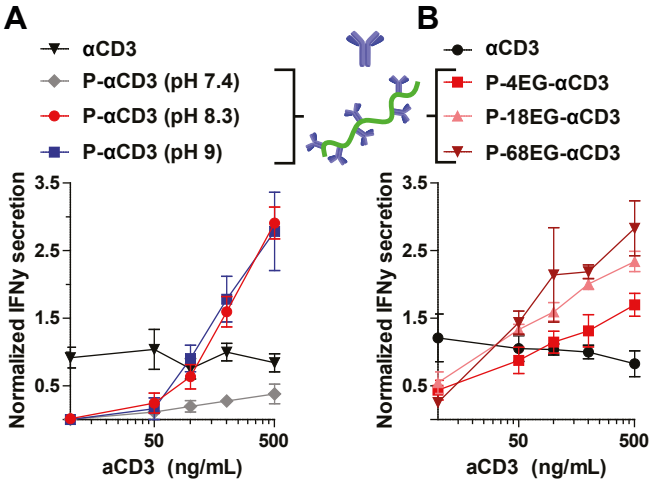

Figure 4 IFNγ secretion by T cells after different P-αCD3 stimulations of PBLs. **(A)** Normalized IFNγ concentrations in supernatant after stimulation of PBLs with P-αCD3 synthesized from CD3 antibodies that were functionalized with DBCO-4EG-NHS at different pH. **(B)** IFNγ concentrations in supernatant after stimulation of PBLs with P-αCD3 synthesized from CD3 antibodies that were functionalized with DBCO-PEG-NHS with different linker lengths at pH 8,3. IFNγ concentrations from duplicate stimulations of PBLs from two donors were normalized to the concentration induced by 200 ng/mL αCD3 stimulation and the mean concentrations ± SEM were depicted.

PIC-αCD3/CD28 conjugates [33], there is a great synergy when αCD3 and αCD28 are linked to one and the same polymer chain using a purified PEG-linked sDC. Because of the simplified design of our polymers, we demonstrate that this synergistic effect is caused through co-conjugation on PICs, and not co-conjugation on streptavidin. PEG linker length slightly affects T cell activation for P-αCD3, but not for P-αCD28 or P-αCD3/CD28. As CD3, and not CD28, can act as a mechanosensor [40], this receptor may detect differences in PEG linker length as differences in substrate flexibility on P-αCD3, but not on P-αCD28. Because synthesis with the 4EG linker is more efficient and therefore requires lower amounts of protein to be used in conjugation reactions, DBCO-4EG-NHS was chosen for development of future sDCs.

Small scale synthesis of sDCs containing αCD27, α4-1BB, αOX40 and αCD150. Having established a successful synthetic strategy to conjugate αCD3 and αCD28 to PICs, we aimed to incorporate additional co-stimulatory molecules into our sDC design and test their stimulatory capacity. To allow for development of a larger variety of sDCs, synthesis of these complexes was done at a smaller scale. Furthermore, to differentiate

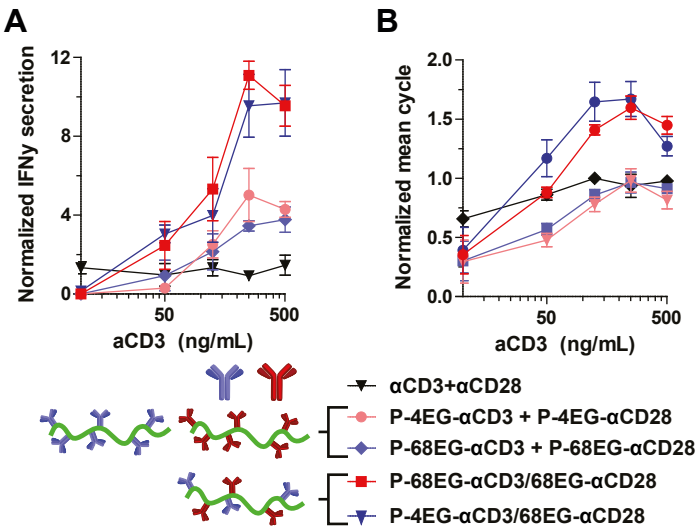

Figure 5 PBL stimulation with αCD28-containing PICs. **(A)** IFNy secretion after 18 h and **(A)** proliferation after 3 days of stimulation of PBLs with αCD3 + αCD28, P-αCD28 with different PEG linker lengths + P-αCD3, and P-αCD3/CD28 with different PEG linker lengths. IFNy concentrations and mean number of proliferation cycles from duplicate stimulations of PBLs from two donors were normalized to the concentration induced by 200 ng/mL αCD3 stimulation and the mean concentrations ± SEM were depicted.

between different co-stimuli conjugated to PICs, antibodies were labelled with a fluorophore during DBCO functionalization (Figure 6a). Because fluorophores can interact with filter membranes, spin filtration of fluorophore-labelled antibodies results in loss of proteins during spin filtration and therefore requires high amounts of starting materials. For a more cost-effective approach, antibodies were instead purified using size exclusion spin columns, resulting in quantitative yields after purification. Directly after purification, the degree of DBCO and fluorophore labelling was again assessed using UV/Vis spectrophotometry (Figure S4a). The resulting functionalized antibodies were used to develop sDCs using the strategy described before (Figure 3a).

After purification of PIC-protein conjugates, antibody concentration was determined using fluorescence measurements and protein density was calculated for each conjugate (Figure 6b). Unfortunately, when working with antibodies purified over spin columns we did not have the high level of control over this synthetic strategy as reported for the earlier CD3- and CD3/CD28-polymers. This resulted in relatively low amounts of αCD3 and high amounts of co-stimuli being conjugated to most of the PICs. αCD3 spacing was generally between 100-150 nm (~2-4 antibodies per polymer), except for P-CD3/CD150, which had a spacing of ~40 nm (~10 antibodies per polymer). Spacing of co-stimuli was between 5-25 nm (~15-80 antibodies per polymer).

sDC stimulation of inducible co-stimulatory molecules. Although these sDCs should be further optimized, their stimulatory potential was tested on isolated T cells. Similar to the results described before, CD28-containing sDCs induced strong proliferation of T cells (Figure 6c). Again, stimulation with P-αCD3/CD28 resulted in an enhanced effect compared to a combination of P-αCD3 and P-αCD28. Separately, P-αCD3 and P-αCD28 do not induce proliferation (Figure S6b). While PBL stimulation with unbound αCD3 and αCD28 is able to induce a low level of T cell proliferation, no proliferation is observed for stimulation of purified T cells.

To determine the effect of the other sDCs, expression of co-stimuli was induced by stimulation of purified T cells with CD3/CD28-T cell activator Dynabeads for 3 days. Because these beads are magnetic, they can be easily removed from T cells after stimulation. Next, 3-day-activated T cells were stimulated with a mix of unbound αCD3 and co-stimulatory antibody, mixed P-αCD3 and co-stimulatory PIC or with corresponding concentrations of PICs containing both αCD3 and co-stimulatory antibody. Measurement of IFNγ production after 24 h revealed a similar trend compared to the αCD28-containing PICs (Figure 6d). Irrespective of the co-stimulus used, when both signal 1 and 2 are conjugated to one and the same polymer, IFNγ concentrations were increased compared to stimulation with a mixture of signal-1-PIC and signal-2-PIC. However, IFNγ concentrations were relatively low compared to re-stimulations with αCD28-containing PICs (Figure 6e). Thus, we could not induce

strong T-cell activation with co-stimulatory sDCs, and to achieve this more optimization of the sDC design is required.

The sDCs described here contain low densities of αCD3 and high densities of co-stimulatory antibodies, which could contribute to their low stimulatory capacity. To optimize conjugation of co-stimulatory molecules, a lower degree of DBCO labeling (of around 2-3 DBCO per antibody would be better suitable. For functionalized αCD3, DBCO content was in this desired range. Unexpectedly, when this functionalized antibody was purified using size exclusion columns, as was done for the sDCs described in Figure 6, conjugation efficiency to PICs was low. To determine whether the size exclusion columns affected the stability of DBCO-functionalized antibodies, αCD3 functionalization with DBCO and ATTO488 was repeated and degree of DBCO labeling was re-assessed immediately after and 24 h after purification (Figure S4d). These measurements demonstrated that functional DBCO was lost 24 h after purification over size exclusion columns. At the same time, DBCO content was stabile when antibodies were purified using spin filtrations or when columns were washed at least 5 times (instead of 3) before use. Probably, antibodies used to develop sDCs depicted in figure 6 were contaminated with small amounts of sodium azide present in the size exclusion columns used for purification. This contamination competes for DBCO with PIC-bound azides. Further optimization to remove these contaminations should give us more control over small scale PIC-protein synthesis.

Conclusions and outlook

In this chapter, a highly modular strategy was developed to produce sDCs with a wide variety of co-stimulatory molecules. Co-stimulatory molecules can be used to control the speed of T cell differentiation. In plate-bound assays antibodies against CD27 induced strong naive T cell proliferation and CD3/CD27-stimulated T cells exhibits a faster differentiation compared to CD3/CD28-stimulated T cells. In pre-activated T cells, 4-1BB induces a more differentiated phenotype compared to CD27, OX40, and CD150. Incorporation of these antibodies onto co-stim-sDCs may therefore lead to powerful nanosized tools to direct T cell functionality.

For the development of modular sDCs PEG-linked PIC-antibody conjugates were successfully synthesized and applied in T cell activation experiments. To synthesize sDCs with high stimulatory capacity towards T cells, αCD3 functionalization with DBCO should be done at pH 8.3 or higher, since functionalization at lower pH results in diminished T cell stimulation. Making use of longer PEG linkers between αCD3 and PICs slightly increases IFNγ secretion, but not when αCD28-containing polymers are used. Using the optimized and purified sDC design it was demonstrated that conjugating αCD3 and αCD28 to one and the same PIC results in highly enhanced T cell activation.

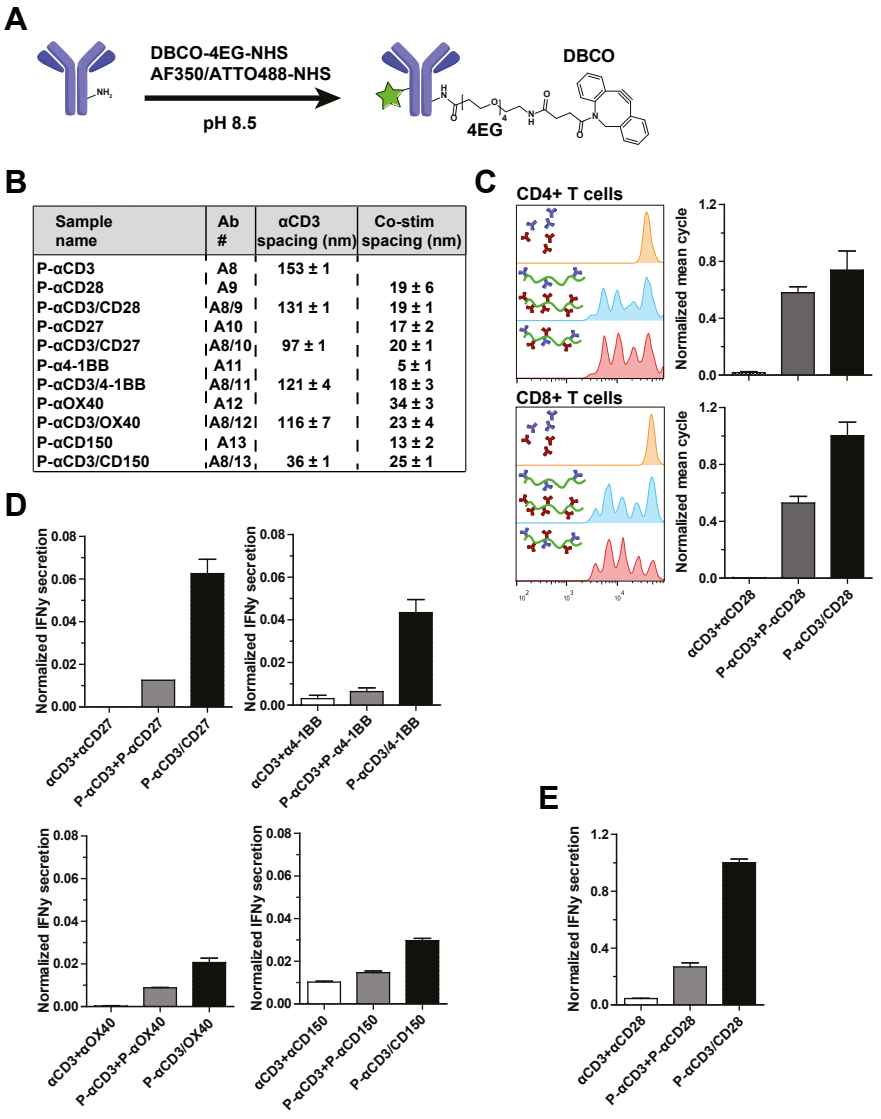

Sample name	Ab #	αCD3 spacing (nm)	Co-stim spacing (nm)
P-αCD3	A8	153 ± 1	
P-αCD28	A9		19 ± 6
P-αCD3/CD28	A8/9	131 ± 1	19 ± 1
P-αCD27	A10		17 ± 2
P-αCD3/CD27	A8/10	97 ± 1	20 ± 1
P-α4-1BB	A11		5 ± 1
P-αCD3/4-1BB	A8/11	121 ± 4	18 ± 3
P-αOX40	A12		34 ± 3
P-αCD3/OX40	A8/12	116 ± 7	23 ± 4
P-αCD150	A13		13 ± 2
P-αCD3/CD150	A8/13	36 ± 1	25 ± 1

Figure 6 Development of sDCs that can trigger a wide variety of co-stimulatory molecules. **(A)** Functionalization of antibodies with DBCO and fluorophores. Antibodies were incubated in Borate Buffer with pH 8.5, after which DBCO-4EG-NHS ester and ATTO488-NHS (for αCD3) or AF350 (for co-stimulatory antibodies) were added. After 2 h, functionalized antibodies were purified using size exclusion spin columns. **(B)** Analysis of antibody densities conjugated onto sDCs. Mean values ± SD of two independent measurements. **(C)** Proliferation as determined by Celltrace Violet dilution of CD4+ (top) and CD8+ (bottom) T cells after 3 days of stimulation with αCD3 and αCD28 at a concentration of 100 ng/mL. Bar graphs show

mean values ± SEM of mean number of proliferation cycles from two donors, normalized to mean cycles of CD8+ T cells stimulated by P-CD3/CD28. **(D)** Normalized IFNγ secretion 24 h after re-stimulation of Dynabead-primed pan T cells with co-stimulatory antibodies αCD27, α4-1BB, αOX40, αCD150 and **(E)** αCD28. Data is shown of duplicate stimulation of T cells from one donor representative for observations from three independent experiments.

Modularity of the novel 4EG-linked sDC design was further increased by improving yields of functionalization during small scale antibody functionalization, which was done through use of size exclusion spin columns. However, DBCO-functionalized antibodies showed variable stability due to spin column contaminations, which resulted in PIC-antibody conjugates with sub-optimal antibody densities. Although these co-stim-sDCs only induced low levels of T cell activation, co-conjugation of co-stimulatory antibodies together with αCD3 on one and the same polymer showed a trend towards higher stimulatory capacity. Nonetheless, only αCD28 co-stimulation is capable of inducing high levels of IFNγ secretion at these sub-optimal αCD3 densities.

To fully understand this synergistic effect of co-conjugation of signal 1 and 2, and use co-stimulatory polymers to control T cell differentiation and function, the small scale sDC synthesis should be further optimized. The PICs with optimized antibody densities can be used to induce strong T cell responses with a wide variety of co-stimulatory molecules. It is expected that αCD27 and/or α4-1BB-presenting sDCs should be able to speed up T cell differentiation. Due to the modular synthesis, testing the effect of additional co-stimulatory molecules and cytokines can be done in a highly straightforward fashion. This novel synthetic strategy can then be exploited to gain a high level of control over T cell differentiation and functionality. Due to their bio-compatibility, the resulting co-stim-sDCs could eventually be applied to induce these functions in T cells used in a clinical setting.

Experimental section

Materials. Zeba™ Spin Desalting Columns (40K MWCO), Celltrace Violet and CFSE Cell proliferation kit, Dynabeads human T-activator CD3/CD28 and AlexaFluor350-NHS ester (AF350) were purchased from ThermoFisher. Magnetic mono-avidin beads were from Bioclone. Anti-CD3 (Clone OKT3) and Anti-CD28 (Clone 9.3) was from BioXCell. Human Pan T cell isolation kit, naïve CD8+ T cell isolation kit and propidium iodide solution were obtained from Miltenyi. Antibodies anti-OX40 (Clone L106) and anti-CD4-APC-H7 were from BD Biosciences, and antibodies anti-4-1BB (Clone 4B4-1), anti-Notch2 (Clone MHN2-25), anti-GITR (Clone 621), anti-CD30 (BY88), anti-CD28-PECy7, anti-CD45RA-BV510, anti-CD27-PE, anti-Notch2-APC, anti-OX40-FITC, anti-

CD30-FITC, anti-4-1BB-APC and anti-CD127-PerCP-Cy5.5 were from Biolegend. eFluor 780 live-dead cell marker was from eBioscience. Anti-CD27 (Clone 1A4CD27) was from Beckman Coultier. DBCO- 4EG-NHS was purchased from Jena Bioscience. DBCO-16EG-NHS and DBCO- 68EG-NHS were obtained from Biochempeg. Atto488-NHS ester (A488) was obtained from Atto-TEC GmbH. 30 kDa Amicon Ultra-15 ultrafiltration membranes were from Merck Millipore. X-vivo medium was purchased from Lonza.

Antibody functionalization. For functionalization, around 1-5 mg of αCD3 or αCD28 antibodies was diluted in PBS or Borate buffer to a concentration ~1 mg/mL to adjust the pH. DBCO-PEG-NHS ester, and in some cases ATTO488-NHS ester or AF350-NHS ester, was added and the reaction mixture was incubated for 2 h at 4 °C on a rotator. After this, functionalized antibodies were purified by washing four times with 15 mL PBS using Amicon ultrafiltration membranes (30 kD MWCO). Antibodies that were also labelled with a fluorophore were purified over Zebaspin size exclusion columns (40 kD MWCO). Before use, size exclusion columns were washed with PBS three times according to the manufacturer's protocol.

Analysis of functionalized antibodies. To determine the degree of DBCO and fluorophore functionalization, the functionalized antibodies were analyzed with UV/Vis spectrophotometry using a Nanodrop 2000c spectrophotometer. Absorbance at 280, 309, 350 and 501 nm were measured to calculate the concentrations of protein, DBCO, AF350 and ATTO488. Overlap of the spectra of the individual molecules was corrected using the formulas:

$$A280c = A280 - c1A309 + c1c4A501 - c2A5011 - c1c3$$

$$A309c = A309 - c3A280c - c4A501$$

A280c: Corrected absorbance at 280 nm
A309c: Corrected absorbance at 309 nm
A280: Absorbance signal measured at 280 nm
A309: Absorbance signal measured at 309 nm
A501: Absorbance signal measured at 501 nm
c1: Correction factor DBCO on A280, determined as A280/A309 of DBCO-PEG-NHS
c2: Correction factor ATTO488 on A280, determined as A280/A501 of ATTO488-NHS
c3: Correction factor antibody on A309, determined as A309/A280 of non-functionalized antibody
c4: Correction factor ATTO488 on A309, determined as A309/A501 of ATTO488-NHS

The respective concentrations were calculate using molar extinction coefficients of the individual molecules: 210000 M^{-1} cm^{-1} for antibodies, 12000 M^{-1} cm^{-1} for DBCO, 90000 M^{-1} cm^{-1} for ATTO488 and 19000 M^{-1} cm^{-1} for AF350.

PIC-antibody conjugate synthesis. To synthesize PIC-antibody conjugates, DBCO-functionalized antibodies (Generally 0.2 equivalents with respect to the reactive azide groups on the polymer for 4EG-DBCO and 0.4 equivalents for longer PEG chains) were added to azide-biotin-PIC in (1 mg/mL in PBS). αCD3 and co-stimuli were added in a 1:1 ratio. The reaction mixture was incubated at 4 °C on a rotator overnight. After conjugation, the PIC-antibody conjugates were purified using magnetic mono-avidin beads as described in chapter 3 [35]. The conjugates were incubated with magnetic mono-avidin beads for 2h at 4 °C. The polymer-bound beads were then washed extensively with PBS+0.1% Tween-20 (2x) and PBS (4x), on a Dynal MPC-L Magnetic Particle Concentrator. After this, the conjugates were eluted from the beads using PBS containing 2 mM biotin (biotin elution buffer) on a rotator for 2h at 4 °C.

Analysis of PIC-antibody conjugates. For non-fluorescent antibodies, concentrations on PIC-antibody conjugates were determined using a micro BCA assay. Unbound DBCO-functionalized antibodies were used as a standard. For fluorophore-labeled antibodies, concentrations on PIC conjugates were determined using a Tecan Spark 10M fluorescence microplate reader. Unbound functionalized antibodies were used as standard for each measurement. The PIC-antibody conjugate samples (100 µl) were pipetted into black, flat-bottom non-binding 96-well microplates (Greiner Bio-One). A488 and A350 were excited at 490 nm and 360 nm, and detected at 535 nm and 442 nm, respectively. The PIC concentrations was measured using circular dichroism (CD) (JASCO J-810). 100 µl of each PIC-antibody conjugate was pipetted into a 1 cm cuvette and the CD spectrum was measured using biotin elution buffer as a blank. The peak value at 272 nm was used to determine the polymer concentration, using an extinction coefficient of 547.8 mdeg ml cm-1, which was determined with a standard curve of different polymer concentrations as described previously [35].

Human T cell stimulation assays. Peripheral blood mononuclear cells (PBMCs) were isolated from buffy coats, obtained from healthy donors, using Ficoll density centrifugation. To isolate peripheral blood lymphocytes (PBLs), PBMCs were adhered to culture plates for 1 h, after which non-adherent cells were taken. PBLs were either used directly for T cell activation assays, or used for isolation of T cells with the Miltenyi Pan T cell isolation kit or naïve CD8+ T cells with the Miltenyi naïve CD8+ T cell isolation kit. To follow T cell proliferation, for some experiments T cells were labeled with CFSE or Celltrace Violet. For this, the dye was added to the cells at a final

concentration of 2.5 μM in PBS and cells were incubated in the dark at RT for 15 minutes. The reaction was quenched by addition of 3 reaction volumes of cold Fetal Bovine Serum (FBS), followed by washing the cells 3 times. PIC-protein conjugates were added to 100.000 PBLs or 50.000 T cells in round-bottom 96-well cell culture plates, with final volumes of 100 μl per well. For plate-bound antibody stimulations, 50 uL PBS containing 1 μg/mL αCD3 and 5 μg/mL co-stimulatory antibody was added to ELISA plates and incubated at 4 °C overnight. Plates were washed with PBS twice and naïve CD8+ T cells were added. For stimulation of inducible co-stimulatory molecules, T cells were stimulated for three days using plate-bound antibodies or CD3/CD28 T cell activator Dynabeads. After these three days, cells were removed from the plate or beads, washed 3x and re-stimulated. Cell culture was performed at 37 °C using X-Vivo medium containing 4% human serum.

Analysis of early T cell activation. After 18 h of stimulation, supernatant from the stimulated cells was collected to determine the concentration of IFNy secreted. These concentrations were determined by ELISA measurements (human IFNy ELISA, Thermo Scientific). For detection, absorbance was measured at 450 nm on a Bio-rad iMark plate reader. IFNy concentrations were determined using 4-paramer fits in Microplate Manager 6 software. After 3 days of stimulation, cells were stained for CD4 and CD8 and the dilution of CFSE or Celltrace Violet label was determined using FACS (BD FACSVerse). The mean number of cycles (i.e. the average number of cell divisions) was determined as ^{2}log of the ratio of the mean fluorescence intensity (MFI) of non-divided cells (as determined using FlowJo) divided by the MFI of all cells. To determine expression kinetics of co-stimulatory molecules after activation, at various time points after stimulation cells were split in three groups that were stained with either anti-CD27-PE, anti-CD28-PECy7 and anti-4-1BB-APC, or anti-OX40-FITC and anti-GITR-APC, or anti-CD150-AF568, anti-CD30-FITC and anti-Notch2-APC. Expression of the different co-stimulatory molecules was determined using FACS (BD FACSVerse).

Analysis of late T cell activation and differentiation. To determine proliferation after 6 days of stimulation, cells were stained for CD4 and CD8 (if necessary) and counted using a Miltenyi MACSQuant Analyzer 10. Propidium iodide staining of dead cells was done using the MACSQuant before flow cytometry measurement. To analyze the differentiation of naïve CD8+ T cells, cells were stained with eFluor 780 live-dead cell marker and anti-CD28-PECy7, anti-CD45RA-BV510, anti-CD27-PE, anti-CD127-PerCP-Cy5.5, anti-CCR7-AF647 and anti-CD4-APC-H7. Expression of the different makers was determined using FACS (BD FACSVerse).

References

1 Iwai, Y. *et al.* (2017) Cancer immunotherapies targeting the PD-1 signaling pathway. *J. Biomed. Sci.* 24, 26

2 Pardoll, D.M. (2012) The blockade of immune checkpoints in cancer immunotherapy. *Nat. Rev. Cancer* 12, 252–264

3 Pico de Coaña, Y. *et al.* (2015) Checkpoint blockade for cancer therapy: revitalizing a suppressed immune system. *Trends Mol. Med.* 21, 482–491

4 Sanmamed, M.F. *et al.* (2015) Agonists of Co-stimulation in Cancer Immunotherapy Directed Against CD137, OX40, GITR, CD27, CD28, and ICOS. *Semin. Oncol.* 42, 640–655

5 Melero, I. *et al.* (2013) Clinical Development of Immunostimulatory Monoclonal Antibodies and Opportunities for Combination. *Clin. Cancer Res.* 19, 997–1008

6 Chen, L. and Flies, D.B. (2013) Molecular mechanisms of T cell co-stimulation and co-inhibition. *Nat. Rev. Immunol.* 13, 227–242

7 Gimmi, C.D. *et al.* (1993) Human T-cell clonal anergy is induced by antigen presentation in the absence of B7 costimulation. *Proc. Natl. Acad. Sci. U. S. A.* 90, 6586–90

8 Appleman, L.J. and Boussiotis, V.A. (2003) T cell anergy and costimulation. *Immunol. Rev.* 192, 161–180

9 June, C.H. *et al.* (1987) T-cell proliferation involving the CD28 pathway is associated with cyclosporine-resistant interleukin 2 gene expression. *Mol. Cell. Biol.* 7, 4472–81

10 Shahinian, A. *et al.* (1993) Differential T cell costimulatory requirements in CD28-deficient mice. *Science (80-.).* 261, 609–612

11 Denoeud, J. and Moser, M. (2011) Role of CD27/CD70 pathway of activation in immunity and tolerance. *J. Leukoc. Biol.* 89, 195–203

12 Sharpe, A.H. (2009) Mechanisms of costimulation. *Immunol. Rev.* 229, 5–11

13 Rudd, C.E. *et al.* (2009) CD28 and CTLA-4 coreceptor expression and signal transduction. *Immunol. Rev.* 229, 12–26

14 van de Ven, K. and Borst, J. (2015) Targeting the T-cell co-stimulatory CD27/CD70 pathway in cancer immunotherapy: rationale and potential. *Immunotherapy* 7, 655–667

15 Hintzen, R.Q. *et al.* (1995) Engagement of CD27 with its ligand CD70 provides a second signal for T cell activation. *J. Immunol.* 154, 2612–23

16 Hendriks, J. *et al.* (2003) CD27 Promotes Survival of Activated T Cells and Complements CD28 in Generation and Establishment of the Effector T Cell Pool. *J. Exp. Med.* 198, 1369–1380

17 Croft, M. (2014) The TNF family in T cell differentiation and function – Unanswered questions and future directions. *Semin. Immunol.* 26, 183–190

18 Cannons, J.L. *et al.* (2011) SLAM Family Receptors and SAP Adaptors in Immunity. *Annu. Rev. Immunol.* 29, 665–705

19 Laky, K. *et al.* (2015) Notch Signaling Regulates Antigen Sensitivity of Naive CD4+ T Cells by Tuning Co-stimulation. *Immunity* 42, 80–94

20 Willoughby, J.E. *et al.* (2014) Differential Impact of CD27 and 4-1BB Costimulation on Effector and Memory CD8 T Cell Generation following Peptide Immunization. *J. Immunol.* 193, 244–251

21 Crompton, J.G. *et al.* (2014) Uncoupling T-cell expansion from effector differentiation in cell-based immunotherapy. *Immunol. Rev.* 257, 264–276

22 Cieri, N. *et al.* (2013) IL-7 and IL-15 instruct the generation of human memory stem T cells from naive precursors. *Blood* 121, 573–584

23 Chacon, J.A. *et al.* (2013) Co-Stimulation through 4-1BB/CD137 Improves the Expansion and Function of CD8+ Melanoma Tumor-Infiltrating Lymphocytes for Adoptive T-Cell Therapy. *PLoS One* 8, e60031

24 Klebanoff, C.A. *et al.* (2012) Sorting Through Subsets. *J. Immunother.* 35, 651–660

25 Klebanoff, C.A. *et al.* (2005) Central memory self/tumor-reactive CD8+ T cells confer superior antitumor immunity compared with effector memory T cells. *Proc. Natl. Acad. Sci.* 102, 9571–9576

26 Hombach, A.A. and Abken, H. (2011) Costimulation by chimeric antigen receptors revisited the T cell antitumor response benefits from combined CD28-OX40 signalling. *Int. J. Cancer* 129, 2935–2944

27 Song, D.-G. *et al.* (2011) In Vivo Persistence, Tumor Localization, and Antitumor Activity of CAR-Engineered T Cells Is Enhanced by Costimulatory Signaling through CD137 (4-1BB). *Cancer Res.* 71, 4617–4627

28 Long, A.H. *et al.* (2015) 4-1BB costimulation ameliorates T cell exhaustion induced by tonic signaling of chimeric antigen receptors. *Nat. Med.* 21, 581–590

29 Eggermont, L.J. *et al.* (2014) Towards efficient cancer immunotherapy: advances in developing artificial antigen-presenting cells. *Trends Biotechnol.* 32, 456–465

30 Rudolf, D. *et al.* (2007) Potent costimulation of human CD8 T cells by anti-4-1BB and anti-CD28 on synthetic artificial antigen presenting cells. *Cancer Immunol. Immunother.* 57, 175–183

31 Shen, C. *et al.* (2013) Latex bead-based artificial antigen-presenting cells induce tumor-specific CTL responses in the native T-cell repertoires and inhibit tumor growth. *Immunol. Lett.* 150, 1–11

32 Hammink, R. *et al.* (2017) Controlling T-Cell Activation with Synthetic Dendritic Cells Using the Multivalency Effect. *ACS Omega* 2, 937–945

33 Mandal, S. *et al.* (2015) Polymer-Based Synthetic Dendritic Cells for Tailoring Robust and Multifunctional T Cell Responses. *ACS Chem. Biol.* 10, 485–492

34 Mandal, S. *et al.* (2013) Therapeutic nanoworms: towards novel synthetic dendritic cells for immunotherapy. *Chem. Sci.* 4, 4168

35 Hammink, R. *et al.* (2017) Affinity-Based Purification of Polyisocyanopeptide Bioconjugates. *Bioconjug. Chem.* 28, 2560–2568

36 van Vught, R. *et al.* (2014) Site-specific functionalization of proteins and their applications to therapeutic antibodies. *Comput. Struct. Biotechnol. J.* 9, e201402001

37 O'Connor, R.S. *et al.* (2012) Substrate Rigidity Regulates Human T Cell Activation and Proliferation. *J. Immunol.* 189, 1330–1339

38 Lambert, L.H. *et al.* (2017) Improving T Cell Expansion with a Soft Touch. *Nano Lett.* 17, 821–826

39 Lee, H. *et al.* (2008) Molecular Dynamics Studies of Polyethylene Oxide and Polyethylene Glycol: Hydrodynamic Radius and Shape Anisotropy. *Biophys. J.* 95, 1590–1599

40 Judokusumo, E. *et al.* (2012) Mechanosensing in T Lymphocyte Activation. *Biophys. J.* 102, L5–L7

41 Mahnke, Y.D. *et al.* (2013) The who's who of T-cell differentiation: Human memory T-cell subsets. *Eur. J. Immunol.* 43, 2797–2809

42 Willoughby, J.E. *et al.* (2014) Differential Impact of CD27 and 4-1BB Costimulation on Effector and Memory CD8 T Cell Generation following Peptide Immunization. *J. Immunol.* 193, 244–251

43 Nolte, M.A. *et al.* (2009) Timing and tuning of CD27-CD70 interactions: the impact of signal strength in setting the balance between adaptive responses and immunopathology. *Immunol. Rev.* 229, 216–231

44 Dong, H. *et al.* (2012) CD27 Stimulation Promotes the Frequency of IL-7 Receptor-Expressing Memory Precursors and Prevents IL-12-Mediated Loss of CD8+ T Cell Memory in the Absence of CD4+ T Cell Help. *J. Immunol.* 188, 3829–3838

45 Carr, J.M. *et al.* (2006) CD27 mediates interleukin-2-independent clonal expansion of the CD8+ T cell without effector differentiation. *Proc. Natl. Acad. Sci.* 103, 19454–19459

46 Kaech, S.M. and Cui, W. (2012) Transcriptional control of effector and memory CD8+ T cell differentiation. *Nat. Rev. Immunol.* 12, 749–761

47 Mehrle, S. *et al.* (2005) SAP and SLAM expression in anti-CD3 activated lymphocytes correlates with cytotoxic activity. *Immunol. Cell Biol.* 83, 33–39

48 Croft, M. (2003) Costimulation of T cells by OX40, 4-1BB, and CD27. *Cytokine Growth Factor Rev.* 14, 265–273

49 Lee, S.-W. *et al.* (2006) Functional Dichotomy between OX40 and 4-1BB in Modulating Effector CD8 T Cell Responses. *J. Immunol.* 177, 4464–4472

50 Irving, M. *et al.* (2017) Engineering Chimeric Antigen Receptor T-Cells for Racing in Solid Tumors: Don't Forget the Fuel. *Front. Immunol.* 8, 267

51 Laderach, D. *et al.* (2002) 4-1BB co-stimulation enhances human CD8(+) T cell priming by augmenting the proliferation and survival of effector CD8(+) T cells. *Int. Immunol.* 14, 1155–67

Supplementary figures

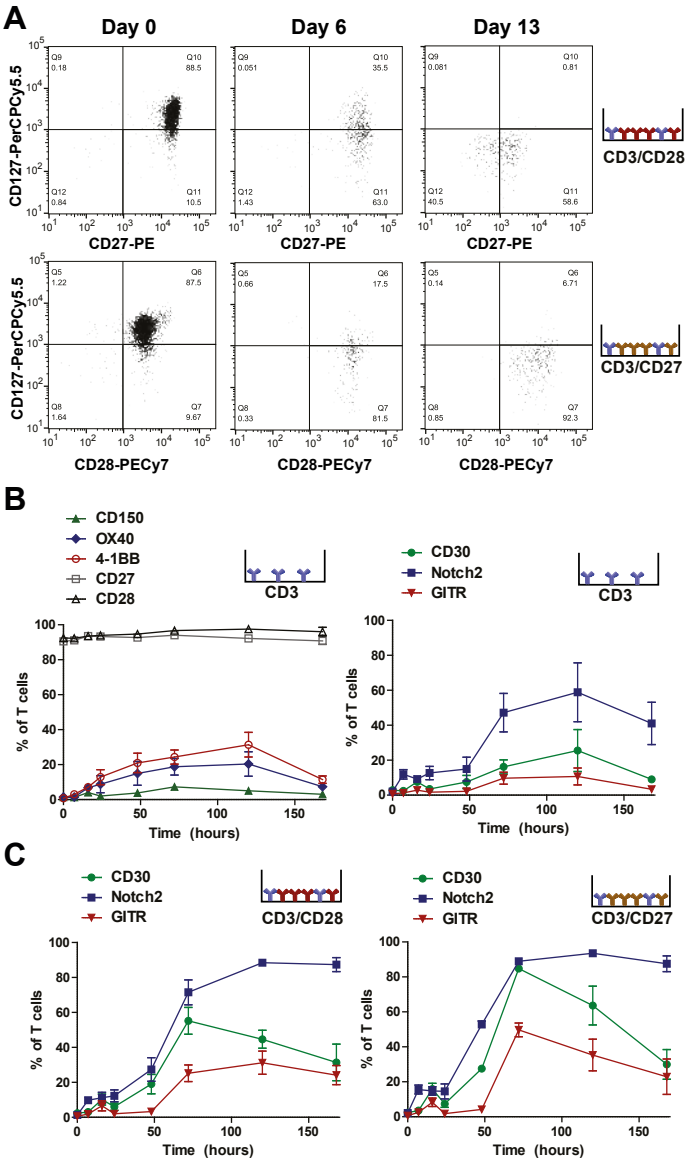

Figure S1 Screening of αCD28 and αCD27 by plate-bound antibody stimulations of naïve CD8+ T cells. **(A)** Expression of CD127 and CD27 or CD28 as determined by flow cytometry after 6 days and 13 days of stimulation with plate-bound antibodies. Because the stimulating antibodies block the receptor for staining antibodies, CD27 expression is shown for CD3/

CD28-stimulation and CD28 expression is shown for CD3/CD27 stimulation. Dot plots show representative example of three independent observations. **(B)** Expression of co-stimulatory molecules after stimulation with plate-coated αCD3 only. **(C)** Expression of co-stimulatory molecules CD30, Notch2 and GITR after stimulation with plate-coated αCD3/CD28 (right) or CD3/CD27 (left). Average percentage of co-stimulati-expressing T cells after duplicate stimulations of two donors is depicted.

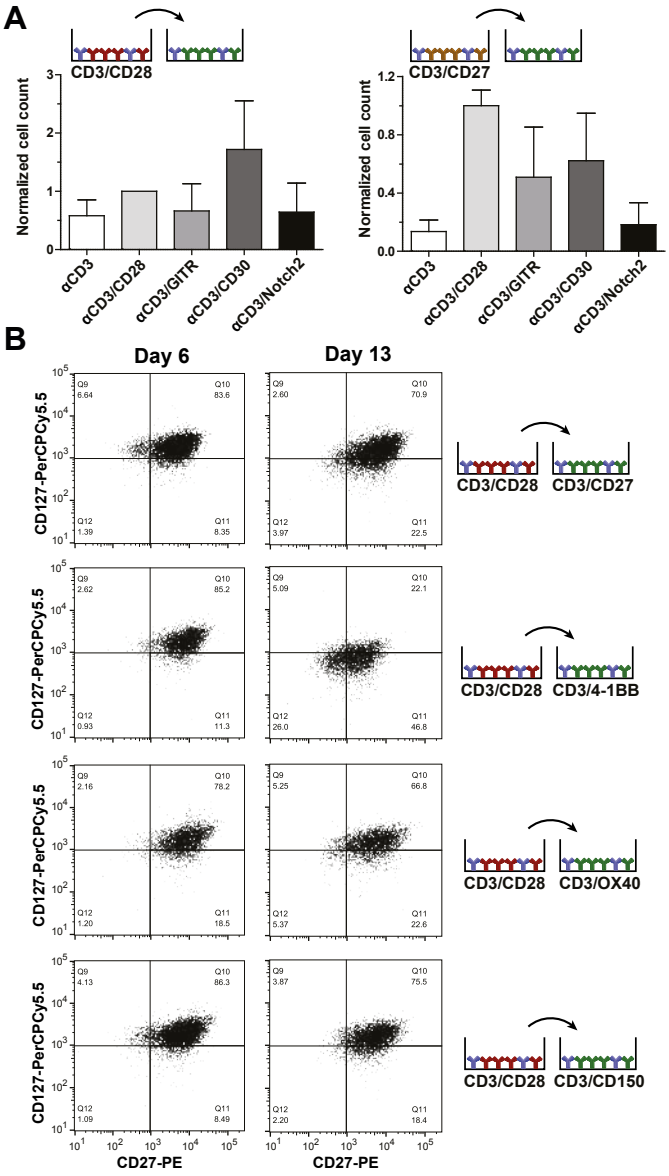

Figure S2 Stimulation of inducible co-stimulatory molecules on pre-activated CD8 T cells by plate-bound antibodies. **(A)** Normalized cell counts at day 6 (or 3 days after second stimulation). Naïve CD8+ T cells were pre-stimulated with αCD3/CD28 (left) or αCD3/CD27 (right). After 3 days, cells were stimulated with antibodies depicted on x-axis. Values were normalized to CD3/CD28-stimulated cell count and the average values + SEM from stimulation of two donors were plotted. **(B)** Expression of CD127 and CD45RA as determined

by flow cytometry after 6 days and 13 days of stimulation with plate-bound antibodies. Naïve CD8 T cells were pre-stimulated with plate-bound αCD3/CD28 and transferred to a new antibody-coated plate after 3 days. Dot plots show representative example of three independent observations.

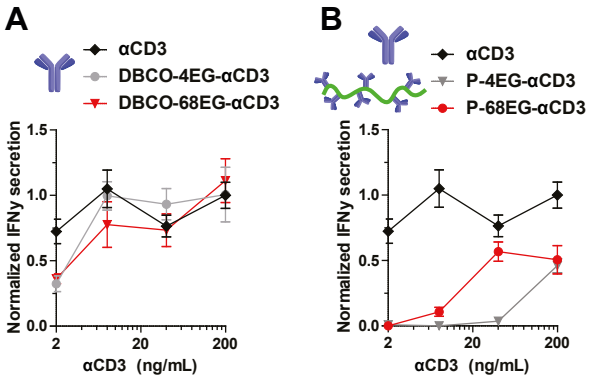

Figure S3 T cell stimulation with DBCO-αCD3 and P-αCD3 functionalized at pH 7.4. **(A)** Normalized IFNy concentrations in supernatant after stimulation of PBLs with unbound αCD3, unbound DBCO-4EG-αCD3 and unbound DBCO-68EG-αCD3. Antibodies were functionalized at pH 7.4. **(B)** Normalized IFNy concentrations in supernatant after stimulation of PBLs with P-αCD3 synthesized from CD3 antibodies that were functionalized with DBCO-PEG-NHS at pH 7.4. For P-4EG-αCD3 and P-68EG-αCD3 antibodies had a relative spacing of 45 and 68 nm, respectively. IFNy concentrations from duplicate stimulations of PBLs from three donors were normalized to the concentration induced by 200 ng/mL αCD3 stimulation and the mean concentrations ± SEM were depicted.

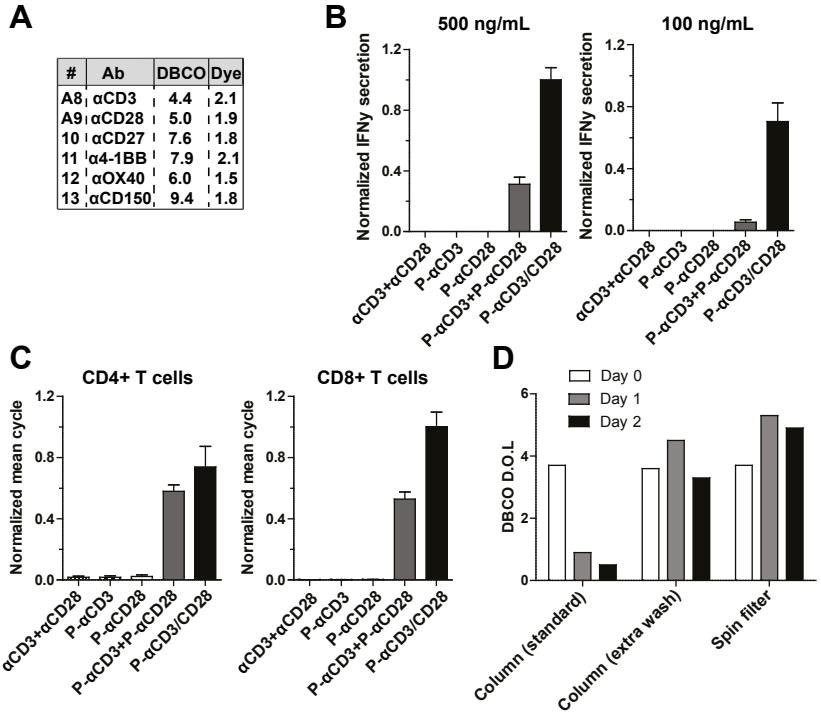

#	Ab	DBCO	Dye
A8	αCD3	4.4	2.1
A9	αCD28	5.0	1.9
10	αCD27	7.6	1.8
11	α4-1BB	7.9	2.1
12	αOX40	6.0	1.5
13	αCD150	9.4	1.8

Figure S4 Development of sDCs that can trigger a wide variety of co-stimulatory molecules. **(A)** Degree of DBCO and Dye labeling for antibodies used to make the PIC-antibody conjugates depicted in figure 6. **(B)** IFNy secretion as determined by ELISA of T cells stimulated with 500 ng/mL (left) and 100 ng/mL (right) of αCD3 for 24 h. Bar graphs show mean values ± SEM of IFNy secreted into the supernatant by T cells from two donors, normalized to T cells stimulated with 500 ng/mL P-αCD3/CD28. **(C)** Proliferation as determined by Celltrace Violet dilution of CD4+ (left) and CD8+ (right) T cells after 3 days of stimulation with αCD3 and αCD28 at a concentration of 100 ng/mL. Bar graphs show mean values ± SEM of mean number of proliferation cycles from duplicate stimulation of two donors, normalized to mean cycles of CD8+ T cells stimulated by P-CD3/CD28. **(D)** Stability of antibody-functionalized DBCO during storage. Degree of DBCO labeling after antibody functionalization and purification (Day 0), and stability after 1 and 2 days are depicted as measured by UV/Vis spectrophotometry.

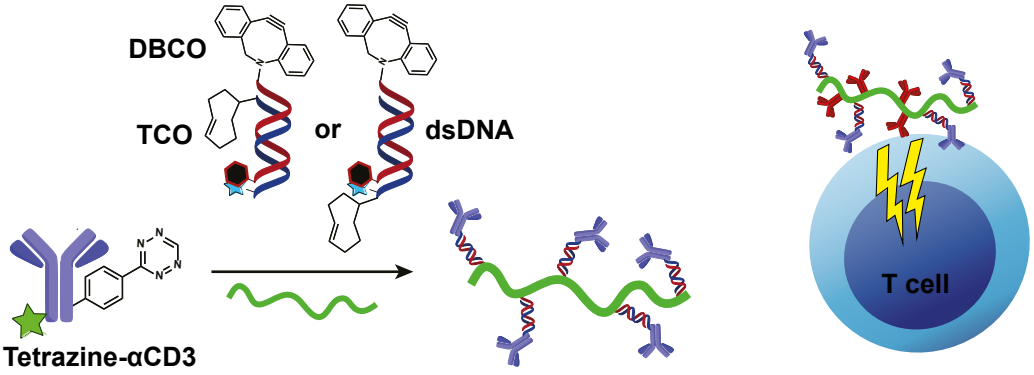
DBCO
TCO
or
dsDNA
Tetrazine-αCD3
T cell

5

Development of DNA-linked PIC-antibody conjugates for generation of force-sensitive synthetic Dendritic Cells

Loek Eggermont, Roel Hammink, Swapneel Deshpande, Hans Heus, Alan Rowan, Jurjen Tel, Kerstin Blank, Carl Figdor

Abstract

TCR triggering is initiated after binding to specific pMHC complexes on both antigen presenting cells or synthetic mimics thereof, so-called artificial Antigen-Presenting Cells (aAPCs). It is becoming increasingly clear that force generation is important in TCR stimulation, but it is not always evident how aAPCs can generate these forces necessary for T cell activation. Importantly, better understanding of the role of force in artificial stimulations could be exploited to develop both improved aAPC designs and force-responsive systems. To generate force-responsive aAPCs, DNA duplexes that rupture under specific pN-range tensions can be exploited. In this chapter, DNA duplexes were incorporated as linkers into filamentous nanosized aAPCs to develop a force-sensitive material that may be used to study and manipulate receptor cluster movement on the T cell surface. For this, filamentous polyisocyanopeptides (PICs) were stably linked to antibodies through DNA hybridization. Importantly, these constructs induced strong activation when incubated with T cells. Furthermore, a DNA duplex was introduced into PIC-antibody conjugates in two different geometries, which could either unzip or shear upon force application. Fluorescence of fluorophore-quencher or FRET pairs allowed for assessment of force-induced DNA duplex rupture. In addition to DNA-linked anti-CD3, the PIC-antibody conjugates contained antibodies against CD28 or CD45. These molecules could possibly provide anchoring points on the T cell surface that can be used to study relative forces and manipulate clustering between moving receptors. A preliminary experiment indicated that incubation of these conjugates with T cells led to unexpected shearing, rather than unzipping of linkers. Additional experiments are required to fully understand how this high force DNA duplex shearing is induced and to establish whether these force-sensitive sDCs can be used to manipulate receptor clustering and T cell activation.

Introduction

Adaptive immunity against cancer cells and invading pathogens is driven by activation of T cells. In the past decade, anti-cancer T cell responses induced by immunotherapy have led to a marked increase in clinical responses, but also gave rise to dangerous side effects as a result of non-specific immune activation [1,2]. To improve our understanding of T cell triggering and fully harness the potential of T-cell-based immunotherapy, methods for precise manipulation of T cell activation are essential. It is now increasingly recognized that force generation plays an important role in TCR stimulation, which could give novel opportunities to control T cell stimulation. Artificial antigen-presenting cells (aAPCs), are specifically designed to initiate and control activation of T cells [3,4], because the use of cell-free synthetic scaffolds allows controlled presentation of signals [4,5]. In the previous chapters, we developed a promising aAPC that is based on polyisocyanopeptide (PIC)-antibody conjugates, called synthetic Dendritic Cells (sDCs). Their filamentous shape combined with their small size allow for straightforward characterization and should accommodate application *in vivo* [6–9]. Increased understanding of sDC force generation may be exploited for the development of force-responsive scaffolds that allow for additional control over T cell stimulation. Although sDCs can induce robust T cell activation, it is not clear how they generate forces at the T cell surface necessary for TCR triggering.

In nature, stimulation of T cells starts with binding of T cell receptors (TCRs) to peptides presented on mature antigen-presenting cells (APCs) in the context of MHC molecules. During this process, TCRs need to distinguish between foreign and self-derived antigens based on interactions with short peptides presented on MHC complexes. Remarkably, T cells are able to recognize foreign ligands in a sea of self-derived peptides that have only minimal differences in affinity for their TCR [10,11]. To achieve this high level of selectivity and sensitivity, several mechanisms for TCR triggering by pMHC have evolved. TCRs are clustered on the membrane of T cells and stimulation of TCRs leads to increased clustering, which allows for rapid release and rebinding of pMHCs [12,13]. Sensitivity of this process is enhanced through spatial segregation of clustered TCRs from phosphatases such as CD45 [14]. In addition, the close contacts formed between T-cells and antigen-presenting cells lead to application of 10-50 pN forces on TCRs. Force is essential for signal transduction in T cell activation and enhances the specificity of TCR-pMHC interactions [15–17].

Forces on TCRs are generated through the formation of close contacts and relative receptor movements between T cells and APCs. To establish these TCR-pMHC interactions in close contacts, a thick layer of glycocalyx and large membrane-bound proteins needs to be pushed away or compressed, leading to tension on the TCR-pMHC complexes [18–20]. Forces may also be generated when T cells and APC membranes are moving relative to each other. Furthermore, the cytoskeleton of T cells is essential for

signal transduction by TCRs [21]. When activation is initiated, clusters of TCRs are moved over the membrane by myosin-II and actin retrograde flow-dependent processes [22,23]. During movement of clusters, which can ultimately lead to immune synapse formation, binding of TCRs to immobilized ligands leads to generation of forces that are directly correlated to proximal signaling events [17]. Ultimately, these processes combined lead to tension between TCRs and pMHCs. A different type of force may be generated to initiate segregation of TCRs from other receptors, such as CD28.

Direct evidence that established T cells as force sensors was given by experiments where forces were directly applied to the TCR-CD3 complex. Micropipette manipulation of T cells immobilized through non-stimulatory anti-CD3 antibodies is able to induce robust Ca^{2+} responses [24]. Similarly, forces exerted on non-stimulatory anti-CD3-beads by optical tweezers can initiate signaling in T cells [25,26]. When the same forces are applied to other receptors, such as CD28, no effect on activation is observed [27,28]. Studies using biomolecular force probes, micropipettes with a probe bead attached, have further defined the TCR-intrinsic forces necessary for efficient signal transduction. Using these probes it was demonstrated that 10 pN forces applied to a single OT-1 TCR induced the highest Ca^{2+}-responses. Interestingly, bond lifetimes also peaked at 10 pN, indicating catch bond behavior of TCR-pMHC interactions [29]. Thus, exerting force on a TCR does not just lead to enhanced signaling, but may also prolong interaction (via catch bonds) instead of breaking it [17]. A role for catch bond formation is further backed up by structural analysis of the TCR complex, which indicates that bond lifetimes can be prolonged through a force-driven conformation change [30]. However, it is unclear whether catch bonds are important for every agonist pMHC-TCR pair [17,31].

To further probe the exact tensions applied to TCRs during activation, DNA-based tension sensors have been developed [32]. These DNAs contain a hairpin loop that dehybridizes at defined force thresholds, which leads to unquenching of a fluorophore. In this way, these sensors allow for highly sensitive detection of tension generated by specific TCRs. Using these tension sensors, it has been demonstrated that 19-pN forces are generated in a defined pattern before the onset of Ca^{2+}-signaling [32]. A similar approach that also allows for physical modulation of TCR forces makes use of DNA tension gauge tethers (TGTs). These tethers consist of DNA duplexes that rupture when a tension greater than a certain threshold is applied [33]. In particular, force thresholds can be set by changing the geometry in which TGTs are attached to a surface via one DNA strand and to a ligand via the complementary strand. This leads to double-stranded DNA that needs to be either unzipped to rupture, which requires low force, or sheared, which requires a higher force [33,34]. These TGTs, which act as force-responsive linkers, have demonstrated that TCR signaling is stronger when higher amounts of force can be applied on TCRs [32]. Therefore, incorporation of TGTs into sDCs may

lead to development of force-responsive aAPCs, which may allow for additional control over T cell activation.

Besides forces between TCRs and pMHCs, forces need to be generated during T cell activation to cluster and separate receptors in the membrane. Early during T cell activation, CD45 is excluded from TCR-CD28 microclusters due to its large size. CD28 is separated later on, when the clusters are moving into the cSMAC of the immune synapse. In chapter 4 it was demonstrated that triggering TCRs and CD28 with one and the same polymer greatly enhances T cell activation. However, it is unclear whether keeping these receptors in close proximity is still needed after cSMAC formation. Until now, forces needed for separation of these receptors have not been analyzed. The use of force-responsive nanosized sDCs that move along with TCR microclusters makes it possible to study and manipulate this process. Manipulation of receptor clustering may be used to precisely control T cell responses.

Here, PIC-antibody conjugates that are stably linked through double-stranded DNA (dsDNA) TGTs are developed. In the second part of this chapter these PIC-dsDNA-antibody conjugates are developed into force-sensitive sDCs using the DNA-based TGTs previously described in [32]. These TGTs are incorporated into this sDC design together with anti-CD28 or anti-CD45 antibodies as anchoring points, which may allow for examination of relative receptor movement and the forces involved. The force-responsive dsDNA-linked sDCs developed here can be used to study the role of mechanical force and membrane receptor movements in sDC-induced T cell activation. Through manipulation of force-induced receptor segregation, the force-sensitive sDCs may allow for additional control over T cell activation.

Results and discussion

Synthesis and analysis of PICs with dsDNA-linked antibodies. Before introduction of force-sensitive linkers, it was first established whether sDCs could be synthesized by using DNA hybridization as linker between PICs and antibodies. To develop these stable double-stranded DNA (dsDNA)-linked PIC-antibody conjugates, clickable dsDNAs were synthesized (**Figure 1a**). Complementary DNA strands functionalized with an amine at the 5' end or 3' end were functionalized using NHS esters, such that one strand contained a trans-cyclooctene (TCO) group at the 5' end and the other strand had a dibenzocyclooctyne (DBCO) moiety at the 3' end. Depending on the synthetic strategy, the functionalized DNA strands were either used as single strands or hybridized before application in biorthogonal click reactions with antibodies. Two different strategies were applied to synthesize sDCs using the clickable DNAs: the dsDNA and ssDNA Click strategies (**Figure 1b**). For both methods, anti-CD3 antibodies were first functionalized with tetrazine using NHS ester chemistry as described in

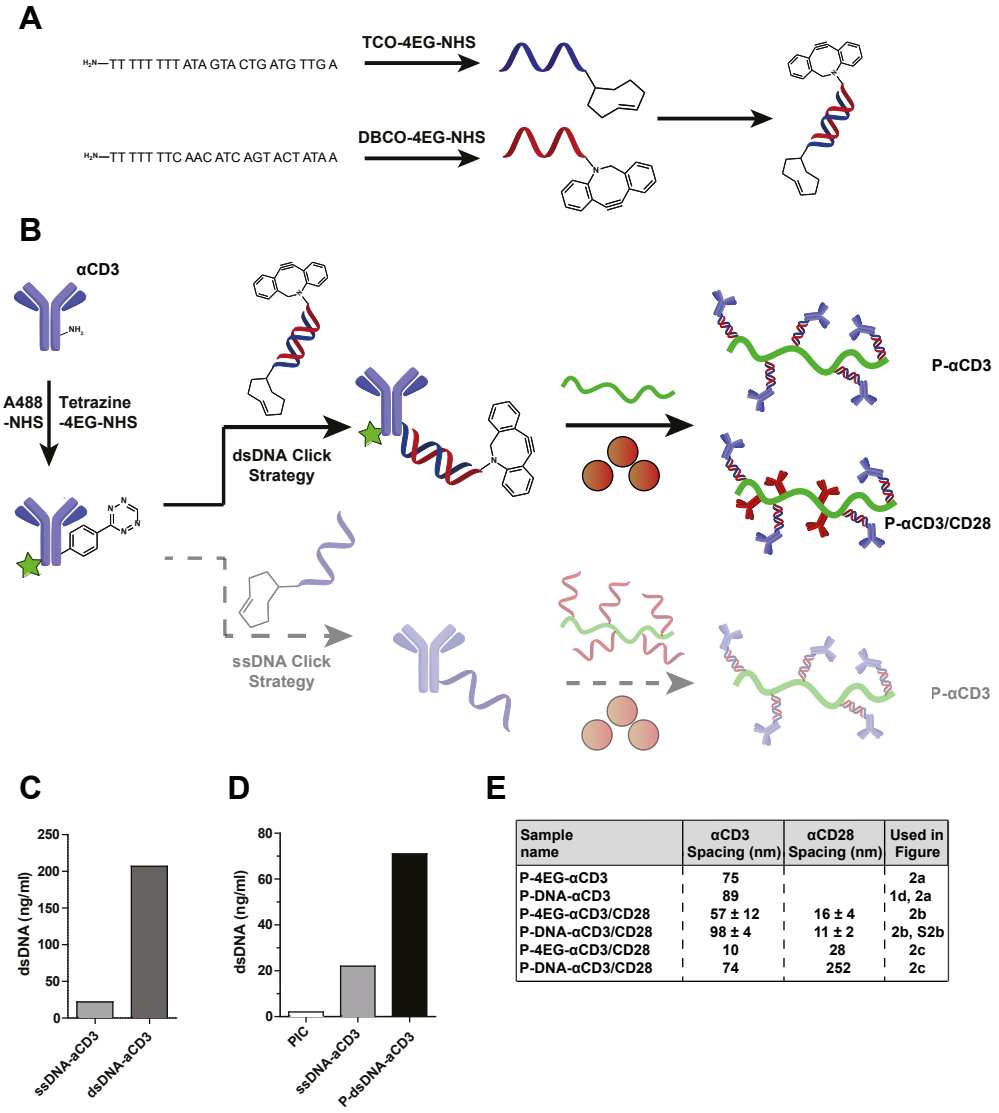

E

Sample name	αCD3 Spacing (nm)	αCD28 Spacing (nm)	Used in Figure
P-4EG-αCD3	75		2a
P-DNA-αCD3	89		1d, 2a
P-4EG-αCD3/CD28	57 ± 12	16 ± 4	2b
P-DNA-αCD3/CD28	98 ± 4	11 ± 2	2b, S2b
P-4EG-αCD3/CD28	10	28	2c
P-DNA-αCD3/CD28	74	252	2c

Figure 1 Synthesis and characterization of dsDNA-linked PIC-antibody conjugates. **(A)** DNA functionalization with DBCO and TCO. Two complementary DNA strands were functionalized with either TCO-4EG-NHS esters or DBCO-4EG-NHS esters. The resulting DNA strands were hybridized to form a TCO- and DBCO-functionalized duplex. **(B)** Synthetic strategies used for the development of dsDNA-linked PIC-antibody conjugates. Antibodies were either reacted with single stranded DNA (lower transparent route, ssDNA click strategy) or DBCO-containing double-stranded DNA (upper route, dsDNA click strategy). **(C)** Picogreen staining of ssDNA-αCD3 before (ssDNA-αCD3) and after (dsDNA-αCD3) formation of a DNA

duplex. **(D)** Picogreen staining of polymer, ssDNA-αCD3 and P-αCD3 showing presence of dsDNA in the synthesized sDC. Picogreen measurements were done relative to a dsDNA standard to show the amount of DNA hybridization. **(E)** Analysis of antibody densities conjugated onto sDCs.

chapter 4 for DBCO-NHS esters. In the dsDNA click strategy, tetrazine-functionalized αCD3 was reacted with TCO/DBCO-functionalized dsDNA via reverse-electron demand Diels Alder reactions to give antibodies functionalized with DBCO through dsDNA hybridization. Subsequently, this complex was reacted with azide- and biotin-functionalized PICs. To provide additional signals important for T cell activation, αCD28-containing sDCs were synthesized through addition of DBCO-functionalized anti-CD28 antibodies to the reaction mixture. The resulting PIC-dsDNA-αCD3 conjugates were purified over monovalent avidin beads as described in chapter 3 [7].

As alternative synthetic method, the ssDNA click strategy, was applied to assess the dsDNA-linkage of the newly synthesized sDCs. For this, tetrazine-αCD3 was reacted to single-stranded TCO-DNA to give antibodies functionalized with single-stranded DNA (ssDNA). By adding a complementary DNA strand to these antibodies, DNA hybridization was measured using the dsDNA-sensitive fluorophore picogreen (**Figure 1c**). Picogreen fluorescence was highly increased when dsDNA- αCD3 was compared to ssDNA, which demonstrated that stabile dsDNA-αCD3 conjugates were formed. Furthermore, ssDNA-αCD3 was also efficiently hybridized with complementary ssDNA-functionalized PICs (**Figure 1d**). For PICs and ssDNA- αCD3, low background levels of picogreen staining were observed, whereas PIC-dsDNA-αCD3 showed a strong signal. These measurements demonstrated that dsDNA hybridization can be used as linkage between PICs and antibodies. Because this second strategy leads to a final product that potentially contains non-hybridized ssDNA, the first method was used to develop sDCs for functional experiments.

Anti-CD3 concentrations of PIC-αCD3 conjugates were determined using BCA assays, and PIC concentrations were determined using circular dichroism (**Figure 1e**). Antibodies on P-DNA-αCD3 were spaced around 90 nm on average (~4-5 αCD3/PIC). As a control, covalently linked conjugates were synthesized as described in chapter 4. This sDC had a similar antibody spacing of ~80 nm. When both αCD3 and αCD28 were used in PIC-antibody conjugates, antibodies were fluorescently labeled to determine antibody concentrations. Also for these sDCs, two controls were synthesized with 4EG-linked αCD3, which contained one αCD3 every 60 nm or 10 nm and a αCD28 every 15 nm or 30 nm (~7 αCD3 and 26 αCD28, or ~40 αCD3 and 13 αCD28 per polymer respectively). The DNA-linked PIC-antibody conjugates contained one αCD3 every 100 or 75 nm and an αCD28 every 10 or 250 nm (~4 αCD3 and 40 αCD28 per polymer, or 40 αCD3 and 2 αCD28 per polymer). It is important to note that there are marked

differences in densities between the different DNA-linked PICs and between DNA-linked and 4EG-linked sDCs. As discussed in chapter 4, this is probably a result of small sodium azide contamination that renders DBCO unreactive towards polymer-bound azides. As a result, antibody conjugations to PICs could not be fully controlled and antibody densities were not consistent. In the future, this problem can be circumvented by extensive pre-treatment of the purification columns. Nonetheless, antibody densities on the synthesized conjugates are sufficiently high to allow for T cell activation.

sDCs with agonistic antibodies stably linked through dsDNA efficiently stimulate T cells. In chapter 2 and 4, it was shown that streptavidin and PEG-linkers can be used to conjugate PICs and αCD3 to form efficient sDCs. To ensure that PIC-dsDNA-antibody conjugates may be used as force-responsive stimulant in the future, it is essential to demonstrate that DNA hybridization also can yield potent sDCs. To establish this, PBLs were stimulated with the synthesized PIC-dsDNA-αCD3 conjugates. Similar to cells stimulated with PEG-linked αCD3 (P-4EG-αCD3), IFNγ secretion by PBLs stimulated with the novel dsDNA-linked sDCs was increased compared to unbound antibodies (**Figure 2a**). Because stimulation with unbound dsDNA-αCD3 induced comparable IFNγ secretion to non-functionalized αCD3, presence of the short double-stranded DNA strand is not responsible for the observed increase in IFNγ secretion (**Figure S1a**). In chapter 4 it was demonstrated that αCD3 functionalization with DBCO-PEG-NHS esters at pH 7.4 did not result in functional sDCs. Interestingly, when dsDNA linkers are used, αCD3 functionalization at low pH results in sDCs that can induce markedly increased levels of IFNγ secretion (**Figure S1a**). Possibly, the rigidity of dsDNA linkers diminishes steric blocking of αCD3 activity by the PICs compared to the highly flexible PEG linkers.

Also for αCD28-containing sDCs it was shown that PICs with dsDNA-linked αCD3 induce strong activation of T cells. For this, IFNγ secretion was measured from purified T cells stimulated with PICs containing dsDNA-linked αCD3 and 4EG-linked αCD28 (**Figure 2b**). As a positive control, P-4EG-αCD3/CD28 was also used. Because the αCD3 density of P-DNA-αCD3/CD28 is lower than that of P-4EG-αCD3/CD28, their stimulatory capacity cannot be directly compared. Nonetheless, stimulation with dsDNA-linked PICs resulted in high levels of IFNγ secretion. To further demonstrate the strong stimulatory capacity of DNA-linked P-αCD3/CD28, celltrace violet-labeled purified T cells were stimulated with dsDNA-αCD3 + αCD28, P-dsDNA-αCD3/CD28 and P-4EG-αCD3/CD28 for 3 days (**Figure 2c**). P-dsDNA-αCD3/CD28 induced a strong proliferative T cell response, similar to that of P-4EG-αCD3/CD28. Stimulation with P-dsDNA-αCD3/CD28 conjugates with low αCD3 densities did not induce activation of T cells (**Figure S1b**), which is in agreement with results presented in chapter 2 and

chapter 4 for streptavidin-linked and PEG-linked PIC-antibody conjugates. Taken together, these results demonstrate that DNA hybridization can be used as stable linkage in PIC-antibody conjugates to obtain sDCs that efficiently stimulate T cells, which is essential for the development of force-sensitive sDCs.

Development of force-sensitive sDCs through different TGT DNA geometries. After having demonstrated that dsDNA-linked sDCs induce strong T cell activation, we made use of the dsDNA-linkage to develop force-sensitive PIC-antibody conjugates. To introduce force sensitivity, dsDNA linkers that are ruptured under defined pN-range forces can be used. In pioneering work by the group of Liu et al., two identical dsDNA sequences were used to immobilize ligands in two different ways, as such that rupturing these TGT DNAs would require different amounts of force [32]. By immobilizing ligands at the same end of the dsDNA where it was immobilized, dsDNA could be ruptured using a low 12 pN force by 'unzipping' of the helix. Alternatively, ligands were immobilized on the opposing end of the dsDNA, which required a 56 pN force to 'shear' the two DNA strands. Using this calibrated system, it was demonstrated that T cells exert forces on pMHCs or αCD3 that can rupture dsDNA in the unzipping geometry, but not when the shearing geometry was used. The forces generated by T cells were demonstrated to be essential for downstream signaling. Because the thermal stability, rupture force and compatibility with T cell stimulation of these DNA sequences and geometries are already optimized by Liu et al., we applied the same sequences in PIC-antibody conjugates to develop force-sensitive sDCs and measure rupture forces in the nanosized sDC with CD28 or CD45 as anchoring points. Early (CD45) and later (CD28) after TCR triggering, these receptors move away from the TCR-CD3 complex. Using these molecules as anchoring points in sDCs may allow us to study this process in more detail. In this way, forces necessary for these receptor movements may be determined and receptor clustering can be manipulated to further control T cell activation.

To synthesize force-sensitive sDCs with both an unzipping or a shearing DNA rupture geometry (**Figure 3a**), the same DNA sequences were used. For both geometries, the same 5'-DBCO modified DNA strand was used, whereas the complementary strand was functionalized with TCO at either the 5' or 3' end (**Figure 3b**). Hybridization of these strands gave a DNA duplex with DBCO and TCO at either the same end or opposing ends to obtain dsDNA in an unzipping or shearing geometry, respectively. A Cy5 dye and a quencher were used on the opposing strands to measure rupturing of DNA. Alternatively, Cy3 was used instead of a quencher to obtain dsDNA linkers where FRET could be used as additional method to measure duplex stability (**Figure S2a**).

The unzipping and shearing dsDNAs were used to synthesize a variety of P-αCD3/CD28 conjugates with comparable 4EG-linked αCD28 spacing of ~120-150 nm (~3 αCD28 per polymer; **Figure 3c**). Since CD28 could be used as an anchoring point to rupture

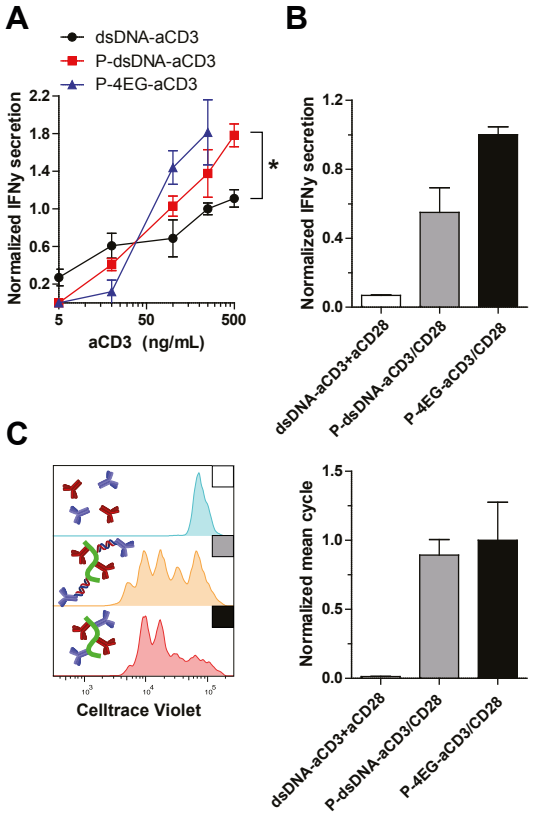

Figure 2 T cell activation after stimulation with dsDNA-linked sDCs. **(A)** Normalized IFNγ concentrations in supernatant 18 h after stimulation of PBLs with unbound dsDNA-αCD3, P-dsDNA-αCD3 and P-4EG-αCD3. IFNγ concentrations from stimulation of PBLs from two donors were normalized to the concentration induced by 250 ng/mL dsDNA-αCD3 stimulation and the mean concentrations ± SEM were depicted. **(B)** Normalized IFNγ concentrations in supernatant 18 h and (C) proliferation 3 days after stimulation of purified T cells with 500 ng/ml dsDNA-αCD3 + αCD28, P-dsDNA-αCD3/CD28 and P-4EG-αCD3/CD28. Two different batches of conjugates were used for IFNγ secretion and proliferation experiments (Figure 1e). Measurement values from stimulation of PBLs from two donors were normalized to the IFNγ concentration or mean value induced by P-4EG-CD3/CD28 stimulation and the mean values ± SEM were depicted.

αCD3-bound dsDNA, sDCs with low αCD3 and high αCD28 densities may lead to an increased unquenched signal because a larger part of DNA strands can be separated as a result of stronger multivalent sDC binding to CD28. To be able to test this hypothesis for the unzipping geometry, conjugates were generated with two different αCD3

densities, containing either one αCD3 every 175 nm (~2-3 αCD3 per polymer) or one αCD3 every 500 nm (<1 αCD3 per polymer). P-αCD3/CD28 with DNA in shearing geometry was made with a similar αCD3 density (1 αCD3 every 440 nm, <1 per polymer). Furthermore, FRET-based P-αCD3/CD28 conjugates with low αCD3 densities were made with Cy3 instead of a quencher. These PICs also contained less than 1 αCD3 per polymer. During TCR stimulation, CD45 is separated from CD3 further than CD28. Therefore, CD45 could be an interesting anchoring point to induce αCD3-linked dsDNA rupture. Two different conjugates containing 4EG-linked αCD45 were synthesized, containing either αCD3 attached in the unzipping geometry or shearing geometry. As was demonstrated for P-4EG-αCD3/CD45, αCD45 does not block activation of T cells, and may even lead to increased IFNγ secretion compared to P-αCD3 conjugates (**Figure S2d**).

To test whether the DNA-linked Cy5 fluorophore is sufficiently quenched after formation of DNA duplexes, Cy5 fluorescence of unreacted dsDNA, αCD3-bound dsDNA and P-dsDNA-antibody conjugates was measured (**Figure 3d**). In each case, only low background levels of Cy5 fluorescence were observed, which was increased more than 100-fold by releasing DNA hybridization using sodium hydroxide. A very low background signal was observed for the shearing geometry DNA, which was slightly higher than the low background observed for the unzipping geometry. This is probably caused by the different position of the fluorophore on the DNA strand, which results in a slight difference in distance between Cy5 and BHQ in the corresponding dsDNA. The efficient hybridization of the two dsDNAs was further confirmed using FRET of Cy3-containing DNAs (**Figure S2b**) Additionally, the stability of the DNA duplexes was analyzed by incubation of dsDNA-bound antibodies and dsDNA-containing conjugates at 37 °C (**Figure 3d**). No significant decrease in DNA hybridization was observed over two days, demonstrating that the produced sDCs are thermally stabile and suitable for use in biological assays.

sDCs containing dsDNA linkers show increased Cy5 fluorescence after incubation with T cells. Although it is known that unzipping, but not shearing dsDNA linker geometries can be ruptured by T cells when immobilized on a surface, they have not yet been tested in nanosized aAPC designs. Therefore, we measured Cy5 fluorescence of purified T cells after overnight incubation with the synthesized P-dsDNA-αCD3/CD28 using flow cytometry. Although this dsDNA rupture is expected to occur much earlier during T cell activation, this late time point was chosen as a first test to allow for the Cy5-signal to be amplified by binding of multiple sDCs to each T cell. T cells were first incubated with P-αCD3/CD28 conjugates with different αCD3 densities, linked through dsDNA in unzipping geometry, to determine the effect of αCD3 density on dsDNA rupture (**Figure 4a**). Cy5 fluorescence from the two sDCs was compared with the background levels of the corresponding unconjugated dsDNA-αCD3s.

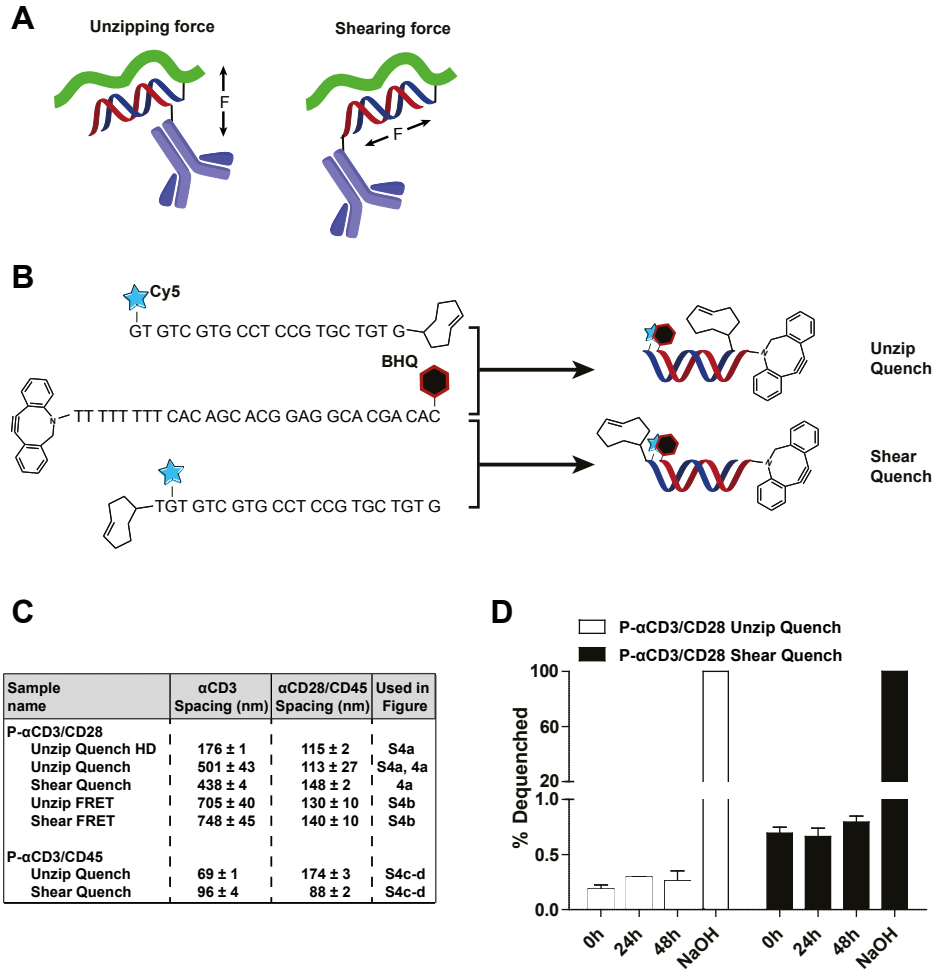

Sample name	αCD3 Spacing (nm)	αCD28/CD45 Spacing (nm)	Used in Figure
P-αCD3/CD28			
Unzip Quench HD	176 ± 1	115 ± 2	S4a
Unzip Quench	501 ± 43	113 ± 27	S4a, 4a
Shear Quench	438 ± 4	148 ± 2	4a
Unzip FRET	705 ± 40	130 ± 10	S4b
Shear FRET	748 ± 45	140 ± 10	S4b
P-αCD3/CD45			
Unzip Quench	69 ± 1	174 ± 3	S4c-d
Shear Quench	96 ± 4	88 ± 2	S4c-d

Figure 3 Synthesis and characterization of unzipping and shearing TGT-dsDNA-containing sDCs. **(A)** The different dsDNA geometries are ruptured by either unzipping or shearing, which requires a different direction of applied forces. **(B)** Sequences and structure of clickable dsDNA linkers that can be ruptured by unzipping or shearing. DNA duplex stability can be followed due to presence of a Cy5 fluorophore and Black Hole Quencher (BHQ) on both strands. **(C)** Analysis of densities of TGT-linked antibodies conjugated onto sDCs. **(D)** Stability and quenching efficiency of TGT-linked sDCs. Background Cy5 signal was measured after 0 h (before), 24 h and 48 h of incubation of PIC-dsDNA-antibody conjugates at 37 °C. After measurement, dsDNA strands were separated by addition of NaOH, allowing for measurement of 100% dequenched cy5 signals.

P-αCD3/CD28 high density (HD) incubation with T cells did not lead to an increase in fluorescence, whereas fluorescence was slightly increased for the conjugates with lower density. This result indicates that αCD3 multivalency reduces DNA duplex rupture. Because no signal was observed for conjugates with higher densities, conjugates with low αCD3 densities were used to further study the differences between the unzipping and shearing dsDNA linker geometries. Because of the low antibody densities, T cell activation was not yet assessed at this point.

Next, Cy5 fluorescence of T cells incubated with P-αCD3/CD28 with unzipping and shearing linker geometries were compared (**Figure 4b**). As earlier, P-αCD3/CD28 unzipping showed a slight increase in Cy5 fluorescence. Remarkably, baseline-corrected P-αCD3/CD28 dsDNA shearing showed a three-fold increase in Cy5 signal compared to unzipped dsDNA. No fluorescent signal was observed when these conjugates were incubated with T cells at 4 °C (**Figure S3a**) and comparable amounts of αCD3 were bound to T cells for both unzipping and shearing conjugates, as could be determined from the αCD3-bound A488 fluorescence (**Figure S3b**). This indicates that the observed signal is a result of duplex rupture. However, it needs to be further investigated whether this is a result of Cy5 quenching, since a similar trend was observed when measuring the Cy5 signal in FRET-based DNA duplexes. For these conjugates, Cy5 signals also increased after incubation with T cells, indicating that the increased Cy5 signals may not be the result of unquenching (**Figure S3c**). Also in this case αCD3 binding was similar for both of the conjugates (**Figure S3d**). At this point, the Cy5-Cy3 FRET signal was not exploited. Measurement of FRET signals could be done to confirm whether shearing is more efficient than dsDNA unzipping in our PIC-based sDCs. Similarly, αCD45-containing PICs also showed increased unquenched Cy5 signals in the shearing mode (**Figure S3e**), although it should be noted that antibody densities for these two conjugates are not comparable, which could significantly influence the results of T cell stimulation.

If significant, these results seem to contradict the work of Liu et al., which demonstrated that T cells can rupture DNA strands when dsDNA is used to immobilize ligands to a surface in unzipping, but not in shearing geometry [32]. As surface bound tension probes, the unzipping geometry was calibrated with a 12 pN rupture force, while the shearing geometry requires 56 pN to rupture. Since identical DNA sequences were used for the linkers developed in this chapter, it is unexpected that there is an increased T-cell induced rupture of the shearing geometry dsDNA used in our sDCs. Liu et al. did not include a dye in their design. In the designs presented here, the location of the Cy5 fluorophore slightly differs between the two geometries. It is possible that the Cy5 dye at the end of the unzipping sequence could slightly stabilize the DNA duplex, although this should only lead to a minimal increase in stability [35]. More importantly, the dsDNAs are not immobilized on a rigid surface, but on a small and semi-flexible scaffold. When immobilized on a surface, immobilized ligands

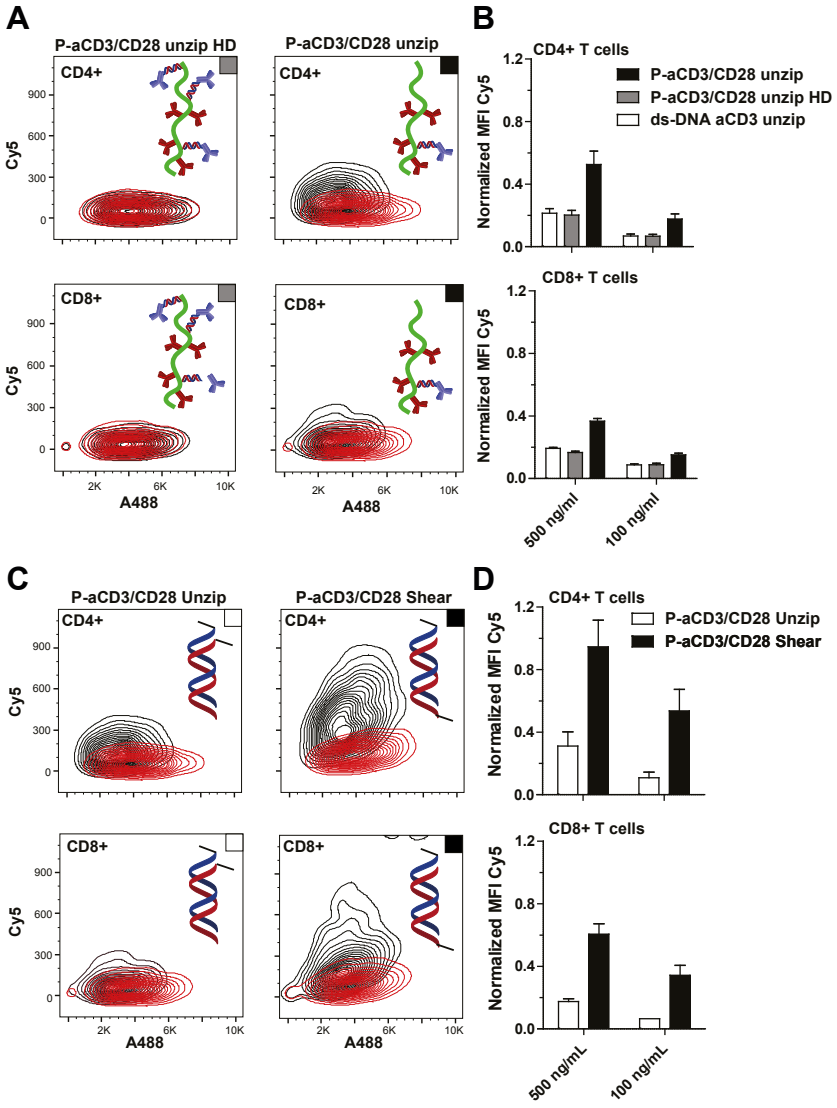

Figure 4 DNA duplex rupture of TGT-linkers after incubation with T cells. **(A)** Representative histograms depicting Cy5 and A488 signal of dsDNA-αCD3 control (red lines) and P-αCD3/CD28 conjugates (black lines) with low (left) and high (HD, right) αCD3 density bound to CD4+ (top) and CD8+ (bottom) T cells after 18 h of incubation. **(B)** Normalized mean Cy5 fluorescence intensity (MFI) from TGTs bound to CD4+ (top) and CD8+ (bottom) of duplicate measurements performed on two donors. **(C)** Representative histograms depicting Cy5 and A488 signal of dsDNA-αCD3 control (red lines) and P-αCD3/CD28 conjugates (black lines) with unzipping (left) and shearing (right) dsDNA geometries bound to CD4+ (top) and CD8+

(bottom) T cells after 18 h of incubation. **(D)** Normalized and background (dsDNA-Ab)-corrected mean Cy5 fluorescence intensity (MFI) from TGTs bound to CD4+ (top) and CD8+ (bottom) of duplicate measurements performed on two donors. Fluoresence was normalized to fluorescence measured on CD8+ T cells after incubation of P-αCD3/CD28 shear.

cannot traffic to the center of the immune synapse together with moving TCR microclusters. The size of PIC-based sDCs matches that of the moving microclusters, which could result in the movement of sDCs together with these clusters. This leads to lower forces that are applied to the dsDNAs at this point, and these forces are more likely to be the result of receptor movement, rather than TCR pulling. Forces that are exerted onto the TGT linkers could be further reduced by the semi-flexible scaffold, which may partly absorb some of the applied force. The effects of scaffold flexibility and aAPC size could be further explored by repeating these experiments using surface-immobilized PICs or PICs with different rigidities. Nonetheless, the size and semi-flexibility of the scaffold might explain why only low levels of unzipping are observed, but do not provide an explanation for the relatively high shearing of dsDNA linkers.

Although CD3 and CD28 are clustered together in TCR microclusters, they separate in the immune synapse [36]. Since Cy5 signals are mostly observed when conjugates have low αCD3 density combined with higher αCD28 densities, CD28 might act as an anchor point for dsDNA rupture at low αCD3 densities. The dependence of dsDNA duplex rupture on αCD3 and anchor point densities needs to be further explored to pinpoint whether this is indeed a result of relative receptor movements. Possibly, the different direction of these forces, compared to movement of CD3-receptors alone, could provide an explanation for the enhanced shearing of dsDNA linkers. The results presented here are a first step towards force-responsive sDCs that could manipulate this process, but more experiments are needed to confirm this.

Conclusions and outlook

DNA hybridization was successfully exploited to stably link antibodies to PICs, which allowed for the development of functional and potentially force-sensitive sDCs. DNA-linked PIC-antibody conjugates were synthesized by using a combination of biorthogonal click reactions. Complementary DNA strands clicked onto PICs and αCD3 can form stabile DNA duplexes and these PIC-dsDNA-αCD3 conjugates were demonstrated to induce efficient T cell activation, which was further increased when αCD28 was co-conjugated to these PICs.

To develop sDCs that exhibit force sensitivity, PIC-antibody conjugates containing αCD3 linked through two previously reported TGT dsDNA geometries were synthesized. To follow strand rupture of the TGT linkers, conjugates were made containing either a fluorophore and quencher, or a FRET pair. The synthesized sDCs were highly stabile and showed only low background fluorescence. Compared to the unzipping geometry DNA linker, the shearing dsDNA geometry unexpectedly showed more strand separation during stimulation of T cells. Further experimentation is needed to explain the observed differences in dsDNA rupture. Nonetheless, the sDC design presented here may be used in the future to measure and manipulate forces associated with receptor clustering on the T cell surface.

In the initial experiments with TGT-sDCs, Cy5 signals were measured after overnight incubation with T cells. To determine which events are responsible for rupturing the dsDNA linkers, signals from these sDCs could be determined in the first minutes or hours after stimulation. Confocal imaging of the interactions could also contribute to a better understanding of the location of the forces that are being applied on the sDCs. Our PIC-antibody conjugates contained covalently linked αCD28 or αCD45 that could be used as anchoring points on the T cell surfaces. This may potentiate measurement of forces required for the relative movements of receptors in the T cell membrane. To fully assess the types of forces applied on sDCs by T cells, and whether these forces are responsible for strand rupture of dsDNA linkers, the exact timing and localization of dsDNA separation should be studied in more detail. Furthermore, the effect of anchoring points on force application could be studied further by using anchor points that do not separate from CD3 or study TGT dsDNA linkers in sDCs without anchor points. This could lead to a better understanding of the relative movement of membrane receptors. In addition, the dependence of T cells on the linker rupture force can be studied. After optimizing the force threshold of dsDNA linkers, future sDCs may be developed that use force application as a trigger. This trigger may then be exploited to either visualize ongoing immune responses or release stimulatory molecules, allowing for additional levels of control over T cell activation.

Experimental section

Materials. Zeba™ Spin Desalting Columns (40K MWCO), Celltrace Violet Cell proliferation kit, AlexaFluor350-NHS ester (AF350), Quant-iT Picogreen dsDNA assay kit and mono-avidin beads were purchased from ThermoFisher. Anti-CD3 (Clone OKT3) and Anti-CD28 (Clone 9.3) was from BioXCell. Anti-CD45 (Clone HI30) and anti-CD8-PECy7 were obtained from Biolegend. Human Pan T cell isolation kit, naïve CD8+ T cell isolation kit and propidium iodide solution were obtained from Miltenyi. Anti-CD4-APC-H7 was from BD Biosciences. eFluor 780 live-dead cell marker was from

eBioscience. DBCO-4EG-NHS, TCO-4EG-NHS and Tetrazine-5EG-NHS were purchased from Jena Bioscience. Atto488-NHS ester (A488) was obtained from Atto-TEC GmbH. 30 kDa Amicon Ultra-15 ultrafiltration membranes were from Merck Millipore. X-vivo medium was purchased from Lonza. G25 spin columns were from GE. Amine-functionalized DNAs were purchased from Integrated DNA technologies Inc.

DNA functionalization. The amine DNAs were functionalized with DBCO or TCO using a previously described protocol [37]. Briefly, 50 µl of 100 mM borate buffer (pH 8.5) was added to 50 µl of a 1mM stock of amine-DNA. To this 2.5 equivalents of the TCO or DBCO-NHS ester was added (12.5 µl of a 10 mM stock in DMSO). After mixing for 2 h at room temperature the functionalized DNAs were purified over G25 spin columns and the concentration of DNA was determined by Nanodrop.

Antibody functionalization with clickable moieties. Before functionalization, buffer exchange to 50 mM Borate Buffer (pH 8.5) was done using Amicon ultrafiltration membranes (30 kD MWCO). After this, NHS esters were added to a ~1 mg/mL concentration of antibodies in borate buffer and the reaction mixture was incubated for 2 h at 4 °C on a rotator. For functionalization of αCD3, 5 equivalents of tetrazine-5EG-NHS ester was used. When αCD3 antibodies needed a fluorescent label, 2.5 equivalents of ATTO488 (A488)-NHS ester was added at the same time. For αCD28 and αCD45, 5 equivalents of DBCO-4EG-NHS and 2.5 equivalents of AlexaFluor350 (AF350)-NHS ester were added. Antibodies were purified over Zebaspin size exclusion colums (40 kD MWCO) according to the manufacturer's protocol. Degree of DBCO and fluorophore labeling, and concentration were determined using UV/Vis spectrophotometry with a Nanodrop 2000c spectrophotometer. After correcting for the overlap of the spectra of the individual molecules, the concentrations of the individual molecules were calculated using their molar extinction coefficients (210000 M^{-1} cm^{-1} for antibodies, 12000 M^{-1} cm^{-1} for DBCO, 90000 M^{-1} cm^{-1} for ATTO488 and 19000 M^{-1} cm^{-1} for AF350).

Antibody-DNA conjugation. Tetrazine-functionalized αCD3 antibodies were reacted to either single stranded or double-stranded TCO-functionalized DNA. For this, 1 equivalent of ssDNA or 1.5 equivalents of dsDNA was added to ~1 mg/mL αCD3 in PBS. DNA labeling of antibodies was analyzed using UV/Vis spectrophotometry with a Nanodrop 2000c spectrophotometer, using the absorption of the antibody-conjugated fluorophore to determine antibody concentrations.

Synthesis of synthetic DCs. Synthetic DCs were synthesized using two different strategies. For the first strategy, azide- and biotin-containing PICs were reacted with 1 eq (with respect to PIC-bound azides) of a DBCO-functionalized DNA strand. After this,

0.6 equivalents of αCD3 functionalized with the complementary ssDNA strand was added to the ssDNA-PICs. The mixture was incubated overnight at 4 °C on a rotator. In the second strategy, 0.4-0.6 equivalents of dsDNA-containing αCD3 was reacted to azide-and biotin-containing PICs. When required, 0.2 equivalents of DBCO-αCD28 or DBCO-αCD45 were also added at this step. The reaction mixtures were incubated overnight at 4 °C on a rotator. The synthesized PIC-antibody conjugates were purified over monovalent avidin beads as described in chapter 3. The conjugates were incubated with mono-avidin beads for 2 h at 4 °C. The polymer-bound beads were washed extensively using PBS+0.1% Tween-20 (2x) and PBS (4x). The conjugates were eluted from the beads by incubation with PBS+2mM biotin (biotin elution buffer) on a rotator for 2 h at 4 °C.

Analysis of PIC-antibody conjugates. Concentrations of P-αCD3 conjugates were determined with a micro BCA assay, using the corresponding unbound DBCO- or DNA-functionalized antibodies as a standard. For P-αCD3/CD28 and P-αCD3/CD45 conjugates, that contain fluorescently labeled antibodies, concentrations were determined using a Tecan Spark 10M fluorescence microplate reader. Again, the corresponding unbound functionalized antibodies were used as a standard for each measurement. The PIC-antibody conjugate samples (100 µl) were pipetted into black, flat-bottom non-binding 96-well microplates (Greiner Bio-One). A488 and A350 were excited at 490 nm and 360 nm, and detected at 535 nm and 442 nm, respectively. To determine antibody densities, PIC concentrations were determined using circular dichroism (CD) (JASCO J-810). 100 µl of each PIC-antibody conjugate was pipetted into a 1 cm cuvette and the CD spectrum was measured using biotin elution buffer as a blank. The peak value at 272 nm was used to determine the polymer concentration, using an extinction coefficient of 547.8 mdeg ml cm-1, which was determined with a standard curve of different polymer concentrations as described in chapter 3.

Analysis of DNA hybridization. To analyze whether antibodies were bound to the PICs via DNA hybridization, a picogreen assay was performed using the protocol supplied by the manufacturer. The dsDNA linker without antibody and polymer was used as standard to determine the apparent dsDNA concentrations. Both duplex stability as well as the efficiency of the quencher and FRET of the antibody dsDNA-PICs, antibody dsDNA and dsDNA was analyzed by measuring the fluorescence over time. The samples (100 µl) were pipetted in a black flat bottom 96-well plate and measured on the indicated times. The Cy5-ssDNAs used for unzipping and shearing geometries were used as the standard. To measure the effect of dequenching the samples and standards were treated with 25 µl of a 1 M NaOH solution, which leads to dsDNA dehybridization.

Human T cell assays. Ficoll density centrifugation was used to isolate Peripheral blood mononuclear cells (PBMCs) from buffy coats obtained from healthy donors using. After this, peripheral blood lymphocytes (PBLs) were obtained by adhering PBMCs to culture plates for 1 h, after which non-adherent cells were taken. For stimulation with P-αCD3, PBLs were used directly for T cell activation assays. In the other assays, T cells were first purified with the Miltenyi Pan T cell isolation kit. When T cell proliferation needed to be measured, cells were labeled with Celltrace Violet. For this, Celltrace Violet was added to the cells at a final concentration of 2.5 μM in PBS and cells were incubated for 15 minutes in the dark at RT. The reaction was quenched with 3 reaction volumes of cold Fetal Bovine Serum (FBS), and washed 3 times. For stimulation of PBLs and isolated T cells, 100.000 and 50.000 cells per condition were used, respectively. sDCs were incubated at indicated concentrations of αCD3 in round-bottom 96-well cell culture plates with final volumes of 100 μl per well. Cell culture was performed at 37 °C using X-Vivo medium containing 4% human serum.

Analysis of stimulated T cells. Supernatants from stimulated T cells were collected after 18 h of stimulation to determine their level of IFNγ secretion using ELISA (human IFNγ ELISA, Thermo Scientific). For detection, absorbance was measured at 450 nm on a Bio-rad iMark plate reader. IFNγ concentrations were determined using 4-paramer fits in Microplate Manager 6 software. To measure fluorescent signals from the bound PIC-antibody conjugates, cells were collected after 24 h, stained for CD4 and CD8, and measured using FACS (BD FACSVerse). To determine T cell proliferation, cells were stimulated for 3 days, stained for CD4 and CD8, and Celltrace Violet dilution was determined using FACS (BD FACSVerse). The mean number of cycles (i.e. the average number of cell divisions) was determined as ^{2}log of the ratio of the mean fluorescence intensity (MFI) of non-divided cells (as determined using FlowJo) divided by the MFI of all cells.

References

1 Mellman, I. *et al.* (2011) Cancer immunotherapy comes of age. *Nature* 480, 480–489
2 Spurrell, E.L. and Lockley, M. (2014) Adaptive immunity in cancer immunology and therapeutics. *Ecancermedicalscience* 8, 441
3 Oelke, M. *et al.* (2005) Artificial antigen-presenting cells: artificial solutions for real diseases. *Trends Mol. Med.* 11, 412–420
4 Eggermont, L.J. *et al.* (2014) Towards efficient cancer immunotherapy: advances in developing artificial antigen-presenting cells. *Trends Biotechnol.* 32, 456–465
5 Oelke, M. and Schneck, J.P. (2010) Overview of a HLA-Ig based "Lego-like system" for T cell monitoring, modulation and expansion. *Immunol. Res.* 47, 248–256
6 Hammink, R. *et al.* (2017) Controlling T-Cell Activation with Synthetic Dendritic Cells Using the Multivalency Effect. *ACS Omega* 2, 937–945
7 Hammink, R. *et al.* (2017) Affinity-Based Purification of Polyisocyanopeptide Bioconjugates. *Bioconjug. Chem.* 28, 2560–2568
8 Mandal, S. *et al.* (2015) Polymer-Based Synthetic Dendritic Cells for Tailoring Robust and Multifunctional T Cell Responses. *ACS Chem. Biol.* 10, 485–492
9 Mandal, S. *et al.* (2013) Therapeutic nanoworms: towards novel synthetic dendritic cells for immunotherapy. *Chem. Sci.* 4, 4168
10 Chakraborty, A.K. and Weiss, A. (2014) Insights into the initiation of TCR signaling. *Nat. Immunol.* 15, 798–807
11 Malissen, B. and Bongrand, P. (2015) Early T Cell Activation: Integrating Biochemical, Structural, and Biophysical Cues. *Annu. Rev. Immunol.* 33, 539–561
12 Dushek, O. and van der Merwe, P.A. (2014) An induced rebinding model of antigen discrimination. *Trends Immunol.* 35, 153–158
13 Pageon, S. V *et al.* (2016) Functional role of T-cell receptor nanoclusters in signal initiation and antigen discrimination. *Proc. Natl. Acad. Sci.* 113, E5454–E5463
14 Chang, V.T. *et al.* (2016) Initiation of T cell signaling by CD45 segregation at "close contacts." *Nat. Immunol.* 17, 574–582
15 Ma, Z. *et al.* (2012) Mechanical Force in T Cell Receptor Signal Initiation. *Front. Immunol.* 3, 217
16 Kim, S.T. *et al.* (2012) TCR Mechanobiology: Torques and Tunable Structures Linked to Early T Cell Signaling. *Front. Immunol.* 3, 76
17 Depoil, D. and Dustin, M.L. (2014) Force and affinity in ligand discrimination by the TCR. *Trends Immunol.* 35, 597–603
18 Dustin, M.L. and Depoil, D. (2011) New insights into the T cell synapse from single molecule techniques. *Nat. Rev. Immunol.* 11, 672–684
19 Ma, Z. *et al.* (2014) TCR Triggering by pMHC Ligands Tethered on Surfaces via Poly(Ethylene Glycol) Depends on Polymer Length. *PLoS One* 9, e112292
20 Allard, J.F. *et al.* (2012) Mechanical Modulation of Receptor-Ligand Interactions at Cell-Cell Interfaces. *Biophys. J.* 102, 1265–1273
21 Comrie, W.A. and Burkhardt, J.K. (2016) Action and Traction: Cytoskeletal Control of Receptor Triggering at the Immunological Synapse. *Front. Immunol.* 7, 68
22 Hu, K.H. and Butte, M.J. (2016) T cell activation requires force generation. *J. Cell Biol.* 213, 535–542
23 Hui, K.L. *et al.* (2015) Cytoskeletal forces during signaling activation in Jurkat T-cells. *Mol. Biol. Cell* 26, 685–695
24 Li, Y.C. *et al.* (2010) Cutting Edge: Mechanical Forces Acting on T Cells Immobilized via the TCR Complex Can Trigger TCR Signaling. *J. Immunol.* 184, 5959–5963
25 Feng, Y. *et al.* (2017) Mechanosensing drives acuity of αβ T-cell recognition. *Proc. Natl. Acad. Sci.* 114, E8204–E8213
26 Kim, S.T. *et al.* (2009) The αβ T Cell Receptor Is an Anisotropic Mechanosensor. *J. Biol. Chem.* 284, 31028–31037

27 Judokusumo, E. *et al.* (2012) Mechanosensing in T Lymphocyte Activation. *Biophys. J.* 102, L5–L7

28 Bashour, K.T. *et al.* (2014) CD28 and CD3 have complementary roles in T-cell traction forces. *Proc. Natl. Acad. Sci.* 111, 2241–2246

29 Liu, B. *et al.* (2014) Accumulation of Dynamic Catch Bonds between TCR and Agonist Peptide-MHC Triggers T Cell Signaling. *Cell* 157, 357–368

30 Das, D.K. *et al.* (2015) Force-dependent transition in the T-cell receptor β-subunit allosterically regulates peptide discrimination and pMHC bond lifetime. *Proc. Natl. Acad. Sci.* 112, 1517–1522

31 Robert, P. *et al.* (2012) Kinetics and Mechanics of Two-Dimensional Interactions between T Cell Receptors and Different Activating Ligands. *Biophys. J.* 102, 248–257

32 Liu, Y. *et al.* (2016) DNA-based nanoparticle tension sensors reveal that T-cell receptors transmit defined pN forces to their antigens for enhanced fidelity. *Proc. Natl. Acad. Sci.* 113, 5610–5615

33 Wang, X. and Ha, T. (2013) Defining Single Molecular Forces Required to Activate Integrin and Notch Signaling. *Science (80-.).* 340, 991–994

34 Mosayebi, M. *et al.* (2015) Force-Induced Rupture of a DNA Duplex: From Fundamentals to Force Sensors. *ACS Nano* 9, 11993–12003

35 Moreira, B.G. *et al.* (2015) Cy3 and Cy5 dyes attached to oligonucleotide terminus stabilize DNA duplexes: Predictive thermodynamic model. *Biophys. Chem.* 198, 36–44

36 Yokosuka, T. *et al.* (2008) Spatiotemporal Regulation of T Cell Costimulation by TCR-CD28 Microclusters and Protein Kinase C θ Translocation. *Immunity* 29, 589–601

37 Deshpande, S.R. *et al.* (2016) DNA-Responsive Polyisocyanopeptide Hydrogels with Stress-Stiffening Capacity. *Adv. Funct. Mater.* 26, 9075–9082

Supplementary figures

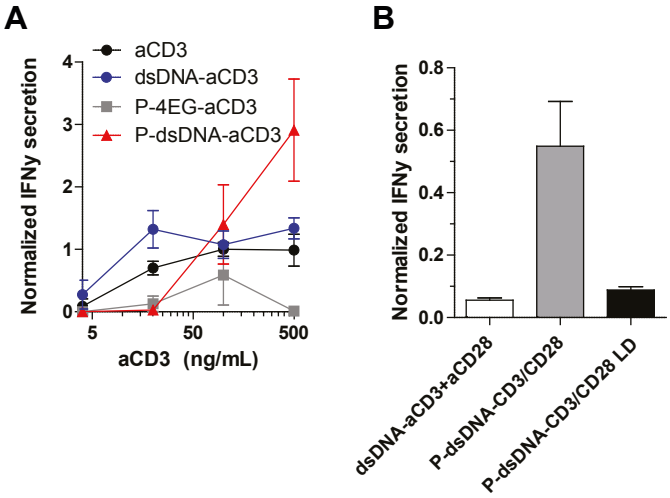

Figure S1 IFNγ secretion after stimulation with dsDNA-linked sDCs. **(A)** Normalized IFNγ concentrations in supernatant 18 h after stimulation of PBLs with αCD3, dsDNA-αCD3, P-4EG-αCD3 (αCD3 spacing of 24 nm) and P-dsDNA-αCD3 (αCD3 spacing of 17 nm). In each condition, αCD3 that was functionalized at pH 7.4 was used. IFNγ concentrations from stimulation of PBLs from two donors were normalized to the concentration induced by 100 ng/mL αCD3 stimulation and the mean concentrations ± SEM were depicted. **(B)** Normalized IFNγ concentrations in supernatant 18 h after stimulation of purified T cells with 500 ng/mL dsDNA-αCD3 + αCD28, P-dsDNA-αCD3/CD28 and P-dsDNA-αCD3/CD28 LD (αCD3 spacing of 445 ± 1 nm, αCD28 spacing of 69 ± 3 nm), which contains a lower density of αCD3. IFNγ concentrations from stimulation of T cells from two donors were normalized to the concentration induced P-4EG-αCD3/CD28 stimulation and the mean concentrations ± SEM were depicted.

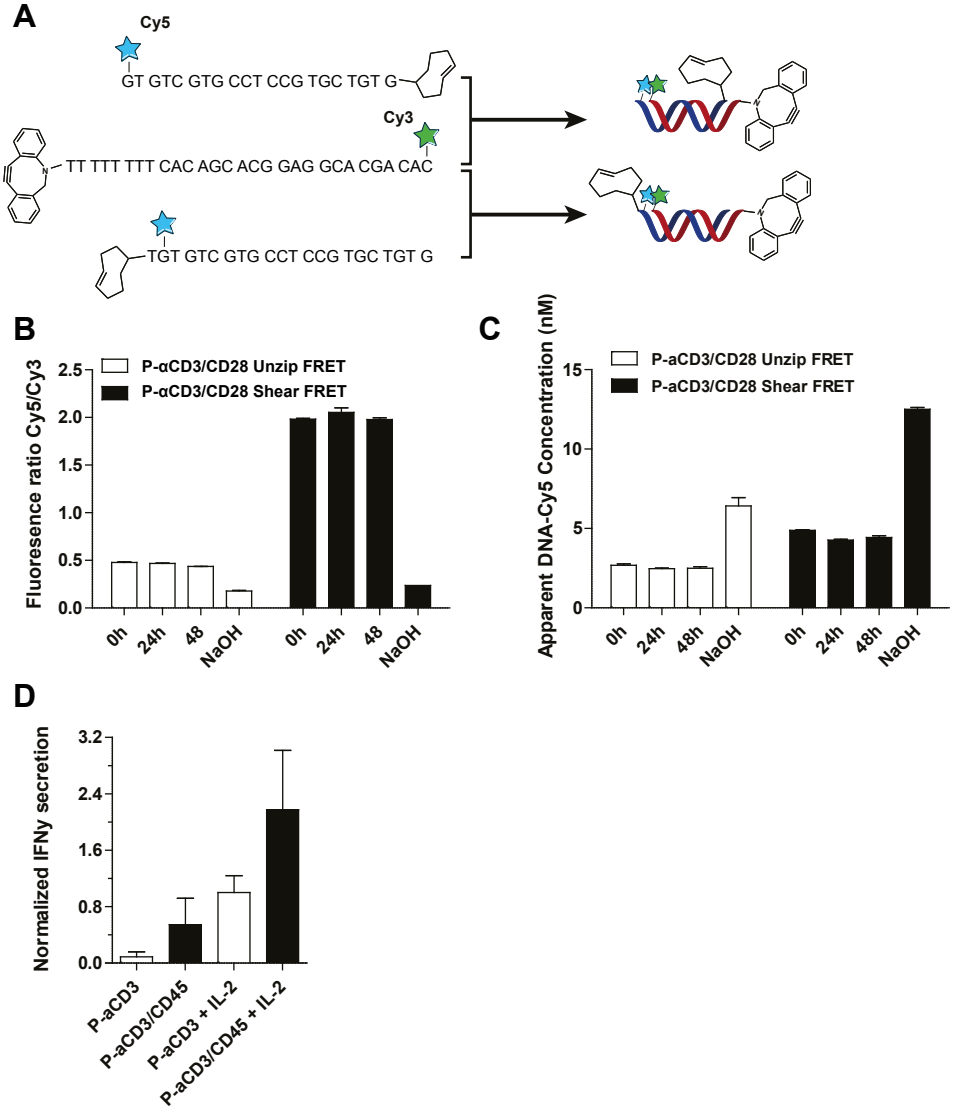
A
Cy5
GT GTC GTG CCT CCG TGC TGT G
Cy3
TT TTT TTT CAC AGC ACG GAG GCA CGA CAC
TGT GTC GTG CCT CCG TGC TGT G
B
Fluorescence ratio Cy5/Cy3
P-αCD3/CD28 Unzip FRET
P-αCD3/CD28 Shear FRET
0h
24h
48
NaOH
C
Apparent DNA-Cy5 Concentration (nM)
P-aCD3/CD28 Unzip FRET
P-aCD3/CD28 Shear FRET
48h
D
Normalized IFNy secretion
P-aCD3
P-aCD3/CD45
P-aCD3 + IL-2
P-aCD3/CD45 + IL-2

Figure S2 Synthesis and characterization of unzipping and shearing TGT-dsDNA-containing sDCs that can be analyzed with FRET. **(A)** Sequences and structure of clickable dsDNA linkers that can be ruptured by unzipping or shearing. DNA duplex stability can be followed due to presence of a Cy5 fluorophore and Cy3 fluorophore on the opposing strands. **(B)** Stability and FRET efficiency of TGT-linked sDCs. FRET ratio was determined as Cy5 signal divided by the Cy3 signal after 0 h (before), 24 h and 48 h of incubation of PIC-dsDNA-antibody conjugates at 37 °C. After measurement, dsDNA strands were separated by addition of NaOH, allowing for measurement of background signals in absence of FRET. **(C)** Stability and quenching efficiency of TGT-linked sDCs. Background Cy5 signal was measured after 0 h (before), 24 h and 48 h of incubation of PIC-dsDNA-antibody conjugates at 37 °C. After measurement, dsDNA strands were separated by addition of NaOH, allowing for measurement of cy5 signal after strand separation. **(D)**. IFNγ secretion induced from purified T cells after stimulation with P-4EG-αCD3 (αCD3 spacing 153 ± 1 nm) and P-4EG-αCD3/CD45 (αCD3 spacing 222 ± 7 nm and αCD45 spacing 232 ± 6 nm) with and without addition of IL-2.

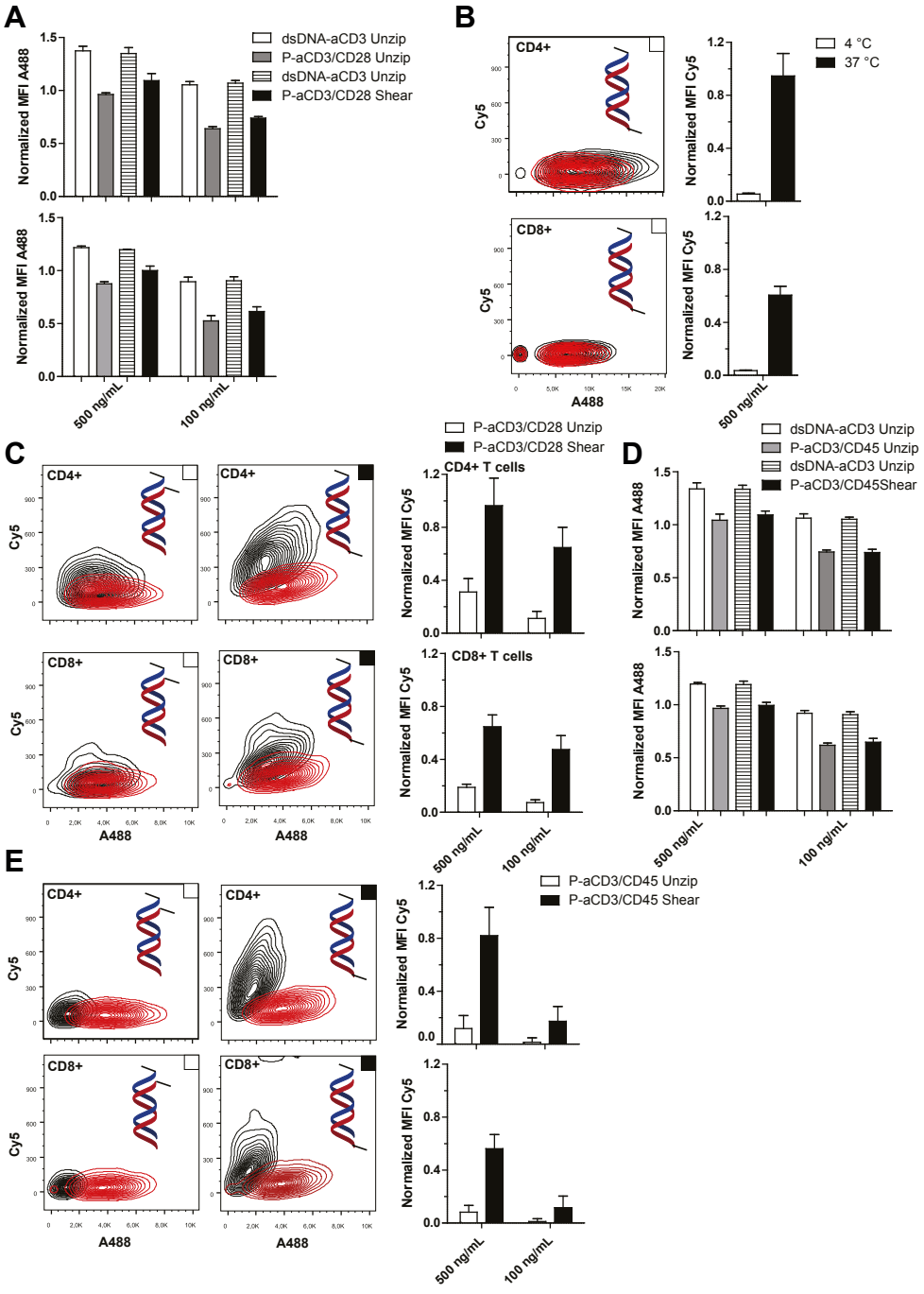
A
dsDNA-aCD3 Unzip
P-aCD3/CD28 Unzip
dsDNA-aCD3 Unzip
P-aCD3/CD28 Shear
Normalized MFI A488
500 ng/mL
100 ng/mL
B
CD4+
CD8+
Cy5
A488
4 °C
37 °C
Normalized MFI Cy5
500 ng/mL
C
P-aCD3/CD28 Unzip
P-aCD3/CD28 Shear
CD4+ T cells
CD8+ T cells
D
dsDNA-aCD3 Unzip
P-aCD3/CD45 Unzip
dsDNA-aCD3 Unzip
P-aCD3/CD45Shear
E
P-aCD3/CD45 Unzip
P-aCD3/CD45 Shear

Figure S3 Binding and duplex rupture of sDCs with TGT linkers after incubation with T cells. **(A)** Normalized mean fluorescence intensities (MFI) of A488 signal from αCD3 bound to T cells. MFIs of duplicate treatment of T cells from two donors were normalized to the signal of P-αCD3/CD28 shear bound to CD8+ T cells and the mean values ± SEM were depicted. **(B)** Histograms showing A488 and Cy5 signal of P-αCD3/CD28 shear (black lines) and dsDNA-αCD3 (red lines) bound to CD4+ and CD8+ T cells after incubation at 4°C. Bar graphs depict normalized mean Cy5 fluorescence intensity (MFI) of P-αCD3/CD28 shear after overnight incubation with CD4+ (top) and CD8+ (bottom) T cells at 4 °C and 37 °C. Duplicate measurements were performed on two donors. **(C)** Representative histograms depicting Cy5 and A488 signal of dsDNA-αCD3 control (red lines) and P-αCD3/CD28 FRET conjugates (black lines) with unzipping (left) and shearing (right) dsDNA geometries bound to CD4+ (top) and CD8+ (bottom) T cells after 18 h of incubation. Bar graphs show normalized mean Cy5 fluorescence intensity (MFI) from TGTs bound to CD4+ (top) and CD8+ (bottom) of duplicate measurements performed on two donors. **(D)** Normalized mean fluorescence intensities (MFI) of A488 signal from αCD3 bound to T cells after 18 h incubation of αCD45-containing conjugates. MFIs of duplicate treatment of T cells from two donors were normalized to the signal of P-αCD3/CD45 shear bound to CD8+ T cells and the mean values ± SEM were depicted. **(E)** Representative histograms depicting Cy5 and A488 signal of dsDNA-αCD3 control (red lines) and P-αCD3/CD45 conjugates (black lines) with unzipping (left) and shearing (right) dsDNA geometries bound to CD4+ (top) and CD8+ (bottom) T cells after 18 h of incubation. Bar graphs show normalized mean Cy5 fluorescence intensity (MFI) from TGTs bound to CD4+ (top) and CD8+ (bottom) of duplicate measurements performed on two donors.

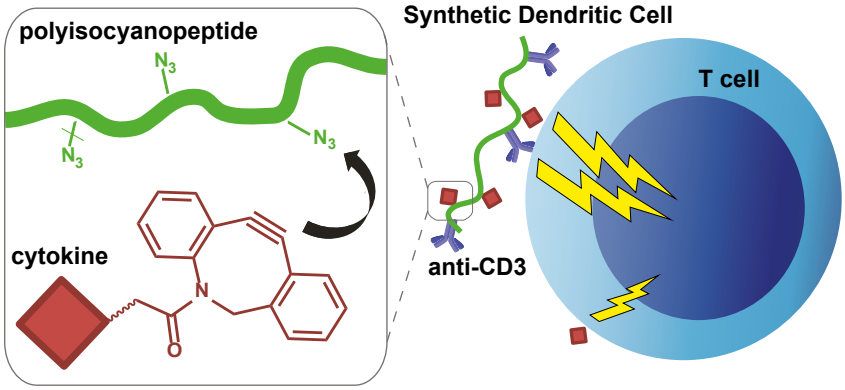
polyisocyanopeptide
N_3
N_3
N_3
cytokine
N
O
Synthetic Dendritic Cell
T cell
anti-CD3

6

Cytokine-functionalized Synthetic Dendritic Cells for T Cell Targeted Immunotherapies

Loek J. Eggermont*, Roel Hammink*, Kerstin G. Blank, Alan E. Rowan, Jurjen Tel, Carl G. Figdor

Advanced Therapeutics, manuscript accepted for publication

*contributed equally

Abstract

Widespread application of cytokine-based therapies is hampered by severe toxic side effects, resulting from off-target (immune) cell stimulation. This emphasizes the need for more precise targeting of cytokines to immune cells. While cytokines are generally active as soluble proteins, we now demonstrate that synthetic mimics of immune cells based on polyiscocyanopeptides (PICs), called synthetic Dendritic Cells (sDCs) can efficiently present immobilized cytokines to T cells, when targeted by anti-CD3 antibodies. Anti-CD3/IL-2-functionalized PICs induce strong T cell activation and proliferation, when compared to PICs functionalized with IL-2 alone. In contrast to the semi-flexible PICs, immobilization of IL-2 on a rigid micro-sized scaffold results in significant loss of IL-2 activity, signifying the importance of molecular flexibility on the PIC polymers to maintain function. Similarly, anti-CD3/IFNα-functionalized PICs support long-term proliferation of T cells. IFNα-containing sDCs additionally promote the development of cytotoxic effector functions of T cells with limited upregulation of the inhibitory immune checkpoint PD-1. This high cytolytic activity and low PD-1 expression are essential to maintain effective anti-cancer activity. Together, these results demonstrate that PICs form unique nano-sized scaffolds that efficiently present immobilized cytokines to T cells, thus creating a powerful tool to improve cytokine-based immunotherapies without concomitant off target toxicity.

KEYWORDS: Immunotherapy, artificial antigen-presenting cell, synthetic dendritic cell, cytokines, polyisocyanopeptides

Introduction

Cytokines are small soluble proteins that mediate immune responses and communication between immune cells. For almost three decades, high-dose cytokine treatment regimens have been applied as cancer immune therapies to treat different malignancies.[1–4] High doses of interleukin-2 (IL-2) have induced cancer regression in a small portion of patients, and even led to complete remission of the disease in rare cases.[2,5,6] Besides being used as a mono-therapy, bolus IL-2 injections are also used to support the survival of adoptively transferred T cells. However, tumor reduction requires cytokine doses that induce severe IL-2-related toxicities. The most common side effects include capillary leak syndrome, which is caused by the direct binding of IL-2 to CD25-positive endothelial cells combined with high concentrations of secondary cytokines, and multi-organ failure, originating from the infiltration of lymphocytes and direct IL-2 stimulation of endothelial cells.[7,8] Similarly, interferon-α (IFNα) has been used in clinical trials with varying success. It has mostly been applied in hematological malignancies and as a post-surgery treatment option for solid tumors.[9] For this cytokine, patients often experience severe flu-like symptoms, induced by the broad immunological activity of IFNα.[10] These dose-dependent side effects pose one of the biggest challenges for the widespread and safe clinical application of cytokines. Due to the need for close monitoring, this frequently results in the hospitalization of patients. Regardless of their clinical efficacy, many clinicians are still hesitant to systemically apply cytokine-based immunotherapies because of their severe side effects.[8]

In many cases, these cytokine-based therapies directly stimulate T cells, resulting in increased proliferation, survival and functionality of tumor-reactive T cells.[2,11] When applying IL-2 and IFNα, these cytokines can also trigger many other (immune) cell types.[12,13] Reducing off-target stimulation is, therefore, of key importance to diminish the observed dose-related side effects so that higher therapeutic efficacy of cytokine-based therapies can be achieved. For IL-2 and IFNα, these strategies have focused on improving their circulation times, reducing non-specific binding, localizing delivery and direct targeting to infected or tumor cells.[14–24] Although these approaches have indeed shown reduced side effects compared to high-dose injections of native cytokines, off-target activation of immune cells can still remain. Clearly, specific targeting of IL-2 and IFNα to T cells is expected to greatly improve the efficacy of cytokine based therapies.

One promising strategy to warrant such specific targeting of cytokines to T cells is the use of artificial antigen-presenting cells (aAPCs). These synthetic mimics of immune cells allow for the highly controlled activation of T cells, based on the multivalent presentation of antigens (signal 1) and co-stimulatory molecules (signal 2) as a cell-free system.[25] Several aAPC designs have incorporated the presentation or

release of IL-2 as a third signal to stimulate T cell activation. Importantly, aAPC-based T cell stimulation leads to an increase in the surface expression of IL-2 receptors.[12] Using IL-2-functionalized poly(lactic-co-glycolic acid) (PLGA) microparticles, it was demonstrated that the slow release of IL-2 in close proximity to T cells significantly increases proliferation of T cells, compared to exogenous non-encapsulated cytokine administration.[26,27] However, the size of these micro-aAPCs limits their potential for *in vivo* application. Alternatively, IL-2-presenting nano-aAPCs with a size of 500 nm have been generated from endoplasmic reticulum membranes of a bioengineered B cell line.[28] Considering the proven potential of cytokine targeting, nano-sized and synthetic aAPCs are needed for the specific delivery of cytokines to T cells.

Recently, we have developed a new aAPC scaffold based on polyisocyanopeptides (PICs): synthetic Dendritic Cells (sDCs).[29,30] These long (100-1000 nm), helical and semi-flexible polymers appeared ideal candidates for multivalent presentation of signals to T cells.[31,32] Previous studies demonstrated that combining multiple different molecules on these polymers markedly enhanced the activation and proliferation of T cells.[33] Importantly, these nanoworm-shaped PICs are cell-free and nano-sized scaffolds that can be applied as efficient sDCs. Because of their semi-flexible nature,[32] which allows for dynamic rearrangement of receptor-bound ligands, which is essential during T cell activation, we hypothesized that they may be ideal for the presentation of cytokines.

Here, we introduce cytokine-functionalized PIC-based sDCs as a new platform for T cell targeted cytokine-based immunotherapies. These sDCs co-present two T cell activating signals: T cell stimulating anti-CD3 antibodies in combination with either IL-2 or IFNα. Comparing co-presentation of anti-CD3 and cytokines on the same scaffold with the presentation of these signals on separate scaffolds, we show how different delivery methods impact T cell responses. We show that the presented and CD3-targeted cytokines efficiently exert their function on human T cells, and that targeting to CD3 is essential for enhanced cytokine activity. Overall, we demonstrate that PIC-based sDCs are the first cell-free, nano-sized aAPC design that allows for the efficient presentation of functional IL-2. Moreover, for the first time, IFNα is incorporated into an aAPC design and is shown to be functional, enhancing cytotoxic T cell functions.

Results

Synthesis and Characterization of IL-2-functionalized sDCs. To create PIC-based sDCs, an azide-functionalized PIC-polymer was synthesized first (Figure S1a). Following previously described protocols, an azide-terminated monomer was co-polymerized with a non-functional methoxy-terminated monomer in a ratio chosen such that the polymer statistically yielded an azide group every 3.5 nm.[31–33] The obtained polymers had a length of ~400 nm, as measured by atomic force microscopy (AFM) (Figure S1b and c). To facilitate purification of the PIC-protein conjugates with a recently introduced affinity-based method, 50 % of the azide groups were converted to biotin.[34] The remaining azide handles were utilized to couple anti-CD3 (αCD3) and IL-2. For this purpose, αCD3 and IL-2 were functionalized with dibenzocyclooctyne (DBCO)-PEG_4-NHS esters and NHS esters of Atto488 (A488) or AlexaFluor647 (AF647), respectively. (Figure S2a). Subsequently, the PIC-protein conjugates were synthesized using strain-promoted azide alkyne cycloaddition (SPAAC) of the fluorescent and DBCO-labeled proteins to the biotin-functionalized azido-PIC polymers (Figure 1a). The fluorescent dyes coupled to both antibody and IL-2, as well as the circular dichroism signal of the PIC polymers (a consequence of the helical polymer backbone), allowed for the straightforward quantification and characterization of the purified sDCs, including their degree of functionalization with αCD3 and IL-2. Figure 1b summarizes the main characteristics of the PIC-protein conjugates used in this study. On average, all synthesized conjugates contain one αCD3 antibody every 140-200 nm (~3 antibodies per polymer). While similar amounts of αCD3 are present, the IL-2 densities vary, depending on the amount of DBCO-IL-2 added to the reaction mixture. In total, sDCs with three different IL-2 densities were synthesized: P-αCD3/IL2low, P-αCD3/IL2med and P-αCD3/IL2high. These sDCs contain one molecule of IL-2 within every 190, 130 and 40 nm, respectively. Thus, on average, P-αCD3/IL-2low is functionalized with ~2 molecules of IL-2, whereas P-αCD3/IL-2med contains ~4 and P-αCD3/IL-2high carries ~10 IL-2 molecules. In addition, two polymers containing only IL-2 were synthesized: P-IL-2low and P-IL-2high. P-IL-2low carries one IL-2 within every 400 nm (on average ~1 IL-2 per polymer) and P-IL-2high contains one IL-2 every 40 nm (on average ~9 IL-2 per polymer). Furthermore, sDCs were synthesized that contained only αCD3 in a density similar to that of P-αCD3/IL-2 sDCs: P-αCD3. As demonstrated previously,[34] biotin-functionalized PIC-protein conjugates can be efficiently purified over monovalent avidin beads, which was verified for the PIC-IL-2 conjugates using SDS-PAGE (Figure 1c). For the PIC-IL-2 conjugates tested, no protein band is visible in the gel. Due to their large size, PIC-protein conjugates cannot enter the gel so that the absence of IL-2 demonstrates the high purity of the sDC samples.

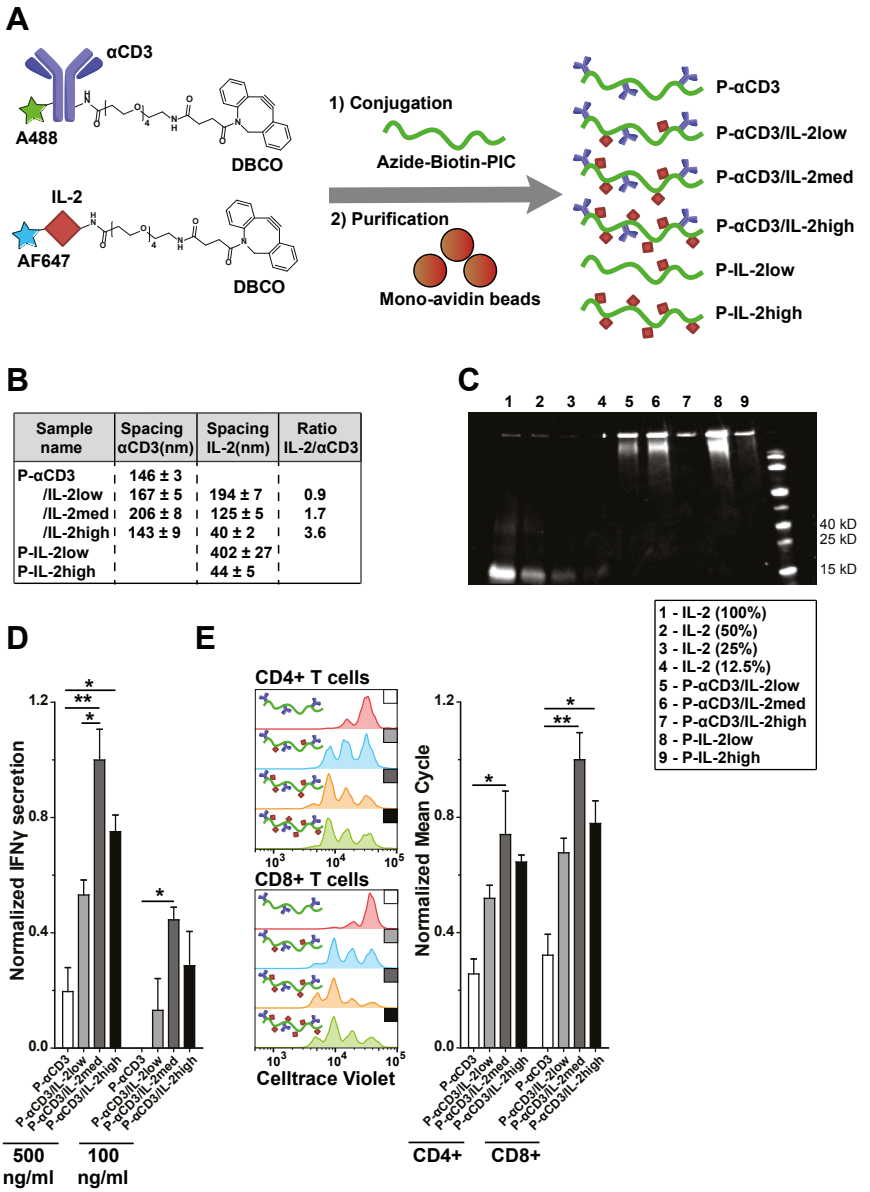

Sample name	Spacing αCD3(nm)	Spacing IL-2(nm)	Ratio IL-2/αCD3
P-αCD3	146 ± 3		
/IL-2low	167 ± 5	194 ± 7	0.9
/IL-2med	206 ± 8	125 ± 5	1.7
/IL-2high	143 ± 9	40 ± 2	3.6
P-IL-2low		402 ± 27	
P-IL-2high		44 ± 5	

Figure 1 Synthesis, characterization and functionality of filamentous, semi-flexible IL-2-presenting sDCs. **(A)** DBCO- and dye-functionalized IL-2 and αCD3 antibodies were covalently coupled to biotin- and azide-functionalized polyisocyanopeptides (PICs) via strain-promoted azide alkyne cycloaddition. The resulting PIC-protein conjugates were purified over magnetic mono-avidin beads. Schematic structures of P-αCD3, P-αCD3/IL-2low, P-αCD3/IL-2med,

P-αCD3/IL-2high, P-IL-2low and P-IL-2high are depicted on the right. **(B)** Analysis of PIC-protein conjugates. To calculate the average spacing between proteins, the protein concentration was determined using the fluorescence intensity of the labeled proteins and the PIC concentration was determined from the circular dichroism (CD) signal at 272 nm. The standard error of the mean (SEM) is depicted next to the mean values of duplicate measurements. **(C)** SDS-PAGE of purified P-IL-2 conjugates (lanes 5-9). Lanes 1-4 were loaded with unbound IL-2 as a standard. The IL-2 concentrations of P-IL-2 conjugates correspond to 100% IL-2 (lane 1), except for lane 5 (loading of 63%, due to a lower concentration of the purified polymer conjugate). **(D)** IFNγ secretion into the supernatant after stimulation of T cells for 16 h with αCD3-functionalized sDCs containing different amounts of IL-2. The cells were stimulated using 500 ng/ml αCD3 or 100 ng/ml αCD3. **(E)** Proliferation of T cells after 72 h of stimulation with αCD3-functionalized sDCs containing different amounts of IL-2. Proliferation was determined using flow cytometry analysis, measuring the dilution of Celltrace Violet (x-axis of histograms). The histograms show one representative experiment of duplicate stimulation of T cells from three healthy donors for CD4+ T cells (upper panel) and CD8+ T cells (lower panel). The mean number of cycles was calculated for each experiment. After T cell stimulation, the values were normalized, using the stimulation with 500 ng/ml of P-αCD3/IL-2med (CD8+ T cells) as the reference. The normalized values of duplicate stimulations of three donors were pooled to obtain mean and SEM values as depicted in the bar graphs. $^{*}p < 0.05$, $^{**}p < 0.01$, $^{***}p < 0.001$.

PIC-bound IL-2 induces efficient T cell activation. In natural immune responses, IL-2 is mostly active as a soluble cytokine, whereas immobilization of this cytokine onto a more rigid aAPC surface impedes activity.[27] To analyze the binding and stimulatory capacity of IL-2 when immobilized on PIC-based sDCs, the newly synthesized P-αCD3/IL-2 polymers were tested with human T cells. T cells were isolated from peripheral blood of healthy donors, reacted with the dye CellTrace Violet for tracking cell proliferation and stimulated with P-αCD3/IL-2 polymers functionalized with varying IL-2 densities. For all IL-2 densities, IFNγ secretion by T cells was increased at least two-fold after 16 h, compared to the control polymer, functionalized with αCD3 only (P-αCD3). The optimal αCD3/IL-2-ratio was found on P-αCD3/IL-2med, which increased IFNγ secretion 5-fold (Figure 1d). In addition, incubation with P-αCD3/IL-2 lead to activation-induced expression of the IL-2 receptor (CD25). Expression was significantly increased and followed a similar dependence on IL-2 density (Figure S3c). Furthermore, T cell proliferation was increased after three subsequent days of incubation with P-αCD3/IL-2 (Figure 1e and S3d), also demonstrating that IL-2 is active when bound to PICs. As demonstrated using A488-labeled-αCD3 (Figure S3a) and AF647-labeled IL-2 (Figure S3b), the amount of αCD3 bound to T cells was not significantly affected when comparing the different sDCs, while the amount of bound IL-2 showed the expected increase when using sDCs with higher IL-2 densities. Together, these measurements

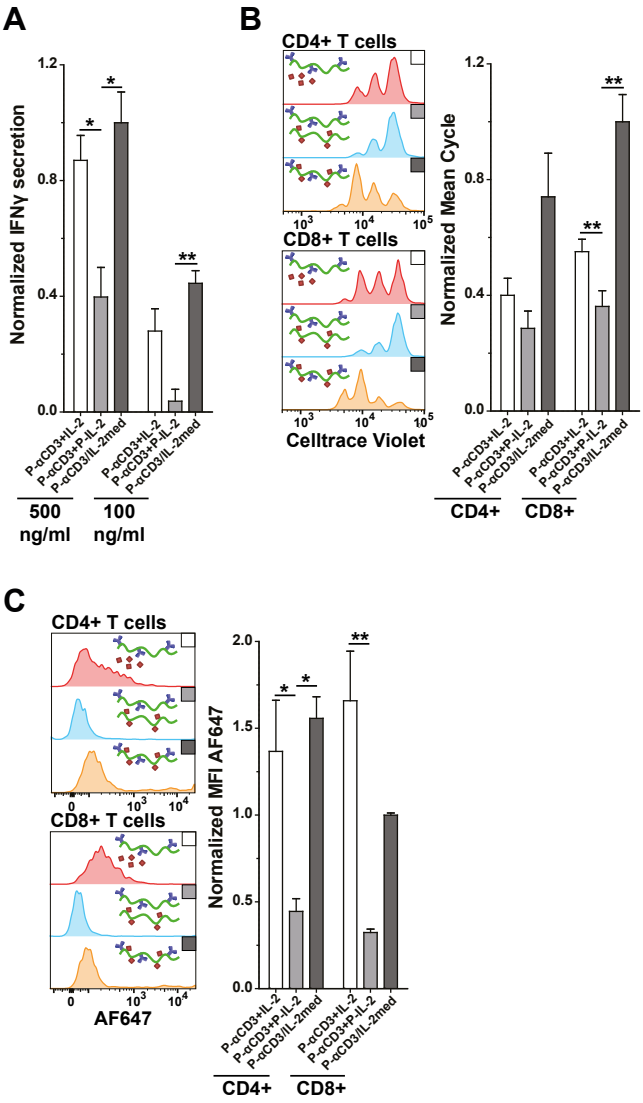

Figure 2 The role of sDC scaffolds in T cell stimulation by cytokines. **(A)** IFNγ secretion into the supernatant after stimulating T cells with P-αCD3 mixed with unbound IL-2 or P-IL-2, or P-αCD3/IL-2med for 16 h. In each stimulation, the same amount of IL-2 was used. The cells were stimulated using 500 ng/ml or 100 ng/ml αCD3. **(B)** Proliferation of T cells after 72 h of stimulation with 500 ng/ml P-αCD3 mixed with unbound IL-2 or P-IL-2, or P-αCD3/IL-2med. Proliferation was determined by flow cytometry analysis, measuring the dilution of Celltrace Violet (x-axis of histograms). **(C)** Amount of IL-2 bound to T cells after 16 h of incubation with 500 ng/ml P-αCD3 mixed with unbound IL-2 or P-IL-2, or P-αCD3/IL-2med.

Bound IL-2 was determined by flow cytometry analysis of AF647 signals (x-axis of histograms). For both proliferation and binding analysis, the histograms show one representative experiment of duplicate stimulation of T cells from three healthy donors for CD4+ T cells (upper panel) and CD8+ T cells (lower panel). After T cell stimulation, the values were normalized, using the stimulation with 500 ng/ml of P-αCD3/IL-2med (CD8+ T cells) as the reference. The normalized values of duplicate stimulations of three donors were pooled to obtain mean and SEM values, as depicted in the bar graphs. *$p < 0.05$, **$p < 0.01$, ***$p < 0.001$.

indicate that IL-2 is active when coupled to PICs and that the binding of P-αCD3/IL-2 to T cells is predominantly αCD3-dependent. P-αCD3/IL-2med contained the most potent ratio of αCD3 and IL-2 and was, therefore, selected for further studies.

CD3-targeting of PIC-IL-2 conjugates significantly increases cytokine activity. Having established that IL-2-functionalized PICs induce strong T cell responses, we analyzed the exact role of the polymer scaffold in IL-2 presentation**.** Purified human T cells were stimulated with P-αCD3/IL-2med and, alternatively, with the corresponding concentrations (as determined through AF647 fluorescence) of P-IL-2 or unbound IL-2 in the presence of P-αCD3. Although IFNγ secretion induced by P-IL-2 + P-αCD3 was two-fold lower compared to the same concentration of unbound IL-2 + P-αCD3, targeting P-IL-2 to CD3 by co-conjugation of αCD3 on one and the same PIC (P-αCD3/IL-2med) restored IFNγ levels to those that can be achieved with unbound IL-2 + P-αCD3 (Figure 2a). A comparable trend was observed for the secretion of TNFα (Figure S4a). Along the same way, when compared to unbound IL-2 + P-αCD3, the induction of CD25 expression (Figure S4e) and T cell proliferation (Figure 2b and S4d) was significantly reduced for P-IL-2 + P-αCD3-stimulated CD8+ T cells, but was again increased to higher levels for P-αCD3/IL-2med. This increase points towards a synergistic effect when co-delivering αCD3 and IL-2 on one and the same polymer. To explain this phenomenon, we quantified the amount of IL-2 bound to T cells exploiting the AF647 signal. Indeed, binding of P-IL-2 is greatly reduced compared to that of unbound IL-2 when used in combination with P-αCD3, probably due to steric hindrance. This reduced binding, which explains the lower stimulatory capacity, can be restored by CD3+ T cell-targeting using P-αCD3/IL-2med (Figure 2c and S4c). For each condition, comparable levels of αCD3 were bound to the stimulated T cells (Figure S4b).

T cells can bind IL-2 through either the high affinity trimeric αβγ-receptor, or, as happens in the absence of IL-2Rα (CD25), via the low affinity dimeric βγ-receptor.[12] While non-activated T cells only express the low affinity receptor, CD25 is upregulated upon TCR stimulation and the affinity towards IL-2 increases. CD25 is also expressed on other (immune) cells, including endothelial cells that are thought to be responsible

for part of the side effects of IL-2. To investigate the response of CD25-positive cells when stimulated under different IL-2 treatment regiments, T cells were first activated with the commonly used CD3/CD28 Dynabeads to activate T cellsand induce CD25 expression. Next, these CD25 high T cells were incubated with unbound IL-2 + P-αCD3, P-IL-2 + P-αCD3 or P-αCD3/IL-2med. Binding of IL-2 to activated T cells was increased in all three cases, indicating that binding to CD25-positive T cells is not exclusively dependent on αCD3 (Figure S4f-g). Importantly, P-IL-2 treatment showed the lowest amount of bound IL-2, also for CD25-high T cells. Therefore, decreased P-IL-2 binding may reduce off-target effects of PIC-cytokine conjugates in future therapeutic applications, even though a possible effect on other cells still needs to be investigated. Together, the synergistic effect of co-targeting IL-2 and αCD3 shows that IL-2 exerts its highest activity on cells that are simultaneously triggered via αCD3. These results, therefore, clearly demonstrate the potential of PICs as a scaffold for IL-2 immobilization and T cell targeting.

IL-2 activity is abrogated when presented on solid microbeads. Having determined that IL-2 can be efficiently presented to T cells on PIC-based sDCs, we investigated whether IL-2 is also active on more conventional microbead-based aAPCs. Such rigid microparticles, coated with antibodies against CD3 and CD28, are routinely used for *in vitro* T cell expansion.[35] To synthesize αCD3 and IL-2-coated beads, tosyl-actived microbeads were reacted with NH_2-PEG_5-azide. The resulting azide-functionalized beads were then mixed with DBCO-labeled αCD3 to yield αCD3-functionalized microbeads B-αCD3. Following this step, one fraction of these αCD3-beads was reacted with DBCO- and AF647-labeled IL-2 to obtain B-αCD3/IL-2. Flow cytometry analysis demonstrated that microbeads were positive for fluorescently labeled αCD3 and IL-2 (Figure S4h). Bead-conjugated αCD3 and IL-2 concentrations were determined, measuring A488 and AF647 fluorescence of unreacted proteins in the supernatant. Stimulation of T cells with unbound IL-2 + B-αCD3 induced modest secretion of IFNγ, which was absent when the same amount of IL-2 was conjugated onto these aAPCs (B-αCD3/IL-2; Figure 3a). Additionally, some proliferation of CD8+ T cells was observed when the T cells were stimulated with unbound IL-2 + B-αCD3, while B-αCD3/IL-2-stimulated T cells did not proliferate at all (Figure 3b). These experiments demonstrate that IL-2 presentation is not effective on conventional aAPCs, while it induces strong T cell activation when similar concentrations of IL-2 are presented on the more flexible sDCs.

Synthesis and characterization of IFNα-functionalized PICs. Having demonstrated the suitability of PIC scaffolds for IL-2 presentation, we next determined whether this sDC design can also be used for targeting other types of cytokines. IFNα is known to play an important role in anti-viral immune responses and is produced in large

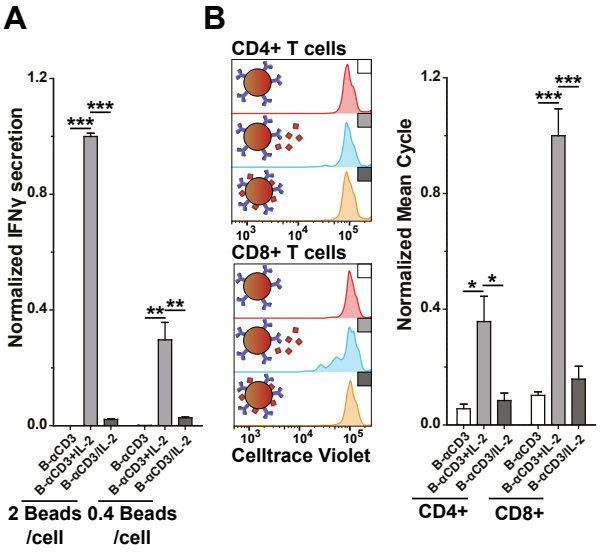

Figure 3 Low IL-2 activity on αCD3/IL-2-functionalized microbeads. **(A)** IFNγ secretion into the supernatant after stimulating T cells with B-αCD3, B-αCD3 mixed with unbound IL-2 and B-αCD3/IL-2 for 16 h. Cells were stimulated using 2 beads per cell or 0.4 beads per cell. **(B)** Proliferation of T cells after 72 h of stimulation with B-αCD3, B-αCD3 mixed with unbound IL-2 and B-αCD3/IL-2 determined by flow cytometry analysis, measuring the dilution of Celltrace Violet (x-axis of histograms). Histograms show one representative experiment of duplicate stimulation of T cells from three healthy donors for CD4+ T cells (upper panel) and CD8+ T cells (lower panel). After T cell stimulation, the values were normalized, using the stimulation with 2 beads per cell of B-αCD3+IL-2 (CD8+ T cells) as the reference. The normalized values of duplicate stimulations of three donors were pooled to obtain mean and SEM values, as depicted in the bar graphs. *$p < 0.05$, **$p < 0.01$, ***$p < 0.001$.

quantities by plasmacytoid dendritic cells. As a signal 3 cytokine, IFNα stimulates T cells in combination with CD3-stimulation and co-stimulation to promote the acquisition of effector functions and to enhance cell proliferation.[36] In this way, IFNα stimulation contributes to the differentiation of CD4+ T cells into type 1 helper cells (Th1), increases IFNγ secretion and induces the expression of cytotoxic molecules in CD8+ T cell.[37] However, when stimulation of IFNα is not combined with a TCR trigger, T cell proliferation is inhibited.[38,39] Thus, combining this cytokine on an sDC scaffold could both target this cytokine to T cells and at the same time link these two signals, thereby avoiding inhibition of T cell proliferation.

P-αCD3/IFNα conjugates were synthesized according to the same method as described above for P-αCD3/IL-2 conjugates. In the first step, DBCO-PEG_4-NHS ester and

AF647-NHS ester were conjugated to IFNα (Figure S2b). The biological activity of the resulting DBCO- and AF647-functionalized IFNα was equally effective as the unconjugated cytokine, as determined in a T cell proliferation assay using in Dynabead-stimulated human T cells (Figure S5a). Subsequently, the functionalized cytokine was reacted with the azide-biotin-PICs. The resulting IFNα-PIC conjugates were purified over magnetic mono-avidin beads. After purification, the protein concentration on the PIC-protein conjugates was analyzed, using fluorescence and circular dichroism as described before. Again, different sDCs with different IFNα densities were prepared and characterized with fluorescence and circular dichroism measurements. The spacings between IFNα molecules were 190 nm (P-αCD3/IFNαlow), 90 nm (P-αCD3/IFNαmed) and 40 nm (P-αCD3/IFNαhigh). This corresponds to 2, 4 and 10 molecules of IFNα per polymer. For the different samples with varying IFNα densities, the average αCD3 spacing varied between 90-130 nm (Figure 4a). On average, these conjugates contained ~4 antibodies per polymer. Also, PICs containing only IFNα were synthesized with two different densities. P-IFNαlow contained ~2 proteins per PIC (spacing of 200 nm) and P-IFNαhigh carried ~8 proteins (spacing of 50 nm). SDS-PAGE revealed that only low amounts of unconjugated cytokine were present in the purified samples (Figure 4b).

PIC-conjugated IFNα induces T cell activation and proliferation. Stimulation of T cells with P-αCD3/IFNα with varying cytokine densities induced the increased secretion of IFNγ compared to the P-αCD3 control, demonstrating that also this cytokine is functional when conjugated to PICs (Figure 4c). Surprisingly, P-αCD3/IFNα samples seem to inhibit the release of TNFα and IL-2 by T cells (Figure S5d-e). In contrast to P-αCD3/IL-2, no clear pattern emerges when investigating the binding of P-αCD3/IFNα with different IFNα densities, possibly because this interaction does not dependent on CD3 (figure S5b-c). To establish how PIC-conjugated IFNα affects T cells, the cells were stimulated with unbound IFNα + P-αCD3, P-IFNα + P-αCD3 and P-αCD3/IFNαhigh. For these three conditions, little differences were observed when comparing the amount of IFNα bound to T cells. All three conditions also induced comparable amounts of IFNγsecretion (after 16 h; Figure 4d), demonstrating that IFNα conjugation to PICs does not reduce its initial activity.

When analyzing T cells 3 days after stimulation, no significant influence of IFNα on T cell proliferation could be detected (Figure S5f-g). Since IFNα is known to support T cell proliferation at later stages after TCR stimulation,[36] cell numbers were assessed 7 days after stimulation. At this time point, P-αCD3/IFNα stimulation increased CD8+ T cell numbers more than four-fold compared to P-αCD3-stimulated cells, both in the presence or absence of unbound IFNα (Figure 4e). These results clearly illustrate that PIC-conjugated IFNα can stimulate T cells to induce IFNγ secretion and (late) proliferation. While PIC-conjugation of IL-2 in the absence of CD3-targeting antibodies

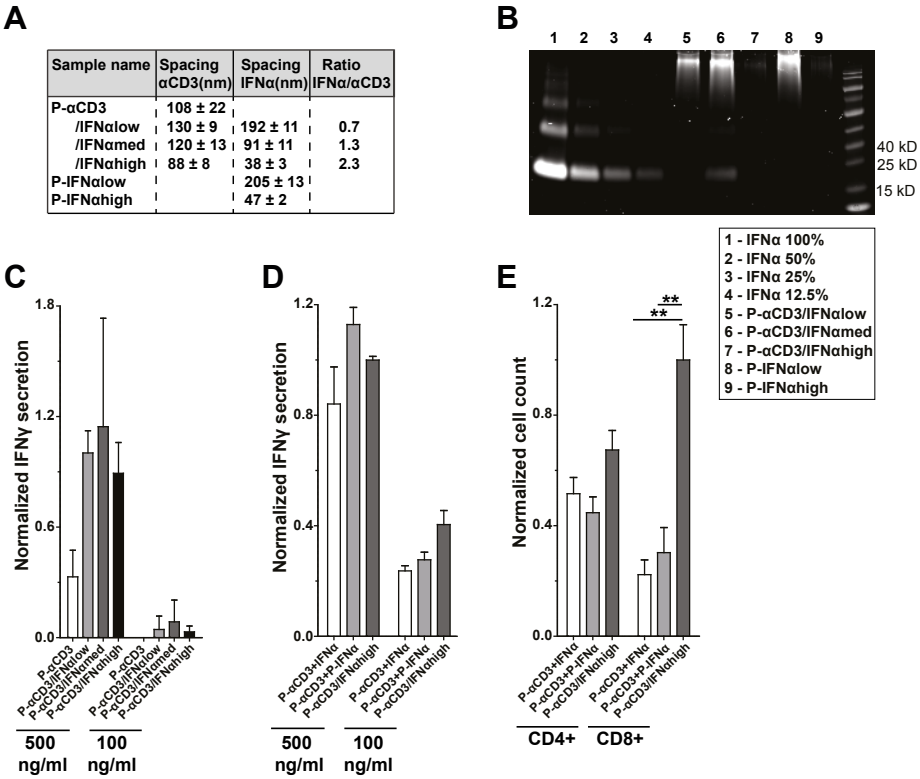

Sample name	Spacing αCD3(nm)	Spacing IFNα(nm)	Ratio IFNα/αCD3
P-αCD3	108 ± 22		
/IFNαlow	130 ± 9	192 ± 11	0.7
/IFNαmed	120 ± 13	91 ± 11	1.3
/IFNαhigh	88 ± 8	38 ± 3	2.3
P-IFNαlow		205 ± 13	
P-IFNαhigh		47 ± 2	

Figure 4 Synthesis, characterization and biological activity of PIC-IFNα conjugates. **(A)** Characteristics of PIC-protein conjugates. To calculate the average spacing between proteins, the protein concentration was determined using the fluorescence intensity of the labeled proteins and the PIC concentration was determined from the circular dichroism (CD) signal at 272 nm. The standard error of the mean (SEM) is depicted next to the mean values of duplicate measurements. **(B)** SDS-PAGE of purified PIC-IFNα conjugates (lanes 5-9). Lanes 1-4 were loaded with an IFNα standard. The amount of IFNα conjugated to the PIC-IFNα samples corresponds to 100% (lane 1). **(C)** IFNγ secretion into the supernatant after stimulating T cells with αCD3-functionalized sDCs containing different amounts of IFNα for 16 h. The cells were stimulated using 500 ng/ml αCD3 or 100 ng/ml αCD3. **(D)** IFNγ secretion into the supernatant after 16 h of T cell stimulation with P-αCD3 mixed with unbound IFNα or P-IFNα, or P-αCD3/IFNαhigh. In each stimulation, the same amount of IFNα was used. The cells were stimulated using 500 ng/ml αCD3 or 100 ng/ml αCD3. **(E)** Cell counts after 7 days of T cell stimulation with 100 ng/ml P-αCD3, P-αCD3 mixed with unbound IFNα or P-αCD3/IFNαhigh. After T cell stimulation, the values were normalized using the stimulation with P-αCD3/IFNαhigh (CD8+ T cells) as the reference. The normalized values of duplicate stimulations of three donors were pooled to obtain mean and SEM values, as depicted in the bar graphs. *$p < 0.05$, **$p < 0.01$.

resulted in a significant loss of binding and activity, IFNα can be readily conjugated to PICs without losing its stimulatory capacity. Importantly, stimulation with P-αCD3/IFNα leads to a significant increase in the CD8+ T cell number after 7 days.

T cells stimulated with PIC-conjugated cytokines develop multiple effector functions. After having confirmed that P-αCD3/IL-2 and P-αCD3/IFNα are capable of targeting cytokines to T cells and of inducing potent T cell responses, we investigated the functionality of the stimulated T cells after 14 days. Different functionalities of T cells, such as cytokine production and cytotoxicity, determine their capacity to induce a potent immune response. Expression of pro-inflammatory cytokines IL-2, IFNγ and TNFα can be essential in anti-tumor immunity, especially when produced in combination, each having their own role in orchestrating an immune response.[40] Cytokines are known to be important for equipping T cells with these functionalities. To ensure that the desired immune response is not affected when stimulating T cells with our sDCs, it is essential that these functions are also preserved after stimulation with cytokine-functionalized sDCs.

To determine these functionalities, T cells were stimulated with cytokine-functionalized sDCs (or Dynabeads as a positive control for long-term T cell expansion) and re-stimulated after 7 days. After 14 days, intracellular staining for IL-2, IFNγ and TNFα was performed to determine the percentage of cells capable of producing these cytokines. Long-term stimulation resulted in T cells capable of producing multiple cytokines, demonstrating the presence of functional T cells. Stimulation with P-αCD3/IFNα induced high numbers of IFNγ-producing T cells, but led to a decrease in TNFα-producing cells. For IL-2-stimulated cells, a decrease in IL-2 production was observed (Figure 5a-b). In general, the stimulation with cytokine-functionalized sDCs resulted in cytokine expression profiles comparable to stimulation with unconjugated cytokines (Figure S6a-b), further demonstrating that IL-2 and IFNα are still fully capable of exerting their function after conjugation to PICs.

One of the most important functions of T cells, especially for CD8+ cells, is to kill pathogen infected cells or cancer cells through the release of granules that contain cytotoxic molecules, such as Granzyme B. As the release of cytotoxic molecules from these vesicles exposes CD107a on the cell surface, this can be used as a surrogate marker for cytotoxic activity and measured by flow cytometry.[41] After 14 days of stimulation, T cells expressed high levels of CD107a and Granzyme B, demonstrating their capacity of killing target cells (Figure 4c-d). Especially after stimulation with IFNα, expression of the degranulation marker CD107a was significantly increased, while degranulation in IL-2-stimulated cells was much lower. Degranulation was not dependent on whether IL-2 and IFNα were conjugated to PICs during stimulation (Figure S6c), whereas Granzyme B levels were somewhat increased when using PIC-cytokine conjugates for stimulation (Figure S6d). These findings demonstrate that

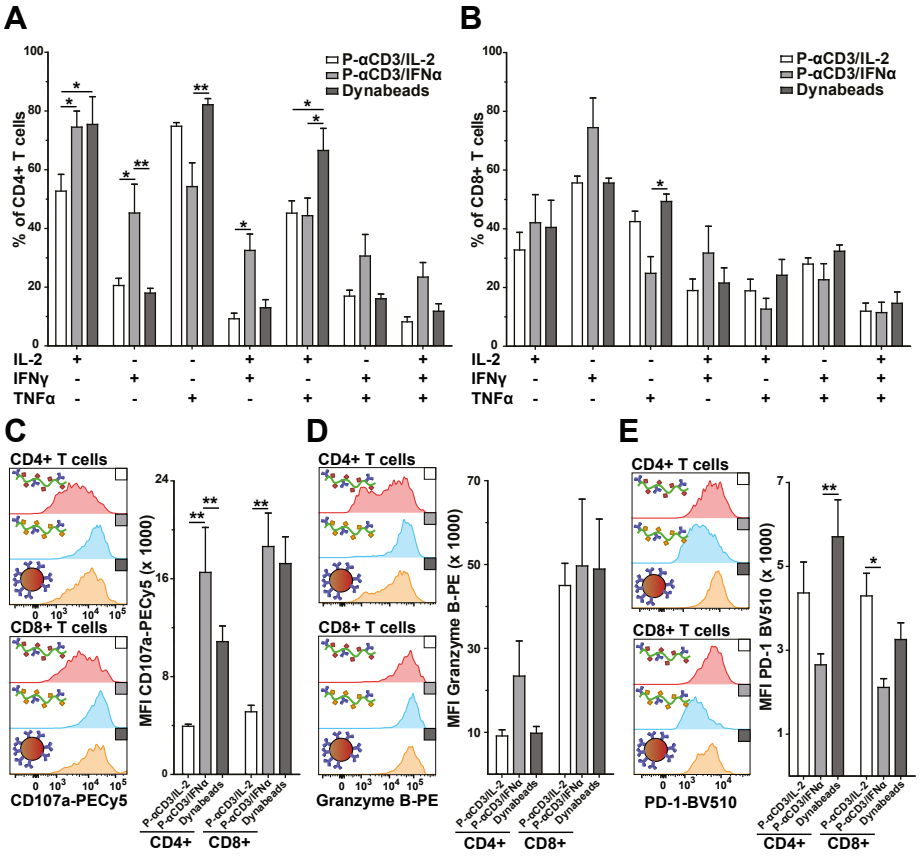

Figure 5 Functional consequences of 14-day T cell stimulation with cytokine-PIC conjugates. T cells were stimulated with 500 ng/ml P-αCD3/IL-2, P-αCD3/IFNα and Dynabeads and re-stimulated after 7 days. After 14 days, the cytokine production capacity of these T cells was determined after 6 h PMA + ionomycin stimulation in the presence of Brefeldin A and monensin. Using intracellular staining and flow cytometry analysis, the cytokine expression profiles for IL-2, IFNγ and TNFα were determined for **(A)** CD4+ T cells and **(B)** CD8+ T cells. **(C-E)** Expression of **(C)** CD107a, **(D)** Granzyme B and **(E)** PD-1. T cells stimulated for 14 days were re-stimulated with PMA + ionomycin in the presence of Brefeldin A and monensin. An anti-CD107a-PECy5 antibody was used to determine the expression of the degranulation marker CD107a (C, x-axis of histograms) using flow cytometry analysis. Intracellular staining for Granzyme B and cell surface staining for PD-1 were performed to determine the expression of these molecules. The histograms show one representative experiment of duplicate stimulation of T cells from three healthy donors for CD4+ T cells (upper panel) and CD8+ T cells (lower panel). Pooled mean fluorescence intensities (MFI) ± SEM are depicted in the bar graph. *$p < 0.05$, **$p < 0.01$.

IL-2- and IFNα- induced cytotoxic T cell functions are retained or slightly increased upon P-αCD3/cytokine stimulation. Complying with their cytotoxic function, CD8+ T cells were the main producers of Granzyme B, although CD4+ T cells also showed degranulation and some Granzyme B production. Indeed, similar to CD8+ T cells, CD4+ T cells have recently been found to be capable of antigen-specific cytotoxicity in some cases.[42]

Besides showing expression of cytotoxic markers, cell surface expression of PD-1 was determined after 14 days. Interaction of PD-1 with its ligand, PD-L1, restrains T cell activity and can inhibit T cell function. Expression levels of PD-1 are therefore an indication of the ability of a T cell to be functional within immunosuppressive environments, including many tumors.[43] After stimulation with P-αCD3/IFNα, T cells expressed relatively low levels of PD-1, while the PD-1 expression level for P-αCD3/IL-2-stimulated cells was higher and more comparable to the expression level of Dynabead-stimulated T cells (Figure 5e). Stimulation of T cells with unbound cytokines resulted in comparable PD-1 expression (Figure S6e). The relatively low expression of PD-1 on IFNα-stimulated cells might make T cells less susceptible to PD-L1-expressing tumor cells or APCs, and is thus beneficial for their functionality. Contrary to our findings, increased PD-1 expression has been reported for mouse T cells stimulated with IFNα, although these measurements were done at an earlier time point after stimulation.[44]

Together, these experiments demonstrate that T cells stimulated with cytokine-functionalized PICs are capable of producing multiple cytokines and of expressing cytotoxic markers. Although IFNα-stimulated T cells exhibit lower proliferation than IL-2 treated cells, they are potentially more capable of killing their target cells. On top of this, their relatively low PD-1 expression makes them less susceptible for inhibition by PD-L1. Taken together, co-conjugation of αCD3 and cytokines to PIC-based sDCs increases the early activation and proliferation of T cells, while retaining the capacity of these cytokines to bring about important functional characteristics in these T cells.

Discussion

Lack of specificity seriously hampers widespread clinical application of cytokine-based immunotherapies. Therefore, more precise targeting of cytokines to T cells would greatly reduce the off-target side effects of these therapies. To accomplish this, there is a great need for cytokine-functionalized aAPCs that allow antigen specific targeting of T cells, that could be applied directly *in vivo* in an off-the-shelf approach. However, to this point no nanosized cell-free aAPCs capable of cytokine delivery have been developed.

In this study, cytokine-functionalized PIC-based sDCs, containing αCD3 antibodies combined with IL-2 or IFNα, were successfully synthesized and applied in T cell activation experiments. Although IL-2 and IFNα are cytokines with distinct functional and structural characteristics, both of them could be efficiently conjugated to PICs and remain biologically active. For both cytokines, proliferation was enhanced when cells were stimulated with PICs that were functionalized with both αCD3 and cytokines. Whereas PIC-conjugation of IL-2 alone diminished binding and reduced cytokine activity, co-conjugation of αCD3 targeted these IL-2 conjugates to the CD3 receptor and greatly increased all aspects of T cell activation. PIC-based sDCs are therefore a unique scaffold for the presentation of IL-2 to T cells. PIC-conjugation of IFNα did not alter biological activity in early activation assays and was mostly beneficial for the induction of late T cell proliferation as well as for the induction of potent cytotoxic functionality. Thus, these experiments demonstrate that IL-2-presenting sDCs can efficiently enhance T cell proliferation, while IFNα-functionalized PICs can be used to induce more potent T cells.

Comparing T cell activation of cells stimulated with unbound IL-2, P-IL-2 and P-αCD3/IL-2med we found a synergistic effect when combining αCD3 and IL-2 on one and the same polymer chain. This enhanced activation may partially be explained by the increased amount of bound IL-2 when using P-αCD3/IL-2med. On top of this, the observed synergistic effect could be the result of co-localized TCR (CD3) and IL-2 signaling, especially since components of the IL-2 receptor complex can be present in clusters together with (co-receptors of) TCRs.[45] In addition, localized paracrine delivery can greatly enhance stimulatory capacity of IL-2, as was reported for IL-2-releasing micro-aAPCs.[27] Also in natural DC-T cell or T-T cell interactions, synapses formed where TCR clusters are present may facilitate polarized IL-2 release.[46] Similarly, we previously observed that after sDC stimulation, TCRs polarize and form immune synapse-like structures on one side of the T cell.[32] Thus, polarization of IL-2 signaling complexes to these synapses could allow for more efficient IL-2-induced signaling and explain the synergistic effect of closely spaced αCD3 and IL-2.[46] Similar to the enhanced proliferation observed after stimulation with P-αCD3/IL-2, the enhanced effect of P-αCD3/IFNα could be the result of co-triggering IFNα receptors

in close proximity to CD3. Indeed, TCRs and IFNα share similar early signaling complexes and functional TCRs are required for efficient IFNα signaling,[47] which could indicate co-localization of both receptors. In addition, for IFNγ receptors, which are related to IFNα receptors, inclusion within immune synapses in CD4+ T cells has been described as a mechanism to enhance signal transduction.[48]

Importantly, we demonstrated here that IL-2 activity is abrogated when immobilized on classical rigid (dynabead-based) aAPCs. Similarly, IL-2 presentation on αCD3/αCD28-coated PLGA particles is known to be inefficient and requires high IL-2 densities for stimulating T cells.[27] In contrast to rigid particles, liposome-conjugated IL-2 retain their activity towards T cells, which could result from the mobility of liposome-anchored molecules, although the use of Fc-bound IL-2 could also play a role here.[20] In addition, no negative effect of IL-2 surface conjugation was reported when using hydroxyethyl starch nanocapsules.[22] As rigid microparticles are not able to present active IL-2, size and/or nano-scale flexibility seem to be essential for the activity of immobilized IL-2. This observation is also in line with our result that the amount of T cell bound P-IL-2 is low. By contrast, for our semi-flexible PICs T cell responses greatly increase when IL2 is co-conjugated with αCD3 to the same polymer. In addition, the multivalent presentation of both αCD3 and IL-2 seems to play an important role in this synergistic effect, since αCD3-IL-2 fusion proteins did not show the same synergy.[49] Probably, flexible scaffolds that can dynamically rearrange, appear to be better mimics of natural DC surfaces, facilitating a more efficient interaction of multiple ligands with T cells. Semi-flexible PIC scaffolds consequently allow for presenting IL-2 in close spatial proximity with a TCR trigger, resembling the trans-presentation observed in natural immune synapses formed between DCs and T cells. In this case, IL-2 can be presented on the DC surface by CD25, which is located in close proximity to peptide-MHC complexes, leading to robust T cell responses.[50] Taken together, our results demonstrate that classical solid microparticles are less suitable as scaffolds for IL-2-presentation, while IL-2-conjugation to PIC-based sDCs can induce excellent T cell responses. For IFNα-functionalized sDCs retention of biological activity was demonstrated when measuring early T cell activation markers. A similar retention of biological activity after scaffold conjugation has also been observed when stimulating other cell types with IFNα-functionalized scaffolds, such as the stimulation of B-lymphoblasts with gold nanoparticles.[17]

The biological activity of these novel cytokine-functionalized sDCs may be further optimized when combining these two different cytokines on a single CD3-targeting PIC. This approach may allow for more substantial T cell proliferation combined with the induction of strong cytotoxic effector function, leading to high numbers of highly effective cytotoxic T cells. In this proof of concept study, cytokines were targeted to T cells using αCD3 antibodies, which bind closely to the TCR and generically trigger all CD3 expressing T cells. Having demonstrated synergistic effects

of simultaneous triggering of TCRs and cytokine receptors in close proximity, it is possible to transform this approach towards antigen-specific cytokine delivery, by replacing αCD3 antibodies with peptide-MHC complexes. Furthermore, *in vivo* tumor models will have to be used to further validate the benefit of cytokine presentation on PIC-based sDCs. Here, to the best of our knowledge, we demonstrate for the first time that the cytokines IL-2 and IFNα are capable of inducing potent T cell responses when presented on synthetic nano-sized aAPCs. Thus, the results of the presented study establish PIC-based sDCs as highly suitable vehicles for the delivery and presentation of otherwise soluble cytokines to T cells. The small size and straightforward synthesis of these conjugates makes them particularly promising for future off-the-shelf immune therapies.

Experimental Section

Materials. Zeba™ Spin Desalting Columns (7K and 40K MWCO), Celltrace Violet Cell proliferation kit, tosyl-activated Dynabeads M450, Dynabeads human T-activator CD3/CD28 and AlexaFluorF647-NHS ester (AF647) were purchased from ThermoFisher. Magnetic mono-avidin beads were from Bioclone. Azide-PEG_5-NH_2 (O-(2-Aminoethyl)-O′-(2-azidoethyl)pentaethylene glycol) was obtained from Sigma-Aldrich, anti-CD3 (Clone OKT3) was from BioXCell. Recombinant human IL-2 and IFNα were purchased from Cell Sciences, IL-2 and TNFα ELISA Ready-set go kits were from eBioscience. Pan T cell isolation kit and propidium iodide solution were obtained from Miltenyi. Antibodies anti-CD4-APC-Cy7, anti-PD-1-BV510, anti-CD107a-PECy5, anti-CD25-PE, anti-CD4-BV421, anti-CD8-BV510 and anti-IFNγ-BV421 were from BD Biosciences, and antibodies anti-Granzyme B-PE, anti-CD8-PECy7 and anti-CD4-PECy7 were from Biolegend. Antibodies anti-TNFα-PerCPCy5.5 and anti-IL-2-PE were from eBioscience. DBCO-PEG_4-NHS was purchased from Jena Bioscience. Atto488-NHS ester (A488) was obtained from Atto-TEC GmbH. 30 kDa Amicon Ultra-15 ultrafiltration membranes were from Merck Millipore. X-vivo medium was purchased from Lonza. Cytoperm/cytofix buffer kit was purchased from BD Biosciences.

Synthesis of polyisocyanopeptides. The polyisocyanopeptides (PICs) used in this study were synthesized according to literature procedures.[32,33] Briefly, non-functional methoxy- and functional azide-terminated monomers were reacted in a 30:1 ratio using a nickel catalyst (Figure S1a), statistically yielding a polymer with a functional azide group every 3.5 nm. Next, 50 % of the azides were converted to biotin using DBCO-PEG_4-biotin as described in the literature[34]. The resulting azide-biotin-PICs were analyzed with atomic force microscopy (Nanoscope III, Digital Instruments), operating in tapping mode in air, using NSG10 tips. For these experiments, the polymer (10 μg/ml)

was drop-casted onto freshly cleaved mica and incubated for 5 min. After removing the liquid, the substrate was dried under nitrogen flow (Figure S1b). These AFM images were used to determine the polymer length with ImageJ, yielding an average length of 383 nm (figure S1c).

Protein functionalization. In order to functionalize αCD3 antibodies, the storage buffer was exchanged to 50 mM borate buffer pH 8.5, using Amicon ultrafiltration membranes (30 kD MWCO). For αCD3, IL-2 and IFNα functionalization between 1-5 mg of protein was used at concentrations between 1-3 mg/ml. For αCD3, 5 equivalents of DBCO-PEG_4-NHS ester and 2.5 equivalents of A488-NHS ester was added. IL-2 and IFNα were reacted with 4 equivalents of DBCO-PEG_4-NHS ester and 2 equivalents of AF647-NHS ester. After incubation for 2 h at 4 °C on a rotator, functionalized αCD3 was purified over a 5 ml 40K Zeba spin desalting column, while the cytokines were purified over a 2 ml 7K Zeba spin desalting column.

Analysis of functionalized proteins. To determine the degree of DBCO and dye labeling, the proteins were analyzed using a Nanodrop 2000c spectrophotometer. Absorbance at 280, 309, 501 and 650 nm was used to calculate the concentrations of proteins, DBCO and dye. After correcting for the overlap in the absorbance spectra of the individual molecules, the respective concentrations were calculated using the molar extinction coefficients of the proteins used: 210000 M^{-1} cm^{-1} for αCD3, 11900 M^{-1} cm^{-1} for IL-2 and 18700 M^{-1} cm^{-1} for IFNα. This yielded ratios of 1:3.6:2 for αCD3:DBCO:A488, 1:2:0.5 for IL-2:DBCO:AF647 and 1:2:0.5 for IFNα:DBCO:AF647. Protein yields were typically between 60-80%. The degrees of labeling were confirmed for IL-2 and IFNα using MALDI-ToF (Bruker microflex) with sinapinic acid as the matrix (Figure S2a-b).

PIC-protein conjugate synthesis. To obtain the PIC-αCD3/cytokine conjugates, DBCO-functionalized αCD3 (0.25 equivalents with respect to the reactive azide groups on the polymer) was added to the azide-biotin-PIC (100 µg, 1 mg/ml in Phosphate Buffered Saline; PBS) and incubated. After 2 h, IL-2 or IFNα was added to the reaction mixture and incubated at 4 °C on a rotator overnight. To obtain the low, medium and high density samples, 0.1, 0.2 or 0.5 equivalents of cytokine (with respect to azide) were used. After coupling, the protein-functionalized PICs were purified over magnetic mono-avidin beads as described in.[34] The PIC-protein conjugates were incubated with magnetic mono-avidin beads (1 ml bead solution for each polymer sample) for 2 h at 4 °C, after which they were washed extensively with PBS+0.1% Tween-20 (2x) and PBS (4x), making use of a Dynal MPC-L Magnetic Particle Concentrator. To elute the conjugates from the beads, they were incubated in PBS containing 2 mM biotin (biotin elution buffer) on a rotator for 2 h at 4 °C.

Analysis of PIC-protein conjugates. The protein concentrations in all PIC-protein conjugate samples were determined using a Tecan Spark 10M fluorescence microplate reader. Unbound DBCO/dye-functionalized proteins were used as standard for each measurement. The samples (100 µl) were pipetted into black, flat-bottom non-binding 96-well microplates (Greiner Bio-One). A488 and AF647 were exited at 490 nm and 635 nm, and detected at 535 nm and 680 nm, respectively. The polymer concentration was measured using circular dichroism (CD) (JASCO J-810). 100 µl of each PIC-protein conjugate was filled into a 1 cm cuvette and the CD spectrum was measured using biotin elution buffer as a blank. The peak value at 272 nm was used to determine the polymer concentration, using an extinction coefficient of 547.8 mdeg ml cm^{-1}, which was determined with a standard curve of different polymer concentrations as described previously.[34] To confirm the absence of unbound proteins after purification, the PIC-protein conjugates were further analyzed with SDS-PAGE. A standard of unbound protein was loaded onto these gels for quantifying the amount of protein that was not fully removed during purification. After electrophoresis, the gels were scanned with a Typhoon trio+ gel scanner to detect the AF647 dye coupled to the cytokines.

Microbead-protein conjugation. To synthesize microbead-based aAPCs, tosyl-activated Dynabeads were reacted with 1000 equivalents of azide-PEG_5-NH_2 in 50 mM borate buffer (pH 8.5) overnight at room temperature. The beads were washed 4x with PBS to remove excess azide-PEG_5-NH_2. The beads were incubated with the previously synthesized DBCO- and Atto488-labeled αCD3 antibodies. Following overnight reaction at 4 °C, the beads were again washed with PBS (4x) to remove excess αCD3 and DBCO- and AF647-labeled IL-2 was added to one part of the αCD3-labeled beads. Again, the beads were reacted overnight at 4 °C and washed with PBS containing 0.1 % BSA and 2 mM EDTA (2x) and PBS (4x) to remove excess IL-2. αCD3-functionalized and αCD3/IL-2-functionalized beads were analyzed using a BD FACSverse flow cytometer. The αCD3 and IL-2 concentrations were measured in the supernatants of the reaction mixtures to determine the amount of proteins coupled to the different microbeads. For this measurement, the samples were analyzed in a Tecan Spark 10M fluorescence microplate reader, relative to a standard of the unbound and fluorescently labeled proteins. Bead-coupled αCD3 and IL-2 densities were 43 and 58 ng/10^6 beads, respectively.

Human T cell activation assays. Peripheral blood lymphocytes were isolated from buffy coats, obtained from healthy donors using Ficoll density centrifugation. T cells were isolated from peripheral blood lymphocytes with the Miltenyi Pan T cell isolation kit. To follow T cell proliferation, Celltrace Violet was added to the cells at a final concentration of 2.5 µM. The labeling reaction was performed for 15 min at room

temperature. The reaction was quenched upon addition of 3 reaction volumes of cold Fetal Bovine Serum (FBS), followed by washing the cells 3 times. The PIC-protein conjugates were added to Celltrace Violet labeled T cells (50.000) to obtain a final concentrations of 100 ng/ml or 500 ng/ml of PIC-conjugated αCD3. Incubation was performed in round-bottom 96-well cell culture plates, with final volumes of 100 µl per well. Cell culture was performed at 37 °C using X-Vivo medium, containing 4% human serum.

Analysis of T cell stimulation. After 16 h of stimulation, a fraction of the cells was collected for analysis. The supernatants were collected for ELISA measurements to determine the concentrations of IFNγ (human IFNγ ELISA, Thermo Scientific), IL-2 (ready-set go IL-2 ELISA kit, eBioscience) and TNFα (ready-set go TNFα ELISA kit, eBioscience). For detection, absorbance was measured at 450 nm on a Bio-rad iMark plate reader. The respective cytokine concentrations were determined using 4-paramater fits in Microplate Manager 6 software. In addition, to assess binding of the conjugates and the T cell activation status, T cells were stained for CD4, CD8 and CD25 expression and measured using a BD FACSverse flow cytometer.

Analysis of T cell proliferation. After 3 days, the supernatants were collected for IL-2 and TNFα ELISAs, and the cells were stained for CD4 and CD8. CD4 and CD8 expression as well as the dilution of the Celltrace Violet label was determined using FACS (BD FACSVerse). The mean number of cycles (i.e. the average number of cell divisions) was determined as ^{2}log of the ratio of the mean fluorescence intensity (MFI) of non-divided cells (as determined using FlowJo) divided by the MFI of all cells. To determine long-term T cell proliferation (7 days), T cells were stimulated with 100 ng/ml of the respective PIC-protein conjugates or with CD3/CD28 T cell activator Dynabeads in a 2:1 bead:cell ratio. After 7 days, the cells were stained for CD4 and CD8 and counted using a Miltenyi MACSQuant Analyzer 10. Propidium iodide staining (1:1000 dilution) of dead cells was done using MACSQuant before flow cytometry measurements.

Binding analysis using activated T cells. To determine binding to activated CD25-positive cells, T cells were stimulated with CD3/CD28 T cell activator Dynabeads in a 1:1 bead:cell ratio at 37°C in X-vivo medium, containing 4% human serum. After 24 h, the beads were removed over a Dynal MPC-L Magnetic Particle Concentrator (2x). After this step, the PIC-protein conjugates were added to 50.000 of activated T cells and cultured at 37°C. After 16 h, the cells were collected, stained for CD4, CD8 and CD25. Binding of IL-2 was analyzed on the BD FACSverse flow cytometer.

Long-term T cell functionality assay. Pan T cells were isolated from healthy peripheral blood lymphocytes using a Miltenyi Pan T cell isolation kit. The cells were stimulated

with the PIC-protein conjugates, using an αCD3-concentration of 500 ng/ml and CD3/CD28 human T cell activator Dynabeads in a 2:1 bead:cell ratio in X-vivo medium, containing 4% human serum at 37 °C. After 7 days, the cells were washed with X-vivo medium and a fraction of the cells was re-stimulated with the same concentration of stimulant. After 14 days, a portion of the T cells was stimulated with PMA and ionomycin for 6 h to induce cytokine production in the presence of Brefeldin A and monensin to trap the cytokines in the cells.[51] The cells were fixed and permeabilized with the BD cytofix/cytoperm kit, and stained for intracellular IL-2, IFNγ and TNFα. In addition, 14-day-stimulated T cells were incubated with PMA and ionomycin for 6 h (to induce degranulation of cytotoxic granules) in the presence of brefeldin A, monensin and anti-CD107a-PECy5 antibody. After stimulation, intracellular staining for Granzyme B was performed. Additionally, surface staining for PD-1 was done (14-day-stimulated T cells). All stained T cells were measured using the BD FACSverse flow cytometer.

Data Analysis. Flow cytometry data were analyzed using FlowJo software. Gating was done as depicted in Figure S7. Each experiment was performed with T cells from 3 different donors. Each donor was measured in duplicate and the corresponding values were averaged. To account for variations between donors, all conditions measured with samples from the same donor were first normalized by dividing each value by that of the most important condition. After this step, the mean and the standard error of the mean (SEM) were calculated, using the normalized values of the different donors. Statistical analysis was performed using GraphPad Prism (5.03) software. Statistical significances were calculated with one-way ANOVA and Bonferroni post tests. *P* values of 0.05 or less were considered significant. Bar graphs show the mean ± SEM of calculated values.

Acknowledgments

This work was supported by ERC Adv grant PATHFINDER (269019). J Tel received NWO Veni grant 863.13.024. A Rowan received NWO Vici grant 700.56.444. K Blank received Vidi grant 700.58.430. C Figdor received the NWO Spinoza grant and Dutch Cancer Society KWO grant KUN2009-4402.

Supporting information

Polymer, protein and bead characterization, as well as additional T cell stimulation experiments are described in the Supporting Information.

References

[1] T. Jiang, C. Zhou, S. Ren, *Oncoimmunology* **2016**, *5*, e1163462.
[2] S. A. Rosenberg, *J. Immunol.* **2014**, *192*, 5451.
[3] J. Kirkwood, *Semin. Oncol.* **2002**, *29*, 18.
[4] S. A. Rosenberg, M. T. Lotze, J. C. Yang, W. M. Linehan, C. Seipp, S. Calabro, S. E. Karp, R. M. Sherry, S. Steinberg, D. E. White, *J. Clin. Oncol.* **1989**, *7*, 1863.
[5] G. Fyfe, R. I. Fisher, S. A. Rosenberg, M. Sznol, D. R. Parkinson, A. C. Louie, *J. Clin. Oncol.* **1995**, *13*, 688.
[6] M. B. Atkins, M. T. Lotze, J. P. Dutcher, R. I. Fisher, G. Weiss, K. Margolin, J. Abrams, M. Sznol, D. Parkinson, M. Hawkins, C. Paradise, L. Kunkel, S. A. Rosenberg, *J. Clin. Oncol.* **1999**, *17*, 2105.
[7] C. Krieg, S. Letourneau, G. Pantaleo, O. Boyman, *Proc. Natl. Acad. Sci.* **2010**, *107*, 11906.
[8] R. N. Schwartz, L. Stover, J. Dutcher, *Oncology (Williston Park).* **2002**, *16*, 11.
[9] B. S. Parker, J. Rautela, P. J. Hertzog, *Nat. Rev. Cancer* **2016**, *16*, 131.
[10] S. Sleijfer, M. Bannink, A. R. Gool, W. H. J. Kruit, G. Stoter, *Pharm. World Sci.* **2005**, *27*, 423.
[11] M. Ferrantini, I. Capone, F. Belardelli, *Biochimie* **2007**, *89*, 884.
[12] O. Boyman, J. Sprent, *Nat. Rev. Immunol.* **2012**, *12*, 180.
[13] L. Zitvogel, L. Galluzzi, O. Kepp, M. J. Smyth, G. Kroemer, *Nat. Rev. Immunol.* **2015**, *15*, 405.
[14] A. Cozzio, W. Kempf, R. Schmid-Meyer, M. Gilliet, S. Michaelis, L. Schärer, G. Burg, R. Dummer, *Leuk. Lymphoma* **2006**, *47*, 865.
[15] C. Xuan, K. K. Steward, J. M. Timmerman, S. L. Morrison, *Blood* **2010**, *115*, 2864.
[16] N. Giri, P. Tomar, V. S. Karwasara, R. S. Pandey, V. K. Dixit, *Acta Biochim. Biophys. Sin. (Shanghai).* **2011**, *43*, 877.
[17] M.-Y. Lee, J.-A. Yang, H. S. Jung, S. Beack, J. E. Choi, W. Hur, H. Koo, K. Kim, S. K. Yoon, S. K. Hahn, *ACS Nano* **2012**, *6*, 9522.
[18] Z. Li, L. Li, Y. Liu, H. Zhang, X. Li, F. Luo, X. Mei, *Int. J. Pharm.* **2011**, *410*, 48.
[19] A. Sánchez, M. Tobío, L. González, A. Fabra, M. J. Alonso, *Eur. J. Pharm. Sci.* **2003**, *18*, 221.
[20] B. Kwong, S. A. Gai, J. Elkhader, K. D. Wittrup, D. J. Irvine, *Cancer Res.* **2013**, *73*, 1547.
[21] Y. Zheng, M. T. Stephan, S. A. Gai, W. Abraham, A. Shearer, D. J. Irvine, *J. Control. Release* **2013**, *172*, 426.
[22] S. U. Frick, M. P. Domogalla, G. Baier, F. R. Wurm, V. Mailänder, K. Landfester, K. Steinbrink, *ACS Nano* **2016**, *10*, 9216.
[23] J. Tomala, M. Kovar, *Oncoimmunology* **2016**, *5*, e1102829.
[24] G. H. Y. Lin, J. C. Stone, C. D. Surh, T. H. Watts, *Immunol. Cell Biol.* **2012**, *90*, 743.
[25] L. J. Eggermont, L. E. Paulis, J. Tel, C. G. Figdor, *Trends Biotechnol.* **2014**, *32*, 456.
[26] E. R. Steenblock, T. M. Fahmy, *Mol. Ther.* **2008**, *16*, 765.
[27] E. R. Steenblock, T. Fadel, M. Labowsky, J. S. Pober, T. M. Fahmy, *J. Biol. Chem.* **2011**, *286*, 34883.
[28] M. Liu, T. Miao, H. Zhu, A. L. J. Symonds, L. Li, A. Schurich, M. K. Maini, J. Zhang, P. T. F. Kennedy, S. Li, P. Wang, *J. Immunol.* **2012**, *188*, 1534.
[29] P. H. J. Kouwer, M. Koepf, V. A. A. Le Sage, M. Jaspers, A. M. van Buul, Z. H. Eksteen-Akeroyd, T. Woltinge, E. Schwartz, H. J. Kitto, R. Hoogenboom, S. J. Picken, R. J. M. Nolte, E. Mendes, A. E. Rowan, *Nature* **2013**, *493*, 651.
[30] J. J. L. M. Cornelissen, *Science (80-.).* **2001**, *293*, 676.
[31] R. Hammink, S. Mandal, L. J. Eggermont, M. Nooteboom, P. H. G. M. G. M. Willems, J. Tel, A. E. Rowan, C. G. Figdor, K. G. Blank, *ACS Omega* **2017**, *2*, 937.
[32] S. Mandal, Z. H. Eksteen-Akeroyd, M. J. Jacobs, R. Hammink, M. Koepf, A. J. A. Lambeck, J. C. M. van Hest, C. J. Wilson, K. Blank, C. G. Figdor, A. E. Rowan, *Chem. Sci.* **2013**, *4*, 4168.
[33] S. Mandal, R. Hammink, J. Tel, Z. H. Eksteen-Akeroyd, A. E. Rowan, K. Blank, C. G. Figdor, *ACS Chem. Biol.* **2015**, *10*, 485.
[34] R. Hammink, L. J. Eggermont, T. Zisis, J. Tel, C. G. Figdor, A. E. Rowan, K. G. Blank, *Bioconjug. Chem.* **2017**, *28*, 2560.
[35] Y. Li, R. J. Kurlander, *J. Transl. Med.* **2010**, *8*, 104.
[36] S. Hervas-Stubbs, J.-I. Riezu-Boj, I. Gonzalez, U. Mancheño, J. Dubrot, A. Azpilicueta, I. Gabari, A. Palazon, A. Aranguren, J. Ruiz, J. Prieto, E. Larrea, I. Melero, *Eur. J. Immunol.* **2010**, *40*, 3389.

[37] J. P. Huber, J. David Farrar, *Immunology* **2011**, *132*, 466.
[38] D. F. Tough, *Immunol. Cell Biol.* **2012**, *90*, 492.
[39] J. Crouse, U. Kalinke, A. Oxenius, *Nat. Rev. Immunol.* **2015**, *15*, 231.
[40] F. Wimmers, E. H. J. G. Aarntzen, T. Duiveman-deBoer, C. G. Figdor, J. F. M. Jacobs, J. Tel, I. J. M. de Vries, *Oncoimmunology* **2016**, *5*, e1067745.
[41] M. R. Betts, J. M. Brenchley, D. A. Price, S. C. De Rosa, D. C. Douek, M. Roederer, R. A. Koup, *J. Immunol. Methods* **2003**, *281*, 65.
[42] A. Takeuchi, T. Saito, *Front. Immunol.* **2017**, *8*, 194.
[43] H.-T. Jin, R. Ahmed, T. Okazaki, in *Curr. Top. Microbiol. Immunol.*, **2010**, pp. 17–37.
[44] S. Terawaki, S. Chikuma, S. Shibayama, T. Hayashi, T. Yoshida, T. Okazaki, T. Honjo, *J. Immunol.* **2011**, *186*, 2772.
[45] J. Fan, X. Lu, S. Liu, L. Zhong, *Nanoscale Res. Lett.* **2015**, *10*, 419.
[46] C. A. Sabatos, J. Doh, S. Chakravarti, R. S. Friedman, P. G. Pandurangi, A. J. Tooley, M. F. Krummel, *Immunity* **2008**, *29*, 238.
[47] C. N. Stevens, A.-M. Simeone, S. John, Z. Ahmed, O. M. Lucherini, C. T. Baldari, J. E. Ladbury, *Biochem. J.* **2010**, *428*, 429.
[48] R. A. Maldonado, M. A. Soriano, L. C. Perdomo, K. Sigrist, D. J. Irvine, T. Decker, L. H. Glimcher, *J. Exp. Med.* **2009**, *206*, 877.
[49] K.-D. Lee, H.-W. Chen, C.-C. Chen, Y.-C. Shih, H.-K. Liu, M.-L. Cheng, *Oncol. Rep.* **2006**, *15*, 1211.
[50] S. C. Wuest, J. H. Edwan, J. F. Martin, S. Han, J. S. A. Perry, C. M. Cartagena, E. Matsuura, D. Maric, T. A. Waldmann, B. Bielekova, *Nat. Med.* **2011**, *17*, 604.
[51] G. Freer, L. Rindi, *Methods* **2013**, *61*, 30.

Supplementary figures

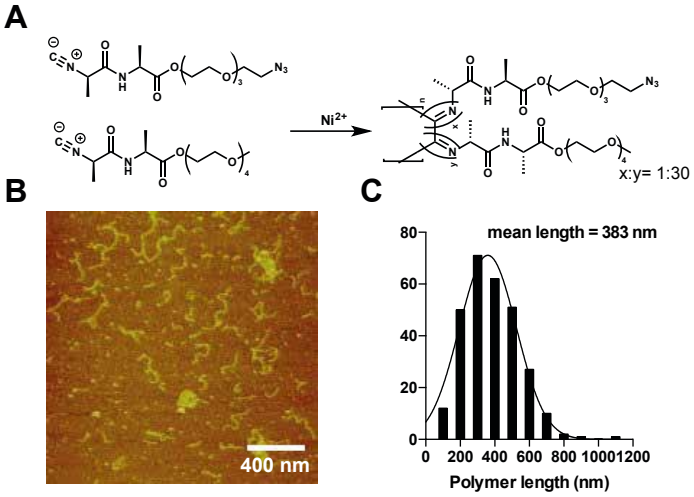

Figure S1 Polymer synthesis and characterization. **(A)** Polymerization reaction of non-functional methoxy- and functional azide-terminated monomers. **(B)** Representative AFM image showing the filamentous polymer structure, scale bar 400 nm **(C)** Histogram of polymer length analysis, fitted with a Gaussian distribution.

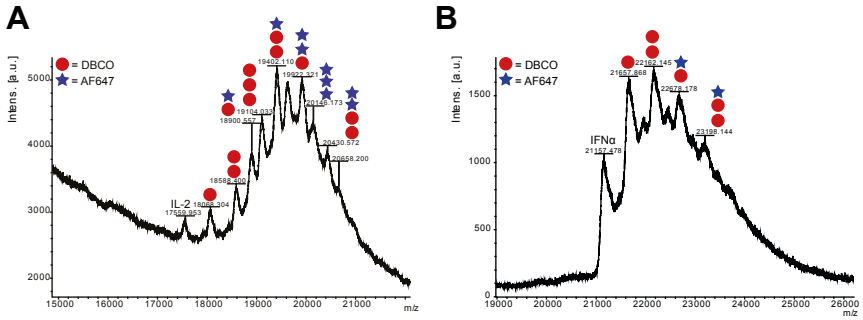

Figure S2 Degree of labeling of IL-2 and IFNα with DBCO and dye. **(A)** Maldi-ToF spectra of functionalized IL-2. **(B)** Maldi-ToF spectra of functionalized IFNα. Red circles are assigned when the mass of DBCO was added to the cytokine, blue stars are assigned for AF647.

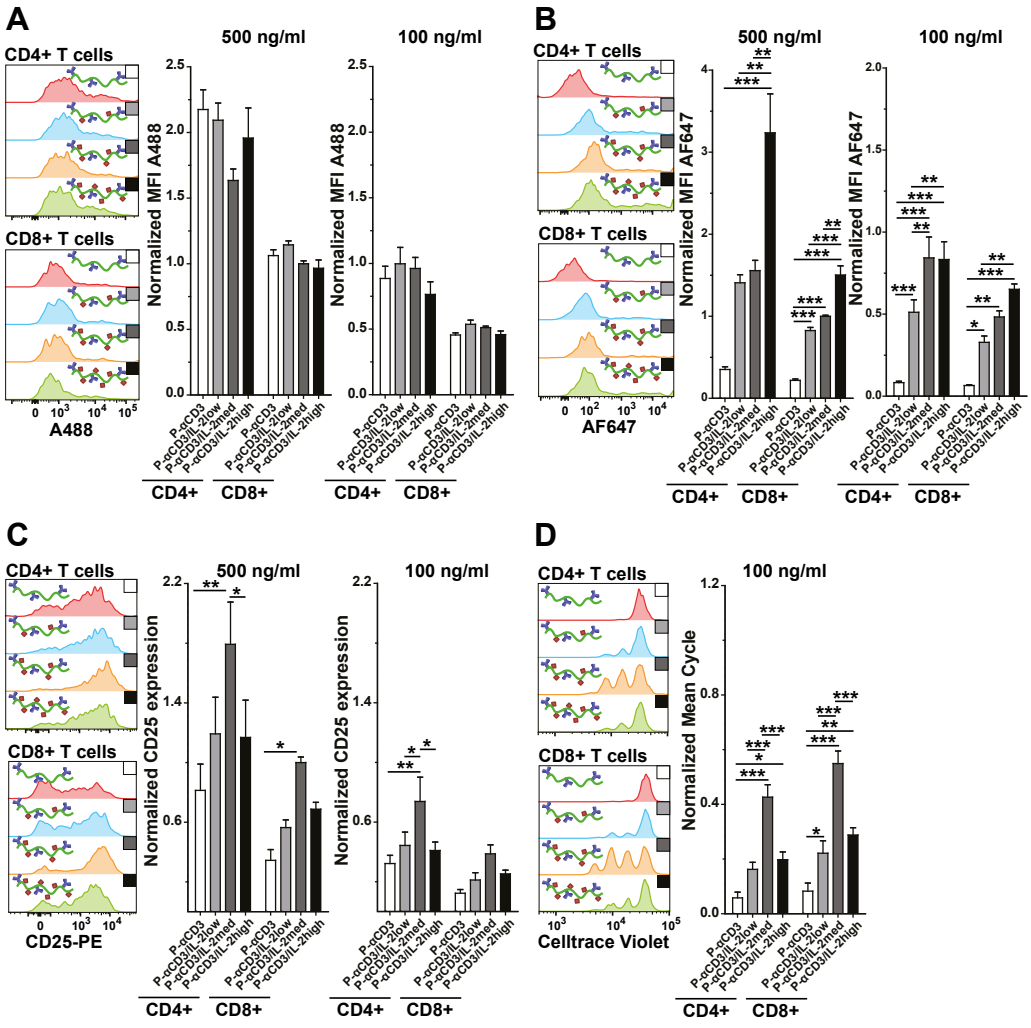
A
CD4+ T cells
CD8+ T cells
A488
500 ng/ml
100 ng/ml
Normalized MFI A488
P-αCD3
P-αCD3/IL-2low
P-αCD3/IL-2med
P-αCD3/IL-2high
CD4+
CD8+
B
CD4+ T cells
CD8+ T cells
AF647
500 ng/ml
100 ng/ml
Normalized MFI AF647
C
CD4+ T cells
CD8+ T cells
CD25-PE
500 ng/ml
100 ng/ml
Normalized CD25 expression
D
CD4+ T cells
CD8+ T cells
Celltrace Violet
100 ng/ml
Normalized Mean Cycle

Figure S3 Biological activity of filamentous semi-flexible IL-2-presenting sDCs. **(A)** Amount of αCD3 bound to T cells after 16 h of incubation with 500 ng/ml and 100 ng/ml P-αCD3 conjugates, functionalized with different IL-2 densities. Bound αCD3 was determined by flow cytometry analysis of A488 signals (x-axis of histograms). **(B)** Amount of IL-2 bound to T cells after 16 h of incubation with 500 ng/ml and 100 ng/ml P-αCD3 conjugates, functionalized with different IL-2 densities. Bound IL-2 was determined by flow cytometry analysis of AF647 signals (x-axis of histograms). **(C)** CD25 expression of T cells after 16 h of incubation with 500 ng/ml and 100 ng/ml P-αCD3 conjugates, functionalized with different IL-2 densities. To determine CD25 expression, the cell surface was stained using an anti-CD25-PE antibody, followed by flow cytometry analysis. **(D)** Proliferation of T cells after 72 h of stimulation with 100 ng/ml P-αCD3, functionalized with different IL-2 densities. Proliferation was analyzed using flow cytometry analysis, measuring the dilution of Celltrace Violet (x-axis of histograms). The histograms show one representative experiment of duplicate stimulation of T cells from three healthy donors for CD4+ T cells (upper panels) and CD8+ T cells (lower panels). The mean number of cycles was calculated for each experiment. After T cell stimulation, the values were normalized using the stimulation with 500 ng/ml of P-αCD3/IL-2med (CD8+ T cells) as the reference. The normalized values of duplicate stimulations of three donors were pooled to obtain mean and SEM values, as depicted in the bar graphs. $^{*}p < 0.05$, $^{**}p < 0.01$, $^{***}p < 0.001$.

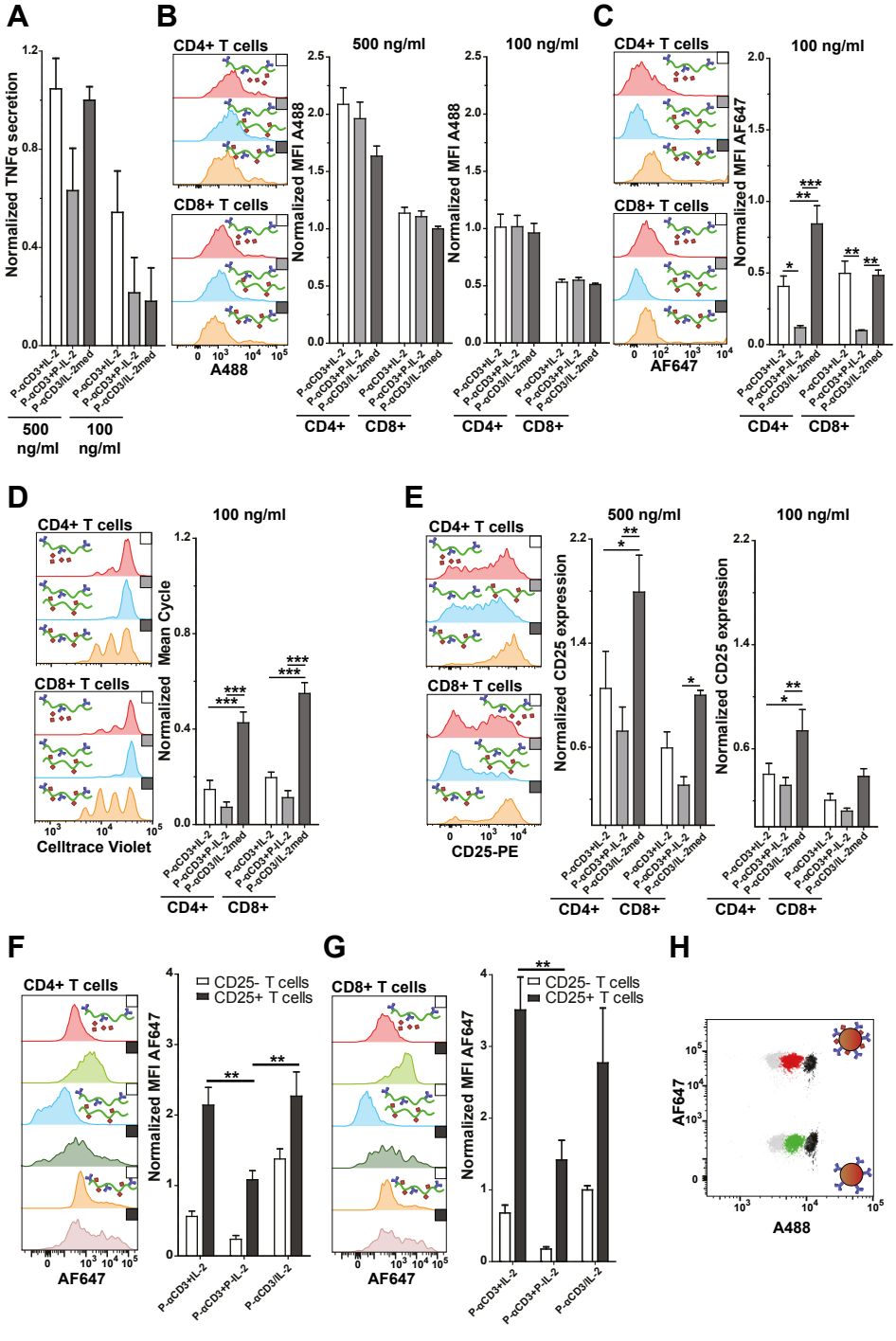
A
B
C
D
E
F
G
H
Normalized TNFα secretion
CD4+ T cells
CD8+ T cells
500 ng/ml
100 ng/ml
A488
Normalized MFI A488
AF647
Normalized MFI AF647
P-αCD3+IL-2
P-αCD3+P-IL-2
P-αCD3/IL-2med
CD4+
CD8+
Normalized Mean Cycle
Celltrace Violet
Normalized CD25 expression
CD25-PE
CD25- T cells
CD25+ T cells

Figure S4 The role of sDC scaffolds in T cell stimulation by cytokines. **(A)** TNFα secretion into supernatant after 16 h of T cell stimulation with P-αCD3 mixed with unbound IL-2 or P-IL-2, or P-αCD3/IL-2med. In each stimulation, the same amount of IL-2 was used. The cells were stimulated using 500 ng/ml αCD3 or 100 ng/ml αCD3. **(B)** Amount of αCD3 bound to T cells after 16 h of incubation with 500 ng/ml and 100 ng/ml P-αCD3 mixed with unbound IL-2 or P-IL-2, or P-αCD3/IL-2med. Bound αCD3 was determined by flow cytometry analysis of A488 signals (x-axis of histograms). **(C)** Amount of IL-2 bound to T cells after 16 h of incubation with 100 ng/ml P-αCD3 mixed with unbound IL-2 or P-IL-2, or P-αCD3/IL-2med. Bound IL-2 was determined by flow cytometry analysis of AF647 signals (x-axis of histograms). **(D)** Proliferation of T cells after 72 h of stimulation with 100 ng/ml P-αCD3 mixed with unbound IL-2 or P-IL-2, or P-αCD3/IL-2med determined by flow cytometry analysis, measuring the dilution of Celltrace Violet (x-axis of histograms). The mean number of cycles was calculated for each experiment. **(E)** CD25 expression of T cells after 16 hours of incubation with 500 ng/ml and 100 ng/ml of P-αCD3 mixed with unbound IL-2 or P-IL-2, or P-αCD3/IL-2med. To determine CD25 expression, the cell surface was stained using an anti-CD25-PE antibody, followed by flow cytometry analysis. **(F)** Amount of IL-2 bound to non-activated and activated CD4+ T cells and (G) CD8+ T cells after 16 hours of incubation with 500 ng/ml of P-αCD3 mixed with unbound IL-2 or P-IL-2, or P-αCD3/IL-2. To obtain activated CD25+ T cells, the cells were stimulated with αCD3/aCD28-functionalized Dynabeads for 24 h. Bound IL-2 was determined by flow cytometry analysis of AF647 signals (x-axis of histograms). The histograms show one representative experiment of duplicate stimulation of T cells from three healthy donors for non-activated (top/white box) and activated (bottom/grey box) T cells. After T cell stimulation, the values were normalized to the stimulation with 500 ng/ml of P-αCD3/IL-2med (non-activated CD8+ T cells). The normalized values of duplicate stimulations of three donors were pooled to obtain mean and SEM values, as depicted in the bar graphs. (H) Dot plot of flow cytometry measurements of αCD3-coated and αCD3/IL-2-coated microbeads to show successful coating with αCD3 and IL-2. Samples used in the T cell stimulation experiments are depicted in green (B-αCD3) and red (B-αCD3/IL-2). *$p < 0.05$, **$p < 0.01$, ***$p < 0.001$.

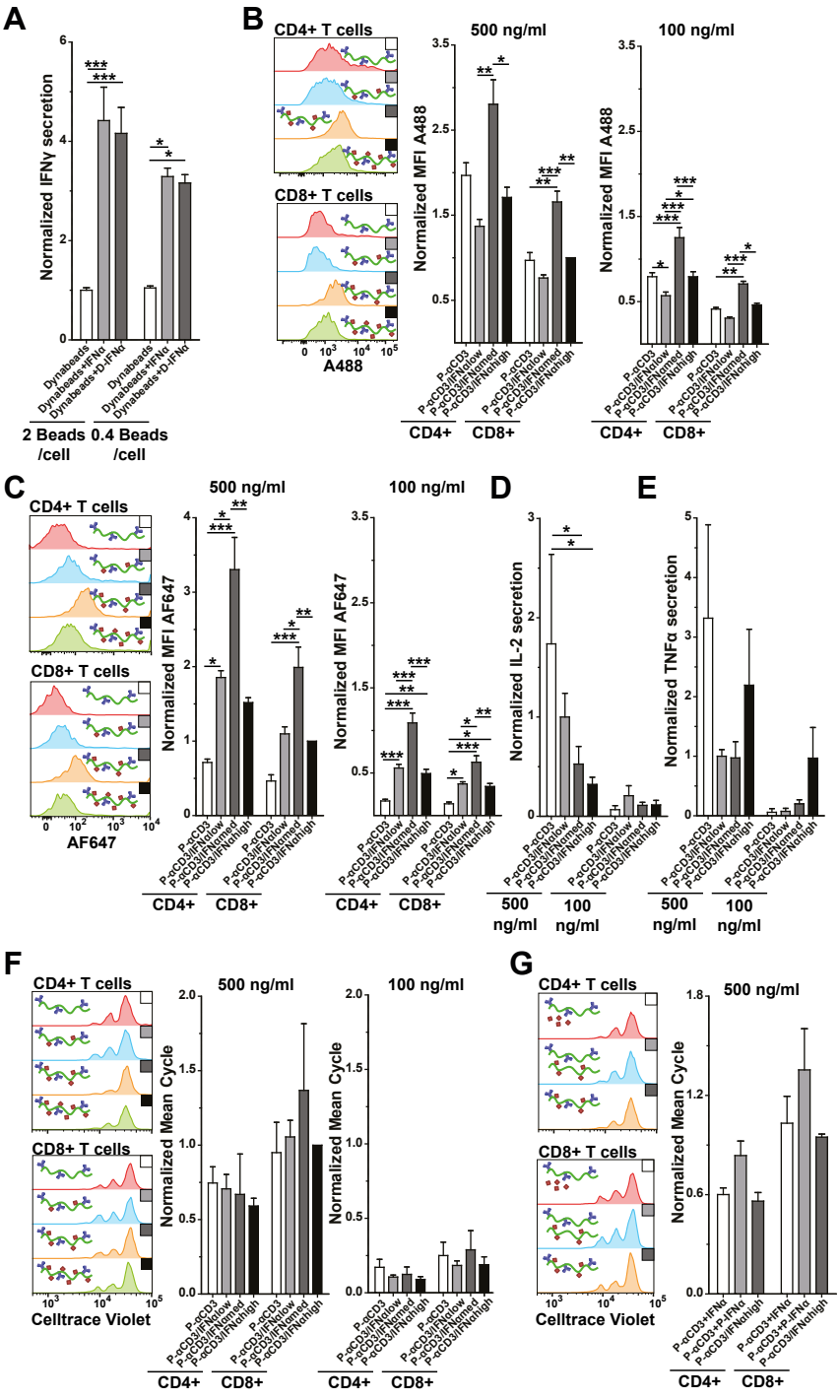
A
Normalized IFNγ secretion
Dynabeads
Dynabeads+IFNα
Dynabeads+D-IFNα
2 Beads /cell
0.4 Beads /cell
B
CD4+ T cells
CD8+ T cells
A488
500 ng/ml
100 ng/ml
Normalized MFI A488
P-αCD3
P-αCD3/IFNαlow
P-αCD3/IFNαmed
P-αCD3/IFNαhigh
CD4+
CD8+
C
CD4+ T cells
CD8+ T cells
AF647
500 ng/ml
100 ng/ml
Normalized MFI AF647
D
Normalized IL-2 secretion
500 ng/ml
100 ng/ml
E
Normalized TNFα secretion
F
CD4+ T cells
CD8+ T cells
Celltrace Violet
500 ng/ml
100 ng/ml
Normalized Mean Cycle
G
CD4+ T cells
CD8+ T cells
Celltrace Violet
500 ng/ml
Normalized Mean Cycle
P-αCD3+IFNα
P-αCD3+P-IFNα
P-αCD3/IFNαhigh
P-αCD3+IFNα
P-αCD3+P-IFNα
P-αCD3/IFNαhigh

Figure S5 Biological activity of PIC-IFNα conjugates **(A)** IFNγ secretion of T cells treated with Dynabeads alone, or together with IFNα or DBCO- and dye-functionalized IFNα (D-IFNα). The cells were stimulated using 2 beads/cell and 33 ng/ml IFNα (left) or 0.4 beads/cell with 6.6 ng/ml IFNα (right). **(B)** Amount of αCD3 bound to T cells after 16 h of incubation with 500 ng/ml and 100 ng/ml P-αCD3, functionalized with different IFNα densities. Bound αCD3 was determined by flow cytometry analysis of A488 signals (x-axis of histograms). **(C)** Amount of IFNα bound to T cells after 16 h of incubation with 500 ng/ml and 100 ng/ml P-αCD3, functionalized with different IFNα densities. Bound IFNα was determined by flow cytometry analysis of AF647 signals (x-axis of histograms). **(D)** IL-2 secretion and **(E)** TNFα secretion into the supernatant after 16 h of stimulation of T cells with P-αCD3, functionalized with different IFNα densities. The cells were stimulated using 500 ng/ml αCD3 or 100 ng/ml αCD3. **(F)** Proliferation of T cells after 72 h of stimulation with 500 ng/ml P-αCD3, functionalized with different IFNα densities. Proliferation was determined using flow cytometry analysis, measuring the dilution of Celltrace Violet (x-axis of histograms). The mean number of cycles was calculated for each experiment. **(G)** Proliferation of T cells after 72 h of stimulation with 500 ng/ml P-αCD3 mixed with unbound IFNα or P-IFNα, or P-αCD3/IFNαhigh. Proliferation was determined by flow cytometry analysis, measuring the dilution of Celltrace Violet (x-axis of histograms). The mean number of cycles was calculated for each experiment. The histograms show one representative experiment of duplicate stimulation of T cells from three healthy donors for CD4+ T cells (upper panel) and CD8+ T cells (lower panel). After T cell stimulation, the values were normalized using the value obtained from stimulation with Dynabeads **(A)** as the reference or, alternatively, the stimulation with 500 ng/ml of P-αCD3/IFNαhigh (CD8+ T cells). The normalized values of duplicate stimulations of three donors were pooled to obtain mean and SEM values, as depicted in the bar graphs. *$p < 0.05$, **$p < 0.01$, ***$p < 0.001$.

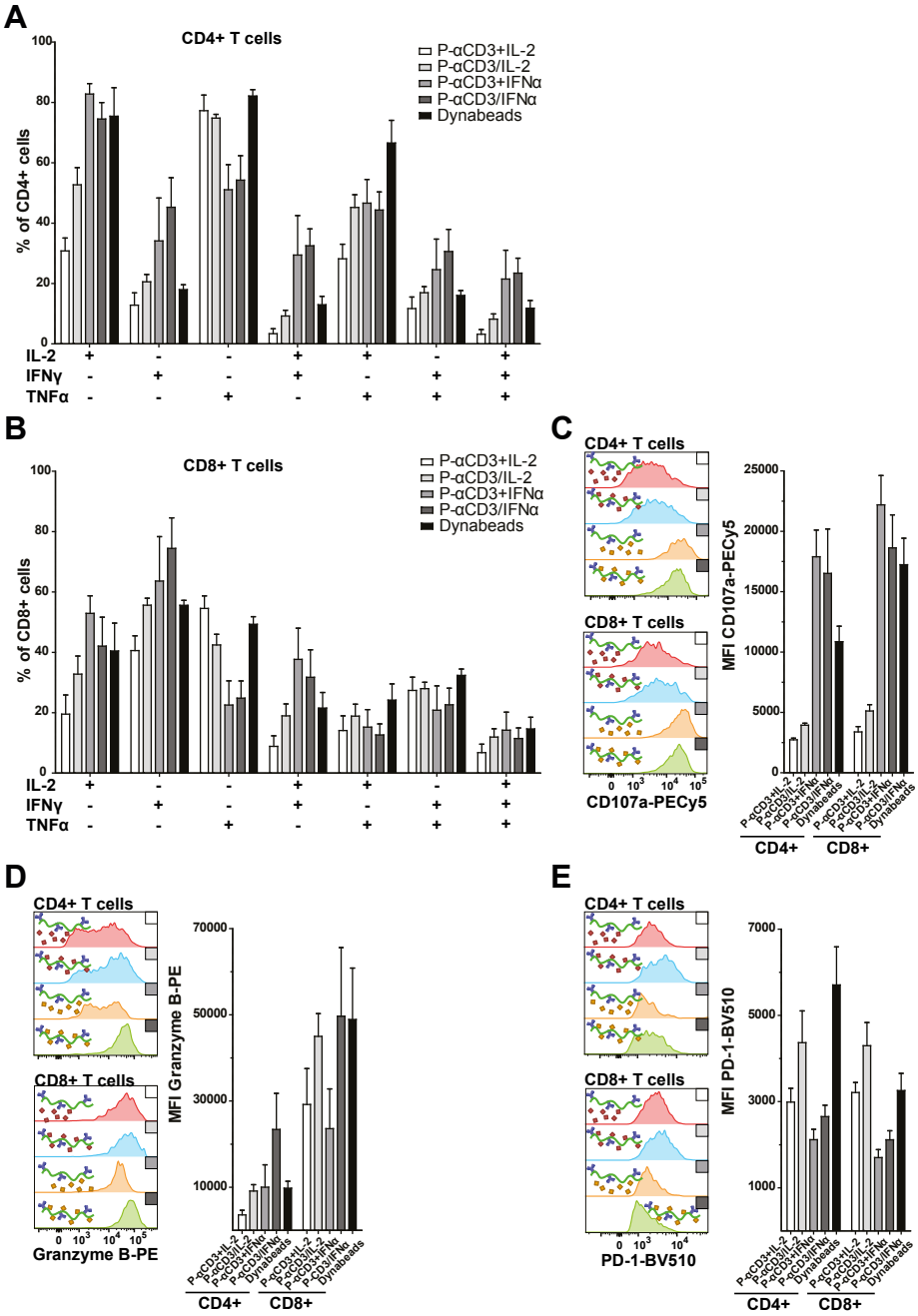
A
CD4+ T cells
% of CD4+ cells
P-αCD3+IL-2
P-αCD3/IL-2
P-αCD3+IFNα
P-αCD3/IFNα
Dynabeads
IL-2
IFNγ
TNFα
B
CD8+ T cells
% of CD8+ cells
C
CD4+ T cells
CD8+ T cells
CD107a-PECy5
MFI CD107a-PECy5
CD4+
CD8+
D
Granzyme B-PE
MFI Granzyme B-PE
E
PD-1-BV510
MFI PD-1-BV510

Figure S6 Functional consequences of 14-day T cell stimulation with PIC-cytokine conjugates. **(A, B)** T cells were stimulated with 500 ng/ml P-αCD3 mixed with IL-2, P-αCD3/IL-2, P-αCD3 mixed with IFNα, P-αCD3/IFNα or Dynabeads and re-stimulated after 7 days. After 14 days, the cytokine production capacity of these T cells was determined after 6 h PMA + ionomycin stimulation in the presence of Brefeldin A and monensin, after which intracellular staining and flow cytometry analysis revealed cytokine expression profiles for IL-2, IFNγ and TNFα of **(A)** CD4+ T cells and **(B)** CD8+ T cells. **(C-E)** Expression of **(C)** CD107a, **(D)** Granzyme B and **(E)** PD-1. 14-day-stimulated T cells were re-stimulated with PMA + ionomycin in the presence of Brefeldin A and monensin. An anti-CD107a-PECy5 antibody was used to determine the expression of the degranulation marker CD107a (C, x-axis of histograms) by flow cytometry analysis. Intracellular staining for Granzyme B and cell surface staining for PD-1 were performed to determine the expression of these molecules. The histograms show one representative experiment of duplicate stimulation of T cells from three healthy donors for CD4+ T cells (upper panel) and CD8+ T cells (lower panel). Pooled mean fluorescence intensities (MFI) ± SEM are depicted in the bar graphs. *p < 0.05, **p < 0.01.

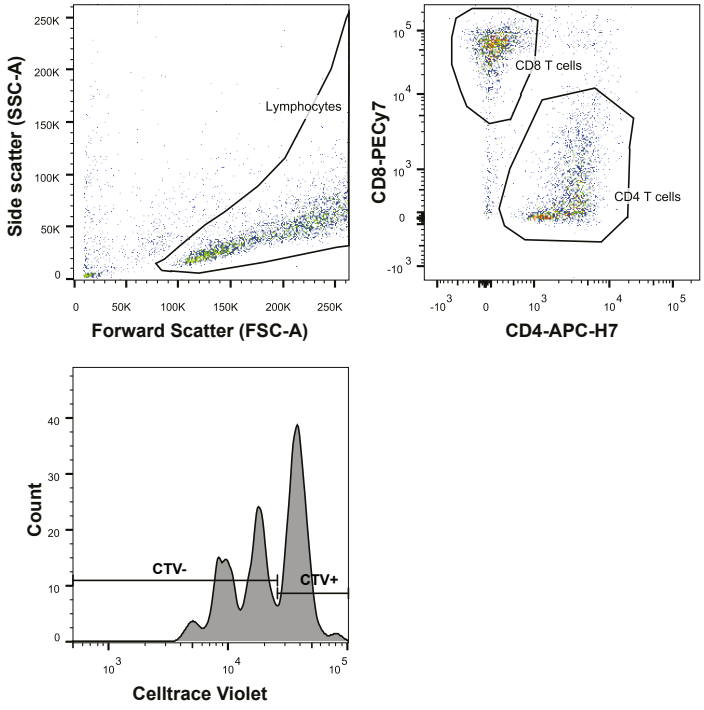

Figure S7 Gating strategy for flow cytometry experiments. Lymphocytes were first gated using forward (FSC-A) and side scatter (SSC-A). Subsequently, CD4 and CD8 T cells were gated using APC-H7 and PECy7 signals, respectively. Non-proliferated T cells were gated as Celltrace Violet (CTV)-positive cells and proliferating T cells as CTV-negative.

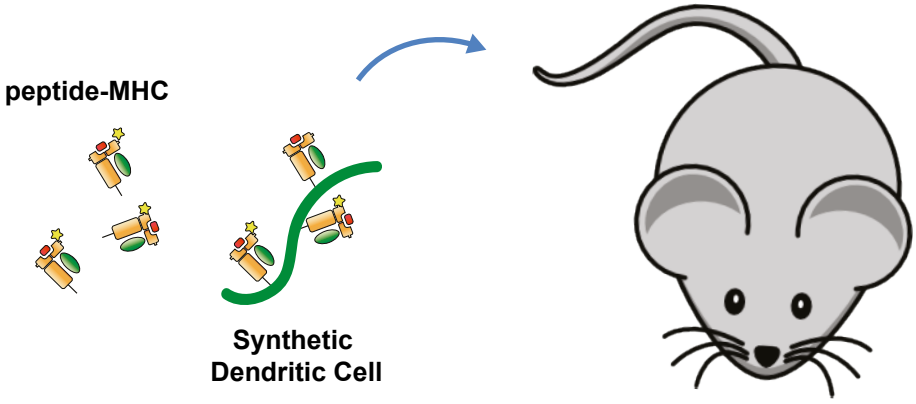
peptide-MHC
Synthetic
Dendritic Cell

7

Antigen-specific T cell activation using filamentous synthetic Dendritic Cells

Loek J. Eggermont, Roel Hammink, Michael Valente,
Carla Rodriguez Mogeda, Jorieke Weiden, Jurjen Tel, Carl G. Figdor

Abstract

Artificial antigen-presenting cells (aAPCs) are powerful tools that can be used to deliver stimulatory signals to T cells for active antigen-specific immunotherapy. In particular, polyisocyanopeptide (PIC)-based synthetic Dendritic Cells (sDCs) are a potent class of aAPCs due to their semi-flexible and filamentous structure. Previous work demonstrated that sDCs can induce strong polyclonal T cell responses. However, they have not been used for antigen-specific activation of T cells to this point. In this chapter, antigen-specific sDCs are developed through conjugation of different peptide-MHC complexes to PICs. We demonstrate that these novel structures are capable of inducing specific activation of human T cells transfected with TCRs recognizing the NY-ESO-I cancer antigen. In addition, sDCs can specifically stimulate mouse OT-1 cells both *in vitro* and *in vivo*. These preliminary results demonstrate that in addition to their capacity to induce polyclonal T cell stimulation, PICs are also promising sDC scaffolds for antigen—specific immunotherapy.

Introduction

Since the introduction of cancer immunotherapy, treatment options for advanced cancers such as metastatic melanoma have greatly increased [1,2]. The application of cytokines (such as IL-2 and IFN-α2b) and checkpoint inhibitors (CTLA-4 and PD-1) have led to significant improvement of survival rates in melanoma patients over the past decades. Cytokine therapies can stimulate immune cells to enhance immune responses, whereas checkpoint blockade releases the brakes on immune cells. This induces anti-tumor immunity in immunologically active cancers [3–6]. However, since these therapies are not antigen-specific, in many cases they can also lead to dangerous side effects due to overstimulation of the immune system [7,8]. This puts limitations on the applicable therapeutic doses of immune-stimulating agents, which has inspired the development of antigen-specific anti- cancer therapies. For these treatments, immune responses are specifically induced against antigens expressed on cancer cells, thereby greatly decreasing off-target side effects [9].

In general, this specific anti-tumor immunity relies on generation of antigen-specific T cells. These cells specifically recognize antigens expressed on tumor cells and subsequently eliminate these cells. In advanced melanoma, presence of functional tumor antigen-specific T cells is correlated with a better prognosis [10]. A successful method to amplify numbers of antigen-specific T cells makes use of Adoptive Cell transfer (ACT) of T cells. Generally, ACT-based therapies exploit tumor infiltrating T lymphocytes isolated from tumor biopsies that specifically recognize tumor antigens [11–14]. These T cells are expanded to large numbers before being re-injected into the patient, which in some successful cases leads to marked tumor regression. The efficacy of these therapies is dependent on the expansion and generation of functional antigen-specific T cells, as was demonstrated by injection of specific T-cell clones [15]. Interestingly, tumor-infiltrated T cells with a wide variety of additional tumor-antigen specificities have been identified [16]. In melanoma, antigens targeted by the infused T cells include cancer-testis antigens, cell-type specific (melanocyte) antigens and neo-antigens. Cancer-germline antigens (e.g. NY-ESO-I) are antigens derived from genes that are not expressed in healthy adult tissue, while melanocyte antigens, (e.g. gp100, tyrosinase and MART-1) are generally also present on healthy melanocytes. Both these types of antigens are often shared between patients [16]. In contrast, neo-antigens are the direct result of cancer-specific somatic mutations, and are therefore often unique peptides. Although more complicated to incorporate into other therapeutic strategies, these peptides have proven to be even more potent targets [17].

Experiments with T cells that express transgenic T cell receptors (TCRs) further demonstrate the potency of (high-affinity) antigen-specific T cells in cancer therapies. Using this approach, T cells transduced with engineered TCRs against MART-1, gp100 and NY-ESO-1 have shown clinical responses after adoptive transfer into cancer

patients [18,19]. Engineering approaches to increase TCR affinity also lead to augmented anti-tumor immunity, but can induce lysis of healthy cells expressing low levels of these antigens [20,21]. Thus, application of antigen-specific T cells can lead to highly potent cancer immunotherapies with lower toxicity.

Alternatively, ex vivo generated antigen-loaded antigen-presenting cells, most prominently dendritic cells (DCs), are widely used for antigen-specific immunotherapy [22]. For this, DCs are isolated from cancer patients, after which they are cultured *ex vivo* with adjuvants and loaded with tumor antigens. After DCs are properly matured and present anti-cancer antigens, they are re-injected back into cancer patients to stimulate specific T cell clones and evoke an antigen-specific response [22]. This form of cell-based immunotherapy induces considerable clinical responses in a small portion of patients with metastatic cancer. Also for this therapy, anti-tumor immune responses are mainly mediated by CD8+ T cells. These cells are activated through peptide-MHC complexes that are expressed on the infused DCs [23]. In this way, long-lasting clinical responses were induced against gp100, tyrosinase, MART-1 and NY-ESO-1 [24,25]. These trials clearly demonstrate objective clinical efficacy through *in vivo* activation of antigen-specific CD8+ T cells with antigens presented on class I MHC complexes.

Although cell-based therapies with T cells and DCs hold great promise of antigen-specific immunotherapies, these approaches are highly laborious and expensive. The need for large investments in infrastructure and tailor-made vaccines that require *ex vivo* cell culture for each patient hampers wide-spread application of ACT. A promising alternative approach towards an off-the-shelf vaccine instead makes use of artificial Antigen-Presenting Cells (aAPCs) [26]. These synthetic mimics of immune cells allow for highly controlled activation of T cells through multivalent binding to TCRs and co-stimulatory molecules [27,28]. We have developed a novel class of aAPCs based on polyisocyanopeptides (PICs) scaffolds. When these semi-flexible filamentous 100-1000 nm-long polymers are modified with biomolecules they can accommodate efficient multivalent interactions with T cells. Previously, we demonstrated that stimulatory anti-CD3 antibodies, that bind and trigger TCR co-receptor CD3, induce potent polyclonal activation of T cells when conjugated to PICs [29,30]. Through conjugation of co-stimulatory antibodies and cytokines to the same polymer chains, T-cell responses can be further enhanced to give full-blown activation and proliferation, as was demonstrated in chapters 4 and 6 [31]. These aAPCs are especially attractive due to their small size and straightforward characterization. Although it was established that PICs are highly suitable scaffolds for aAPCs, the use of anti-CD3 hampers their application in therapeutic settings because of its polyclonal mode of stimulation.

Here, we develop antigen-specific PIC-based aAPC through conjugation of pMHC complexes and establish a modular approach for synthesis of pMHC-PICs. For induction

of T cells against human cancer antigens, peptides derived from NY-ESO-I and MART-1 loaded in class I MHC (HLA*0201) are conjugated to PICs. To further boost T-cell responses, anti-CD28 antibodies and IL-2 are also conjugated to these scaffolds. Additionally, ovalbumin-specific aAPCs were generated and assessed their capacity towards both *in vitro* and *in vivo* stimulation of mouse T cells. Taken together, we here demonstrate the feasibility of producing pMHC-PIC conjugates and establish their potential for *in vivo* antigen-specific immunotherapy.

Results and discussion

Production and characterization of peptide-MHC complexes. Polyisocyanopeptide (PIC)-protein conjugates have been established as efficient synthetic DCs for polyclonal stimulation of human T-cells. For these polyclonal stimulations, anti-CD3 antibodies were used in chapters 2-6 to stimulate the CD3 co-receptor of TCRs, which induces non-specific activation of all human T cells [29–31]. To create PIC-based sDCs that can induce antigen-specific monoclonal T-cell activation, anti-CD3 antibodies need to be replaced by specific peptide-MHC (pMHC) complexes. For this, peptide-MHC-complexes were produced according to a protocol adapted from Toebes et al. [32,33]. Genes encoding for human β2m, human class I HLA-A2 heavy chain and mouse class I H2-K^b heavy chain (Figure S1) were each expressed separately in BL21 bacteria. Inclusion bodies were isolated containing the desired proteins and denatured using urea. To produce the complexes, heavy chain and β2m were refolded in the presence of short peptide antigens (Figure 1a). In this way, human HLA-A*0201 pMHC complexes and mouse pH2-K^b-complexes were developed. Human pMHC was made presenting short immunogenic peptides derived from NY-ESO-1 and MART-1, and mouse pMHC contained an OVA-derived short peptide. Refolded complexes were concentrated and size exclusion chromatography was performed to both purify pMHC complexes and analyze complex formation. SDS-PAGE gel electrophoresis revealed protein bands at 34 kDa and 13 kDa, corresponding with molecular weights of MHC heavy chain and β2m, present in the first protein-containing fractions eluted after size exclusion. This indicates the presence of refolded pMHC, since only completely refolded pMHC complexes are stable [33](Figure 1b).

To determine biological activity of human NY-ESO-I-MHC complexes and their compatibility with aAPCs, NY-ESO-I-MHC was reacted to microbeads to obtain beads with two different pMHC densities. These pMHC-microbeads could be used to determine whether pMHC is active when immobilized. To assess this, human CD8+ T cells were transfected with a TCR specific for the produced NY-ESO-I-presenting HLA-A2 complex. These NY-ESO-I-specific T-cells were then stimulated with pMHC-microbead conjugates and unbound pMHC in presence of IL-2, and IFNy

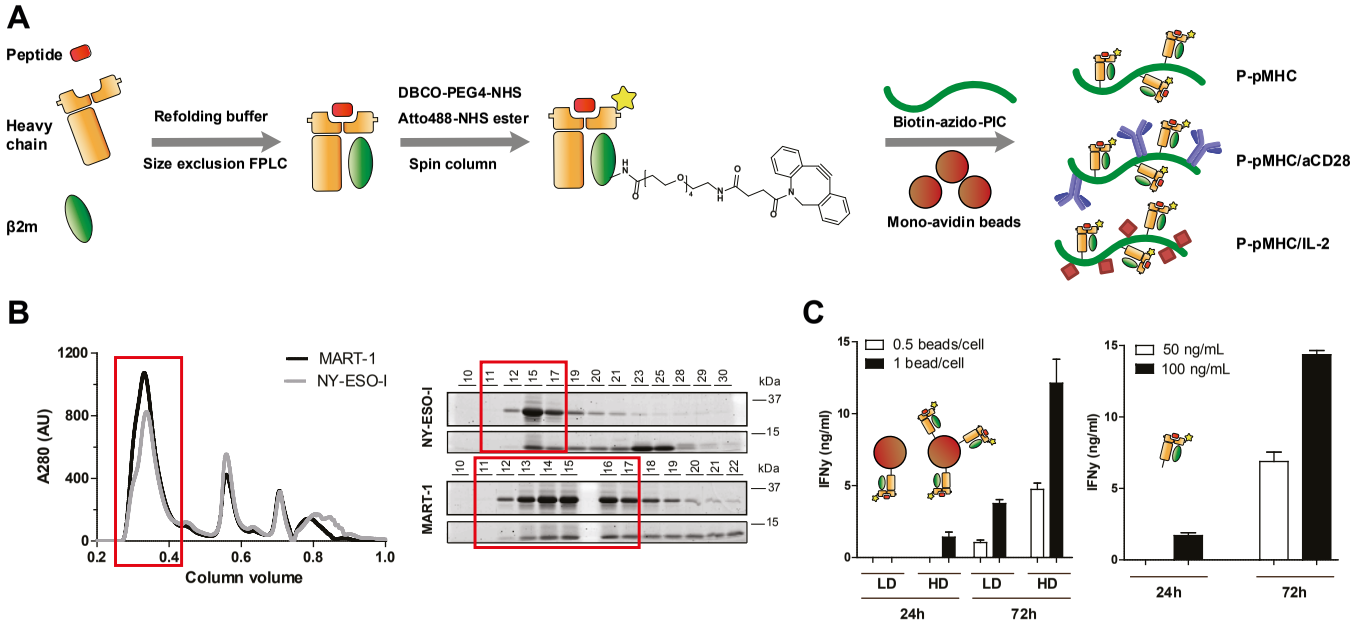

D

Sample	Ratio DBCO/MHC	Ratio Dye/MHC	Nanodrop mg/mL
NY-ESO-I	2.0	2.0	0.29
MART-1	4.1	3.7	0.41
OVA	3.3	2.4	0.5

E

Sample Name	Spacing pMHC (nm)	Spacing aCD28 (nm)	Spacing IL-2 (nm)	Ratio to pMHC
P-NY-ESO-I	251 ± 58			
-/CD28	227 ± 25	206 ± 14		1.1
P-MART-1	175 ± 10			
-/CD28	185 ± 15	187 ± 23		1.0
-/IL-2	175 ± 13		27 ± 2	6.5

Figure 1 Production and characterization of pMHC-PIC conjugates **(A)** Schematic depiction of synthetic strategy for the development of antigen-specific PIC aAPCs. MHC class I heavy chain and β2m were refolded with short peptides and purified using size exclusion chromatography. Refolded pMHC complexes were functionalized with DBCO-4EG NHS ester and Atto488-NHS ester, after which they were conjugated to azide- and biotin-functionalized PICs. The resulting PIC-protein complexes were purified over magnetic mono-avidin beads. **(B)** Trace of Absorbance at 280 nm (top) and SDS-PAGE gel electrophoresis (bottom) of peptide-MHC complex size exclusion purification for MART-1 and NY-ESO-I antigens refolded in HLA-A*0201 complexes. Fractions corresponding with pMHC complex peak are depicted in the red boxes **(C)** IFNy secretion 24h and 72h after stimulation of NY-ESO-I-specific transfected CD8+ T cells. CD8+ T cells were transfected with an NY-ESO-I-specific TCR and stimulated with low (LD)- and high (HD)-density pMHC beads at 1 bead/cell and 0.5 bead/cell (left bar graph), or with 100 ng/mL unbound pMHC (Right bar graph). After 24 hours and 72 hours, supernatant was collected and IFNy secretion was determined by ELISA. **(D)** Degree of DBCO and dye labelling after functionalization and purification of peptide-MHC complexes as determined by spectrophotometry measurements **(E)** Protein densities of PIC-conjugated proteins after purification. Fluorescence of protein-conjugated dyes was used to determine concentrations of the different proteins conjugated to PICs. PIC concentration could be determined using circular dichroism. For both fluorescence and CD signals, duplicate measurements were done.

concentrations in supernatant were measured after 24 and 72 hours (Figure 1c). After 24 hours, secretion of IFNy was detected for high density pMHC-beads, while after 72 hours, also low density-pMHC beads had induced IFNy secretion in a concentration-dependent fashion. Importantly, with this it was demonstrated that functional pMHC complexes were produced and that these complexes can retain functionality when conjugated onto a rigid aAPC scaffold. In contrast to anti-CD3 stimulations reported in previous chapters, unbound pMHC was able to induce high IFNy secretion levels. Although microbead aAPCs have been reported to induce increased T-cell activation compared to unbound pMHC, unbound HLA molecules are known to have some stimulatory capacity as well [34–37]. Although not determined exactly for dynabeads, pMHC concentrations in both experiments are likely in a similar range. Additional concentrations of beads and pMHC should be tested to see whether stimulation of dynabeads at higher concentrations also induce similar IFNy secretion. Further increasing pMHC density and co-conjugation of costimulatory ligands on these beads will probably also increase T-cell responses beyond levels of unbound pMHC [38,39]. Taken together, it was demonstrated that functional pMHC complexes were produced and that these complexes can retain their functionality when used on microbead aAPCs.

Synthesis of pMHC-containing sDCs. After successfully producing peptide-MHC complexes and having established their biological activity, pMHCs were functionalized to prepare them for further conjugation to PICs. For this, complexes were reacted to DBCO-4EG-NHS ester and Atto488-NHS ester as described for other proteins used in chapters 3-6 of this thesis [40]. Spectrophotometry of functionalized complexes revealed successful reactions of NHS-esters (Figure 1d). While aiming for two functional groups per protein complex, NY-ESO-I-MHC, MART-1-MHC and OVA-K^b had protein:DBCO:dye ratios of 1:2:2, 1:4.1:3.7 and 1:3.3:2.4, respectively. These data demonstrate that, similar to antibodies and cytokines used before, pMHC-complexes were also efficiently reacted to NHS esters to introduce a dye and DBCO functionality.

Having demonstrated that pMHC-complexes were properly labelled with DBCO and dye, they were conjugated to azide- and biotin-containing PICs. Functionalized pMHCs were mixed with polymers and PIC-pMHC conjugates were purified over magnetic mono-avidin beads using the biotin tag as described in chapter 3 [40]. To synthesize NY-ESO-I-specific PICs, polymers were reacted to either pMHC alone, or NY-ESO-I MHC together with a DBCO-functionalized AlexaFluor350-labelled anti-CD28 antibody using the approach described in chapter 4. For MART-1, polymers were made containing MART-1-MHC alone, MART-1-MHC/anti-CD28 and MART-1/IL-2 (as described in chapter 6). Mouse H2-K^b-OVA polymers were made with only this complex, or combined with IL-2. Protein concentrations were determined using their respective fluorescent signals and polymer concentration was assessed using circular dichroism. Combining these methods, protein densities conjugated to PICs were calculated for human MHC-containing samples (Figure 1e). With one pMHC every 240 nm for NY-ESO-I-MHC and a spacing of 180 nm for MART-1-MHC (approximately 2 NY-ESO-1-MHC or MART-1-MHC complexes per polymer), pMHC densities were comparable for the different samples. Anti-CD28-containing polymers contained similar amounts of pMHC and anti-CD28. Although pMHC and IL-2 densities were in a similar range as anti-CD3 and IL-2 densities reported in chapter 6, pMHC/IL-2-PICs contained 6.5-fold more IL-2 than pMHC, which is markedly higher than the optimal IL-2/anti-CD3 ratios used in chapter 6. Using lower IL-2 densities may result in conjugates with more optimal T-cell stimulatory capacity. In addition, H2-K^b-OVA polymers were produced using the same method, but no circular dichroism was done to determine the PIC/protein ratios to avoid contamination that could affect *in vivo* experiments later on. Compared to conjugation of antibodies and cytokines to PICs, conjugation reactions with functionalized pMHC were less efficient, since twice the amount of pMHC was needed to obtain similar PIC-bound densities. Probably, the lowered reactivity is a result of unavailable DBCO functionalities due to sodium azide contamination after spin filtration. Since pMHC is prone to aggregation at lower concentrations, small pMHC aggregates in the reaction mixture could also account for a lower availability of functionalized protein complexes to react to these polymers.

With these measurements, it was demonstrated that pMHCs can be conjugated to PICs to create antigen-specific filamentous synthetic DCs. This synthetic strategy is applicable to both human HLA*0201 complexes with NY-ESO-I and MART-1 peptides, and for mouse H2-K^b complexes presenting an OVA-derived peptide. This approach can also be extended to other HLA types and additional peptide antigens.

Stimulation of NY-ESO-I-specific T cells using pMHC-presenting sDCs. After successfully synthesizing NY-ESO-I-specific sDCs, these PIC conjugates were assessed for their ability to stimulate T cells. For this, CD8+ T cells were transfected with mRNA encoding for an NY-ESO-I-specific TCR with over 80% efficiency (Figure 2a). As a control, mock transfected T cells were used to evaluate non-specific T-cell activation. Both NY-ESO-I-specific and mock-transfected T cells were stimulated with unbound NY-ESO-I-MHC or PIC-conjugated NY-ESO-I-MHC, either alone or in combination with anti-CD28 antibody. Additionally, cells were stimulated with the combined NY-ESO-I-MHC/CD28-PIC. After 24 hours, no IFNy could be detected for pMHC-PIC-stimulated cells. Unbound pMHC did induce low levels of IFNy secretion, indicating that polymer-bound stimulation was not efficient within the first 24 hours (Figure 2b). After 72 hours however, IFNy secretion of pMHC-PIC-stimulated was markedly increased, while unbound pMHC did not induce further secretion (Figure 2c). These observations are consistent with long-term stimulations that were done with anti-CD3-presenting PICs in chapter 2 [30]. These anti-CD3-sDCs were also able to induce sustained signalling and IFNy secretion over multiple days, whereas effects induced by unbound anti-CD3 where much shorter [30]. Strikingly, co-conjugation of pMHC and anti-CD28 showed a marked release of IFNy over 24 hours, which was 2.5-fold higher than IFNy secretion from mock-transfected cells, indicating an antigen-specific effect. Also, these levels were greatly increased after 72 hours, again demonstrating a long-term effect on T-cell activation of PIC-based sDCs. Although stimulation of NY-ESO-I-specific T cells clearly exhibited increased IFNy secretion compared to mock-transfected cells when stimulated with pMHC/CD28-PICs, conjugation of anti-CD28 to PICs also induced non-specific activation of T-cells. For other scaffolds, such as magnetic microbeads and iron-dextran nanoparticles, this effect was absent [35,41]. In contrast, PIC-conjugated anti-CD28 can induce low levels of early activation, as was observed for some PIC-antibody conjugates in chapter 4. Natural ligands for CD28, such as B7, or antibodies with lower affinity, could be used to further optimize PIC-aAPCs. Nonetheless, a great enhancement in IFNy secretion was observed for TCR-transfected T cells. With this, a first demonstration was given of functional PIC-based sDCs capable of antigen-specific human T cell activation. So far, the stimulatory capacity of NY-ESO-I-presenting PICs was established on T cells from two donors. To further establish reproducibility and modularity of our approach, these experiments should be extended to more donors and additional antigens such as MART-1 should be used for T-cell stimulation as well.

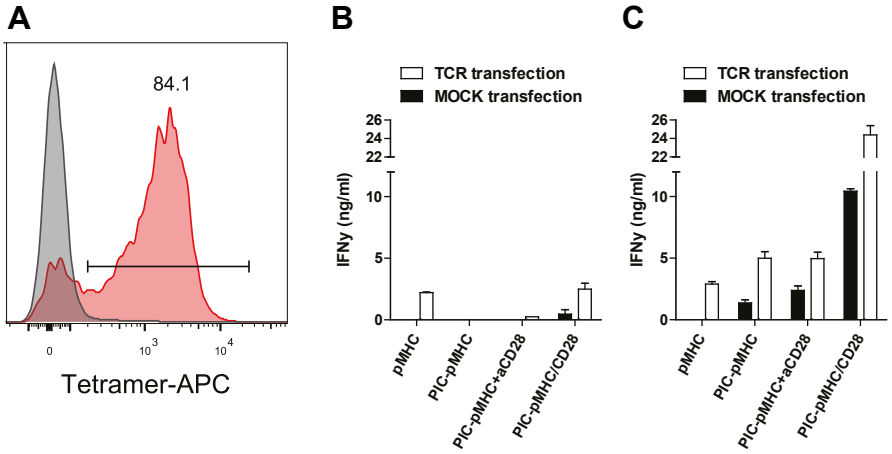

Figure 2 NY-ESO-I-specific *in vitro* stimulation of human CD8+ T cells **(A)** Histogram of TCR-transfected CD8+ T cells stained with NY-ESO-I-MHC tetramers (red). CD8+ T cells were isolated from healthy donor peripheral blood lymphocytes and mRNA transfection was done by electroporation. After this, cells were stained with APC-labelled NY-ESO-I-MHC tetramers and measured by flow cytometry. Staining of mock-transfected cells is shown in grey. **(B)** IFNγ secretion 24h and **(C)** 72h after stimulation of TCR-transfected CD8+ T cells. TCR-transfected CD8+ T cells were stimulated with 100 ng/mL pMHC. Duplicate stimulation of T cells from one healthy donor is shown.

MART-1 could also be used to expand non-transfected T-cells through multiple re-stimulations over several weeks [42]. The results presented here are the first demonstration of the antigen-specific stimulatory capacity of PIC-based sDCs.

***In vitro* stimulation of OVA-specific mouse T cells.** To apply antigen-specific sDCs in an *in vivo* model, mouse OVA-K^b-presenting PICs were synthesized using the same method as was applied for human pMHC-PICs. To test the synthesized OVA-K^b-containing PICs, purified OT-1 T cells were stimulated with OVA-K^b or with P-OVA-K^b. After 24 hours, CD69 expression was measured to evaluate the stimulatory capacity of the different PIC-protein conjugates. OVA-K^b-PICs were capable of inducing high levels of CD69, comparable to levels induced with unbound K^b-OVA, indicating a high potential to activate T cells (Figure 3a). After three days, proliferation was assessed through Celltrace Violet dilution, which revealed that K^b-stimulated T cells proliferated extensively (Figure 3b). For human T cells, presentation of signal 1 on PICs led to increased activation compared to stimulation with unbound anti-CD3 or pMHC, whereas activation of OT-1 T cells was not increased when OVA-K^b was conjugated onto PICs (Figure 3c-d).

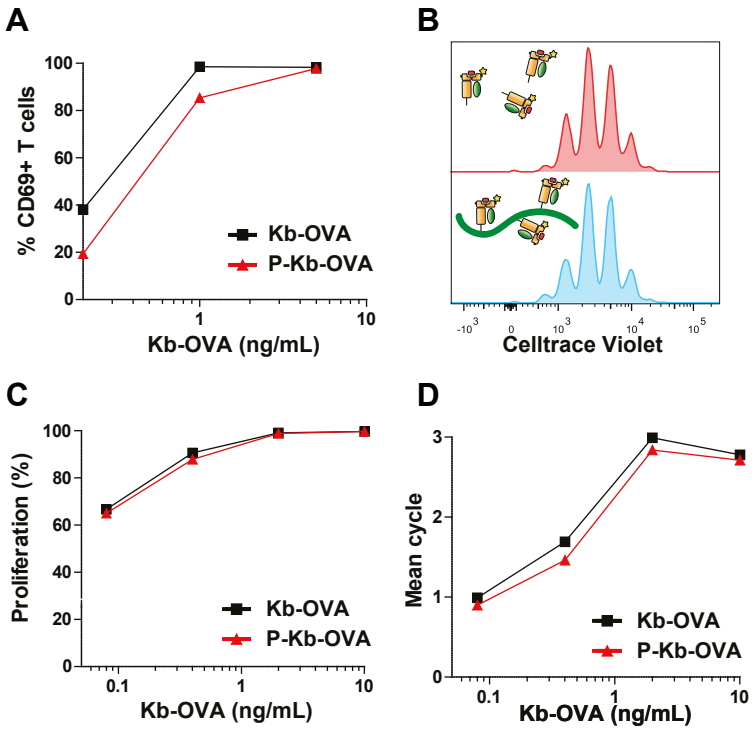

Figure 3 OVA-specific *in vitro* stimulation of mouse OT-1 cells. **(A)** Percentage of CD69-expressing OT-1 T cells 24h after *in vitro* stimulation with K^b-OVA or PIC-K^b-OVA. **(B)** Histrograms of Celltrace Violet dilution to determine proliferation of OT-I T cells after stimulation with K^b-OVA or PIC-K^b-OVA **(C)** Percentage of live OT-1 T cells that are proliferating after stimulation with K^b-OVA or PIC-K^b-OVA as determined by flow cytometry analysis of Celltrace Violet dilution. **(D)** Mean proliferation cycle of live OT-1 T cells after stimulation with K^b-OVA or PIC-K^b-OVA as determined by flow cytometry analysis of Celltrace Violet dilution. Representative experiment from two independent stimulations is depicted.

It is important to note that K^b-OVA densities conjugated onto the PICs was not determined. P-K^b-OVA conjugates with higher densities may be able to further increase T cell activation beyond levels of unbound K^b-OVA. Generally, monomeric pMHC complexes do not induce activation of CD8 T cells [43]. However, it is possible that interactions of OVA-K^b with the T cell surface or transfer of peptides to T cell MHC can explain the stimulatory capacity of monomeric OVA-K^b [36]. For stimulation with soluble dimers or tetramers of OVA-K^b, some induction of OT-1 T cell activation has also been reported [44,45]. Possibly, linking recombinant pMHC complexes to proteins like

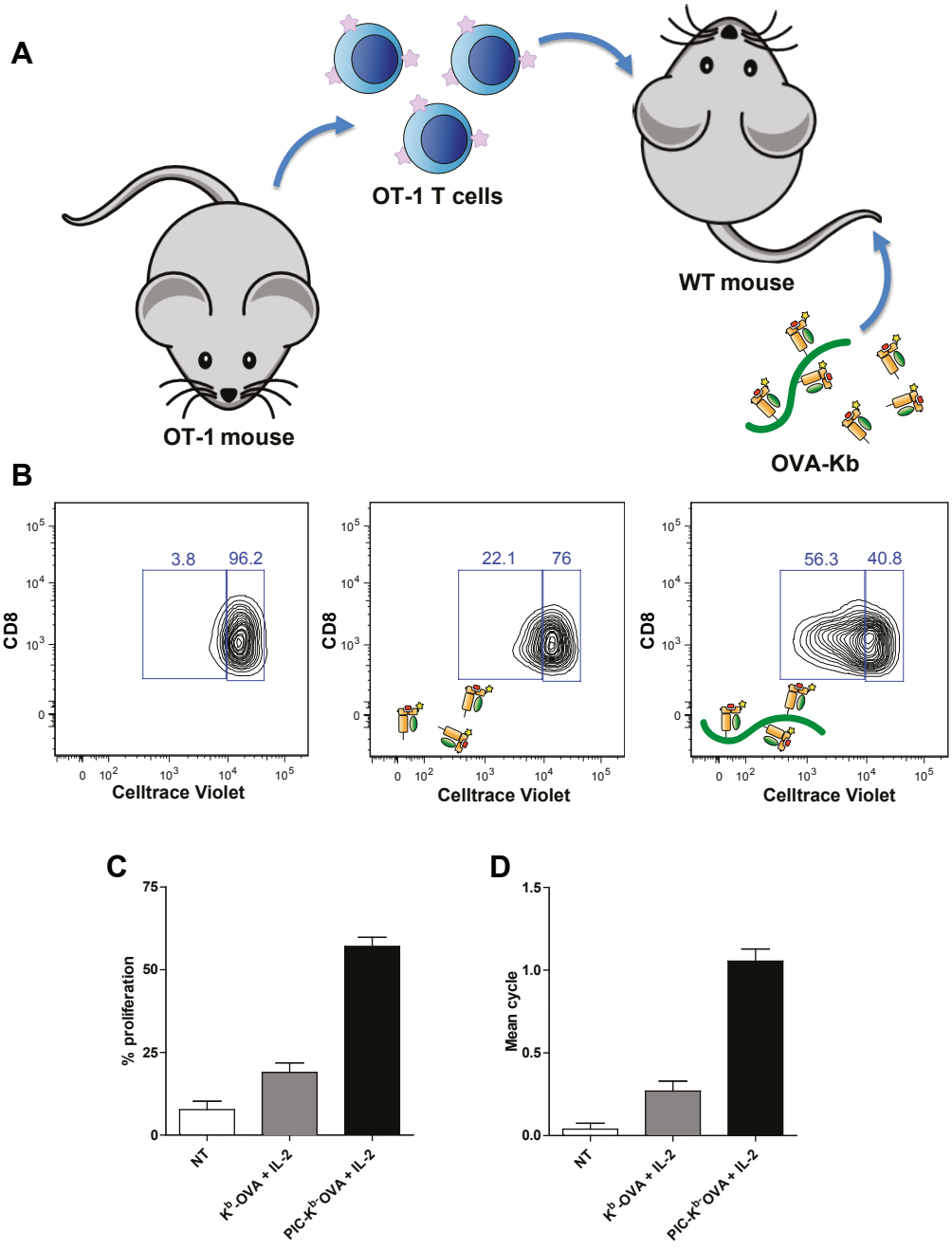
A
OT-1 T cells
OT-1 mouse
WT mouse
OVA-Kb
B
CD8
Celltrace Violet
3.8
96.2
22.1
76
56.3
40.8
C
% proliferation
NT
K^b-OVA + IL-2
PIC-K^b-OVA + IL-2
D
Mean cycle
NT
K^b-OVA + IL-2
PIC-K^b-OVA + IL-2

Figure 4 *in vivo* stimulation of OT-1 T cells in C57/BL6J mice **(A)** Schematic representation of *in vivo* stimulation of OT-1 T cells with K^b-OVA-PICs. CD8+ T cells are isolated from an OT-1 mouse, stained with Celltrace Violet dye and injected into C57/BL6J mice. After 1 day, 240 ng OVA-K^b-containing samples and 380 ng IL-2 are injected and after another two days, cells are harvested from spleens to measure proliferation **(B)** Histograms showing Celltrace Violet dye dilution to indicate proliferation of OT-1 T cells retrieved from spleens of treated mice. **(C)** Percentage of proliferating OT-1 T cells as determined by Celltrace Violet dye dilution. **(D)** Mean proliferation cycle of OT-1 T cells as determined by Celltrace Violet dye dilution. Stimulations were done on two mice per condition.

immunoglobulins and streptavidin could increase their stability, decrease interactions with cell membranes and decrease aggregation. This could help to limit stimulation in unbound form. In addition, cells that were stimulated with PICs containing a second stimulatory molecule, such as anti-CD28 or IL-2, did not further increase their activation compared to stimulation with unconjugated anti-CD28 (Figure S2a-b) or IL-2 (Figure S2c-d). OT-1 cells are highly sensitive to antigen-specific stimulation, as is apparent from the observed proliferation cycles OVA-K^b-stimulated cells undergo. Since these cells may be maximally stimulated with just this first signal, we could not observe an effect of additional co-stimuli or cytokines. In recent literature, elevated responses have been reported for OT-1 stimulation with microsized aAPCs presenting multiple signals [45–48], indicating that our PIC-pMHC conjugates could be further optimized to allow for optimal co-stimulation. Still, we have established that OVA-K^b does not lose its stimulatory capacity when conjugated to PICs. This confirms that PIC-pMHC conjugates can be efficient aAPCs for antigen-specific stimulation of mouse T cells.

***In vivo* treatment with PIC sDCs induces antigen-specific T-cell activation.** After having established that OVA-K^b-bearing PICs are capable of inducing potent T-cell responses *in vitro*, their capacity for *in vivo* antigen-specific T-cell stimulation was tested. For this, isolated OT-1 T cells were labelled with Celltrace Violet and adoptively transferred in C57/BL6J mice (Figure 4a). The following day, mice were vaccinated intravenously with OVA-K^b or OVA-K^b-PIC together with IL-2 and 2 days later, T cell activation was assessed by Celltrace dilution (Figure 4b). While OVA-K^b-stimulated cells showed some proliferation (approximately 20%), this was increased almost 3-fold when OT-1 T cells were stimulated with PIC-conjugated OVA-K^b (Figure 4c). Furthermore, PIC-OVA-K^b-stimulated T cells showed more rounds of proliferation compared to stimulation with the unbound complex (Figure 4d). This clearly demonstrates the potential of using PIC-based sDCs for *in vivo* T-cell stimulation. Thus, intravenously injected pMHC-PICs can stimulate T cells in the spleen and deliver

a stronger signal compared to unbound OVA-K^b, whereas no difference in effect was observed *in vitro*

Taken together, our results signify that pMHC conjugation to PICs can both improve their bio-distribution and increase their antigen-specific stimulatory capacity *in vivo*. Furthermore, injection of OVA-K^b/IL-2-PIC was performed to test the effect of co-conjugating this cytokine in an *in vivo* setting. However, stimulation with PIC-conjugated IL-2 did not markedly change T-cell proliferation compared to unbound IL-2 stimulation. This further highlights the need for optimizing MHC/IL-2 ratios in these multiple-signal conjugates, as protein densities of conjugates used in these experiments were not determined (Figure S3). As demonstrate in chapter 6, IL-2 densities should be tightly controlled to obtain a potent stimulatory effect of cytokine-presenting sDCs. Optimal pMHC and IL-2 densities still has to be determined for stimulation of mouse T cells. To further track the full effect of PIC-conjugated IL-2 *in vivo*, it may be necessary to assess effects of stimulation over longer periods of time and to make use of a less sensitive model for T-cell stimulation, that is more reflective of physiological activation. Nonetheless, these experiments demonstrated that PIC scaffolds are highly suitable for *in vivo* stimulation of antigen-specific T-cells.

Conclusions

Cancer immunotherapy has significantly improved clinical outcomes in patients with advanced disease, but can be limited by their non-specific side effects. Therefore, antigen-specific immunotherapies are being developed that show great promise towards both reducing these side effects and greatly improving potency of anti-cancer immune responses. With these therapies, antigen-specific T cells can be induced that accurately and potently target and kill cancer cells. However, many of these therapies are based on adoptive cell transfer, and require culture of immune cells *ex vivo*. This makes these strategies laborious and difficult to apply on a wide-spread clinical level. To circumvent the use of ACT, aAPCs can be used as cell-free systems to efficiently stimulate T cells.

In chapters 2-6 of this thesis, PICs have been established as potent artificial antigen-presenting cells for polyclonal stimulation of T cells by triggering CD3. Here, we have demonstrated that, instead of conjugating anti-CD3 antibodies, we can effectively produce pMHC-PIC conjugates. To this end, PIC-protein conjugates were demonstrated to be capable to act as potent aAPCs for antigen-specific stimulation of human T cells. Importantly, pMHC-PICs can also stimulate antigen-specific T cells *in vivo*.

The use of multiple antigens in addition to both human and mouse MHC complexes shows that these aAPCs are highly modular. To further broaden the scope

of cancers that can be targeted with this therapy, PIC-conjugates should be synthesized using additional HLA types and antigens. Furthermore, ratios with co-stimulatory molecules and cytokines can be further optimized to induce more potent stimulation of T-cells. These optimized pMHC-PICs need to be tested for T-cell stimulation in models that may be more biologically relevant than TCR- transfected T cells or OT-1 T cells used here. Instead, expansion of both naïve and intratumoral antigen-specific T cells, present within large populations of cells not specific for these antigens, could give a better idea of the clinical potency of these aAPCs. In conclusion, the preliminary experiments presented in this chapter have demonstrated the promise of semi-flexible filamentous PIC scaffolds as aAPCs for antigen-specific immunotherapy. More experiments on non-transgenic T cells and application of sDCs in *in vivo* tumor models are needed to further establish their potency.

Experimental Procedures

Materials and mice. OT-1 and C57/BL6J mice (female, 5-8 weeks old) were purchased from Charles River. DNA encoding b2m and mouse H2-K^b heavy chain were a kind gift from the Ton Schumacher lab. DNA for human HLA-A2 heavy chain was obtained from Thermofisher geneart. Amicon Ultra 30 kDa cut-off spin filters were obtained from Merck. Micro BCA assay kit, M-450 tosylactivated dynabeads, one Shot BL21(DE3) chemically competent E. Coli, human IFNy ELISA kit, RPMI, AlexaFluor-NHS esters and CellTrace Violet Cell Proliferation kit were from Thermofisher. Human and mouse CD8+ T cell isolation kits were purchased from Miltenyi Biotec. DBCO-4EG-NHS ester was from Jenabioscience. Atto488-NHS ester was from atto-tec. Human anti-CD28 (Clone 9.3) and mouse anti-CD28 (clone 37.51) were obtained from BioXCell. Recombinant IL-2 was purchased from cell sciences. X-vivo 15 medium was from Lonza. NY-ESO-I mRNA was a kind gift from Ugur Sahin, BioNTech AG (Mainz, Germany). NY-ESO-I tetramer (APC-A2/Kb Chimeric SLLWITQV-loaded) was from Proimmune. Mouse anti-CD69-PE antibody was from Biolegend.

Biotin-azido PIC synthesis. The polyisocyanopeptides (PICs) used in this study were synthesized according to literature procedures [29,31]. Briefly, non-functional methoxy and functional azide terminated monomers were reacted in a 30:1 ratio using a nickel catalyst (Figure S1a), statistically yielding a polymer with every 3.5 nm a functional azide group. Next, 60 % of the azide were converted to biotin using DBCO-4EG-biotin as described in literature [40]. The resulting azide biotin PICS were analyzed with Atomic Force Microscopy (Nanoscope III, digital instruments) operating in tapping mode in air, using NSG10 tips. For this, the polymer (10 ug/ml) was dropcasted on freshly cleaved mica for 5 minutes after which the substrate was dried under a

nitrogen flow (Figure S1b). From these images the polymer length could be established with imageJ, yielding an average length of 383 nm.

Production of pMHC complexes. Class I MHC refolding reactions were performed as described in literature [32,33]. Briefly, human HLA-A2, human b2m and mouse H2-K^b (sequences in figure S1) were produced by expression in *Escherichia Coli* and isolated as inclusion bodies. Proteins were denatured in 8M urea in 100mM Tris-HCl buffer (pH 8). For refolding reactions, short peptide antigens (MART-1_{26-35}: ELAGIGILTV, NY-ESO-$I_{157-165}$: SLLMWITQV, $OVA_{257-264}$: SIINFEKL) were dissolved in 50 mL of cold refolding buffer to a final concentration of 60 μM. To this solution, denatured b2m and class I MHC were added dropwise to a final concentration of 2 μM and 1 μM, respectively. Refolding reactions were incubated on a rotator at 4 °C overnight. Addition of denatured proteins and overnight incubation was repeated twice, after which the reaction mixtures were incubated on a rotator at 4 °C for 48 hours. After removal of aggregates, refolding reactions were concentrated on Amicon 30 kDa cut-off spin filters to a volume of 1-2 mL and pMHC complexes were purified using a Bio-Rad Enrich SEC70 size exclusion column in Bio-rad NGC medium-pressure liquid chromatography system. Fractions were collected with a Biofrac fraction collector, and analyzed for presence of pMHC using SDS-PAGE gel electrophoresis. Pooled fractions containing refolded pMHC complexes were concentrated over Amicon 30 kDa cut-off spin filters. Absorbance at 280 nm was used to calculate protein concentrations using the molar extinction coefficient of the pMHC complexes (99930 $M^{-1}cm^{-1}$ for human HLA-A2 complexes, 94770 $M^{-1}cm^{-1}$ for mouse H2-K^b-complexes). This method was verified using a micro BCA protein assay. For later use, the produced protein complexes, samples were snap-freezed in liquid nitrogen and stored at -80 °C.

Conjugation of pMHC to microbeads. To test whether the newly refolded pMHC complexes were functional when conjugated to conventional artificial APCs, 4.5 μm beads were coated with these complexes. For this, $8*10^7$ M-450 tosyl-activated dynabeads were dissolved in 200 μL PBS and 12.5 μg or 4.2 μg of NY-ESO-I-MHC complex was added to obtain beads with two different pMHC densities. The reaction mixture was incubated overnight at 4 °C on an rotator, after which beads were washed on Dynal MPC-L Magnetic Particle Concentrator (3x PBS+0.1%BSA+2mM EDTA, 3x PBS). pMHC-beads were used for functional experiments immediately after synthesis.

Functionalization of pMHC complexes. To functionalize pMHC with DBCO and Atto488 dyes, between 200-1000 ug of protein complexes were mixed with DBCO-4EG-NHS ester and Atto488-NHS ester in PBS in 1:4:4 ratios. After incubation for 2h at 4 °C on a rotator, functionalized pMHC was purified over a 2 mL 7K Zeba spin column. To determine the degree of DBCO and Atto488 labelling, the purified

complexes were analyzed by measuring their absorbance at 280, 309 and 501 nm on a nanodrop 200c spectrophotometer. After correcting for overlap of absorbance spectra of the individual molecules, protein, DBCO and Atto488 concentrations were calculated using molar extinction coefficients of the individual molecules (12000 $M^{-1}cm^{-1}$ for DBCO, 90000 $M^{-1}cm^{-1}$ for Atto488). Protein concentrations determined by nanodrop were verified using a micro BCA protein assay. Protein yields were typically around 30-70%.

Conjugation of pMHC to PICs. To develop antigen-specific PIC-based aAPCs, DBCO/Atto488-functionalized pMHC (0.5 equivalents with respect to azide groups on the PICS), DBCO/AlexaFluor350-functionalized anti-CD28 (0.2 equivalents) and/or DBCO/AlexaFluor647-functionalized IL-2 (0.5 equivalents) were added to 60 ug of azide-biotin functionalized PICs (1 mg/mL in PBS) and incubated overnight at 4 °C on a rotator. PIC-protein conjugates were purified over magnetic monoavidin beads as described in literature [40]. For this, reaction mixtures were incubated with 1mL of magnetic monoavidin bead solution for 2 hours at 4 °C, after which they were washed with PBS+0.1%tween-20 (2x) and PBS (4x) on a Dynal MPC-L Magnetic Particle Concentrator. Polymers were eluted from beads by incubation with PBS containing 2 mM biotin for 2 hours at 4 °C on a rotator. Concentrations of proteins conjugated to PICs were determined as described in previous chapters using a Tecan Spark 10M fluorescence plate reader. For human pMHC-PICs, polymer concentration was measured using circular dichroism (CD) (JASCO J-810).

Antigen-specific stimulation of NY-ESO-I TCR-expressing CD8 T cells. pMHC-PIC performance as antigen-specific aAPCs was tested on CD8 T cells expressing NY-ESO-I-specific T cell receptors (TCRs). For this, human peripheral blood lymphocytes were isolated from buffy coats obtained from healthy donors using ficoll density centrifugation. CD8+ T cells were isolated from peripheral blood lymphocytes using the Miltenyi CD8+ T cell isolation kit. After isolation, mRNA transfection using a Bio-rad gene pulser was done to induce expression of an NY-ESO-I-specific TCR. As a control, a mock transfection was performed. Transfection efficiency was determined by flow cytometry after cells were stained with NY-ESO-I-MHC-tetramers. 50.000 TCR-transfected CD8+ T cells were stimulated with 50-100 ng/mL pMHC or 25.000-50.000 protein-coated microbeads in X-Vivo medium containing 2% human serum at 37 °C. After 24h and 72h, supernatant was collected for ELISA measurement of IFNγ concentrations.

***In vitro* stimulation of mouse OT-1 T cells.** For stimulation of OVA-specific mouse T cells (OT-1 T cells), PIC-K^b-OVA conjugates were produced using the same method as described for human PIC-MHC-peptide conjugates. OT-1 CD8 T cells were isolated from

spleen and lymph nodes of OT-1 mice using the Miltenyi CD8 isolation kit. Cells were labelled with 5 uM Celltrace Violet to monitor proliferation, after which 30.000 OT-1 T cells were stimulated with varying concentrations of H2-K^b-OVA. Stimulations were done either in complete RPMI medium containing 10% FCS in presence of 2 µg/mL stimulatory anti-CD28 antibody or with addition of IL-2 amounts matching PIC-bound IL-2 concentrations. After 1 day, CD69 expression was determined using a FACSVerse flow cytometer and after 3 days, proliferation was analyzed by measuring Celltrace Violet dilution on the FACSverse flow cytometer.

***In vivo* stimulation of mouse OT-1 T cells.** Preliminary experiments on two mice per stimulation were done to establish the *in vivo* stimulatory capacity of our antigen-specific PIC-based aAPCs. CD8+ T cells were isolated from an OT-I mouse and labelled with Celltrace Violet as described before. C57/BL6J mice (5-8 week-old females from Charles River) were injected with 10^5 Celltrace-labelled OT-I cells. After 24h, 240 ng of K^b-OVA or PIC-K^b-OVA were injected intravenously together with 380 ng of IL-2. Furthermore, one mouse was injected with PIC-K^b-OVA/IL-2 (240 ng K^b-OVA and 380 ng IL-2 bound to PICs). Two days after injection, splenocytes were collected, stained for CD8 expression and T-cell proliferation of OT-I T cells was analyzed using a FACSverse flow cytometer.

References

1 Giavina-Bianchi, M.H. *et al.* (2017) Melanoma: tumor microenvironment and new treatments. *An. Bras. Dermatol.* 92, 156–166

2 Diamantopoulos, P. and Gogas, H. (2016) Melanoma immunotherapy dominates the field. *Ann. Transl. Med.* 4, 269

3 Tarhini, A.A. *et al.* (2012) IFN- in the Treatment of Melanoma. *J. Immunol.* 189, 3789–3793

4 Dillman, R.O. *et al.* (2012) Should High-Dose Interleukin-2 Still Be the Preferred Treatment for Patients with Metastatic Melanoma? *Cancer Biother. Radiopharm.* 27, 337–343

5 Topalian, S.L. *et al.* Immune checkpoint blockade: A common denominator approach to cancer therapy. , *Cancer Cell*, 27. 13-Apr-(2015) , Cell Press, 451–461

6 Yang, Y. Cancer immunotherapy: Harnessing the immune system to battle cancer. , *Journal of Clinical Investigation*, 125. Sep-(2015) , American Society for Clinical Investigation, 3335–3337

7 Villadolid, J. and Amin, A. (2015) Immune checkpoint inhibitors in clinical practice: update on management of immune-related toxicities. *Transl. Lung Cancer Res.* 4, 560–575

8 Kirkwood, J.M. *et al.* Mechanisms and management of toxicities associated with high-dose interferon alfa-2b therapy. , *Journal of Clinical Oncology*, 20. 01-Sep-(2002) , American Society of Clinical Oncology, 3703–3718

9 Weber, J.S. *et al.* Toxicities of immunotherapy for the practitioner. , *Journal of Clinical Oncology*, 33. 20-Jun-(2015) , American Society of Clinical Oncology, 2092–2099

10 Weide, B. *et al.* (2012) Functional T cells targeting NY-ESO-1 or Melan-A are predictive for survival of patients with distant melanoma metastasis. *J. Clin. Oncol.* 30, 1835–1841

11 Rosenberg, S.A. *et al.* (2008) Adoptive cell transfer: a clinical path to effective cancer immunotherapy. *Nat. Rev. Cancer* 8, 299–308

12 Rosenberg, S.A. *et al.* (1988) Use of tumor-infiltrating lymphocytes and interleukin-2 in the immunotherapy of patients with metastatic melanoma. A preliminary report. *N. Engl. J. Med.* 319, 1676–80

13 Coulie, P.G. *et al.* (2014) Tumour antigens recognized by T lymphocytes: at the core of cancer immunotherapy. *Nat. Rev. Cancer* 14, 135–146

14 Hadrup, S.R. (2012) The antigen specific composition of melanoma tumor infiltrating lymphocytes? *Oncoimmunology* 1, 935–936

15 Yee, C. *et al.* (2002) Adoptive T cell therapy using antigen-specific CD8+ T cell clones for the treatment of patients with metastatic melanoma: In vivo persistence, migration, and antitumor effect of transferred T cells. *Proc. Natl. Acad. Sci.* 99, 16168–16173

16 Andersen, R.S. *et al.* (2012) Dissection of T-cell antigen specificity in human melanoma. *Cancer Res.* 72, 1642–1650

17 Schumacher, T.N. and Schreiber, R.D. (2015) Neoantigens in cancer immunotherapy. *Science (80-.).* 348, 69–74

18 Morgan, R.A. *et al.* (2006) Cancer Regression in Patients After Transfer of Genetically Engineered Lymphocytes. *Science (80-.).* 314, 126–129

19 Robbins, P.F. *et al.* (2011) Tumor regression in patients with metastatic synovial cell sarcoma and melanoma using genetically engineered lymphocytes reactive with NY-ESO-1. *J. Clin. Oncol.* 29, 917–924

20 Stone, J.D. *et al.* (2015) TCR affinity for p/MHC formed by tumor antigens that are self-proteins: Impact on efficacy and toxicity. *Curr. Opin. Immunol.* 33, 16–22

21 Tan, M.P. *et al.* (2015) T cell receptor binding affinity governs the functional profile of cancer-specific CD8 + T cells. *Clin. Exp. Immunol.* 180, 255–270

22 Bol, K.F. *et al.* (2016) Dendritic cell-based immunotherapy: State of the art and beyond. *Clin. Cancer Res.* 22, 1897–1906

23 Palucka, K. and Banchereau, J. Dendritic-Cell-Based Therapeutic Cancer Vaccines. , *Immunity*, 39. 25-Jul-(2013) , Cell Press, 38–48

24 Schreibelt, G. *et al.* (2016) Effective clinical responses in metastatic melanoma patients after vaccination with primary myeloid dendritic cells. *Clin. Cancer Res.* 22, 2155–2166

25 Gross, S. *et al.* (2017) Twelve-year survival and immune correlates in dendritic cell-vaccinated melanoma patients. *JCI insight* 2, 1–19

26 Eggermont, L.J. *et al.* Towards efficient cancer immunotherapy: Advances in developing artificial antigen-presenting cells. , *Trends in Biotechnology*, 32. Sep-(2014) , Elsevier, 456–465

27 Perica, K. *et al.* Linking form to function: Biophysical aspects of artificial antigen presenting cell design. , *Biochimica et Biophysica Acta - Molecular Cell Research*, 1853. Apr-(2015) , 781–790

28 van der Weijden, J. *et al.* (2014) The right touch: design of artificial antigen-presenting cells to stimulate the immune system. *Chem. Sci.* 5, 3355

29 Mandal, S. *et al.* (2013) Therapeutic nanoworms: towards novel synthetic dendritic cells for immunotherapy. *Chem. Sci.* 4, 4168

30 Hammink, R. *et al.* (2017) Controlling T-Cell Activation with Synthetic Dendritic Cells Using the Multivalency Effect. *ACS Omega* 2, 937–945

31 Mandal, S. *et al.* (2015) Polymer-based synthetic dendritic cells for tailoring robust and multifunctional T cell responses. *ACS Chem. Biol.* 10, 485–492

32 Garboczi, D.N. *et al.* (1992) HLA-A2-peptide complexes: refolding and crystallization of molecules expressed in Escherichia coli and complexed with single antigenic peptides. *Proc. Natl. Acad. Sci. U. S. A.* 89, 3429–3433

33 Toebes, M. *et al.* (2006) Design and use of conditional MHC class I ligands. *Nat. Med.* 12, 246–251

34 Motta, I. *et al.* (1998) In vitro induction of naive cytotoxic T lymphocytes with complexes of peptide and recombinant MHC class I molecules coated onto beads: Role of TCR/ligand density. *Eur. J. Immunol.* 28, 3685–3695

35 Perica, K. *et al.* (2014) Nanoscale artificial antigen presenting cells for T cell immunotherapy. *Nanomedicine Nanotechnology, Biol. Med.* 10, 119–129

36 Ge, Q. *et al.* (2002) Soluble peptide-MHC monomers cause activation of CD8+ T cells through transfer of the peptide to T cell MHC molecules. *Proc. Natl. Acad. Sci.* 99, 13729–13734

37 Lone, Y.C. *et al.* (1998) In vitro induction of specific cytotoxic T lymphocytes using recombinant single-chain MHC class I/peptide complexes. *J. Immunother.* 21, 283–94

38 Schilbach, K. *et al.* (2005) Cytotoxic minor histocompatibility antigen HA-1-specific CD8+ effector memory T cells: Artificial APCs pave the way for clinical application by potent primary in vitro induction. *Blood* 106, 144–149

39 Curtsinger, J. *et al.* (1997) Artificial cell surface constructs for studying receptor-ligand contributions to lymphocyte activation. *J. Immunol. Methods* 209, 47–57

40 Hammink, R. *et al.* (2017) Affinity-Based Purification of Polyisocyanopeptide Bioconjugates. *Bioconjug. Chem.* DOI: 10.1021/acs.bioconjchem.7b00398

41 Oelke, M. *et al.* (2003) Ex vivo induction and expansion of antigen-specific cytotoxic T cells by HLA-Ig–coated artificial antigen-presenting cells. *Nat. Med.* 9, 619–625

42 Wölfl, M. and Greenberg, P.D. (2014) Antigen-specific activation and cytokine-facilitated expansion of naive, human CD8+ T cells. *Nat. Protoc.* 9, 950–966

43 Stone, J.D. and Stern, L.J. (2006) CD8 T cells, like CD4 T cells, are triggered by multivalent engagement of TCRs by MHC-peptide ligands but not by monovalent engagement. *J. Immunol. (Baltimore, Md 1950)* 176, 1498–1505

44 Fadel, T.R. *et al.* (2013) Adsorption of multimeric T cell antigens on carbon nanotubes: Effect on protein structure and antigen-specific T cell stimulation. *Small* 9, 666–672

45 Steenblock, E.R. and Fahmy, T.M. (2008) A Comprehensive Platform for Ex Vivo T-cell Expansion Based on Biodegradable Polymeric Artificial Antigen-presenting Cells. *Mol. Ther.* 16, 765–772

46 Zhang, Q. *et al.* (2017) Biomimetic Magnetosomes as Versatile Artificial Antigen-Presenting Cells to Potentiate T-Cell-Based Anticancer Therapy. *ACS Nano* DOI: 10.1021/acsnano.7b04955

47 Fadel, T.R. *et al.* (2014) A carbon nanotube–polymer composite for T-cell therapy. *Nat. Nanotechnol.* 9, 639–647

48 Sun, X. *et al.* (2017) Surface-Engineering of Red Blood Cells as Artificial Antigen Presenting Cells Promising for Cancer Immunotherapy. *Small* DOI: 10.1002/smll.201701864

Supplementary figures

A HLA-A2 Heavy Chain

MGSHSMRYFF	TSVSRPGRGE	PRFIAVGYVD	DTQFVRFDSD	AASQRMEPRA	PWIEQEGPEY
WDGETRKVKA	HSQTHRVDLG	TLRGYYNQSE	AGSHTVQRMC	GCDVGSDWRF	LRGYHQYAYD
GKDYIALKED	LRSWTAADMA	AQTTKHKWEA	AHVAEQLRAY	LEGTCVEWLR	RYLENGKETL
QRTDAPKTHM	THHAVSDHEA	TLRCWALSFY	PAEITLTWQR	DGEDQTQDTE	LVETRPAGDG
TFQKWAAVVV	PSGQEQRYTC	HVQHEGLPKP	LTLRLPETGG	LE	

B H2-Kb Heavy chain

MGPHSLRYFV	TAVSRPGLGE	PRYMEVGYVD	DTEFVRFDSD	AENPRYEPRA	RWMEQEGPEY
WERETQKAKG	NEQSFRVDLR	TLLGYYNQSK	GGSHTIQVIS	GCEVGSDGRL	LRGYQQYAYD
GCDYIALNED	LKTWTAADMA	ALITKHKWEQ	AGEAERLRAY	LEGTCVEWLR	RYLKNGNATL
LRTDSPKAHV	THHSRPEDKV	TLRCWALGFY	PADITLTWQL	NGEELIQDME	LVETRPAGDG
TFQKWASVVV	PLGKEQYYTC	HVYHQGLPEP	LTLRWELPET GG		

C Human β2m

MARSVTLVFL	VLVSLTGLYA	IQKTPQIQVY	SRHPPENGKP	NILNCYVTQF	HPPHIEIQML
KNGKKIPKVE	MSDMSFSKDW	SFYILAHTEF	TPTETDTYAC	RVKHASMAEP	KTVYWDRDM

Figure S1 Protein sequences of **(A)** HLA-A*0201 heavy chain, **(B)** H2-K^b heavy chain and **(C)** human β2m. Heavy chains also contain C-terminal sortase tag motives (LPETGG) for optional site-specific modifications.

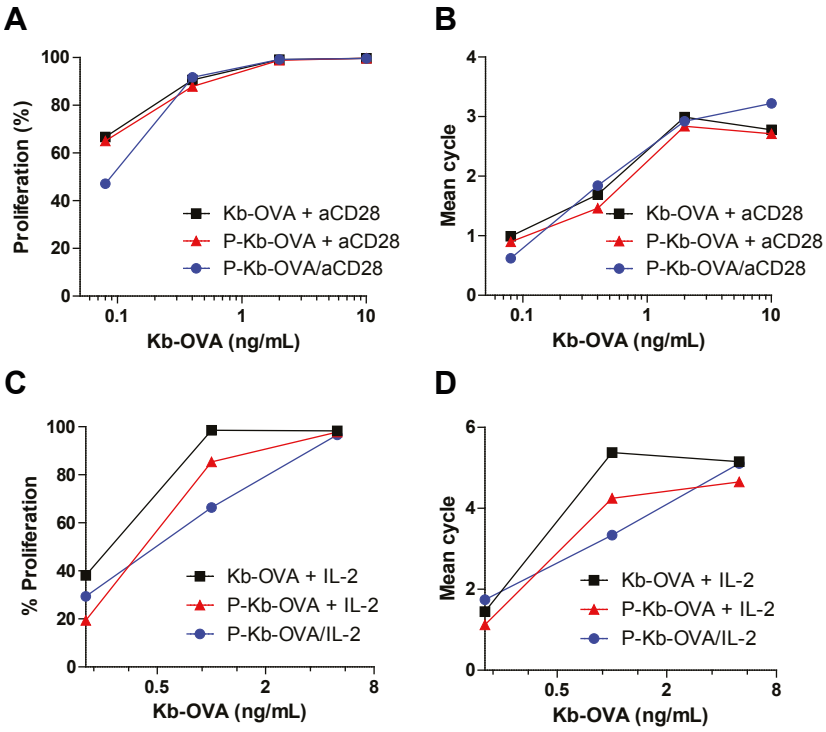

Figure S2 Proliferation after *in vitro* stimulation of mouse OT-1 cells. **(A)** OT-1 T cells were labelled with Celltrace Violet, stimulated with different concentrations of OVA-K^b or PIC-OVA-K^b in presence of unbound anti-CD28, or with PIC-OVA-K^b/aCD28, and after three days percentage of proliferating cells and **(B)** mean proliferation cycle was determined by Celltrace Violet dye dilution measurement. **(C)** OT-1 T cells were labelled with Celltrace Violet, stimulated with different concentrations of OVA-K^b or PIC-OVA-K^b in presence of unbound IL-2, or with PIC-OVA-K^b/IL-2, and after three days percentage of proliferating cells and **(B)** mean proliferation cycle was determined by Celltrace Violet dye dilution measurement.

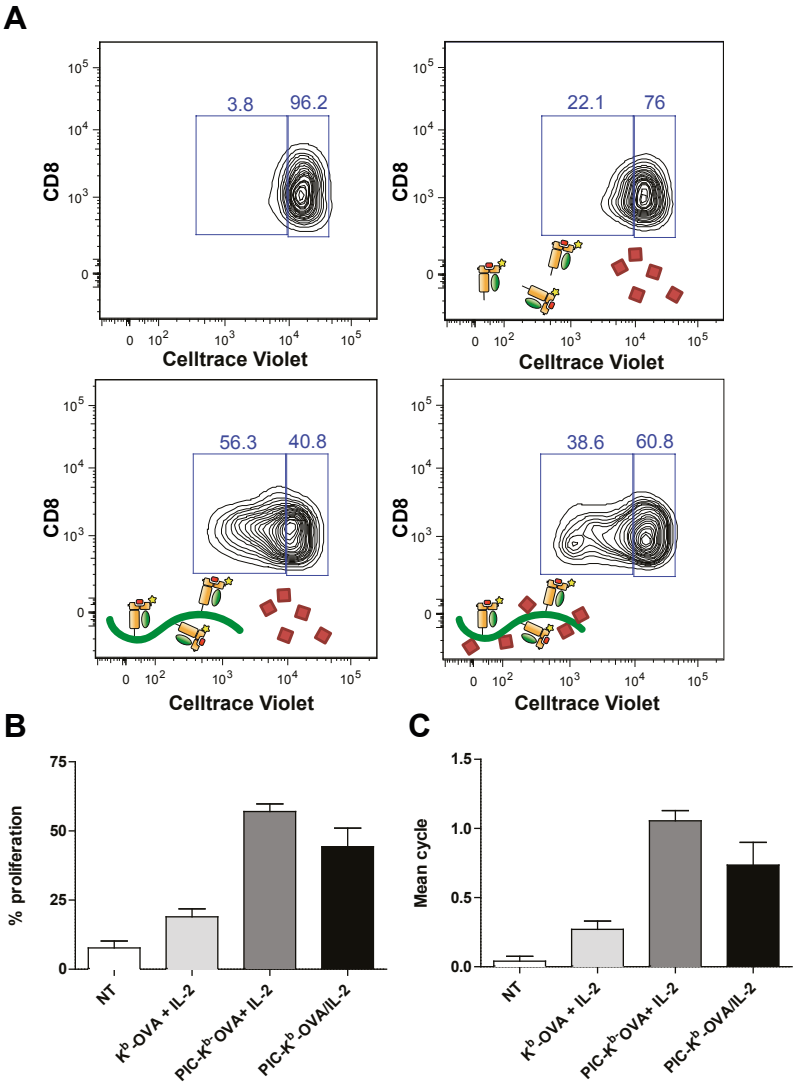

Figure S3 *in vivo* stimulation of OT-1 T cells in C57/BL6J mice with 240 ng OVA-K^b and 380 ng IL-2 **(A)** Histograms showing Celltrace Violet dye dilution to indicate proliferation of OT-1 T cells retrieved from spleens of treated mice. **(C)** Percentage of proliferating OT-1 T cells as determined by Celltrace Violet dye dilution. **(D)** Mean proliferation cycle of OT-1 T cells as determined by Celltrace Violet dye dilution.

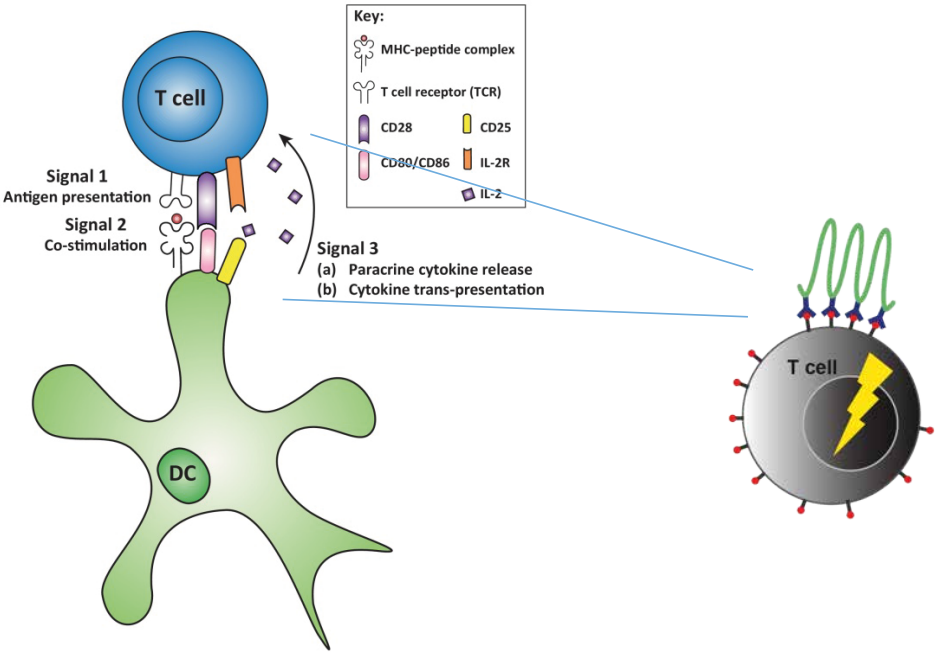
Key:
MHC-peptide complex
T cell receptor (TCR)
CD28
CD25
CD80/CD86
IL-2R
IL-2
T cell
Signal 1
Antigen presentation
Signal 2
Co-stimulation
Signal 3
(a) Paracrine cytokine release
(b) Cytokine trans-presentation
DC
T cell

8

Summary, general discussion and future perspectives

8.1 Summary

Artificial antigen-presenting cells for improved immunotherapy. During the past decade, immunotherapy has been established as a promising novel cancer treatment option. The important role of the immune system in supporting and reducing tumor growth has triggered development of therapies targeting different aspects of immunity. In particular, the clinical success of immune check-point blockade antibodies has sparked a renewed interest for immune modulation in cancer. By binding to overexpressed inhibitory molecules on tumor cells or suppressive/suppressed immune cells, these antibodies can restore anti-tumor immunity by releasing the brakes that were put in place by cancer. Alternatively, cytokine therapies have induced objective clinical responses through direct stimulation of immune cells. This approach directly induces immune responses, rather than targeting inhibitory mechanisms. To this end, also monoclonal anti- bodies that can trigger costimulatory receptors have been applied in clinical trials. Although these non-specific cytokine and antibody treatments have induced potent anti- tumor immunity, application of these therapies is limited by their severe toxicity.

To gain more direct control over immune cells, several cell-based therapies have been developed. These approaches make use of *ex vivo*-cultured autologous immune cells, and are generally more specific towards tumor antigens. In T-cell based therapies, tumor-infiltrating lymphocytes can be expanded and re-infused to induce potent and long-lasting tumor regression. To further increase potency, affinity and antigen-specificity of these cells, genetically modified T cells have induced potent and durable clinical responses, especially for hematologic malignancies. Alternatively, dendritic cells have been applied in vaccination strategies to successfully induce tumor regression in a number of patients with advanced cancer. These dendritic cells can be loaded with antigens and stimulated *ex vivo* to give them the ability to properly stimulate specific T cells *in vivo*. The unprecedented clinical success stories of these cell-based therapies have further established cancer immunotherapy as a promising approach to treat a wide variety of malignancies.

However, the need for tailor-made personalized vaccines using *ex vivo* cell culture make these strategies costly and highly laborious, also due to the large investments in infrastructure needed for these therapies. Therefore, there is a great need for cell-free immunotherapies that can match the anti-tumor immunity induced by cell-based vaccines. To provide such a system, artificial Antigen-Presenting Cells (aAPCs) are being developed as synthetic mimics of dendritic cells. Besides offering an off-the-shelf approach, aAPCs allow for more direct control over the signals that are presented to T cells compared to cell-based approaches.

As was discussed in chapter 1, several different types of aAPCs have been developed to this point, which has revealed design parameters important to properly

activate T cells. As was reported for *in vitro* T cell stimulations, size, shape, ligand density, ligand clustering and surface flexibility of aAPC scaffolds all play a role to optimize T cell activation. Experiments with rigid bead-based scaffolds demonstrated that a sizes over several micrometers and a high aspect ratio (stretched shape) are more favorable for proper stimulation. When the size of scaffolds was reduced, increasing ligand densities were needed on these beads to maintain their stimulatory potential [1]. Furthermore, aAPCs with softer surfaces have been demonstrated to enhance expansion of T cells, as was shown for PDMS surfaces and supported lipid bilayers (SLBs) with different fluidities. Pre-clustering ligands on beads or SLBs can further increase their stimulatory capacity, as this creates a high local density of stimulatory molecules on aAPCs.

To apply aAPCs *in vivo*, several additional (and sometimes conflicting) characteristics have to be taken into account. Especially the size and shape of the synthetic scaffolds were shown to be important parameters for optimal biodistribution. Scaffolds with stretched shapes have a more favorable distribution *in vivo*, since they can reach lymphoid organs better and show lower uptake into phagocytic cells. Conveniently, stretched particles with higher aspect ratios are also better at multivalently interacting with and stimulating T cells *in vitro*, which makes particle shape one of the most important parameters to optimize for *in vivo* T cell activation. Predictably, the biodistribution of smaller particles is more effective than that of large, microsized particles. Although the latter particles are better T cell stimulators, they do not move far from injection points and cannot access lymphoid organs.

Thus, for *in vivo* aAPC therapy, scaffolds need to be nano-sized and preferably have a high aspect ratio. Additionally, a certain degree of flexibility to allow for receptor rearrangements is favorable for these scaffolds. To incorporate these properties in a single aAPC design, we have developed aAPCs making use of polyisocyanopeptides (PICs) as scaffolds, called synthetic Dendritic Cells (sDCs). PICs can be made with lengths of 100 – 1000 nm and have a filamentous shape. These polymers are thought to be excellent aAPC scaffolds due to their high aspect ratio and semi-flexibility. Importantly, these polymers are biocompatible and presence of azide-functionalities in their side chains allow for straightforward and controlled modification with biomolecules. In the experiments described in chapter 2, these azides were used for streptavidin conjugation to PICs. By binding of biotinylated antibodies to these streptavidin-coated PICs, the first PIC-based sDCs were developed [2,3].

Polyisocyanopeptides as synthetic dendritic cells. To establish proof of principle of PIC-based sDCs, 200 nm-long streptavidin-coated PICs were coated with stimulatory antibodies against CD3. These anti-CD3-PICs were more effective than PLGA microparticles with similar ligand densities [3]. Conjugation of a stimulatory anti-CD28 antibody to provide costimulation was able to further enhance immune

responses. Again, anti-CD3/CD28-PICs were more potent than corresponding PLGA microparticles [2]. Although these initial experiments demonstrated that PICs can be effective sDCs, design parameters responsible for their efficient T cell stimulation could be further analyzed and optimized. As described in chapter 2 of this thesis, anti-CD3 multivalency on the semi-flexible scaffolds is essential for optimal T cell stimulation. With increasing length and antibody density, PICs induced more effective activation and prolonged TCR signaling. Because polymer length was found to be an important parameter, in the work described in the following chapters longer PICs (~400 nm) were used. Furthermore, anti-CD3 density (relative distances between antibodies) has a significant influence on T cell activation, and needs to be tightly controlled when analyzing the effect of conjugating additional stimulatory molecules to PICs.

Because the purification with spin filtration used for the PIC-streptavidin-antibody conjugates used in chapter 2 was inefficient and gave low yields, direct measurement of anti-CD3 density was difficult. Therefore, streptavidin densities were determined by Atomic Force Microscopy and to determine antibody spacing it is assumed that each streptavidin molecule binds to one anti-CD3. To increase yields of purified PIC-protein conjugates, in chapter 3 a novel affinity-based purification method was introduced for PICs. The increased yields and high purity of PIC-protein conjugates obtained using this method allowed for direct quantification of PIC concentrations using Circular Dichroism (CD). This method allows for more straightforward quantification of anti-CD3/PIC-ratios compared to the AFM method described before. Furthermore, the streptavidin linker was replaced by a short PEG to make sDCs synthesis even more straightforward. Due to the removal of streptavidin (which has 4 binding sites), the anti-CD3/PIC-ratios are directly correlated to the anti-CD3 density on PICs. Taken together, the simplified design and improved purification introduced in chapter 3 led to increased yields and more straightforward synthesis and analysis, thereby allowing for more rapid development of higher numbers of PIC-protein conjugates. This higher synthetic throughput was essential to develop the sDCs presented in chapters 4-7.

The introduction of simple PEG linkers instead of streptavidin paved the way for the development of sDCs containing a wide variety of co-stimulatory antibodies. In chapter 4, the synthesis of PIC-antibody conjugates was optimized to obtain a modular strategy that can rapidly produce a wide variety of sDCs. Screening of plate-bound co-stimulatory antibodies revealed that the speed of differentiation of CD8 T cells can be controlled through co-stimulatory antibodies. CD27 co-stimulation of naïve cells and 4-1BB co-stimulation of pre-stimulated cells resulted in more rapid differentiation compared to stimulation of CD28, OX40 and CD150. Conjugates of PICs and co-stimulatory antibodies can stimulate T cells, especially when anti-CD3 and co-stimulatory antibodies are co-conjugated to one and the same polymer.

Optimization of co-stimulatory sDCs using the modular synthetic strategy presented in chapter 4 could lead to nanofilaments that can control the differentiation and functionality of T cells.

The same modular synthetic strategy also allowed for incorporation of DNA-based linkers into PIC-antibody conjugates, as was described in chapter 5. Antibodies were efficiently conjugated to PICs through DNA hybridization, which resulted in sDCs that could efficiently stimulate T cells. By anchoring complementary DNA strands in different geometries to PICs and anti-CD3, linkers were developed that could act as tension gauge tethers when forces are applied on the sDCs by T cells. In this way, the force-responsive behavior of T cell activation can be studied and forces that rupture the DNA duplexes between antibodies and PICs can be measured. The small size and multivalent binding of sDCs allows for measurement of forces that regulate relative movement and segregation of receptors on the T cell surface.

In chapters 2-5, only antibodies were conjugated to PICs. It was demonstrated in chapter 6 that cytokines can also be conjugated to the same polymers using a similar strategy. Cytokines are essential in T cell biology and have been applied in a variety of immunotherapeutic approaches. However, their application is limited by their toxic side effects, highlighting that there is a need for targeting cytokines to T cells. Conjugation of cytokines onto PICs allowed for the development of sDCs that can be used to target immobilized cytokines IL-2 and IFNα directly to T cells. It was demonstrated that conjugation of IL-2 to PICs resulted in diminished cytokine activity. However, when IL-2-PICs were targeted to T cells by co-conjugation of anti-CD3 to one and the same polymer, cytokine activity of the PIC-immobilized IL-2 was increased compared to unbound cytokines. Anti-CD3/IL-2-PICs and anti-CD3/IFNα-PICs could thus be used as a potent tool to lower the side effects and increase the potency of cytokine-based immunotherapy.

Side effects of sDC-based immunotherapies, such as the cytokine-sDCs, could be further diminished with antigen-specific T cell stimulation. As was demonstrated in chapters 2-6, potent polyclonal T cell activation could be achieved through conjugation of stimulatory anti-CD3 antibodies to PICs. The use of anti-CD3 provided a straightforward method to activate T cells, and the OKT3 clone provides a good model to simulate peptide-MHC (pMHC) binding of TCRs. However, for safe *in vivo* application, monoclonal antigen-specific T cell stimulation should be achieved. In chapter 7, pMHCs are produced and conjugated onto PICs instead of anti-CD3 antibodies to provide antigen-specific stimulation of T cells. sDCs were generated that were specific for cancer germline antigen NY-ESO-I, and human T cells transfected with a TCR that can recognize this antigen were efficiently and specifically activated with these sDCs. Co-conjugation of anti-CD28 onto the same PIC resulted in a synergistic enhancement of T cell activation, although some non-antigen-specific stimulation was also observed. In addition, OVA-specific pMHC-complexes were generated that could be

recognized by the OT-1 mouse T cell clone. *In vitro* activation of OT-1 T cells with the produced sDCs was similar to activation of cells stimulated with unbound pMHC. Importantly, *in vivo* stimulation of OT-1 T cells with i.v. injected pMHC-PIC conjugates resulted in a markedly enhanced T cell activation compared to unbound pMHCs. Although additional experiments are needed to show that sDCs can stimulate natural antigen-specific T cells, these initial results clearly demonstrate the great potential of using sDCs as an 'off-the-shelf' approach for active *in vivo* immunization in cancer immunotherapy. An overview of the developed PIC-conjugates used in this thesis is depicted in figure 1.

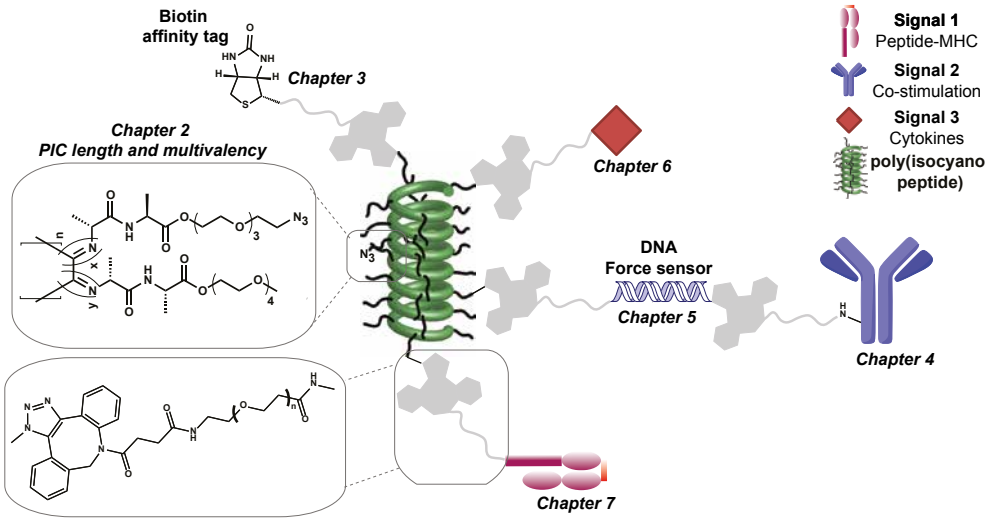

Figure 1 Molecular structure, linkers and biomolecules used in PIC-bioconjugates in the work presented in this thesis.

8.2 Manipulation of T cell activation mechanisms with sDCs

T cell activation is initiated upon recognition of specific pMHC complexes on the surface of antigen presenting cells. To induce potent T cell responses while avoiding auto-immunity, this process needs to be highly selective. In this regard, T cells have to be able to respond to very low numbers of foreign peptide antigens in a sea of self-peptides. In addition, the TCR repertoire is highly diverse due to somatic

recombination that occurs in the thymus, which means that pMHC-TCR interactions need to span a range of affinities. Because the peptides presented by MHCs are short, TCRs need to differentiate between self-pMHC and agonists based on minimal differences in affinity. Therefore, several mechanisms are in place to translate small differences in affinity to strong TCR signaling [4,5]. Since sDCs mimic the function of antigen-presenting cells, their interactions with T-cells should also impact these mechanisms. In addition, sDCs can be used to further study molecular mechanisms of T cell activation.

1. Kinetic proofreading with serial engagement

Interactions between pMHCs and TCRs are generally much weaker than other receptor-ligand pairs. Nonetheless, T cells can readily detect small differences in affinity and the weak interactions of these ligands are sufficient to induce strong downstream signaling [4,6,7]. Mechanisms in which TCR binding by pMHC directly leads to downstream signaling are not able to properly explain the high selectivity of T cells [8]. Thus, T cell activation is not proportional to the number of occupied TCRs, because such a mechanism would not account for the ability of T cells to differentiate between foreign and self-antigens.

Instead, pMHC recognition is more consistent with a kinetic proofreading model (**Figure 2**) [8,9]. This model states that T cell activation is initiated after a minimal number of TCRs has been bound by pMHCs for the minimal duration it takes to trigger a downstream signal. This means that there is a time delay in between the initial

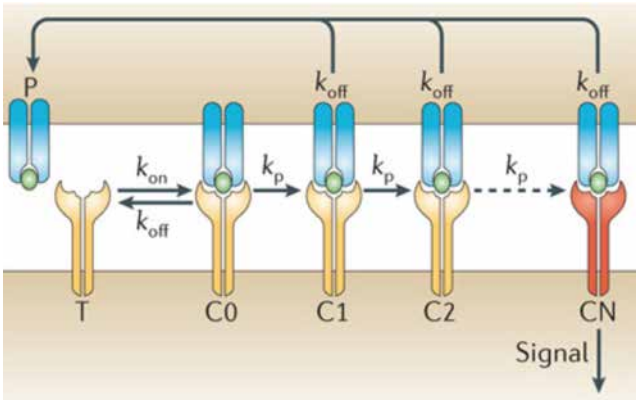

Figure 2 Kinetic proofreading model of TCR triggering. In the kinetic proofreading model, pMHC (P) binding to TCRs (T) requires a series of biochemical transformations to form intermediates (C), before downstream signaling can occur. The signaling-competent TCR state (CN) is depicted in red. Each modification can be reversed completely after dissociation of pMHC. Adapted with permission from [8].

binding event and signaling output. In other words, TCRs can be 'turned on', which is dependent on the off-rate of the pMHC-TCR interaction [10]. After dissociation of the pMHC, the TCR will remain in an active state for a certain time, in which other TCRs can be triggered as well. This allows a small number of pMHCs to trigger multiple TCRs and in this way T cells can discriminate between peptides based on their dissociation times from TCRs [8,9,11]. Indeed, it has been observed that a small number or even a single pMHC can be sufficient to induce cytokine production in T cells [12].

Although the molecular players in initial TCR signaling are known, it is still difficult to completely explain kinetic proofreading using the described signaling cascades. During interactions of TCRs with self pMHCs, T cells are already primed to rapidly respond upon encounter of agonist peptides [13]. During the short interactions between TCRs and self (non-agonist) pMHCs, co-receptors CD4 and CD8 can dynamically interact with the (shortly) bound MHC. Active Lck that is bound to intracellular tails of these co-receptors can in this way phosphorylate ITAMs of CD3-ζ-chains present in the TCR complex (**Figure 3**) [14]. CD3-ζ-phophorylation can recruit ZAP70 from the cytosol, which is bound to CD3 in an inactive state. Subsequent phosphorylation of ZAP70 would initiate productive downstream TCR signaling, but the short self pMHC-TCR interaction time does not allow for this to happen. Upon ligation of an agonist pMHC, which is bound to the TCR for a sufficient duration, ZAP70 is phosphorylated by co-receptor bound Lck [15]. Thus, in this way the TCR-CD3-ZAP70 complex is 'turned on' [4,5,14]. Because the TCR has two CD3 chains, the active, phosphorylated state of ZAP70 is probably stabilized through trans-

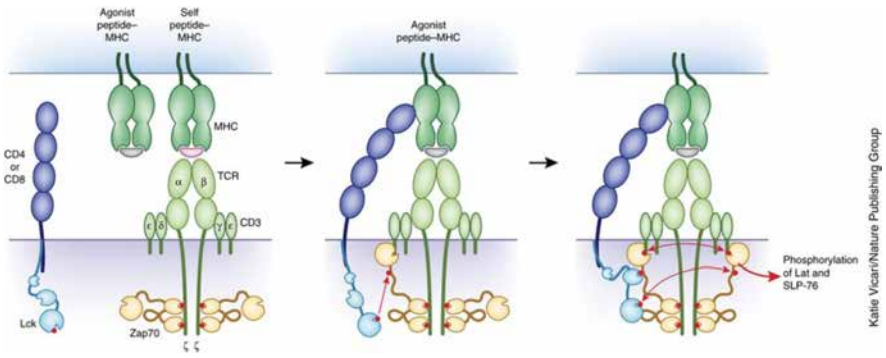

Figure 3 Lck initiation of TCR-bound ZAP-70 signalling. In resting T cells, inactive ZAP70 is bound to TCRs. Lck initiates TCR signalling through phosphorylation (red dots) of ZAP70, which stabilizes binding of Lck. This leads to a positive feedback loop in which Lck and ZAP70 can phosphorylate nearby proteins. Conversely, unbound Lck may also initiate signalling in absence of CD4/CD8 co-receptors. Adapted with permission from [5].

autophosphorylation by ZAP70 bound to a neighboring CD3 chain [16,17]. As a result, proximity of Lck is no longer required and ZAP70 will remain active even after dissociation of pMHC, which is enhanced by temporary protection from constitutively active phosphatases [5]. To promote further signal stabilization, ZAP70 can bind Lck and keep it in close proximity to the TCR. Alternatively, the co-receptor-Lck complex can dissociate from MHC, with which it was weakly interacting, and find a nearby pMHC-TCR interaction to repeat this sequence of events [5]. Accumulation of phosphorylated ZAP70 can then form a starting point for LAT phosphorylation and the formation of LAT signalosomes [18].

Although this model for the initiation of TCR signaling works well for natural DC-T cell interactions, in case of polyclonal aAPC stimulations (using anti-CD3 antibodies), there is no binding of CD4 or CD8 co-receptors to initiate ZAP70 phosphorylation. Therefore, co-receptor binding of Lck does not play an essential role in the initiation of TCR signaling, but helps to increase sensitivity [19]. In case of anti-CD3 aAPC stimulation, free Lck that is present in the cytoplasm is important to initiate signaling, which may also be the essential in natural T-cell-DC interactions [20]. Although kinetic proofreading fits well with most literature on pMHC-TCR interactions, to this point there is no consensus on how signaling mechanisms can provide kinetic proofreading for T-cell activation. TCR mechanosensing, spatial redistribution of phosphatases and cluster formation provide explanations on how increased sensitivity could be achieved [4].

For sDC stimulation of T cells, kinetic proofreading may be achieved through multivalent ligand binding. Since a minimal number (or density) of anti-CD3 antibodies is essential for productive T cell activation (Chapter 2), serial engagement of anti-CD3 may be needed to trigger sufficient TCRs. Binding of the anti-CD3 clone we used, OKT3, is known to exhibit off-rates in the range of natural agonist pMHCs [21,22]. This off-rate, combined with a high on-rate, could allow for rapid rebinding of neighboring CD3 molecules.

2. Mechanosensing

Binding affinities of interacting molecules are often measured in solution. However, in nature pMHCs and TCR interact while both molecules are embedded in cell membranes. Also in aAPC stimulations, the interacting molecules are presented on a surface (two-dimensional interaction). A single soluble pMHC cannot induce TCR triggering, whereas a single immobilized pMHC can effectively trigger multiple TCRs [12]. This illustrates that interactions between membrane- bound receptors are fundamentally different from interactions of molecules in solution. Importantly, variability in on-rates of membrane-bound pMHC binding to TCRs is much greater than that of in solution pMHCs. These two-dimensional on-rates of pMHCs are correlate well with their stimulatory capacity [23]. In addition, off-rates of immobilized

pMHCs are generally faster, in part due to presence of mechanical forces between the interacting planes [24,25].

During T cell-DC interactions, forces in the range of 10 to 100 pN per TCR are generated [4,26,27]. In part, this is caused by the small size of the interacting pMHC-TCR, which repels or compresses larger molecules and the glycocalyx in the contact area [28,29]. Furthermore, forces are actively induced by cytoskeletal movement of membrane-bound receptors [30]. The generated forces seem to play an important role in the induction of TCR signaling, and could help to increase sensitivity and selectivity of antigen recognition by T cells. Both F-actin flow and myosin II contractility, processes that put considerable strain on the pMHC-TCR interaction are essential for efficient force-dependent TCR triggering [31,32]. An externally applied force of 10 pN can induce triggering of a single TCR [33]. Interestingly, when forces are applied on non-agonist anti-TCR antibody coated beads, TCR signaling is also observed [34]. Thus, force generation and TCR mechanosensing both benefit TCR signaling. Possibly, these forces lead to release of CD3 ITAMs from the cell membrane, in this way exposing them for phosphorylation by Lck [35,36].

Force generation can also contribute to ligand discrimination through formation of pMHC-TCR catch bonds [38–40]. Self-pMHC and TCRs form 'slip bonds', bonds that are destabilized by force application. As expected, exerting a force on self-pMHC-TCR interactions leads to a decrease in force lifetime. However, several agonist pMHC have been reported to form 'catch bonds'. For these interactions, binding is stabilized when a (small) force is exerted on the two molecules [41]. pMHC-TCR catch bond formation was most effective at forces of ~10 pN, which is in the same range as the forces necessary for potent TCR signaling [26,40]. These findings are supported by single molecule force measurements suggesting that forces applied by agonist pMHCs lead to a conformational change in TCRs that stabilize pMHC-TCR interactions [42]. Although catch bonds have been reported for multiple antigens, it is unclear whether

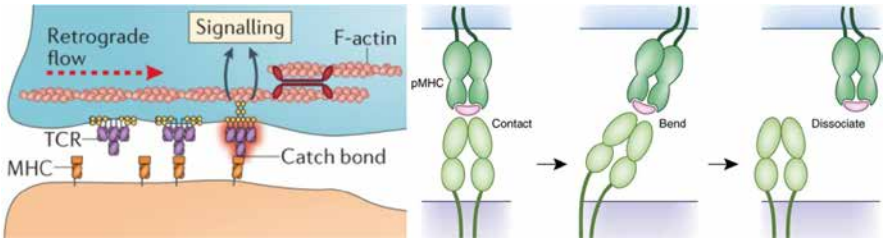

Figure 4 Force generation between pMHCs and TCRs. Movement of TCRs, regulated by retrograde actin flow, is responsible for catch bond formation, conformational change and mechanotransduction in TCRs. Adapted with permission from [37] and [5].

catch bond formation is a general mechanism needed for productive TCR signaling [41].

The ability of TCRs to sense force also impacts their interactions with aAPCs. As mentioned in the introduction, surface properties of aAPC scaffolds play an important role in their efficacy. In general, providing a certain level of rigidity by immobilization on a surface is essential, but aAPCs with a softer surfaces seem to be more efficient [43,44]. Therefore, the semi-flexibility of PICs could be important for their signal transduction. To confirm the role of substrate stiffness of filamentous polymers, interactions of T cells and PICs with different rigidities should be tested. Since PIC rigidity is directly related to intramolecular hydrogen bonding, these polymers can be synthesized through variation of amino acids in the PIC side chains [45,46]. To further understand the role of forces in T cell activation, sDCs containing force-sensitive linkers, such as those generated in chapter 5, could be used.

3. Spatial redistribution and segregation

The close contacts formed due to the small size of pMHC-TCR interactions also give rise to an additional mechanism for T-cell activation (**Figure 5**). In resting T cells, several kinases, including Lck, are present in active form and are therefore able to phosphorylate CD3-ζ and ZAP70 [47,48]. This kinase activity is balanced by membrane-bound phosphatases CD45 and CD148. Because these phosphatases contain large extracellular domains, they are segregated from TCRs during close-contact pMHC interactions [49,50]. Long-lasting spatial segregation of phosphatases stabilizes phosphorylation of CD3 and ZAP70, which contributes to propagation of TCR signaling. In the absence of TCR stimuli, artificial segregation of CD45 is sufficient to initiate TCR signaling [51]. Altogether, agonist pMHCs induce formation of close contacts between APCs and T cells to keep TCRs in an environment that favors Lck kinase activity over CD45 phosphatase activity. Similarly, CD148 can destabilize TCR signals, but acts further downstream in the signaling cascade [52].

For several types of aAPCs, such as minimally sized bead-based scaffolds and antibody-coated surfaces, phosphatase-excluded close contact zones might form and contribute to T cell activation [51]. Because of the filamentous shape of PICs, it is doubtful whether the close contact zones needed for spatial segregation of phosphatases are present in PIC-T cell interactions. Possibly, the (semi-)rigidity of PIC clusters with a high density of polymers could lead to a certain level of phosphatase exclusion. Presence of clustered PIC networks on the T cell membrane should be studied using high-resolution imaging to further clarify mechanisms of PIC-based T cell activation. Experiments with CD3/CD45-PIC indicate that CD3 signaling could still occur in proximity of CD45, although it was not confirmed whether these PICs indeed bind to CD45. Taken together, spatial segregation of phosphatases may not be a dominant mechanism for the activity of sDCs described in this thesis.

4. TCR clustering and immune synapse formation

In resting T cells, TCRs are present in small linear 20-200 nm clusters, containing 1-20 TCRs, that grow coalesce upon TCR stimulation [54–56]. This spatial organization of TCRs is important for T cell activation and also plays an important role in the previously mentioned mechanisms [57]. Proximity of TCRs allows for rapid rebinding of a single agonist pMHC, which can trigger multiple receptors in this way [58]. Furthermore, TCR clustering stabilizes close contacts that allow for force generation and phosphatase segregation [57]. In addition, nanodomain membrane organization allows for fast signaling kinetics and amplification. Many kinases involved in TCR signal transduction, including LAT, Lck and ZAP70 may also reside in distinct nanoclusters in before T cell activation [59]. Size increase of TCR clusters after triggering further increases pMHC rebinding and T cell sensitivity. Indeed, larger TCR clusters can be triggered at lower agonist pMHC doses due to increased avidity and signal propagation [60]. The important role of TCR clustering is further highlighted by the observation that active clustering of nanoscale aAPCs in a magnetic field can lead to a marked increase in T cell activation [61,1].

Thus, T cell activation is most efficiently initiated at TCR nanoclusters. TCR stimulation at nanoclusters leads to an increase of cluster size to form of TCR microclusters containing ~50-300 TCRs, transiently surrounded by a ring of adhesion molecules [62,63]. Simultaneously, clustering and phosphorylation of ZAP70 and LAT occur at these microclusters [64,65]. While initial TCR signals, such as LAT phosphorylation and calcium release, are generated within minutes, sustained signaling from microclusters is required to induce cytokine production and proliferation. Blockade of

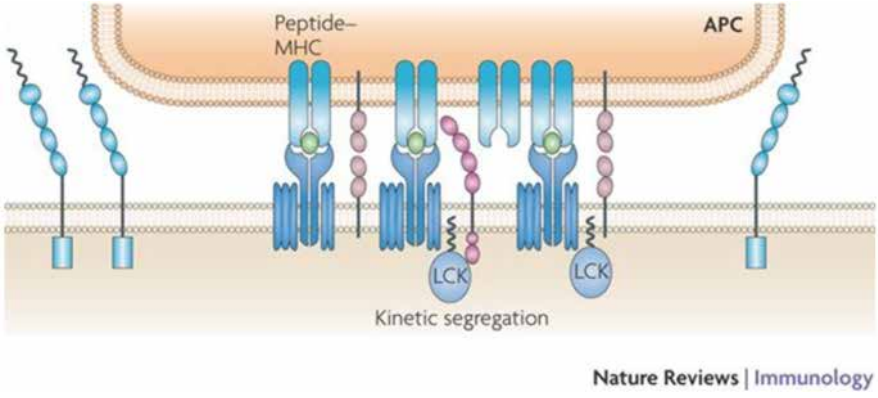

Figure 5 Kinetic segregation of TCR and CD45 phosphatases initiates signaling. Close contacts between T cells and APCs after pMHC-TCR binding lead to exclusion of large phosphatases, such as CD45. Reprinted with permission from [53].

pMHC signals after microcluster formation inhibits TCR signaling from these clusters and blocks formation of newly formed clusters [66]. When T cells are strongly stimulated with high ligand densities, an immune synapse can be formed [67]. The classical synapse structure is characterized by accumulation of TCRs in a central area, called the central Supra Molecular Activation Cluster (cSMAC). The cSMAC is surrounded by a peripheral SMAC (pSMAC), containing adhesion molecules. Immune synapse formation is initiated when TCR microclusters start moving towards a central spot on the T cell membrane. At the periphery, this process is regulated by F-actin retrograde flow and is dynein-dependent closer to the cSMAC [68]. Movement of microclusters leads to strong TCR signaling, possibly due to force generation. In the center of the cSMAC, TCR signaling is abrogated and TCRs are endocytosed to dampen their stimulatory action. However, on the borders of the cSMAC and pSMAC, a signaling cSMAC is formed where TCR signaling is maintained (**Figure 6**) [62].

Experiments with nanosized beads demonstrate that aAPCs need to be able to target nanoclusters to induce efficient activation [1]. Since PICs are ~400 nm in length, they may be able to efficiently bind to and trigger TCR nanoclusters. Possibly, the filamentous shape of our sDCs is particularly suitable to target these clusters, since EM measurements indicate that nanoclusters consist of linear TCR arrangements, meaning that short rows of TCRs are present on the T cell surface [56]. Binding to a TCR in these clusters could allow for rapid release and rebinding of nearby TCRs to ligands presented on PICs. Movement of TCRs is important for the formation of microclusters, generation of signals from microclusters and formation of a signaling cSMAC. aAPCs

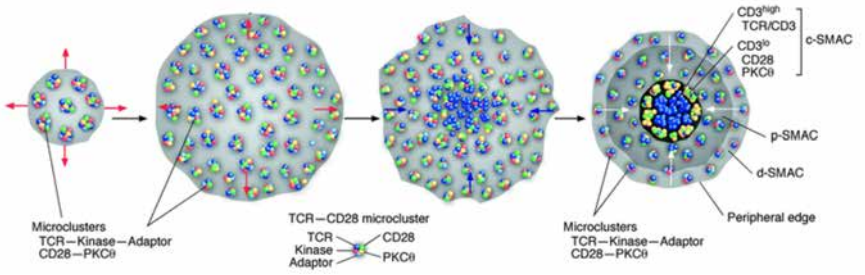

Figure 6 TCR microcluster movement and immune synapse formation. TCR triggering leads to formation of TCR microclusters, containing TCRs, CD28, kinases and adaptors. With continued stimulation, these microclusters start moving towards a central spot on the T cell membrane, which leads to force-induced signaling. In the centre of this immunological synapse (cSMAC), TCRs are recycled and signaling is abrogated, while CD28 remains at the edge of the cSMAC and may continue signaling. During stimulation, TCRs are continuously transported from the periphery towards the cSMAc, leading to maintained TCR signaling. Adapted with permission from [62].

that allow for a certain level of TCR movement due to scaffold flexibility may be able to better accommodate these changes in the T cell membrane. However, to this point these mechanisms of PIC-based TCR triggering are speculative. High resolution microscopy experiments should be performed to reveal PIC binding to TCR microclusters and the formation of different immune synapse-like structures for PICs or aAPCs with different stiffness. In addition, electron microscopy measurements of PIC-T-cell interactions could be done to shed light on nanocluster binding of sDCs.

Each of the mechanisms mentioned above can be sufficient to initiate T cell activation. Thus, by artificially inducing one of these mechanisms, signaling cascades are triggered. Either applying force to receptors, or inducing phosphates-kinase segregation, or inducing TCR clustering activates T cells. In nature, all of these mechanisms are probably contributing to enhance selectivity and sensitivity of TCR signaling. To induce optimized T cell responses with novel sDCs, these mechanisms should be considered in sDC designs.

Co-stimulation at TCR microclusters further potentiates T cell activation

TCR triggering by itself does not produce potent T cell activation, but leads to T cell anergy. When dendritic cells are activated due to the presence of danger signals, co-stimulatory ligands are upregulated. Together with TCR stimulation, co-stimulation leads to productive T cell activation, characterized by high levels of cytokine production and proliferation [69]. CD28, being the most studied and one of the most essential costimulatory molecules expressed by T cells, is also present in signaling TCR microclusters. During immune synapse formation, CD28 moves to the edge of the cSMAC (between the cSMAC and pSMAC), where it delivers sustained co-stimulatory signaling [70]. Co-stimulation through CD28 can both enhance TCR signaling and induce distinct signaling cascades [71].

PKCθ recruitment is directly regulated through CD28, as it binds to the CD28 cytoplasmic tail via Lck. In resting T cells, cytoplasmic tails of CD28 are bound to the plasma membrane, and therefore unable to interact with Lck. Triggering by CD80 or CD86 leads to release of these tails, which allows for a stabile interaction with Lck [72]. CD28 stimulation does not significantly contribute to microcluster formation. Instead, CD28 signaling could be potentiated by the microcluster environment that favors Lck activity [73]. In addition, the high affinity of Lck for the CD28 cytoplasmic tail may assist the induction of TCR signaling [72]. Thus, TCR and co-stimulatory signaling are co-localized and synchronized in microclusters. In addition to synergy in early signaling, downstream pathways may also be enhanced by CD28, for example due to PKCθ recruitment [74]. The synergistic signaling of CD3 and CD28, together with their colocalization in microclusters explains the enhanced T cell activation observed when co-presenting anti-CD3 and anti-CD28 on one and the same PIC. For these polymers, both the enhanced CD28 binding (due to CD3 targeting) in microclusters, as well as

simultaneously triggering synergistic signaling pathways in close proximity, could contribute to the observed activation boost.

For other co-stimulatory molecules, such as the TNF receptor superfamily receptors used in chapter 4, localization in relation to signaling has not been studied extensively. Proximal signaling molecules of this receptor family appear to be different from TCR and CD28 kinases [69]. Nonetheless, more downstream signaling pathways are overlapping and may account for the observed synergy with TCR signaling [75]. CD70, the ligand for CD27, is recruited to the immune synapse in DCs together with MHCII and CD27 may thus signal in close proximity to TCRs [76]. Furthermore, 4-1BB stimulation can lead to phosphorylation of CD3, Lck and LAT [77]. Co-localization of TCR signals and co-stimulation could be a general mechanism to avoid antigen-independent co-stimulatory signaling. Also cytokine receptors are can be recruited to the immune synapse, and possibly to signaling microclusters. Experiments in chapers 4 and 6 indicate that co-triggering receptors in close proximity to each other may be a general mechanism to enhance signaling of T cell stimulatory signals 2 and 3. Multiple co-stimulatory molecules and cytokines exhibit some level of synergy when co-presented on one and the same PIC, which allows for closely spaced signal induction. This characteristic of PIC-based sDCs makes them particularly promising for clinical application, since it allows for the delivery of immunostimulatory factors with less off-target toxicity.

8.3 Further pre-clinical development of sDCs

The small size and filamentous shape of sDCs make them a particularly attractive option for active *in vivo* immunization. This could lead to potent 'off-the-shelf' cancer immunotherapies that could possibly replace or augment cell-based therapies. To develop these novel therapies, it is essential that sDCs can induce antigen-specific T cell activation. Therefore, it was first demonstrated in chapter 7 that sDCs can induce antigen-specific T cell activation both *in vitro* and *in vivo*. Although these results established that monoclonal T cell stimulation is possible, efficient antigen-specific activation of natural T cells, rather than transfected or transgenic cells, is needed to fully exploit the potential of sDCs. This means that sDCs should be optimized to induce expansion a small number of antigen-specific T cells within a large mixed group of T cells. Importantly, additional *in vivo* experiments are needed to further demonstrate the applicability of sDCs in cancer immunotherapy. Although transgenic OT-1 T cells work well for initial proof of the *in vivo* activity of sDCs, tumor models in mice should also be explored without injections of antigen-specific T cell clones.

Incorporation of stimulatory signals. To achieve antigen-specific stimulation of only a small population of T cells within a large group of cells with different specificities, specialized optimization of the signals presented on sDCs is needed. Similar to experiments using anti-CD3 antibodies (chapter 2/4), multivalent pMHC presentation dictates that a high density of pMHC molecules should also lead to potent activation of antigen-specific T cells. Furthermore, incorporation of signals 2 and/or 3 is essential to induce full-blown activation and anti-tumor activity, as was demonstrated in chapters 4 and 6 [2]. However, the same co-stimulatory molecules and cytokines could lead to off-target binding of sDCs in non-purified cell populations and because of this, high doses of conjugates may be needed to observe clinical responses. Especially the use of high affinity ligands, such as co-stimulatory antibodies, may lead to off-target binding. As a result, natural B7 ligands are generally used for active *in vivo* immunization using aAPCs [78,79]. Nonetheless, injection of anti-CD28-containing microbeads have been shown to induce antigen-specific anti-tumor responses [80], indicating that incorporation using anti-CD28 is a feasible approach. For use in human trials, caution is needed when using anti-CD28, as a stimulatory anti-CD28 antibody induced dangerous toxicity during a clinical trial in 2006 [81]. In contrast to antibodies used on aAPCs, this superagonist stimulated CD28 in the absence of TCR triggering. Taken together, the use of natural ligands may be more appropriate for *in vivo* application of sDCs.

Alternatively, or simultaneously, cytokines can be conjugated onto PICs to induce anti-tumor T cell responses. In chapter 6 it was demonstrated that PIC-cytokine conjugates, PIC-IL-2 in particular, have reduced interactions with T cells compared to unbound cytokines. Because of this, cytokines can be targeted to T cells using other ligands, such as anti-CD3 antibodies or pMHC. Several cytokines, including IL-2 and IFNα, are already approved for treatment of a number of malignancies [82]. By using cytokines immobilized onto PICs, sDCs could be developed that may efficiently target and strongly stimulate specific T cell clones. To further demonstrate whether cytokine targeting can be used for cancer treatment, sDCs based on PIC-cytokine conjugates need to be applied in tumor models in mice. However, at this point it is not known whether efficient targeting of PIC-immobilized cytokines to mouse T cells is also possible. *In vitro* experiments with optimized sDCs should determine whether humanized mouse models are needed before testing this type of sDCs *in vivo*. Nonetheless, the experiments presented in chapter 6 indicate that cytokine-containing sDCs may allow for efficient antigen-specific immunotherapy through TCR targeting.

Immunotherapies should target a wide variety of antigens. To develop broadly applicable immunotherapies, commonly shared tumor antigens such as MART-1, GP100 and NY-ESO-1 have been widely studied as targets [83,84]. Cell-based vaccines

targeting these antigens have induced anti-melanoma immune responses in pre-clinical and clinical tests, which demonstrated the great promise of antigen-specific immunotherapy [85,86]. In chapter 7, we developed sDCs targeting MART-1 and NY-ESO-1. Optimization of these sDCs may allow for 'off-the-shelf' immunotherapies, since application of these synthetic constructs do not require to culture cells for each individual patient.

However, targeting of these shared tumor-associated antigens have also shown several disadvantages. Some of these antigens may also be expressed by healthy cells, and can therefore induce tolerance of T cells, which may impede their anti-tumor activity. In addition, strong stimulation of some of these antigens can induce off-target toxicity of cells that express low levels of these antigens [87]. For example, treatments using high affinity MART-1-specific T cells can lead to skin rashes and hearing loss [88]. On-target off-tumor toxicity of high-affinity TCR immunotherapy has led to a search for more specific antigens. Analysis of the antigen repertoire of T cells induced by non-specific cancer immunotherapies, such as checkpoint blockade antibodies, has identified neo-antigens as another group of antigens that could be even more potent as targets of antigen-specific therapies [89]. Because these neo-antigens are peptides directly derived from mutated protein, they are specific only to the tumor tissue. Broadening the antigen repertoire of immunotherapies to include these neo-antigens could greatly benefit clinical responses and prevent recurrence of tumor growth [89,90]. Also in the development of sDCs, the use of multiple antigens, including neo-antigens, is an interesting approach that could lead to more complete tumor control.

A strategy for personalized sDC-based immunotherapy. Since neo-antigens stem from random mutations, these antigens are not shared between patients. Because of this, neo-antigen-specific therapies need to be personalized to each individual patient. sDCs that present neo-antigens are therefore difficult to produce as 'off-the-shelf' therapies, as this requires the production and conjugation of a wide variety of pMHCs. As a result, application of personalized sDCs would require several steps after diagnosis of a patient, and is not directly applicable. However, a strategy could be envisioned that could make personalized sDC treatments, while still partly retaining their 'off-the-shelf' character. This proposed strategy contains several steps:

1. *Determine (neo-)antigens in tumor biopsy.* To determine antigens specifically expressed by tumor cells, whole exome sequencing of both normal and tumor cells can be done. HLA types of patients should then be determined and mutated peptides likely to be presented onto MHC complexes can be predicted using established HLA/peptide binding algorithms [87]. For peptide binding to the most common HLA types, prediction algorithms are fairly accurate. An alternative approach that circumvents the use of prediction algorithms makes use of mass

spectrometry. However, peptide purification and subsequent mass spectrometry may not be sensitive enough to detect all expressed antigens [91].

2. *Peptide synthesis*. After prediction of the expressed antigens, short peptides can be readily synthesized using standard solid-phase peptide synthesis. As peptide synthesis is cheap, fast and can be done under GMP conditions, this method is suitable to quickly yield short MHC-binding peptides. For the production of a neo-antigen-based vaccine consisting of long peptides and TLR ligands, this strategy (from exome sequencing up to long peptide synthesis) was successfully applied in a phase I clinical trial [92].
3. *UV-induced MHC-bound peptide exchange*. A straightforward method to produce a variety different PIC-pMHC conjugates will be essential to target neo-antigens using sDCs. A method that could facilitate this was developed by Schumacher et al. [93]. To produce a large library of MHC complexes containing different peptides, a strategy can be used in which MHC complexes are loaded with a UV-cleavable peptde. By applying UV light to cleave this conditional ligand in presence of another MHC-binding peptide, peptide exchange will occur with high efficiency, which facilitates rapid production of pMHC libraries. This method was shown successful for a wide variety of peptides and MHCs of different HLA types [93,94]. Possibly, peptide exchange could also be done for PIC-bound MHC complexes that contain UV-cleavable ligands, thereby facilitating production of sDCs with a variety of targets.

Taken together, sDCs could be either applied as 'off-the-shelf' therapy to target commonly shared tumor antigens, or in a personalized approach that includes the detection or prediction of neo-antigens to synthesize a variety of PIC-pMHC conjugates. These approaches need to be further developed in future pre-clinical studies.

8.4 Challenges for clinical application of sDCs in cancer therapy

Nanomedicines, such as sDCs, have paved the way to exploit novel targeted strategies to treat diseases. Nanoscale materials have proven to efficient scaffolds to target cancers in a variety of strategies, but their clinical translation has been relatively slow [95]. From a regulatory point of view, application of small molecule drugs and biologicals is easier, leading to faster clinical translation of these drugs [96]. For commercialization of drugs, it is therefore often more attractive for industry to invest in less complex therapeutics. However, interest in nanotherapeutics is growing due to their limited side effects, but some major issues that slow down regulatory approval still remain [97]. Importantly, bio-distribution and resulting long-term safety profiles

are not comparable to most available drugs and nanomedicines often consist of hybrid structures that each need individual GMP-grade production and approval. For many nanomaterials it is currently unclear whether their bio-distribution in humans is comparable to pre-clinical animal models. Furthermore, they are often produced in a batch process, which can result in batch-to-batch variability, especially when production is scaled up for clinical use [96,97]. Nanomedicines often require more complex characterization and toxicity tests before they can be implemented in therapies. Many of these issues have resulted in lack of commercialization, although industry is now catching up and increasing numbers of nanotherapeutics are being approved because of this [98,99].

Nanomedicines being developed for immunotherapy are facing similar issues [100]. Because of their more straightforward translation, non-specific immunotherapies, most notably checkpoint blockade antibodies, have become standard practice in cancer immunotherapy. These therapies have demonstrated the great potential of immunotherapy, but are still limited by dangerous side effects [101]. As targeted treatments, cell-based immunotherapies have been applied in successful clinical trials. Although some of these therapies have demonstrated great clinical benefits, widespread application of cell-based treatments is challenging because of their laborious personalized preparation. Despite their complexity, DC and CAR-T cell-based therapies have been approved for several clinical applications [102,103]. As discussed in this thesis, clinical translation of nanomedicines, such as sDCs, could give rise to targeted immunotherapies that do not require specialized cell culture facilities and are therefore less personalized and easier to scale up. Several challenges, that are also a problem for translation of nanomedicine in general, need to be addressed for clinical translation of sDCs.

At this point, cell-free aAPCs have been used in clinical trials for *ex vivo* T cell stimulation, but not for active *in vivo* immunization. PIC-based sDCs may be used for this in the future, but extensive characterization of their toxicity profile is still needed for clinical translation. PIC filaments and PIC-antibody conjugates were determined to be non-toxic using cell culture [3], and also PIC-based hydrogels are non-toxic *in vitro* [104]. In addition, both seem to be well tolerated in initial *in vivo* experiments, but more extensive toxicity and bio-distribution studies need to be done. Some of the proteins that can be conjugated onto PICs, including cytokines and co-stimulatory antibodies, have been approved for clinical use. However, cytokines can give rise to dangerous side effects, and reduced toxicity profiles of PIC-cytokine conjugates need to be demonstrated *in vivo* to allow clinical translation. Importantly, production of these proteins is possible at clinical scale, which allows for rapid upscaling of sDC production. For preparation of GMP-grade (nano)therapeutics, it is essential that clean and highly pure products can be developed. As is described in chapter 3, the final step of our sDC production consists of affinity-based purification of PIC-conjugates.

Impurities and contaminants can easily be removed during this process, leading to a highly pure product. For clinical translation, it is essential to extensively characterize therapeutics, which can be more difficult for nanomedicines [105]. Analysis of our sDCs can be done in a more straightforward manner compared to other aAPCs through a combination of circular dichroism (CD) and protein assays. Particle-based aAPCs rely on indirect measurement of protein content, which is often less reproducible. Taken together, PICs still require extensive toxicological tests to allow for clinical translation, whereas their straightforward synthesis and analysis may facilitate approval. Due to their clinical benefit, complex cell-based immunotherapies are being applied and approved in clinical trials regularly. Continued multidisciplinary efforts leading to translation of nanomedicines are needed to supplement these cell-based therapies with 'off-the-shelf' strategies [105].

References

1 Hickey, J.W. *et al.* (2017) Biologically Inspired Design of Nanoparticle Artificial Antigen-Presenting Cells for Immunomodulation. *Nano Lett.* 17, 7045–7054

2 Mandal, S. *et al.* (2015) Polymer-Based Synthetic Dendritic Cells for Tailoring Robust and Multifunctional T Cell Responses. *ACS Chem. Biol.* 10, 485–492

3 Mandal, S. *et al.* (2013) Therapeutic nanoworms: towards novel synthetic dendritic cells for immunotherapy. *Chem. Sci.* 4, 4168

4 Malissen, B. and Bongrand, P. (2015) Early T Cell Activation: Integrating Biochemical, Structural, and Biophysical Cues. *Annu. Rev. Immunol.* 33, 539–561

5 Chakraborty, A.K. and Weiss, A. (2014) Insights into the initiation of TCR signaling. *Nat. Immunol.* 15, 798–807

6 Naeher, D. *et al.* (2007) A constant affinity threshold for T cell tolerance. *J. Exp. Med.* 204, 2553–2559

7 Davis, M.M. *et al.* (1998) LIGAND RECOGNITION BY αβ T CELL RECEPTORS. *Annu. Rev. Immunol.* 16, 523–544

8 Lever, M. *et al.* (2014) Phenotypic models of T cell activation. *Nat. Rev. Immunol.* 14, 619–629

9 McKeithan, T.W. (1995) Kinetic proofreading in T-cell receptor signal transduction. *Proc. Natl. Acad. Sci.* 92, 5042–5046

10 Kalergis, A.M. *et al.* (2001) Efficient T cell activation requires an optimal dwell-time of interaction between the TCR and the pMHC complex. *Nat. Immunol.* 2, 229–234

11 Rosette, C. *et al.* (2001) The Impact of Duration versus Extent of TCR Occupancy on T Cell Activation. *Immunity* 15, 59–70

12 Huang, J. *et al.* (2013) A Single Peptide-Major Histocompatibility Complex Ligand Triggers Digital Cytokine Secretion in CD4+ T Cells. *Immunity* 39, 846–857

13 Fulton, R.B. *et al.* (2014) The TCR's sensitivity to self peptide–MHC dictates the ability of naive CD8+ T cells to respond to foreign antigens. *Nat. Immunol.* 16, 107–117

14 van Oers, N.S. *et al.* (1993) Constitutive tyrosine phosphorylation of the T-cell receptor (TCR) zeta subunit: regulation of TCR-associated protein tyrosine kinase activity by TCR zeta. *Mol. Cell. Biol.* 13, 5771–80

15 Klammt, C. *et al.* (2015) T cell receptor dwell times control the kinase activity of Zap70. *Nat. Immunol.* 16, 961–969

16 Brdicka, T. *et al.* (2005) Intramolecular Regulatory Switch in ZAP-70: Analogy with Receptor Tyrosine Kinases. *Mol. Cell. Biol.* 25, 4924–4933

17 Katz, Z.B. *et al.* (2016) A cycle of Zap70 kinase activation and release from the TCR amplifies and disperses antigenic stimuli. *Nat. Immunol.* 18, 86–95

18 Brownlie, R.J. and Zamoyska, R. (2013) T cell receptor signalling networks: branched, diversified and bounded. *Nat. Rev. Immunol.* 13, 257–269

19 Artyomov, M.N. *et al.* (2010) CD4 and CD8 binding to MHC molecules primarily acts to enhance Lck delivery. *Proc. Natl. Acad. Sci.* 107, 16916–16921

20 Casas, J. *et al.* (2014) Ligand-engaged TCR is triggered by Lck not associated with CD8 coreceptor. *Nat. Commun.* 5, 5624

21 Stone, J.D. *et al.* (2009) T-cell receptor binding affinities and kinetics: impact on T-cell activity and specificity. *Immunology* 126, 165–176

22 Kjer-Nielsen, L. *et al.* (2004) Crystal structure of the human T cell receptor CD3 heterodimer complexed to the therapeutic mAb OKT3. *Proc. Natl. Acad. Sci.* 101, 7675–7680

23 Edwards, L.J. *et al.* (2012) Insights into T Cell Recognition of Antigen: Significance of Two-Dimensional Kinetic Parameters. *Front. Immunol.* 3, 86

24 Huppa, J.B. *et al.* (2010) TCR–peptide–MHC interactions in situ show accelerated kinetics and increased affinity. *Nature* 463, 963–967

25 Huang, J. *et al.* (2010) The kinetics of two-dimensional TCR and pMHC interactions determine T-cell responsiveness. *Nature* 464, 932–936

26 Liu, Y. *et al.* (2016) DNA-based nanoparticle tension sensors reveal that T-cell receptors transmit defined pN forces to their antigens for enhanced fidelity. *Proc. Natl. Acad. Sci.* 113, 5610–5615

27 Bashour, K.T. *et al.* (2014) CD28 and CD3 have complementary roles in T-cell traction forces. *Proc. Natl. Acad. Sci. U. S. A.* 111, 2241–6

28 James, J.R. (2017) Using the force to find the peptides you're looking for. *Proc. Natl. Acad. Sci.* 114, 10303–10305

29 Ma, Z. *et al.* (2012) Mechanical Force in T Cell Receptor Signal Initiation. *Front. Immunol.* 3, 217

30 Hu, K.H. and Butte, M.J. (2016) T cell activation requires force generation. *J. Cell Biol.* 213, 535–542

31 Dustin, M.L. and Kam, L.C. (2016) Tapping out a mechanical code for T cell triggering. *J. Cell Biol.* 213, 501–503

32 Ilani, T. *et al.* (2009) T cell antigen receptor signaling and immunological synapse stability require myosin IIA. *Nat. Immunol.* 10, 531–539

33 Liu, B. *et al.* (2014) Accumulation of Dynamic Catch Bonds between TCR and Agonist Peptide-MHC Triggers T Cell Signaling. *Cell* 157, 357–368

34 Kim, S.T. *et al.* (2009) The αβ T Cell Receptor Is an Anisotropic Mechanosensor. *J. Biol. Chem.* 284, 31028–31037

35 Xu, C. *et al.* (2008) Regulation of T Cell Receptor Activation by Dynamic Membrane Binding of the CD3ε Cytoplasmic Tyrosine-Based Motif. *Cell* 135, 702–713

36 Li, L. *et al.* (2017) Ionic CD3–Lck interaction regulates the initiation of T-cell receptor signaling. *Proc. Natl. Acad. Sci.* 114, E5891–E5899

37 Huse, M. (2017) Mechanical forces in the immune system. *Nat. Rev. Immunol.* 17, 679–690

38 Hong, J. *et al.* (2015) Force-Regulated In Situ TCR–Peptide-Bound MHC Class II Kinetics Determine Functions of CD4 + T Cells. *J. Immunol.* 195, 3557–3564

39 Das, D.K. *et al.* (2015) Force-dependent transition in the T-cell receptor β-subunit allosterically regulates peptide discrimination and pMHC bond lifetime. *Proc. Natl. Acad. Sci.* 112, 1517–1522

40 Liu, B. *et al.* (2014) Accumulation of Dynamic Catch Bonds between TCR and Agonist Peptide-MHC Triggers T Cell Signaling. *Cell* 157, 357–368

41 Depoil, D. and Dustin, M.L. (2014) Force and affinity in ligand discrimination by the TCR. *Trends Immunol.* 35, 597–603

42 O'Donoghue, G.P. *et al.* (2013) Direct single molecule measurement of TCR triggering by agonist pMHC in living primary T cells. *Elife* 2, e00778

43 O'Connor, R.S. *et al.* (2012) Substrate Rigidity Regulates Human T Cell Activation and Proliferation. *J. Immunol.* 189, 1330–1339

44 Lambert, L.H. *et al.* (2017) Improving T Cell Expansion with a Soft Touch. *Nano Lett.* 17, 821–826

45 van Buul, A.M. *et al.* (2013) Stiffness versus architecture of single helical polyisocyanopeptides. *Chem. Sci.* 4, 2357

46 Metselaar, G.A. *et al.* (2007) Polyisocyanides Derived from Tripeptides of Alanine. *Chem. - A Eur. J.* 13, 950–960

47 Rossy, J. *et al.* (2012) How does the kinase Lck phosphorylate the T cell receptor? Spatial organization as a regulatory mechanism. *Front. Immunol.* 3, 167

48 Nika, K. *et al.* (2010) Constitutively Active Lck Kinase in T Cells Drives Antigen Receptor Signal Transduction. *Immunity* 32, 766–777

49 Carbone, C.B. *et al.* (2017) In vitro reconstitution of T cell receptor-mediated segregation of the CD45 phosphatase. *Proc. Natl. Acad. Sci.* 114, E9338–E9345

50 Cordoba, S.-P. *et al.* (2013) The large ectodomains of CD45 and CD148 regulate their segregation from and inhibition of ligated T-cell receptor. *Blood* 121, 4295–4302

51 Chang, V.T. *et al.* (2016) Initiation of T cell signaling by CD45 segregation at "close contacts." *Nat. Immunol.* 17, 574–582

52 Baker, J.E. *et al.* (2001) Protein Tyrosine Phosphatase CD148-Mediated Inhibition of T-Cell Receptor Signal Transduction Is Associated with Reduced LAT and Phospholipase C 1 Phosphorylation. *Mol. Cell. Biol.* 21, 2393–2403

53 Chakraborty, A.K. and Das, J. (2010) Pairing computation with experimentation: a powerful coupling for understanding T cell signalling. *Nat. Rev. Immunol.* 10, 59–71

54 Dinic, J. *et al.* (2015) The T cell receptor resides in ordered plasma membrane nanodomains that aggregate upon patching of the receptor. *Sci. Rep.* 5, 10082

55 Lillemeier, B.F. *et al.* (2010) TCR and Lat are expressed on separate protein islands on T cell membranes and concatenate during activation. *Nat. Immunol.* 11, 90–96

56 Kumar, R. *et al.* (2011) Increased Sensitivity of Antigen-Experienced T Cells through the Enrichment of Oligomeric T Cell Receptor Complexes. *Immunity* 35, 375–387

57 Pageon, S. V *et al.* (2016) Functional role of T-cell receptor nanoclusters in signal initiation and antigen discrimination. *Proc. Natl. Acad. Sci.* 113, E5454–E5463

58 Dushek, O. and van der Merwe, P.A. (2014) An induced rebinding model of antigen discrimination. *Trends Immunol.* 35, 153–158

59 Sherman, E. *et al.* (2013) Super-resolution characterization of TCR-dependent signaling clusters. *Immunol. Rev.* 251, 21–35

60 Molnár, E. *et al.* (2012) Cholesterol and Sphingomyelin Drive Ligand-independent T-cell Antigen Receptor Nanoclustering. *J. Biol. Chem.* 287, 42664–42674

61 Perica, K. *et al.* (2014) Magnetic field-induced T cell receptor clustering by nanoparticles enhances T cell activation and stimulates antitumor activity. *ACS Nano* 8, 2252–60

62 Hashimoto-Tane, A. and Saito, T. (2016) Dynamic Regulation of TCR–Microclusters and the Microsynapse for T Cell Activation. *Front. Immunol.* 7, 255

63 Hashimoto-Tane, A. *et al.* (2016) Micro–adhesion rings surrounding TCR microclusters are essential for T cell activation. *J. Exp. Med.* 213, 1609–1625

64 Campi, G. *et al.* (2005) Actin and agonist MHC–peptide complex–dependent T cell receptor microclusters as scaffolds for signaling. *J. Exp. Med.* 202, 1031–1036

65 Yokosuka, T. *et al.* (2005) Newly generated T cell receptor microclusters initiate and sustain T cell activation by recruitment of Zap70 and SLP-76. *Nat. Immunol.* 6, 1253–1262

66 Varma, R. *et al.* (2006) T Cell Receptor-Proximal Signals Are Sustained in Peripheral Microclusters and Terminated in the Central Supramolecular Activation Cluster. *Immunity* 25, 117–127

67 Thauland, T.J. and Parker, D.C. (2010) Diversity in immunological synapse structure. *Immunology* 131, 466–472

68 Hashimoto-Tane, A. *et al.* (2011) Dynein-Driven Transport of T Cell Receptor Microclusters Regulates Immune Synapse Formation and T Cell Activation. *Immunity* 34, 919–931

69 Chen, L. and Flies, D.B. (2013) Molecular mechanisms of T cell co-stimulation and co-inhibition. *Nat. Rev. Immunol.* 13, 227–242

70 Yokosuka, T. *et al.* (2008) Spatiotemporal Regulation of T Cell Costimulation by TCR-CD28 Microclusters and Protein Kinase C θ Translocation. *Immunity* 29, 589–601

71 Saito, T. *et al.* (2010) Dynamic regulation of T cell activation and co-stimulation through TCR-microclusters. *FEBS Lett.* 584, 4865–4871

72 Dobbins, J. *et al.* (2016) Binding of the cytoplasmic domain of CD28 to the plasma membrane inhibits Lck recruitment and signaling. *Sci. Signal.* 9, ra75-ra75

73 Bashour, K.T. *et al.* (2014) Cross Talk between CD3 and CD28 Is Spatially Modulated by Protein Lateral Mobility. *Mol. Cell. Biol.* 34, 955–964

74 Isakov, N. and Altman, A. (2012) PKC-theta-mediated signal delivery from the TCR/CD28 surface receptors. *Front. Immunol.* 3, 273

75 Croft, M. (2009) The role of TNF superfamily members in T-cell function and diseases. *Nat. Rev. Immunol.* 9, 271–285

76 Zwart, W. *et al.* (2010) The invariant chain transports TNF family member CD70 to MHC class II compartments in dendritic cells. *J. Cell Sci.* 123, 3817–3827

77 Nam, K.-O. *et al.* (2005) Cross-Linking of 4-1BB Activates TCR-Signaling Pathways in CD8+ T Lymphocytes. *J. Immunol.* 174, 1898–1905

78 Perica, K. *et al.* (2014) Nanoscale artificial antigen presenting cells for T cell immunotherapy. *Nanomedicine Nanotechnology, Biol. Med.* 10, 119–129

79 Ugel, S. *et al.* (2009) In vivo Administration of Artificial Antigen-Presenting Cells Activates Low-Avidity T Cells for Treatment of Cancer. *Cancer Res.* 69, 9376–9384

80 Shen, C. *et al.* (2013) Latex bead-based artificial antigen-presenting cells induce tumor-specific CTL responses in the native T-cell repertoires and inhibit tumor growth. *Immunol. Lett.* 150, 1–11

81 Suntharalingam, G. *et al.* (2006) Cytokine Storm in a Phase 1 Trial of the Anti-CD28 Monoclonal Antibody TGN1412. *N. Engl. J. Med.* 355, 1018–1028

82 Floros, T. and Tarhini, A.A. (2015) Anticancer Cytokines: Biology and Clinical Effects of Interferon- 2, Interleukin (IL)-2, IL-15, IL-21, and IL-12. *Semin. Oncol.* 42, 539–548

83 Weide, B. *et al.* (2012) Functional T Cells Targeting NY-ESO-1 or Melan-A Are Predictive for Survival of Patients With Distant Melanoma Metastasis. *J. Clin. Oncol.* 30, 1835–1841

84 Coulie, P.G. *et al.* (2014) Tumour antigens recognized by T lymphocytes: at the core of cancer immunotherapy. *Nat. Rev. Cancer* 14, 135–146

85 Bol, K.F. *et al.* (2016) Dendritic Cell-Based Immunotherapy: State of the Art and Beyond. *Clin. Cancer Res.* 22, 1897–1906

86 Rosenberg, S.A. and Restifo, N.P. (2015) Adoptive cell transfer as personalized immunotherapy for human cancer. *Science (80-.).* 348, 62–68

87 Lu, Y.-C. and Robbins, P.F. (2016) Cancer immunotherapy targeting neoantigens. *Semin. Immunol.* 28, 22–27

88 Johnson, L.A. *et al.* (2009) Gene therapy with human and mouse T-cell receptors mediates cancer regression and targets normal tissues expressing cognate antigen. *Blood* 114, 535–546

89 Bethune, M.T. and Joglekar, A. V (2017) Personalized T cell-mediated cancer immunotherapy: progress and challenges. *Curr. Opin. Biotechnol.* 48, 142–152

90 Schumacher, T.N. and Schreiber, R.D. (2015) Neoantigens in cancer immunotherapy. *Science* 348, 69–74

91 Yadav, M. *et al.* (2014) Predicting immunogenic tumour mutations by combining mass spectrometry and exome sequencing. *Nature* 515, 572–576

92 Ott, P.A. *et al.* (2017) An immunogenic personal neoantigen vaccine for patients with melanoma. *Nature* 547, 217–221

93 Rodenko, B. *et al.* (2006) Generation of peptide–MHC class I complexes through UV-mediated ligand exchange. *Nat. Protoc.* 1, 1120–1132

94 Bakker, A.H. *et al.* (2008) Conditional MHC class I ligands and peptide exchange technology for the human MHC gene products HLA-A1, -A3, -A11, and -B7. *Proc. Natl. Acad. Sci.* 105, 3825–3830

95 Jang, H.L. *et al.* (2016) Boosting clinical translation of nanomedicine. *Nanomedicine* 11, 1495–1497

96 Valencia, P.M. *et al.* (2012) Microfluidic technologies for accelerating the clinical translation of nanoparticles. *Nat. Nanotechnol.* 7, 623–629

97 Satalkar, P. *et al.* (2016) Challenges of clinical translation in nanomedicine: A qualitative study. *Nanomedicine Nanotechnology, Biol. Med.* 12, 893–900

98 Pandit, A. and Zeugolis, D.I. (2016) Twenty-five years of nano-bio-materials: have we revolutionized healthcare? *Nanomedicine* 11, 985–987

99 Paul Evers (2017) *Nanotechnology in Medical Applications: The Global Market: HLC069D | BCC Research*,

100 Sengupta, S. (2017) Cancer Nanomedicine: Lessons for Immuno-Oncology. *Trends in Cancer* 3, 551–560

101 Postow, M.A. *et al.* (2015) Immune Checkpoint Blockade in Cancer Therapy. *J. Clin. Oncol.* 33, 1974–1982

102 Anguille, S. *et al.* (2014) Clinical use of dendritic cells for cancer therapy. *Lancet Oncol.* 15, e257–e267

103 Morris, E.C. (2018) Editing gene engineering to enhance function. *Blood* 131, 272–273

104 Das, R.K. *et al.* (2016) Stress-stiffening-mediated stem-cell commitment switch in soft responsive hydrogels. *Nat. Mater.* 15, 318–325

105 Eaton, M.A.W. *et al.* (2015) Delivering nanomedicines to patients: A practical guide. *Nanomedicine Nanotechnology, Biol. Med.* 11, 983–992

9

Nederlandse samenvatting
Curriculum Vitae
List of publications
Dankwoord

Nederlandse samenvatting

Immuuntherapie met artificiële antigeen-presenterende cellen.

Immuuntherapie is in de afgelopen jaren opgekomen als een veelbelovende nieuwe therapievorm voor de behandeling van kanker. Klassieke therapieën, zoals chemotherapie of bestraling, richten zich op het direct doden van kankercellen. In immunotherapieën wordt daarentegen geprobeerd om het immuunsysteem te moduleren, zodat dit zelf de kanker kan aanvallen. Immuuncellen kunnen een belangrijke rol spelen in zowel het bevorderen van kanker, als het opruimen van tumoren. Dit heeft geleid tot de ontwikkeling van verschillende immuuntherapieën die op deze kankerstimulerende en kankerremmende processen kunnen inspelen, en zich daarbij richten op verschillende onderdelen van het immuunsysteem.

De hernieuwde belangstelling voor kankerbehandeling door middel van immuunmodulatie is met name aangewakkerd door het klinische succes van antilichamen die immuuncheckpoints kunnen blokkeren. Immuuncellen die aanwezig zijn in tumoren worden vaak door stimulatie van deze immuuncheckpoints (via de receptoren op tumorcellen of andere immuuncellen) geremd om een anti-tumor immuunreactie te voorkomen. Door deze interactie te blokkeren wordt deze remming op het immuunsysteem opgeheven, waardoor de tumor wel weer kan worden aangevallen door immuuncellen. Behalve via het opheffen van remmende mechanismes, kunnen kankerpatiënten ook baat hebben bij directe stimulatie van immuuncellen die kankercellen kunnen vernietigen. Dit kan bijvoorbeeld gedaan worden door injectie van hoge doses cytokinen of (co)stimulerende antilichamen. De hierboven genoemde antilichaam- en cytokinetherapieën hebben laten zien dat modulatie van het immuunsysteem een veelbelovende methode kan zijn om kanker aan te pakken. Helaas zijn deze therapieën niet kankerspecifiek, maar zorgen ze voor stimulatie van het gehele immuunsysteem, wat kan zorgen voor ernstige bijwerkingen omdat het immuun- systeem niet alleen maar de tumor aanvalt. De toepasbaarheid en dosis van deze aspecifieke therapieën is daarom beperkt.

Om meer controle over immuunreacties te krijgen, kunnen uit patiënten geïsoleerde immuuncellen in het lab worden gestimuleerd. Deze cellen kunnen vervolgens teruggeplaatst worden in de patiënt, en kan daarmee een meer gerichte immuunrespons opwekken vergeleken met eerder genoemde strategieën. Zo zijn er verschillende celtherapieën ontwikkeld die gebruik maken van T-cellen, omdat dit celtype gespecialiseerd is in herkennen en vernietigen van gevaarlijke lichaamseigen cellen, zoals geïnfecteerde cellen of tumorcellen. Om tumor-specifieke T-cellen in te zetten voor immunotherapie kunnen deze cellen worden geïsoleerd uit tumorbiopten, waarnaar ze worden geëxpandeerd en weer worden teruggeïnjecteerd in patiënten. Hier kunnen deze cellen zorgen voor een sterke en langdurige afname van tumoren. Genetische modificatie van T-cellen heeft verder geleid tot een hogere affiniteit en

specificiteit. Dit heeft geleid tot verder een verbeterde klinische respons van T-celtherapieën, met name in leukemie.

Een ander celtype dat met succes is toegepast in vaccinatiestrategieën tegen kanker is de dendritische cel; een celtype dat gespecialiseerd is in het presenteren van stukjes eiwit (antigenen) aan T-cellen. Dendritische cellen kunnen worden geïsoleerd uit het bloed van patiënten, waarna ze worden gestimuleerd en beladen met specifieke tumorantigenen. Vervolgens zorgt dit ervoor dat deze dendritische cellen na injectie tumor-specifieke T-cellen kunnen stimuleren in het lichaam. Ook deze strategie heeft voor tumorregressie gezorgd in een aantal patiënten met vergevorderde kankers. De ongeëvenaarde klinische succesverhalen van deze celtherapieën hebben immuuntherapie verder op de kaart gezet als een veel- belovende aanpak voor het behandelen van een groot aantal kankers.

Hoewel celtherapieën goede resultaten laten zien, moeten deze vaccins persoonlijk geproduceerd worden voor elke patiënt door cellen in het lab op te kweken. Deze arbeidsintensieve productie en hierdoor ook de kosten zijn vaak problematisch. Het stimuleren en kweken van cellen voor behandeling van patiënten moet gebeuren in gespecialiseerde laboratoria, en is daardoor niet overal mogelijk. Er is hierdoor een grote behoefte aan celvrije immunotherapieën die algemeen kunnen worden toegepast en vergelijkbare immuunreacties tegen tumoren kunnen opwekken als cellulaire therapieën. Om dit aan te pakken worden er daarom artificiële Antigen-Presenterende Cellen (aAPCs) ontwikkeld om de functie van dendritische cellen na te bootsen met een synthetisch construct. Deze aAPCs bieden een kant-en-klaar product dat direct kan worden toegepast om T-cellen in patiënten te stimuleren. Daarnaast zorgen aAPCs voor meer directe controle over signalen die aan T-cellen gepresenteerd worden vergeleken met beschikbare celtherapieën.

Tot nu toe zijn er al een aantal verschillende soorten aAPCs ontwikkeld, zoals ook beschreven is in hoofdstuk 1. Deze eerste constructen hebben duidelijk gemaakt welke met welke parameters belangrijk zijn om een sterke activatie van T-cellen te induceren. Via celkweekexperimenten werd met deze biomaterialen aangetoond dat de grootte, vorm, dichtheid en rangschikking van liganderen, en de flexibiliteit op het oppervlak van aAPCs allemaal een rol hebben om optimale T-celactivatie te realiseren. Op deze manier werd duidelijk dat rigide bolvormige deeltjes met een minimale diameter van enkele micrometers en een meer uitgestrekte ovaalvormige vorm voor betere stimulatie zorgen. Wanneer kleinere deeltjes worden gebruikt, bleek er een hogere dichtheid aan stimulerende liganden nodig te zijn op deze bolletjes om hun effectiviteit te behouden. Met behulp van zowel PDMS-bedekte materialen, als deeltjes die bedekt zijn met lipidemembranen van verschillende flexibiliteit, is daarnaast aangetoond een meer flexibel oppervlak zorgt voor betere expansie van T-cellen. T-celstimulatie kan nog verder verbeterd worden door liganden geclusterd vast te zetten op membranen of rigide bolletjes, omdat dit zorgt voor een hoge gelokaliseerde dichtheid van stimulerende moleculen.

Om aAPCs direct in het lichaam toe te passen moet men rekening houden met een aantal extra (en soms conflicterende) karakteristieken. Zo zijn vooral de afmetingen en de vorm van de gebruikte synthetische constructen belangrijk voor een optimale biodistributie na injectie. Ook materialen met een meer uitgestrekte ovaalvormige vorm laten een betere verspreiding en beschikbaarheid zien *in vivo*, omdat meer van deze deeltjes lymfoïde organen (waar immuun- cellen zich bevingen) bereiken en minder worden opgenomen door fagocyterende cellen. Dit is gunstig, aangezien uitgerekte deeltjes ook in celkweekexperimenten beter bleken in het maken van directe multivalente contacten met T-cellen. De vorm van aAPCs is daarom een van de belangrijkste parameters om te optimaliseren voor een goede activatie van T cellen in het lichaam. Grote deeltjes beter zijn in het stimuleren van T-cellen dan kleinere structuren, maar kunnen niet ver van de injectieplaats komen. Deze microdeeltjes komen daardoor niet in lymfoïde organen terecht, waardoor ze slecht bruikbaar zijn voor directe T-celstimulatie in het lichaam.

Voor het toepassen van aAPC-therapie *in vivo* is het dus gebleken dat de gebruikte constructen nano-afmetingen moeten hebben. Daarnaast biedt gebruik van materialen met een langwerpige vorm betere distributie en activatie dan het gebruik van bolvormige deeltjes. Verder is een zeker mate van flexibiliteit, wat beweging van receptoren op het T-celmembraan mogelijk maakt, ook gunstig voor het activerende vermogen van deze constructen. Om deze eigenschappen samen te laten komen in het ontwerp van één enkel construct, hebben wij gebruik gemaakt van polyisocyanopeptides (PICs) als fundament voor de ontwikkeling van nieuwe aAPC: De synthetische Dendritische Cel (sDC). PICs zijn dunne filamentvormige polymeren die gemaakt kunnen worden met lengtes van 100-1000 nm. Door hun langgerekte vorm en semi-flexibiliteit zouden deze polymeren uitermate geschikt moeten zijn voor het ontwikkelen van aAPCs. PICs zijn biocompatibel en kunnen relatief eenvoudig en gecontroleerd worden gemodificeerd met biomoleculen door de aanwezigheid van azidefunctionaliteiten in hun zijketens. In hoofdstuk 2 zijn deze azides gebruikt voor het conjugeren van streptavidine aan de PICs. De eerste sDCs werden gemaakt door biotine-gefunctionaliseerde antilichamen aan deze streptavidine-PICs te binden.

Polyisocyanopeptides als synthetische Dendritische Cellen. Om het principe te bewijzen dat op PICs kunnen werken als sDCs zijn 200-nm-lange streptavidine-PICs bedekt met stimulerende antilichamen tegen CD3. Deze anti-CD3-PICs stimuleerden T-cellen beter dan PLGA microdeeltjes met vergelijkbare liganddichtheid. Immuunreacties konden verder worden versterkt via additionele conjugatie van stimulerend antilichamen tegen CD28, wat voor een co-stimulerend signaal zorgt. Deze eerste experimenten toonden aan dat PICs effectief kunnen zijn als sDCs, maar ontwerpfactoren die zorgen voor deze goede stimulatie van T-cellen kon nog uitgebreider worden geanalyseerd en verbeterd. In hoofdstuk 2 laten we daarom zien

dat de multivalentie van anti-CD3 op deze semi-flexibele polymeren essentieel is voor optimale stimulatie van T-cellen. Hier werd duidelijk dat PICs zorgen voor betere activatie en langdurige T-cel receptor (TCR) signalering in T-cellen wanneer langere constructen worden gebruikt, en wanneer meerdere anti-CD3 antilichamen dichter bij elkaar geplaatst zijn. Omdat de polymeerlengte belangrijk is, hebben we in de latere hoofdstukken langere PICs (~ 400 nm) gebruikt. De dichtheid van anti-CD3 (de relatieve afstand tussen de antilichamen) heeft een significante invloed op activatie van T-cellen en moet daarom goed gecontroleerd worden wanneer we het effect van conjugatie van andere PIC-geconjugeerde stimulerende moleculen analyseren.

De in hoofdstuk 2 gebruikte zuivering van antilichaam-streptavidine-PICs via spinfiltratie was erg inefficiënt en leidde tot erg lage opbrengst van gezuiverd product. Hierdoor was het moeilijk om de anti-CD3-dichtheid direct te meten en werden in plaats daarvan de streptavidinedichtheid bepaald met behulp van Atomic Force Microscopy. Om de opbrengst van gezuiverde PIC-eiwitconjugaten te verhogen hebben we een nieuwe affiniteitzuivering geïntroduceerd voor PICs in hoofdstuk 3. Omdat deze methode zorgt voor een hoge zuiverheid en opbrengst van PIC-eiwitconjugaten, was het vervolgens mogelijk om PIC-concentraties direct te kwantificeren met behulp van Circular Dichroism (CD). Met behulp van deze methode werd het gemakkelijker om anti-CD3/PIC-ratios te bepalen. De synthese van sDCs kon verder worden vereenvoudigd door streptavidine te vervangen door een conjugatiestrategie waarin alleen een korte PEG werd gebruikt als linker. Omdat antilichaambinding aan PICs hierdoor niet meer via streptavidine (wat vier bindingsplaatsen heeft) plaatsvindt, was de anti-CD3/PIC-ratios in deze constructen zich direct gekoppeld aan de relatieve afstand tussen antilichamen op deze PICs. Uiteindelijk hebben de vereenvoudigde structuur en de verbeterde zuivering gezorgd voor een verhoogde syntheseopbrengst en een eenvoudigere syntheseroute en karakterisatie van de geproduceerde conjugaten. Hierdoor konden sneller grote hoeveelheden van verschillende PIC-eiwitconjugaten geproduceerd worden. Deze verbeterde syntheseomzet was essentieel voor het ontwikkelen van de sDCs die worden beschreven in hoofdstukken 4 t/m 7.

Het gebruik van eenvoudige PEG linkers in plaats van streptavidine maakte het mogelijk om een grote verzameling aan sDCs met verschillende co-stimulerende antilichamen te ontwikkelen. In hoofdstuk 4 is beschreven hoe de synthese van PIC-antilichaamconjugaten verder is geoptimaliseerd, waardoor snel een groot aantal verschillende functionele sDCs geproduceerd kon worden. Het screenen van plaatgebonden co-stimulerende antilichamen liet zien dat de snelheid van T-cel-differentiatie kan worden gestuurd door verschillende co-receptoren op T-cellen te stimuleren. Co-stimulatie van naïve CD8+ T-cellen met anti-CD27, of van voor-gestimuleerde cellen met anti-4-1BB resulteerde in een snellere differentiatie in verhouding tot cellen die gestimuleerd waren met anti-CD28, anti-OX40 of anti-CD150.

Stimulatie van T-cellen met deze conjugaten van anti-CD3 en co-stimulerende antilichamen zorgt met name voor verhoogde activatie wanneer anti-CD3 en co-stimulerende antilichamen beide op hetzelfde polymeer zitten. Het optimaliseren van deze co-stimulerende sDCs zou kunnen leiden tot nanofilamenten waarmee de differentiatie en functionaliteit van T-cellen bestuurd kan worden.

Dezelfde modulaire synthesestrategie heeft het ook mogelijk gemaakt om, zoals beschreven in hoofdstuk 5, DNA-linkers in te bouwen in PIC-antilichaamconjugaten. Antilichamen konden efficiënt aan PICs geconjugeerd worden via het hybridiseren van twee DNA-strengen. sDCs die op deze manier werden gemaakt konden efficient T-cellen stimuleren. Door twee complementaire DNA-strengen in verschillende oriëntaties aan PICs en anti-CD3 te conjugeren werd een eerste stap gezet naar de ontwikkeling van sDCs met ingebouwde krachtsensoren. Deze sDCs kunnen vervolgens worden ingezet om te bestuderen welke krachten door T-cellen worden gegenereerd tijdens hun activatie. Door het breken van de DNA-duplexen tussen antilichamen en PICs te meten kan de grootte van deze krachten worden gemeten. Omdat PICs multivalent binden aan T-cellen en relatief klein zijn ten opzichte van klassieke aAPCs, kunnen deze DNA-sDCs mogelijk gebruikt worden voor het meten van relatieve beweging en afscheiding van receptoren op T-cellen.

In hoofdstukken 2-5 zijn alleen antilichamen aan PICs geconjugeerd voor de synthese van sDCs. In hoofdstuk 6 lieten we zien dat ook cytokinen met dezelfde synthesestrategie aan deze polymeren geconjugeerd kunnen worden. T-cellen zijn afhankelijk van cytokinen voor hun overleving, proliferatie en veel van hun andere functies. Deze signaleringsmoleculen worden daarom ook toegepast in verschillende immunotherapieën. Helaas gaat injectie van cytokinen vaak gepaard met gevaarlijke bijwerkingen die de toepassing van deze therapieën limiteren. Het is daarom nodig om ervoor te zorgen dat deze cytokinen zich meer specifiek op T-cellen richten. Door cytokinen aan PICs vast te maken konden sDCs ontwikkeld worden waarmee geïmmobiliseerd IL-2 en IFNα meer specifiek aan T-cellen konden binden. Hierbij werd aangetoond dat conjugatie van IL-2 aan PICs zorgt voor een verminderde bioactiviteit van het cytokine. Wanneer daarentegen deze IL-2-PICs naar specifiek naar T-cellen worden gestuurd door anti-CD3 aan hetzelfde polymeer vast te maken, zorgt dit voor een verhoogde cytokine-activiteit, ook vergeleken met cytokinen die niet aan PICs zijn gebonden. Anti-CD3/IL-2-PICs en anti-CD3/IFNα-PICs kunnen daarom krachtige wapens zijn om de bijwerkingen van deze cytokinen te verminderen en de werking van cytokinetherapieën te verbeteren.

Potentiële bijwerkingen van het gebruik van sDCs (zoals cytokine-sDCs) voor immunotherapie, kunnen verder worden verminderd door alleen T-cellen te stimuleren die specifieke antigenen herkennen. In hoofdstukken 2-6 hebben we gezien dat conjugatie van stimulerende antilichamen tegen CD3 aan PICs kan zorgen voor sterke activatie van polyklonale T-cellen. Het gebruik van anti-CD3 is een relatief

eenvoudige manier om T-cellen te activeren. Hierbij worden interacties tussen peptide-MHC (pMHC) en TCRs goed gesimuleerd met behulp van de OKT3 antilichaamkloon. Om sDCs veilig *in vivo* toe te kunnen passen is het daarentegen belangrijk om niet alle T-cellen, maar alleen T-cellen die bepaalde (tumor)antigenen herkennen te stimuleren. In hoofdstuk 7 is daarom beschreven hoe pMHCs worden geproduceerd en geconjugeerd aan PICs in plaats van anti-CD3, om hiermee antigeen-specifieke stimulatie van T-cellen te bewerkstelligen. Hiervoor werden sDCs geproduceerd die specifiek zijn voor kankerantigeen NY-ESO-I. Menselijke T-cellen waarin een NY-ESO-I-specifieke TCR tot expressie was gebracht konden effectief en specifiek geactiveerd worden met deze sDCs. Ook hier zorgde co-conjugatie van pMHC en anti-CD28 aan dezelfde PIC is een synergistische verhoging van activatie van T-cellen, hoewel hierdoor ook wat aspecifieke stimulatie werd geïnduceerd. Daarnaast werden ook ovalbumine-specifieke geproduceerd die herkend kunnen worden door de T-cellen uit OT-1-muizen. Celkweekstimulatie-experimenten wezen uit dat de geproduceerde sDCs deze T-cellen even goed konden activeren als ongebonden pMHC. Wanneer deze sDCs echter geïnjecteerd werden in het bloed van muizen, werden dezelfde OT-1 T-cellen aanzienlijk beter geactiveerd vergeleken met ongebonden pMHC. Hoewel er meer experimenten gedaan moeten worden om te laten zien dat sDCs ook natuurlijke antigeen-specifieke T-cellen kan stimuleren, laten deze eerste resultaten duidelijk het potentieel van sDCs voor directe *in vivo*-vaccinatie zien. In de toekomst kan het gebruik van sDCs daarom mogelijk een strategie bieden voor een kant-en-klare immunotherapie die direct in patiënten geïnjecteerd kan worden zonder ingewikkelde en dure celkweekprocedures. In figuur 1 is een overzicht weergegeven van de verschillende PIC-conjugaten die zijn ontwikkeld in dit proefschrift.

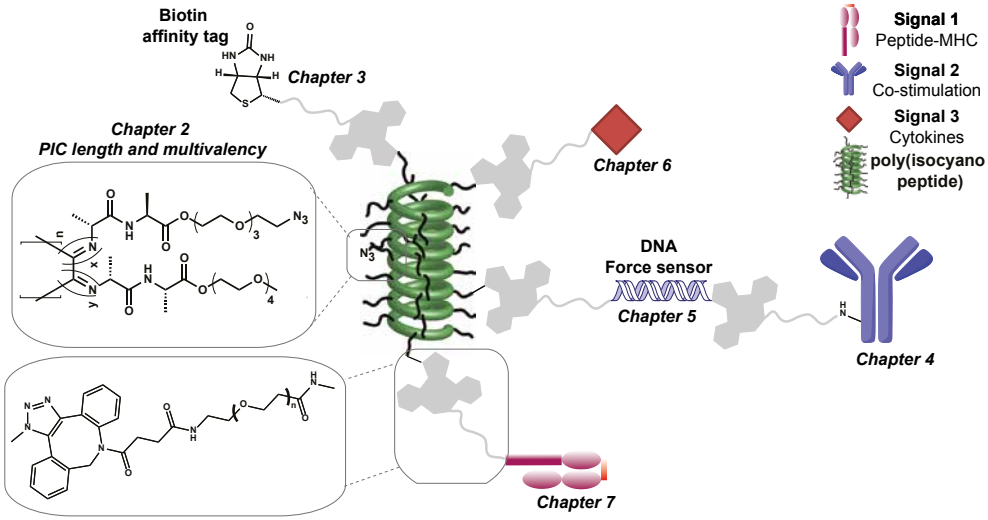

Figuur 1 Moleculaire structuur, linkers en biomoleculen die gebruikt zijn in de PIC-bioconjugaten die in dit proefschrift zijn beschreven.

Curriculum Vitae

Loek Eggermont was born on the 3rd of August 1990 in Kekerdom, The Netherlands. After completing secondary school at the Stedelijk Gymnasium Nijmegen in 2008, he studied Molecular Life Sciences at Radboud University Nijmegen. During his bachelor's studies, he performed a research internship at Synaffix in Nijmegen under supervision of Dr. Floris van Delft. During this internship he worked on the synthesis of bicyclononynes as new tools in biorthogonal chemical reporter strategies. In addition, as part of the Radboud Honours Academy, Loek went to Athens, Georgia, USA for an internship at the Complex Carbohydrate Research Center under supervision of Prof. dr. Geert-Jan Boons. There, his research was focused on the application of different cyclooctynes for biorthogonal labeling and fluorescent imaging of cells. In 2011, he obtained both his Bachelor of Science and Radboud Honours Academy degrees. During his Molecular Life Sciences Master's studies, Loek performed two research internships. During the first project, at the Department of Synthetic Organic Chemistry, under supervision of Prof. dr. Floris Rutjes, he worked on biorthogonal labeling of a cell-penetrating peptide to improve its cytoplasmic targeting. His second master's internship was performed at the Department of Biochemistry under supervision of Prof. dr. Roland Brock. Here, he worked on the development of liposomes for cytoplasmic peptide delivery. After receiving his Master's degree in 2013, he started his PhD research at the Department of Tumor Immunology in Nijmegen under the supervision of Prof. dr. Carl Figdor where he developed a synthetic dendritic cell platform for activation of T-cells. The most important results of his PhD project are described in this thesis. In 2018, Loek continued his research at the Department of Tumor Immunology as postdoctoral researcher.

List of publications

Colombani T, Rezaeeyazdi M, Aldhahri M, Eggermont LJ, Rogers. Z, Memic A, Bencherif SA
Latest advances in cryogel technology for biomedical applications
Manuscript in preparation

Voerman D, Hammink R, Eggermont LJ, Weiden J, Schluck M, Ignacio B, van den Eijnde T, Rowan AE, Verdoes M, Figdor CG
Polyisocyanopeptide brush surface modification via an aqueous grafting onto method
Manuscript in preparation

Weiden J, Voerman D, Dölen Y, Das RK, van Duffelen A, Hammink R, Eggermont LJ, Rowan AE, Tel J, Figdor CG.
Injectable Polyisocyanopeptide Hydrogels for Immunomodulation.
Manuscript submitted

Eggermont LJ*, Hammink R*, Blank KG, Rowan AE, Tel J, Figdor CG.
Cytokine-functionalized Synthetic Dendritic Cells for T Cell Targeted Immunotherapies.
Advanced Therapeutics, manuscript accepted for publication

Le Gall, C, Weiden J, Eggermont LJ, Figdor CG.
Harnessing Dendritic Cells for Immunotherapy.
Nature Materials, 17, 2018, p474-475

Hammink R*, Eggermont LJ*, Zisis T, Tel J, Figdor CG, Rowan AE, Blank KG.
Affinity-Based Purification of Polyisocyanopeptide Bioconjugates.
ACS Bioconjugate Chemistry, 28(10), 2017, p2560-2568

Hammink R*, Mandal S*, Eggermont LJ, Nooteboom M, Willems PHGM, Tel J, Rowan AE, Figdor CG, Blank KG.
Controlling T-Cell Activation with Synthetic Dendritic Cells Using the Multivalency Effect.
ACS Omega, 2(3), 2017, p937-945

Eggermont LJ, Paulis LE, Tel J, Figdor CG.
Towards efficient cancer immunotherapy: advances in developing artificial antigen-presenting cells.
Trends in Biotechnology, 32(9), 2014, p456-465

Temming RP, Eggermont LJ, van Eldijk MB, van Hest JCM, van Delft FL.
N-terminal dual protein functionalization by strain-promoted alkyne-nitrone cycloaddition.
Organic & Biomolecular Chemistry, 11, 2013, p 2772-2779

Patent application

Eggermont LJ, Hammink R, Figdor CG
Immunomodulatory nanofilaments, *2017*

*Equal contributions

Dankwoord

Met dit proefschrift komt er een eind aan vier jaar promotieonderzoek. Gelukkig stond ik hier niet alleen voor, want het afronden van mijn promotie en het schrijven van dit proefschrift was niet mogelijk geweest zonder de hulp en steun van een groot aantal mensen. Ik wil hier dan ook iedereen bedanken die een bijdrage heeft geleverd aan het tot stand komen van dit boekje.

Als eerste wil ik graag mijn promotor, **Carl**, bedanken. Terwijl ik zelf nog bezig was met optimaliseren van de PICs, dacht jij altijd een paar stappen vooruit. Hierdoor hadden we altijd een duidelijk doel voor ogen. Verder waardeer ik de vrijheid die je me gaf om de verschillende projecten ook zelf richting te geven. Je leerde mij om in een vroeg stadium een opzet te maken voor thesishoofdstukken en publicaties, wat essentieel was voor de afronding van mijn promotie. Jouw immunologische kennis en jouw enthousiasme voor het samenwerken met andere disciplines zullen zeker leiden tot mooie nieuwe immunotherapieën.

Ook mijn co-promotoren zijn erg belangrijk geweest tijdens mijn PhD. **Jurjen**, jij zorgde voor regelmatige immunologische input en jouw enthousiasme en positieve instelling was altijd goed om de motivatie vast te houden, vooral als de resultaten tegen zaten. Jouw tips voor het opbreken van verschillende projecten waren ook zeer waardevol, met name om tot publicatie van het cytokineproject te komen. Verder wil ik je bedanken voor de gezellige barbecues tijdens de vierdaagse en bij jullie nieuwe huis. Veel succes met je eigen onderzoeksgroep en het opzetten van immunoengineering in Eindhoven.

Roel, er wordt vaak gezegd dat immunologen en scheikundigen maar moeilijk met elkaar konden praten. In onze samenwerking heb ik daar nooit last van gehad. Vanaf het begin hadden we een goede discussies en konden we urenlang over polymeren en T-cellen praten. Nog steeds gaan onze WhatsAppvergaderingen onophoudend door en zijn deze een soort tweede labjournaal geworden. Zonder jouw polymeerexpertise en samenwerking had ik het niet gered, en ik was daarom ook erg blij dat je besloot om als postdoc bij TIL verder te gaan, zodat we onze projecten konden doorzetten. Ik denk dat het niet meer dan terecht is dat je bent toegevoegd als mijn co-promotor!

Jorieke en Dion, bedankt dat jullie mijn paranimfen willen zijn! **Jorieke**, we hebben lang samen een U'tje gedeeld en dat beviel me altijd erg goed. Ik kon altijd bij jou terecht voor goede wetenschappelijke discussies, immunologische input of gewoon een goed gesprek, bedankt daarvoor! Hopelijk kunnen we in de toekomst blijven samenwerken. **Dion**, bij jou kon ik vaak terecht om het over de chemische kant van het verhaal te hebben. Samen konden we een aantal mooie projecten met nieuwe soorten

sDCs opzetten, waarvan de afronding nu dankzij jouw doorzettingsvermogen in de chemie steeds dichterbij komt.

Tijdens mijn promotie heb ik het geluk gehad een aantal studenten te mogen begeleiden die een belangrijke bijdrage hebben geleverd aan mijn onderzoek. **Sigrid**, jij bent begonnen met het opzetten van het co-stimulatieproject dat is beschreven in hoofdstuk 4. Dit bleek toch ingewikkelder te zijn dan gedacht, maar jouw vele experimenten waren essentieel voor het begrijpen van de functie van deze moleculen. **Anne**, ook jouw werk was belangrijk om erachter te komen hoe we co-stimulerende antilichamen op polymeren konden krijgen en je hebt hier een goede start mee gemaakt. Bedankt daarvoor! **Carla**, thank you for your contributions to my thesis! You also continued working on the co-stimulation project and contributed to chapter 4, but your help in starting up the MHC project, which is described in chapter 7, was probably even more important. I enjoyed your critical scientific attitude, which will definitely help you in your future career.

Hiernaast wil ik een aantal studenten bedanken die ook een bijdrage hebben geleverd aan het werk in deze thesis. **Ruben**, ondanks dat de uitkomst van je experimenten tegenvielen, bleef je altijd enthousiast over de volgende stappen. Jouw resultaten waren belangrijk om duidelijk te maken dat er een zuiveringsmethode nodig was voor het vervolg van het onderzoek. **Bob**, jij hebt de scheikunde achter de polymeersynthese onderzocht om meerdere PICs aan elkaar vast te knopen. Helaas hebben we maar een paar kleine immunologische testen kunnen doen tijdens jouw stage en kon ik je niet overhalen om weer te gaan volleyballen. Veel succes met je carrière als DJ of scheikundige! **Tuur**, jij bedacht je eigen project tijdens een bachelorvak en je begon samen met Dion dit ook uit te voeren tijdens je stage. Hoewel het een moeilijk project was, bleef je steeds nieuwe methoden proberen, wat uiteindelijk belangrijk was voor ons om de PICs beter te begrijpen. **Marjolein**, helaas had ik door het schrijven van dit proefschrift niet veel tijd om je te helpen bij het immunologische deel van je stage. Gelukkig had je hier al ervaring in, wat heeft gezorgd voor mooie resultaten. Ik ben er van overtuigd dat de projecten die ik ben begonnen in goede handen zijn bij jou!

Furthermore, I would like to thank all (former) **TILlers** for the great atmosphere inside and outside of the lab, as well as the legendary (christmas) parties. **Martijn,** ik wil jou ook graag in het bijzonder bedanken. Toen we nog een U'tje deelden kon je me altijd goed vertellen welke vogels er langs vlogen. Bedankt ook voor je kritische blik! Wanneer er input nodig was, had je er geen probleem mee om er met gestrekt been in te komen, wat ik zeker kon waarderen! **Bas**, door jouw aanwezigheid wordt het nooit saai op het lab. Bedankt voor de hulp bij eiwitproductie en de gezelligheid en succes met het afronden van je promotie! **Eric**, of het nu om computerproblemen ging of om

het produceren van MHC-complexen of particles, jij stond altijd klaar om te helpen. De feestjes die je tijdens de vierdaagse organiseert zijn altijd weer goed! **Mika** and **Yusuf**, your vast knowledge and experience on mouse vaccination studies were essential for chapter 7 of this thesis. Thank you for the great collaboration in the *in vivo* projects. **Iris**, bedankt voor de goede sfeer in ons U'tje en voor de potjes tafeltennis! Daar moeten we er zeker meer van gaan doen de komende tijd. **Camille**, it was a pleasure writing the nature materials feature with you. Good luck with you PhD! I also want to thank the other members of the targeting DLM, **Duco, Felix, Edyta, Eliézer, Floris, Koen, Mangala, Massis, Olga Ilina, Olga Koshkina** and **Oya** for the discussions during and outside of meetings.

Subhra and **Leonie**, thank you for helping me to get started with my PhD. **Angela,** thank you for your initial work on the hydrogel project. **Florian,** your help with setting up multi-color flow cytometry panels was greatly appreciated. I always enjoyed our discussions, especially when combined with some good cheese and wine. Good luck and have fun in California! **Marcella**, I am thankful for your help in setting up antigen-specific T cell stimulation protocols. I wish you a lot of happiness with your family in Italy. **Lotte,** bedankt voor de hulp bij de Rubicon. Ook wil ik graag **Jeanette, Ilja** en **Sandy** bedanken voor alle ondersteuning!

During my PhD I had the privilege of being a member of the legendary TIL-band for several years. I would like to thank all the past members, **Christian, Ben, Martijn, Svenja, Jonas** and **Koen**, and present members, **Laurent, Glenn, Iris, Yusuf** and **Danielle**, for the great time rehearsing and playing music in the knowledge square and old cave. Thank you for accepting my mediocre keyboard skills and for giving me reason to play the piano again!

I also would like to thank some people from other departments. **Kerstin**, you put a lot of effort in improving the manuscripts Roel and I sent out for publication. Thanks to your supervision of Roel's PhD, we received a lot of valuable input in our research! **Alan** en **Jan,** bedankt voor jullie inbreng tijdens de meetings die we aan het begin van mijn promotie hebben gehad. **Joep,** ondanks wat interessante resultaten is ons gezamenlijke project nooit helemaal van de grond gekomen. Onze samenwerking heeft wel gezorgd voor goede discussies en voor het testen van verschillende mogelijke conjugatiemethoden, wat erg belangrijk was voor mijn promotieonderzoek. Bedankt daarvoor! **Abbas**, thank you for the synthesis of a cleavable peptide. Hopefully we will be able to use it soon so that we can finally publish a nice paper on it!

Ook wil ik mijn studiegenoten **Tim** en **Ralph** graag bedanken. We kwamen elkaar weer tegen tijdens de PhD introductiecursus (the sky is the limit) en het was in de

jaren daarop altijd gezellig om weer samen een biertje te drinken tijdens de PhD retreats en op Tims promotiefeestje.

Behalve binnen de wetenschap, zijn ook een aantal mensen buiten de wetenschap belangrijk geweest voor de ondersteuning en de nodige afleiding tijdens het soms stressvolle promotietraject. Om te beginnen wil ik de paarse coños van VoCASA heren 2, **Artem, Dennis, Julian, Lars, Michiel, Mick, Niels, Pieter, Roan** en **Teun,** bedanken voor alle gezellige trainingen en wedstrijden. Vooral in de afgelopen twee seizoenen hebben we mooie prestaties neergezet, zoals het winnen van de beker en het behalen van de vijfde plaats in de tweede divisie afgelopen jaar. De feestjes met jullie waren ook onvergetelijk, met als hoogtepunten natuurlijk de teamuitjes naar Budapest en Warschau. Veel succes komend seizoen! Davai!

Tom, ik ben blij dat we na 10 jaar nog steeds beachvolleybalpartners zijn! Door elke zomer hard te trainen en zoveel mogelijk toernooien af te gaan staan is ons niveau elk jaar weer wat beter geworden. Hierdoor staan we tegenwoordig niet meer bekend als Tommieboy en Loeloeman, maar als Beachteam Eggermont/Van de Grift. Vooral het weekend op Ameland is elk jaar weer een groot succes!

Sjoerd, het valt niet mee om tegelijkertijd een promotie te halen, frontman te zijn van onze binnenkort wereldberoemde band en toch de 28 te halen, maar jij doet het alsof het niets is. Het is mooi hoe je je blijft inzetten voor de acceptatie van de snoekbaars zonder een idee te hebben van de prijs van een pot pindakaas. Bedankt voor je mooie teksten en onze hoogstaande potjes pool!

Verder wil ik graag mijn vrienden van de middelbare school, **Ali, Bas, Daan, Martijn** en **Walter** bedanken. Het is mooi dat we elkaar nog altijd regelmatig zien, en dat het dan steeds toch weer (bar) gezellig is. Jullie zorgden voor de nodig afleiding en motivatie tijdens mijn promotie, bijvoorbeeld door samen bier te drinken in de polder of de stad, maar ook door een schitterprachtige en ellendige fietstocht naar Rome te maken. Hierbij werd maar al te duidelijk dat die vrije tijd eigenlijk totaal geen pretje is, en dat er niets mooier is dan werken met een kopje koffie en een gevulde koek erbij.

Jan, Anja, Oma, Sidney en **Robin,** bedankt voor de gezelligheid als we weer in de achterhoek zijn! Het is heel fijn dat ik meteen in de familie ben opgenomen. Ik heb jullie interesse in mijn werk tijdens het gourmetten of bij een kopje koffie met een stuk taart altijd op prijs gesteld. Sidney en Robin, veel geluk gewenst bij het spannende nieuwe hoofdstuk in jullie leven!

Lieve familieleden, ik ben blij dat ik in een gelukkige familie ben opgegroeid die mij altijd hebben gestimuleerd en hebben gesteund om mezelf te ontwikkelen en te doen wat ik leuk vind. Ik kijk er altijd weer naar uit om naar Kekerdom te gaan en iedereen weer te zien. Ook alle aanhangers wil ik graag bedanken. **Naud**, mijn (inmiddels niet meer zo) kleine broertje, het is mooi dat je ondertussen ook bijna bent afgestudeerd en bent gesetteld met **Lisa**, samen met Stewie en Susie. Laten we binnenkort weer eens een biertje drinken of samen gaan eten! **Wieneke**, jij bent er altijd goed in om te regelen dat de hele familie weer bij elkaar komt. Het is altijd gezellig als jij er met **Casper** weer bij bent, of het nou in Kekerdom of bij een volleybalfeestje is! **Florieke,** bedankt voor het goede voorbeeld dat je als grote zus altijd voor mij geweest bent. Het is altijd erg leuk om bij jou en **Rob** over de vloer te komen. Ook mijn kleine neefje **Jens** wil ik graag bedanken! Verder heeft **Daantje** mijn promotie gesteund met een hoop enthousiasme als ik weer in Kekerdom was. **Papa** en **mama,** jullie staan altijd voor ons klaar. Het was misschien niet altijd even duidelijk waar ik nou mee bezig was, maar hopelijk maakt dit boekje iets meer duidelijk. Bedankt voor jullie steun!

Lieve **Colet,** ondanks dat we het heen en weer reizen tussen Amsterdam en Nijmegen goed vol hebben gehouden, is het heel fijn om nu samen te wonen met jou! Het schrijven van dit boek werd een stuk makkelijker doordat we samen in hetzelfde traject zaten. Het heeft ontzettend veel geholpen dat we samen konden schrijven en samen konden klagen over schrijven. Met jouw promotie heb ik alvast een (veel te) goed voorbeeld gehad voor mijn eigen verdediging. Bedankt dat ik altijd op je liefde en steun kan rekenen! Ik kijk uit naar alle avonturen die we samen nog gaan beleven in de VS en daarna!